

University of Nottingham
Faculty of Engineering
School of Civil Engineering

Doctor of Philosophy Dissertation

Fluid Structure Interaction Modelling of Cables Used in Civil Engineering Structures

by

Neil Botterill

Supervisors: Hervé Morvan & John Owen

Nottingham, 2010

To Clare, Niamh, and George . . .

Contents

Contents	i
1 Introduction	4
1.1 Background	4
1.2 Hypothesis	6
1.3 Aims	6
1.4 Objectives	6
1.5 Methodology and Scope	7
1.6 Thesis Plan	8
2 CFD Theory and Practice	9
2.1 Introduction to CFD	9
2.2 Governing Equations	10
2.3 Discretisation	10
2.3.1 Numerical Methods	11
2.3.2 Advection Schemes	12
2.3.3 Meshing	12
2.3.4 Temporal Discretisation	14
2.4 Near Wall Modelling	15
2.5 Turbulence Models	18
2.5.1 RANS	19
2.5.2 LES	23
2.5.3 DES	26
2.6 Verification and Validation	27
2.7 Concluding Remarks	28
3 Literature Review	29
3.1 Flow past a stationary cylinder	29
3.1.1 Experimental work	29
3.1.2 Numerical Work	34
3.2 Aeroelastic Behaviour of Structures	35

3.2.1	Vortex Induced Vibration	36
3.2.2	Flutter	40
3.2.3	Galloping	40
3.2.4	Buffeting	41
3.2.5	Rain-Wind Excitation	42
3.3	Cable Dynamics	42
3.3.1	The Catenary Profile	42
3.3.2	The Parabolic Profile	43
3.3.3	The λ^2 Parameter	43
3.3.4	Relationship Between λ^2 and Modes of Vibration	44
3.4	Numerical Modelling	45
3.4.1	Discrete Vortex Method	45
3.4.2	Arbitrary Lagrangian Eulerian Formulation	46
3.4.3	Coupling	47
4	Static Cylinder	54
4.1	Introduction	54
4.2	Simulation description	54
4.3	Pre-processing recommendations	59
4.3.1	Turbulence Model	59
4.3.2	Discretisation - time step requirements	59
4.3.3	Discretisation - meshing requirements	60
4.3.4	Domain dimensions	60
4.4	Runtime of simulations	67
4.4.1	Stationarity	67
4.5	Results data	71
4.5.1	Turbulence model comparison	71
4.5.2	Blockage correction	73
4.5.3	Mean Drag	74
4.5.4	Separation	86
4.5.5	Base Pressure	89
4.5.6	Strouhal Number	94
4.6	Conclusions	99
5	Fluid Structure Interaction	101
5.1	Introduction	101
5.2	Implementation	101
5.2.1	Solver modification	101
5.2.2	Flow Diagrams	103
5.2.3	Integration methods	103
5.2.4	Verification	110
5.3	Validation	112

5.3.1	Simulation description	112
5.3.2	Reference data	114
5.3.3	Response Plots	116
5.3.4	Phase Plots	116
5.4	Conclusions	126
6	Elastically Mounted Cylinder	127
6.1	Introduction	127
6.2	One Degree of Freedom Simulations	127
6.2.1	Overview	127
6.2.2	Simulation description	128
6.2.3	Results	130
6.3	Two Degree of Freedom Simulations	133
6.3.1	Overview	133
6.3.2	Simulation description	133
6.3.3	Results	134
6.4	Concluding Remarks	151
7	General Conclusions	152
	Bibliography	155
A	User Routine Overview	163
A.1	Junction Box <code>setupdata</code>	163
A.2	Junction Box <code>setdata</code>	164
A.3	Subroutine <code>hybrid</code>	165
A.4	CEL functions <code>getdata</code>	165
A.5	Junction Box <code>writedata</code>	166
B	Additional figures from 2DOF simulations	167
B.1	[Re=90000] simulations	168
B.2	[Re=100000] simulations	188
	List of Symbols and Abbreviations	208
	List of Figures	210
	List of Tables	213

Abstract

Long, thin, flexible cylindrical elements of large scale structures are heavily influenced by the fluid flow around them. Equally, their movement has an appreciable effect on the fluid flow. This two-way interaction leads to complex dynamic behaviour that can cause fatigue and thus reduce operational lifetime. As demand for longer span bridges and drilling in deeper marine environments increases, research into the best modelling practice of this scenario gains importance.

The work described in this thesis establishes a suitable method to model in CFD aero/hydro-elastic behaviour of slender cylindrical elements in large scale structures. In order to achieve this outcome, the author has

- modelled the drag crisis on a static cylindrical element,
- developed a suitable FSI coupling program,
- combined the drag crisis model with the FSI coupling program and validate against published experimental data

The turbulence formulation used was carefully chosen taking into account the flow features that are important to the onset of the drag crisis. An LES formulation capable of adapting the model constant of the SGS model according to local shear conditions was identified as the best candidate to achieve this aim.

The fluid and structural solvers used were loosely coupled by an explicit method that achieved a balance of kinetic energy aswell as matching displacement at the moving fluid/solid interface. The integration method and implementation of this coupling strategy was verified by running a test case at low Reynolds number that produced a regular sinusoidal lift function on the cylinder that was kept stationary. The displacement, velocity, and acceleration response produced by the structural solver was compared against a closed solution and found to match with an acceptable level of error.

A number of FSI simulations with the cylinder free to move in the cross-flow direction only was carried out. The displacement response was compared against published numerical and experimental data and the importance of having a sufficient spanwise dimension of flow domain was highlighted.

Simulations with the cylinder free to move in the along-flow direction as well as cross-flow direction were carried out. In some simulations where lock-in was observed, the effect of the drag crisis was clearly seen. Energy entered into the system as a result of low drag on the upstream motion of the cylinder caused by the drag crisis. More simulations at different velocities are recommended to define a displacement response curve and make further new observations.

Acknowledgements

I wish to thank my supervisors, Hervé Morvan and John Owen, for their help, advice, and support throughout this project. I'd like also to thank David Hargreaves, another member of staff at the University of Nottingham, for his input which I found constructive and thoroughly useful.

I wish to thank the fellow students who have helped make my time at the University of Nottingham enjoyable. This includes James Walker, Graham Knapp, Sumyati Juspi, Jon Paton, and Faye Beaman. A fellow student of particular note is Sawsan Wardeh who, along with her husband Ibrahim Fahdah, have become firm friends with me and my family.

I wish to thank also the management team at Prospect Flow Solutions, my employer, who have been generous in their support during the final stages of the thesis.

I wish to express heartfelt gratitude for the unending love and support from my partner, Clare, and my parents, Alan and Isobel, without which this work would not have been possible.

Chapter 1

Introduction

1.1 Background

In the civil engineering community it is now accepted that care has to be taken in the design of slender elements, of long span bridges in particular. It is known that these are susceptible to large deflections caused by the interaction of the fluid flow of their environment with the inertial and elastic properties of the structure which can, if unchecked, be destructive. This interaction, described as aeroelastic behaviour, was initially studied as aeronautical engineering developed in the early to mid 20th century.

The link between aerodynamics and civil engineering structures was identified after the cause of the Tacoma Narrows Bridge collapse of 1940 was investigated and publicised [3]. Before then, there had been similar disasters where structures collapsed in stormy and windy conditions, such as the Tay Bridge Disaster of 1897 and the collapse of the Brighton Royal Chain Pier of 1850. In these earlier cases the cause of collapse was put down to substandard materials, substandard construction, and/or under-design of the structure. The recognised cause of the Tacoma Narrows Bridge collapse however was something else. Filmed footage of the collapse show the main deck in a twisting mode of vibration taking energy from the steady cross wind until it oscillated with sufficient force to cause structural failure and collapse.

This evidence of destructive aeroelastic behaviour led to a recognition of the need to accurately predict dynamic behaviour in the design of long span bridges. Initially this was fulfilled by the use of physical models in wind tunnels. As advances in numerical methods and computing technology have occurred however, the use of computers to solve fluid flow problems, i.e. Computational Fluid Dynamics (CFD), has become an increasingly important tool. This line of work has been pursued at the University of Nottingham in recent years (Liaw [40]).

In many industries, CFD use was promoted by the appearance and rise in popularity of commercial CFD software in the 1980s, facilitated by an increase in availability of affordable computing resources. This allowed a wider range of engineers to have access

to this technology than solely those who had the resources for in-house or bespoke code development.

A reason for the growth in use of commercial CFD software is that its generic architecture allows it to be relevant to a wide range of industries. At the heart of most popular commercial CFD codes is a complex algorithm that iteratively solves non-linear mathematical expressions that define the fundamental equations of fluid flow, heat and materials transport. Thus all that is required from the engineer who wants a solved flow field is a knowledge of the geometry, the physics, the chemistry, and some initial flow conditions and boundary conditions of the problem they wish to investigate.

Despite these positive aspects, CFD has been slow to gain acceptance by the wind engineering community. The prediction of steady and unsteady wind loading on buildings and structures, the prediction of structural response, and the prediction of air flow patterns in urban environments are demanding tasks. Wind tunnel testing is used to address these challenges, and has long been an integral part of wind engineering. At the same time the capabilities and benefits of CFD technology in this area has been somewhat limited by the size of domain and range of length scales that need to be considered. These are factors of far greater magnitude than for typical problems encountered in other fields of engineering. Thus for the moment CFD cannot be regarded as a potential replacement for wind tunnel tests.

Nevertheless the development of CFD technology has meant that its use is increasing to address problems which wind engineers struggle to simulate physically. Aeroelastic behaviour is a difficult phenomenon to reproduce in a wind tunnel. Firstly the materials used in the model must be chosen carefully in order to reflect the correct structural behaviour. Secondly, measurements of the flow field in the immediate vicinity of a moving structure are physically difficult. As a consequence some aspects of aeroelastic behaviour remain not fully understood. This has been the motivation for research using CFD technology to gain more insight in this area.

As a result of this and other types of problem that involve a coupling of fluid flow with structural dynamic behaviour, a new branch of CFD technology known as Fluid Structure Interaction (FSI) has developed. This is a new field of expertise that involves the concurrent use of fluid and structure solvers, made possible because of increases in general availability of computational resources and advances in numerical solver techniques. There are a number of ways in which FSI capability can be achieved, each appropriate to a certain type of engineering problem. The preference shown in recent work at the University of Nottingham (Liaw [40], Sun et al. [76]) has been to adapt commercially available CFD software to extend its capabilities to FSI. This is an approach that this thesis can develop further, provided it is appropriate for the work presented.

Newman and Karniadakis have successfully simulated aeroelastic behaviour of cables in cross flow [57] [56]. However these have been at low Reynolds numbers in comparison to what is experienced by cables in full scale structures like long span bridges and deep-sea riser systems typically used for offshore drilling. There is interest in a certain flow

phenomena that only occurs for high Reynolds number flows known as the drag crisis. It is so called because of an appreciable change in the drag experienced by a bluff object over a certain range of Reynolds number. Such phenomena which affect drag are considered important for the prediction of aeroelastic behaviour and fatigue life. Despite it having been researched over a long time, it is still a phenomenon which has not been fully explained. The drag crisis is difficult to investigate physically because it has been shown to be very sensitive to numerous physical parameters. For this reason, an extensive review of experimental literature on the subject by Zdravkovich [92] shows a large amount of observations that do not agree well. Numerical simulation of the drag crisis is difficult because of the range of length scales that need to be modelled. Recent numerical work presented by Holloway et al. [29], and Catalano et al. [14] demonstrate the challenges that remain to be addressed when using CFD to simulate this important phenomenon. Thus it is hoped that this thesis adds to the momentum of the increase in CFD use by wind engineers. It will achieve this by extending similar work carried out by others to CFD simulations including greater Reynolds numbers. In so doing, progress will be made in the understanding of the aeroelastic behaviour and flow features in these relatively unexplored flow conditions.

1.2 Hypothesis

Aeroelastic behaviour of large-scale flexible, slender, cylindrical elements of engineering structures can lead to problems of excessive deflection, stress, and fatigue. The proposed hypothesis is that CFD can be used to investigate dynamic behaviour of elements such as risers and bridge cables in their typical fluid flow environments and more generally the physics of the drag crisis in static and dynamic modes.

1.3 Aims

This thesis aims to extend knowledge in the following areas:

- physics of the "drag crisis", a flow phenomena common to bluff objects such as cables;
- flow mechanisms driving cable dynamics;
- the role of structural response on FSI.

1.4 Objectives

In order to achieve the aims given in § 1.3, the following objectives have been set out:

- Identify a suitable CFD software and turbulence formulation to use for the work presented in this thesis.

- Investigate the drag crisis.
- Extend functionality of CFD software to allow FSI capabilities and validate it.
- Using the FSI extended CFD software, carry out numerical simulations of flow past an elastically mounted circular cylinder, in particular in the region of the drag crisis.
- Analyse the outcome of the numerical simulations above to propose an explanation on the role of structural response on the drag crisis.

1.5 Methodology and Scope

The following points elaborate further on how each of the objectives stated in § 1.4 will be achieved:

- Carry out a series of numerical simulations of flow past a circular cylinder. Identify what combination of CFD software and turbulence model perform well by comparing results against published data by Zdravkovich [92] and Norberg [59].
- Numerically simulate the drag crisis, taking cognisance of the challenges encountered by Holloway et al. [29] and Catalano et al. [14] in their attempts to simulate the drag crisis. Compare results with those given by Zdravkovich [92] and data presented by Engineering Sciences Data Unit (ESDU) to confirm validity.
- Implement an FSI coupling strategy found by a survey of literature. Determine suitably by verification and validation. Verification will consist of running a test numerical simulation for flow conditions where the forcing on the structure is known to be simple sinusoid. The structural response given by the FSI code is compared with that calculated from a simple textbook equation predicting the same. Validation will consist of comparison against published numerical work by Saltara et al. [66] and experimental work by Khalak and Williamson [38].

A successful verification and validation of all the above work will build confidence in the final step of the thesis which is numerical simulation of cylinder crossflow in region of the drag crisis using FSI enabled code. Observations to be taken will include, but not be limited to, the following:

- Time histories of lift and drag force experienced by the cylinder
- Time histories of cross flow and in-flow displacement by the cylinder
- Location of separation points on cylinder surface over a range of instants in time
- Local velocity at cylinder surface during movement indicating the local Reynolds number.

- Eddy viscosity distribution at discrete radial locations close to the cylinder, indicating where transition from laminar to turbulent flow takes place. Ultimately, a review of these observations will be carried out and ideas for further work will be discussed.

1.6 Thesis Plan

This section concludes the first chapter that introduces the thesis. The contents of subsequent chapters are as follows.

- Chapter 2 presents an overview of CFD theory and practice that is relevant for the work presented in subsequent chapters.
- Chapter 3 presents a literature review that provides a classification of important aspects of aeroelastic and hydroelastic behaviour, cable dynamics, details of relevant numerical models and experiments, and covers specialist aspects of CFD that applies to this body of work.
- Chapter 4 presents the work carried out by the author to simulate flow past a stationary cylinder. Results are presented that demonstrate the important flow features being captured. In particular the “drag crisis” and the challenges associated with simulating this phenomenon are discussed.
- Chapter 5 presents work to extend the capabilities of a commercial CFD software to handle moving bluff body objects. Simulation results are presented and compared with experimental data for validation. Further new work is presented which involves the combination of drag crisis simulation with FSI.
- Chapter 6 presents an extension to the work carried out in the previous chapter to simulate cable dynamic behaviour. Results are presented that are compared against published experimental data.
- Chapter 7 concludes the thesis by reviewing the work described in previous chapters, discussing advantages this work achieves and areas that merit further investigation.

Chapter 2

CFD Theory and Practice

Computational Fluid Dynamics (CFD) is the use of computers for solving fluid flow problems. This section covers CFD theory and practice commonly covered by textbooks that provide an introduction to the subject, e.g. Versteeg and Malalasekera [87], Ferziger and Peric [21]. For this reason the descriptions contained herein are not intended to be exhaustive but to give an introduction to concepts and ideas that must be known in order to use commercial CFD software effectively.

More specific concepts of CFD relevant for this thesis are given in subsequent chapters.

2.1 Introduction to CFD

CFD is a relatively recent development in the history of fluid dynamics, facilitated by an increase in computing power available over the last few decades. Throughout this time, CFD practice has been advanced by improvements in the numerical methods and algorithms it employs in the solution process, as well as improvements to the tools supplied for pre and post processing. As a result, CFD theory and practice have now reached a level of sophistication where it is regarded as an indispensable tool for engineers and scientists working in numerous disciplines.

In the realm of scientific research, CFD provides insight into the physical processes of fluids, some of which are still not fully understood today. Studies of increasing complexity have been carried out in recent years and it would be reasonable to assume that if this trend continued, further breakthroughs in the understanding of these processes would be inevitable.

The use of CFD has become commonplace in a variety of engineering fields. Originally solely used in aeronautics, it has now spread to diverse areas such as chemical, civil, mechanical, and nuclear engineering, and meteorology.

2.2 Governing Equations

The set of equations that provide the cornerstone of CFD analysis are known collectively as the Navier Stokes Equations (NSEs), named after two people who formulated them independently in the 19th century. Despite these equations having been formulated so long ago, their complexity is such that even today they cannot be solved directly for most fluid flow problems encountered in engineering.

The NSEs for a compressible Newtonian fluid are represented here by equations 2.1a, 2.1b, and 2.1c. They express the physical laws of conservation of mass, momentum, and energy respectively.

$$\frac{\partial \rho}{\partial t} + \nabla \cdot (\rho \mathbf{u}) = S_A \quad (2.1a)$$

$$\frac{\partial(\rho u_i)}{\partial t} + \nabla \cdot (\rho u_i \mathbf{u}) = -\frac{\partial p}{\partial x_i} + \nabla \cdot (\mu \nabla u_i) + S_{Mi} \quad (2.1b)$$

$$\frac{\partial(\rho \iota)}{\partial t} + \nabla \cdot (\rho \iota \mathbf{u}) = -p \nabla \cdot \mathbf{u} + \nabla \cdot (\kappa \nabla T) + \Phi + S_I \quad (2.1c)$$

where ρ is density of the fluid, t is time, \mathbf{u} is the velocity vector of the fluid (whose components are u_i), x_i is the length dimension, μ is dynamic viscosity of the fluid, ι is the internal energy of the fluid, κ is the thermal conductivity of the fluid, T is the temperature of the fluid, and Φ is a dissipation function that describes the internal energy effects due to viscous stresses in the fluid. S_A , S_{Mi} and S_I are source terms for mass, momentum, and energy respectively. The i suffix means ‘in the i^{th} dimension’, hence for a problem set in a three-dimensional cartesian coordinate system there will be three sets of equation 2.1b, one for each orthogonal direction. The derivation of these equations can be found in most CFD textbooks, notably Versteeg and Malalasekera [87].

This thesis is concerned with fluid flow problems where the flow speed is low enough for the fluid to be considered incompressible, i.e. $|\mathbf{u}|$ is less than Mach 0.3. Also there is no heat transfer in the problems considered. Thus the numerical work presented here does not involve the solution of equation 2.1c. The fluid field is solely described by the incompressible formulations of equations 2.1a and 2.1b, as given here:

$$\nabla \cdot \mathbf{u} = S_A \quad (2.2a)$$

$$\frac{\partial u_i}{\partial t} + \nabla \cdot (u_i \mathbf{u}) = -\frac{1}{\rho} \frac{\partial p}{\partial x_i} + \nabla \cdot (\nu \nabla u_i) + S_i \quad (2.2b)$$

where ν is the kinematic viscosity ($\nu = \mu/\rho$), and S_i is a source term.

2.3 Discretisation

The NSEs are non-linear Partial Differential Equations (PDEs) which are too difficult to solve directly except in a few simple cases where the boundary conditions applied sufficiently simplify the problem. *Discretisation* is the process of representing the fluid

flow at a finite number of points. For the purpose of rendering the problem into a set of Ordinary Differential Equations (ODEs) that are easier to solve, a variety of numerical methods can be used.

It is worth noting that this process does not solve the NSEs directly but instead solves a representation of them and thus error is introduced. In order to maintain confidence in the method, the nature of this error must be known and its magnitude estimated.

2.3.1 Numerical Methods

There are many different numerical methods used for CFD. These include the Finite Difference Method (FDM), the Finite Volume Method (FVM), the Finite Element Method (FEM), the Control Volume based Finite Element Method (CVFEM), spectral methods, boundary element methods and meshless methods. The work presented in this thesis is based on solely the use of CFD solvers that are commercially available, so only the numerical methods relevant to them are discussed here.

Finite Volume Method FVM is the most popular approach used in CFD. In this process, each discrete node represents a volumetric region surrounding it. Each node carries a value of the properties flowing through this region. The values are derived by considering them as transported fluxes across the faces of the surrounding volumes and applying the rule that the sum of inflowing properties are balanced exactly by those flowing out. An advantage of this method is that it is more ‘intuitive’ than other methods.

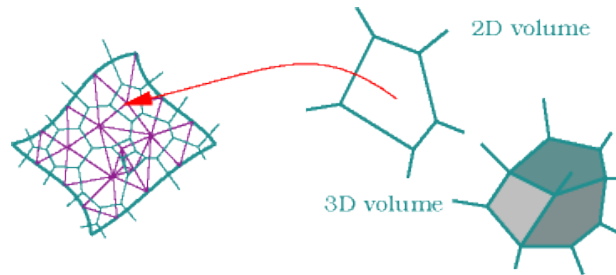


Figure 2.1: Grid topology for FVM

Finite Element Method FEM was developed initially for structural analysis problems, but its use has since extended into other fields of engineering, including CFD. It works on a variational formulation of the PDEs and boundary conditions that describe the problem. The volumetric region occupied by the fluid is split into a finite number of interconnecting elements. A simple basis function is given to each of these volumetric elements from which, using the variational formulation of the problem, a piecewise function of the solution is constructed. The basis function that is implemented and the solution function that results from it can in theory be of any order. For the sake of simplicity of calculation

however they are usually taken to be linear and if this is the case the solution can be defined solely by the values found at the vertices of each element.

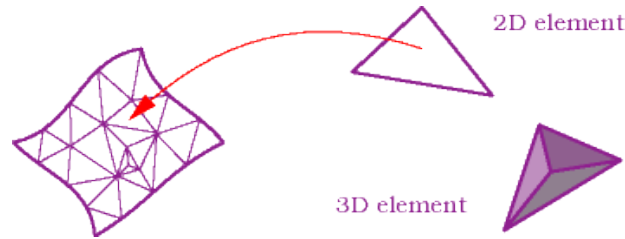


Figure 2.2: Grid topology for FEM

Control Volume based Finite Element Method CVFEM can be regarded as a hybrid of FVM and FEM. Just as for FEM the fluid volumetric region is split into a number of interconnecting elements. For each of the vertices, a control volume is constructed by linking the centroid of each of the surrounding elements and the midpoints of the connecting faces.

Just as for FVM, the vertices carry the values of the solution fields. In addition, however, shape functions are applied to the elements to give the gradient of the solution fields. The fluxes through the surfaces of the control volumes are calculated on a per-element basis.

This is the approach used in the commercial software used for the work presented in this thesis.

2.3.2 Advection Schemes

There is a range of different schemes that the solver can use to discretise the advection term of the transport equations. Choices commonly found in commercial software include upwind, central difference, and Quadratic Upstream Interpolation for Convective Kinetics (QUICK). Some schemes have particular requirements for mesh topology in terms of resolution, alignment of cell faces and nodes, and whether it is structured. The schemes which have comparatively stringent requirements may have to be ruled out if the mesh cannot be adapted to satisfy these.

It is important to choose a scheme that is well suited to the mesh and turbulence model. An inappropriate scheme can lead to over-diffusion problems. For simulations using an Large Eddy Simulation (LES) turbulence model in particular, it has been demonstrated that a second order central differencing scheme is required to ensure turbulence is sustained to an acceptable level (Montavon et al. [52]).

2.3.3 Meshing

Whichever numerical method is used there is a requirement of skill in assembling an appropriate mesh. A mesh that is too coarse can lead to a quick solution but will not

by an increment or decrement to any of the integers. The geometric requirements demanded by a structured solver are more prohibitive than those of an unstructured solver, therefore it can only deal with problems that have relatively uncomplicated geometries. The simpler way in which structured solvers deal with geometries does however require less computational effort.

The more popular of the range of commercial CFD software include unstructured solvers because the ability to deal with complex geometries is important for commercial success. Although there is the drawback of extra computational effort being necessary for unstructured solvers, this has been mitigated by advances in numerical methods and increased availability and cheapness computational of resources over time. It is worth noting that hexahedral meshes can be used with unstructured solvers and this too can produce savings in computational effort. Since a hexahedral cell can occupy more space than a tetrahedral cell of similar dimensions, fewer cells of a hexahedral mesh are required than a tetrahedral mesh of the same problem. Thus although hexahedral meshes would be treated in an unstructured way, their use would keep computational effort to a minimum.

Regardless of the type of solver used and the shape of the cells used in the mesh, a third type of shape is commonly used at the boundaries of a fluid domain where near-wall resolution is important. They are flat slab-like elements made up of 6-noded triangular prisms or 8-noded hexahedra which are stacked together and aligned with their shorter dimension in the wall normal direction in order to achieve an appropriate level of resolution close to the wall. In accordance with boundary layer theory discussed further in this chapter, special treatment is applied to the modelling of fluid close to solid boundaries. The nature of this near wall modelling is dependent on the turbulence model used, of which there is a wide variety (as is also discussed further in this chapter).

2.3.4 Temporal Discretisation

Some flow problems require a solution that is time varying in order to capture transient phenomena, e.g. vortices shed intermittently from bluff objects. This is achieved by the solver producing a solved flow field at instants in time which are, effectively speaking, a set of 'snapshots' of the transient solution. Each 'snapshot' is used as an initial condition for the flow field at the next instant to be solved. Thus the solver works through the problem on a consecutive chronological basis. This approach to solving transient problems is effectively a discretisation of those terms of the governing equations that include the time variable. Thus it should be regarded as another source of error similar to those introduced with other types of discretisation discussed in this chapter.

Resolution of the solution in the time dimension is controlled by the spacing of the 'snapshots' produced by the solver, i.e. the time step. As is similar to the choice of cell spacing in a mesh, care should be taken in the choice of time step size. A time step inappropriately small for the flow problem will lead to unnecessary computational effort. A time step size too large can cause the solver to miss out the transient flow features

that are needed to be captured, can introduce error to an extent where the solution is of little or no value, and can threaten the stability of the numerical method used.

The way in which prior 'snapshots' are used to obtain a solution field to a time instant is important to the stability of the solving process. There are numerous schemes to choose from but all of them fall into two main categories: implicit and explicit.

Explicit methods calculate the solution of a flow field at a given instant using the solved flow fields of previous instants. Implicit methods calculate a solution using equations that include data from the current instant as well as previous instants. To express this mathematically, taking $X(t)$ as a known flow field state at time t , and $X(t + \Delta t)$ as an unknown flow field state at an instant Δt later than t , an explicit method takes the form:

$$X(t + \Delta t) = F(X(t))$$

while for an implicit method, the form would be:

$$G(X(t), X(t + \Delta t)) = 0$$

Seeing as the variables to be solved are included in an implicit formulation, they are harder to implement and require more computational effort to solve for each time step.

Many problems of engineering interest are 'stiff' i.e. they require a small time step to solve within bounds of numerical stability. For these types of problem, explicit methods require a much smaller time step than is required for implicit methods to keep error in the result bounded. This difference in time step requirements is often so pronounced that it takes less computational time to solve using an implicit method than for an explicit method. Thus implicit methods tend to be more popular.

The mesh cell size is another consideration for the allowable size of time step. In most cases it would be ideal to avoid the possibility of the time step being large enough for a fluid particle to travel entirely through one or more cells from one solution step to the next. The *Courant number* is the time step size divided by the residence time of a fluid particle in a cell. Expressed mathematically for a one-dimensional case, the Courant number would be

$$\frac{u \cdot \Delta t}{\Delta x}$$

where u is the velocity, Δt is the time step, and Δx is the cell length dimension. Ideally this number should never be above 1.

2.4 Near Wall Modelling

Special consideration of what happens in a fluid close to a solid boundary began over a century ago. A German mathematician, Prandtl, developed what has come to be known as *Boundary Layer Theory*. Up until then, a major drawback with fluid theory was that it could not account for drag forces experienced by objects in a flow field. Boundary layer theory splits fluid flow around an object into two regions. One region is the free-stream where no appreciable variation of velocity caused by the object is observed. The other

region is close to the boundary of the object where the local fluid velocity is very much influenced by the object.

The shape of the velocity profile throughout the boundary layer is usually defined in terms of two dimensionless variables u^+ and y^+ , relating to local velocity scalar U and distance from wall y respectively. Close to the wall the velocity is considered to be only influenced by fluid density ρ , viscosity μ , and wall shear stress τ_w . Derived using dimensional analysis, expressions for u^+ and y^+ are as follows:

$$u^+ = U/u_\tau$$

$$y^+ = \frac{\rho u_\tau y}{\mu}$$

where u_τ is known as the friction velocity defined as $u_\tau = \sqrt{\tau_w/\rho}$. The relationship $u^+ = f(y^+)$ is commonly referred to as the *law of the wall*. The function $f(y^+)$ varies according to which predominates between viscous, turbulent and inertial forces. Between the solid surface and the nearest position where the local velocity matches the free-stream value, three layers are commonly identified viz. the *linear sub layer*, the *log-law layer*, and the *outer layer*. A separate law of the wall exists for each of these layers, their definitions follow.

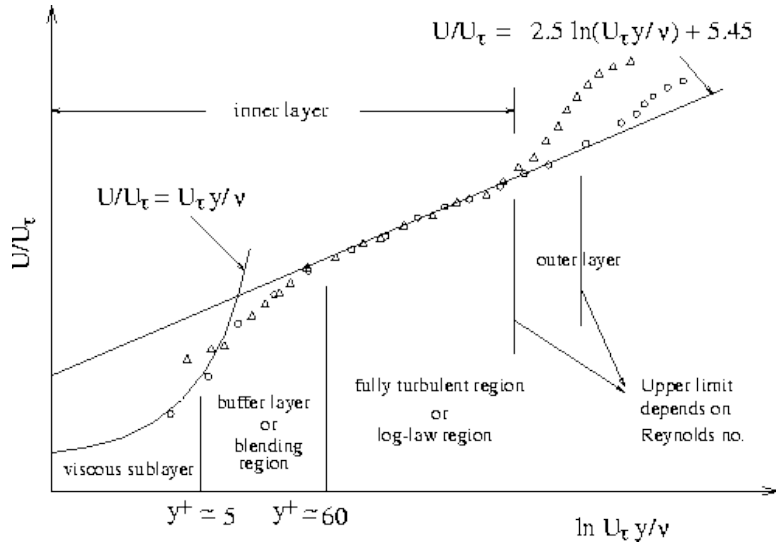


Figure 2.4: Typical layers found in a boundary layer

In the *linear sub layer* the flow is dominated by viscous shear. In practice this is extremely thin so the shear stress throughout is assumed to be the same as the wall shear stress. This leads to the simple linear relationship defined by

$$u^+ = y^+$$

In the *log-law layer*, turbulent as well as viscous effects are important. Empirical terms are included in the law of the wall relationship to account for turbulent effects and

wall roughness, \varkappa and B respectively. The log-law relationship is defined by

$$u^+ = \frac{1}{\varkappa} \ln y^+ + B$$

In the *outer layer* inertia effects are dominant. It is more convenient for the velocity profile definition to be given in terms of how much it differs from the free stream velocity U_{max} and for this reason it is known as the *velocity defect law*. Fluid viscosity μ no longer plays a part in this relationship and it is replaced by the boundary layer thickness δ as a dependent variable. The velocity defect law is thus defined by

$$\frac{U_{max} - U}{u_\tau} = \frac{1}{\varkappa} \ln \frac{y}{\delta} + A$$

where A is a constant.

Other wall functions exist for turbulent quantities and heat transfer. They vary according to which turbulence model is used (see § 2.5).

Since the velocity gradient at a surface is usually very steep, a very refined mesh would be required to resolve this properly. In earlier days of CFD, this would use up the limited computer resources available and so was not practical. As an alternative the influence of the wall is simulated with the use of wall functions. The choice of which function to use is based on the distance of the first grid node away from the wall. Generally if the y^+ value of the first node is less than 11.63 then the functions relevant to the linear sub layer are used and if greater than 11.63 the functions relevant to the log-law layer are used. The y^+ value of 11.63 is based on the point where the wall functions for the two layers coincide.

A useful aspect of boundary layer theory is its ability to predict *flow separation*. An adverse pressure gradient can reduce the velocity gradient at a surface and in certain flow situations the velocity gradient can be reduced to zero.

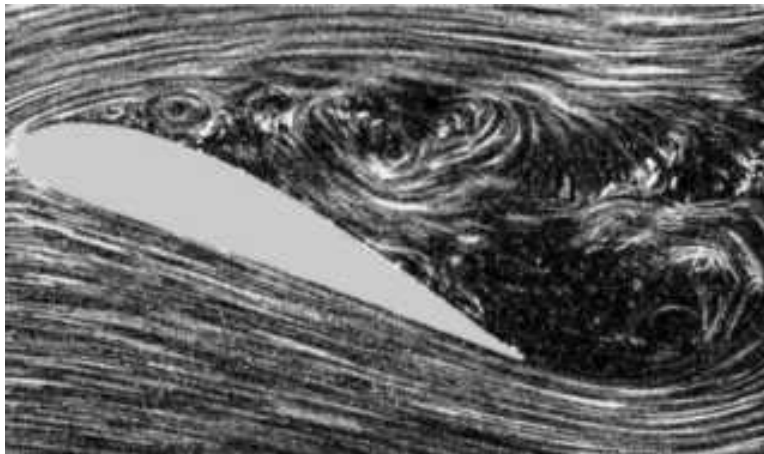


Figure 2.5: Airflow separating from an airfoil at a high angle of attack

When this occurs the boundary layer lifts off the surface and rolls up into vortices downstream. An example of this can be seen in Figure 2.5 which shows airflow separating

from the leading edge of the upper surface of an airfoil. This is an important flow feature since it is responsible for the drag signal experienced by bluff objects.

2.5 Turbulence Models

Many flows in nature exhibit a degree of turbulence which can be observed easily. The plume of a smoke stack or cumulus clouds are typical examples. Tennekes and Lumley [81] give a very thorough introduction to the subject but concede that it is very difficult to give a precise definition of turbulence. It is easier to describe turbulence in terms of its main characteristics which are irregularity, diffusivity, large Reynolds Numbers, and dissipation.

The *irregularity* or randomness of turbulent flows require that generally they are treated in a statistical sense. Of course a direct solution process of the NSEs is a way of treating turbulent flows in a deterministic sense, but this approach known as Direct Numerical Simulation (DNS) is not practical for general use because of the vastness of resources required to solve even simple flow problems. It is fortunate then that most CFD users are not interested in the details of every swirl and eddy in a solution and are happy to deal with turbulence characteristics in more general terms. Thus simplified models to simulate the effects of turbulence are allowed as a viable alternative to DNS.

Diffusivity is a feature of turbulence that causes rapid mixing and increased rates of momentum, heat and mass transfer. For airfoils and bluff objects this is an important concept because turbulent boundary layers tend to have a more even spread of momentum across their thickness than laminar boundary layers. As a result turbulent boundary layers are more resistant to adverse pressure gradients and are therefore less prone to separation.

Turbulent flows occur at *high Reynolds Numbers*. The Reynolds Number is the ratio of the inertial force magnitude to viscous force magnitude in a given flow condition. Expressed mathematically, the Reynold number Re , is defined as $Re = \frac{UD}{\nu}$, where U is a reference velocity (usually freestream velocity), D is a reference length dimension (cylinder diameter for the present work), and ν is the kinematic viscosity of the fluid. When the Reynolds Number is low, viscous forces are large in comparison to inertial forces and dampen any flow instabilities, thus forcing the flow to be laminar. As the Reynolds number increases inertial forces become more dominant, leading to the production of swirls, eddies and other flow fluctuations. At a critical value of Reynolds number, these fluctuations have enough momentum to overcome the viscous damping effect and so they lead to the onset of turbulence.

Turbulent flows require a constant supply of energy to keep them going. Without this supply turbulence dies out quickly because of its *dissipation* characteristics. The energy processes in turbulence are commonly regarded as a cascade which begins with the largest swirls and eddies extracting kinetic energy from the main flow. Viscous shear stresses perform deformation work at the expense of this energy so some of it is dissipated as heat

and the rest of it is passed on to swirls and eddies of smaller length scales. This process continues for an ever decreasing set of length scales until all the energy is dissipated as heat.

The following sections introduce the most common formulations used in external aerodynamics, with a stronger emphasis on LES, used in the later work.

2.5.1 RANS

The NSEs can be reformulated with the velocity and pressure terms split into a steady part* and a fluctuating part, i.e. $\mathbf{u} = \bar{\mathbf{u}} + \mathbf{u}'$, $p = \bar{p} + p'$. This formulation, commonly known as the RANS equations, can be found in most CFD textbooks, including Versteeg and Malalasekera [87].

The RANS equations look very similar to the NSEs, with all the velocity and pressure terms replaced by their steady components. The one important difference to observe is the appearance of an extra term in the conservation of momentum member of the NSEs which expresses the momentum flux related to the fluctuating velocity. This extra expression is a tensor whose components are all permutations of $\overline{\rho u'_i u'_j}$, known collectively as *Reynolds Stresses*.

The appearance of Reynolds Stresses in the RANS equations mean that there are a greater number of unknowns than the number of equations available to solve them, i.e. there is a *closure problem*. Therefore the Reynolds Stresses have to be approximated in some way. An equation used in the course of this approximation is as follows:

$$\overline{\rho u'_i u'_j} = \frac{2}{3} \rho k \delta_{ij} - \mu_t \left(\frac{\partial \bar{u}_i}{\partial x_j} + \frac{\partial \bar{u}_j}{\partial x_i} \right) \quad (2.3)$$

where k is turbulent kinetic energy, and μ_t is the eddy viscosity. In equation 2.3, the term including the Kronecker delta δ_{ij} distributes an equal third of the kinetic energy across the three normal components of the Reynolds stresses, implying isotropic turbulence. In the case of flow past cylinders, this assumption is not correct and thus will adversely affect the quality of prediction. To account for the anisotropy of the turbulence a higher order formulation of equation 2.3 can be used. This has not been implemented in all commercial CFD software however.

Two Equation Models

Two equation turbulence models achieve closure of the RANS equations by modelling two scales relating to turbulence. One is a velocity scale q , and the other is a length scale L . The variable used for velocity scale is commonly the turbulent kinetic energy k , defined as $k = \frac{1}{2} u'_i u'_i$. Thus q is set to $q = \sqrt{k}$. The variable used for length scale can vary among two equation models.

*Steady over the time frame it is averaged, however this value can still be a function of time in unsteady Reynolds Averaged Navier Stokes (RANS) simulations. Time averaged variables are indicated by an overline in this section.

The definition of μ_t , the eddy viscosity, takes the following general form:

$$\mu_t = C\rho qL \quad (2.4)$$

where C is a model constant.

K-Epsilon Formulation The $k\epsilon$ model uses turbulent kinetic energy k for the velocity scale, and turbulent dissipation ϵ for the length scale. Turbulent dissipation is related to length scale L by $L = k^{3/2}/\epsilon$, thus equation 2.4 becomes:

$$\mu_t = C_\mu \rho \frac{k^2}{\epsilon} \quad (2.5)$$

where C_μ is usually set to 0.09.

k and ϵ are defined in a flow domain by the following two transport equations which are solved alongside the RANS equations.

$$\frac{\partial(\rho k)}{\partial t} + \nabla \cdot (\rho k \bar{\mathbf{u}}) = \nabla \cdot \left[\left(\mu + \frac{\mu_t}{\sigma_k} \right) \nabla k \right] + P_k - \rho \epsilon \quad (2.6a)$$

$$\frac{\partial(\rho \epsilon)}{\partial t} + \nabla \cdot (\rho \epsilon \bar{\mathbf{u}}) = \nabla \cdot \left[\left(\mu + \frac{\mu_t}{\sigma_\epsilon} \right) \nabla \epsilon \right] + C_{1\epsilon} \frac{\epsilon}{k} P_k - C_{2\epsilon} \rho \frac{\epsilon^2}{k} \quad (2.6b)$$

where S_{ij} is the rate of strain tensor as defined in equation 2.7, P_k is the production term as defined in equation 2.8, and the model constants are usually set as follows: $\sigma_k = 1.00$, $\sigma_\epsilon = 1.30$, $C_{1\epsilon} = 1.44$, $C_{2\epsilon} = 1.92$.

$$S_{ij} = \frac{1}{2} \left(\frac{\partial \bar{u}_i}{\partial x_j} + \frac{\partial \bar{u}_j}{\partial x_i} \right) \quad (2.7)$$

$$P_k = 2\mu_t S_{ij} \cdot S_{ij} - \frac{2}{3} \rho k \frac{\partial \bar{u}_i}{\partial x_j} \delta_{ij} \quad (2.8)$$

It is stated in literature (e.g. [87]) that $k\epsilon$ models provide poor performance in flows with large extra strains, i.e. curved boundary layers, which is certainly the case for flow past circular cylinders.

K-Omega Formulation The $k\omega$ model proposed by Wilcox [88] uses turbulent kinetic energy k for the velocity scale, and turbulent frequency ω for the length scale. Turbulent frequency is related to length scale L by $L = \sqrt{k}/\omega$, thus equation 2.4 becomes:

$$\mu_t = \rho \frac{k}{\omega} \quad (2.9)$$

k and ω are defined in a flow domain by the following two transport equations which are solved alongside the RANS equations:

$$\frac{\partial(\rho k)}{\partial t} + \nabla \cdot (\rho k \bar{\mathbf{u}}) = \nabla \cdot \left[\left(\mu + \frac{\mu_t}{\sigma_k} \right) \nabla k \right] + P_k - \beta^* \rho k \omega \quad (2.10a)$$

$$\begin{aligned} \frac{\partial(\rho \omega)}{\partial t} + \nabla \cdot (\rho \omega \bar{\mathbf{u}}) = & \nabla \cdot \left[\left(\mu + \frac{\mu_t}{\sigma_\omega} \right) \nabla \omega \right] + \alpha \left(2\rho S_{ij} \cdot S_{ij} - \frac{2}{3} \rho \omega \frac{\partial \bar{u}_i}{\partial x_j} \delta_{ij} \right) \\ & - \beta \rho \omega^2 \end{aligned} \quad (2.10b)$$

The model constants are usually set as follows: $\sigma_k = 2.0$, $\sigma_\omega = 2.0$, $\alpha = 0.556$, $\beta_1 = 0.075$, $\beta^* = 0.09$.

The $k\omega$ model provides a more accurate and robust model than the $k\epsilon$ model in near-wall regions. However it is very sensitive to free stream conditions, so any alteration in ω at the inlet can produce a large variation in results.

Shear Stress Transport (SST) Formulation In an attempt to blend the best and discard the worst of the qualities of the $k\epsilon$ and the $k\omega$ models, Menter [49] introduced the SST model. The $k\epsilon$ model is used in the free stream but approaching the wall the $k\omega$ is gradually introduced with a blending function.

The transport equations for this formulation are as follows:

$$\frac{\partial(\rho k)}{\partial t} + \nabla \cdot (\rho k \bar{\mathbf{u}}) = \nabla \cdot \left[\left(\mu + \frac{\mu_t}{\sigma_k} \right) \nabla k \right] + P_{k\text{SST}} - \beta^* \rho k \omega \quad (2.11a)$$

$$\begin{aligned} \frac{\partial(\rho \omega)}{\partial t} + \nabla \cdot (\rho \omega \bar{\mathbf{u}}) = & \nabla \cdot \left[\left(\mu + \frac{\mu_t}{\sigma_\omega} \right) \nabla \omega \right] + \alpha \left(2\rho S_{ij} \cdot S_{ij} - \frac{2}{3} \rho \omega \frac{\partial \bar{u}_i}{\partial x_j} \delta_{ij} \right) \\ & - \beta \rho \omega^2 + 2(1 - F_C) \frac{\rho}{\sigma_{\omega,2\omega}} \frac{\partial k}{\partial x_k} \frac{\partial \omega}{\partial x_k} \end{aligned} \quad (2.11b)$$

where F_C is a function based on L/y and Re_y the Reynolds Number based on y the distance to the wall, and $P_{k\text{SST}}$ is the production term for kinetic energy defined in equation 2.14.

It can be seen that the transport equation for k remains the same as for the $k\omega$ model while the the transport equation for ω has slight differences, including the addition of an extra term on the right hand side. The derivation of equation 2.11 is based on the identities $\epsilon = C_\mu k \omega$, and $\beta^* = C_\mu = 0.09$.

The blending function ensures a smooth transition of the value of μ_t as one passes from the $k\epsilon$ region in the free stream to the $k\omega$ region close to the wall. It is applied to the following model constants: $\alpha_1 = 0.556$, $\beta_1 = 0.075$, $\sigma_{k1} = 1.176$, $\sigma_{\omega1} = 2.0$, $\alpha_2 = 0.44$, $\beta_2 = 0.0828$, $\sigma_{k2} = 1.0$, $\sigma_{\omega2} = 0.856$.

The general form of the blending function is as follows:

$$C_{\text{SST}} = F_C C_1 + (1 - F_C) C_2 \quad (2.12)$$

where C_{SST} is the blended model constant based on C_1 and C_2 the above respective model constants with 1 and 2 included in their suffixes.

Limiters are applied to the expressions for μ_t and P_k to improve performance in flows with adverse pressure gradients, wake regions, and stagnation regions, all of which exist in flows past circular cylinders. Thus equations 2.8 and 2.9 are rewritten as follows:

$$\mu_t = \frac{a_1 \rho k}{\max(a_1 \omega, SF_2)} \quad (2.13)$$

where a_1 is a constant and F_2 is a blending function.

$$P_k = \min \left(10\beta^* \rho k \omega, 2\mu_t S_{ij} \cdot S_{ij} - \frac{2}{3} \rho k \frac{\partial \bar{u}_i}{\partial x_j} \delta_{ij} \right) \quad (2.14)$$

SAS Formulation The Scale-Adapting Simulation (SAS) model proposed by Menter et al. [51] uses turbulent kinetic energy k for the velocity scale, and a variable Φ for the length scale.

Variable Φ is related to length scale L by $\Phi = \sqrt{k}L$, thus the expression for μ_t becomes:

$$\mu_t = C_\mu^{1/4} \rho \Phi \quad (2.15)$$

C_μ is also used in equation 2.16a.

k and Φ are defined in a flow domain by the following two transport equations which are solved alongside the RANS equations:

$$\frac{\partial(\rho k)}{\partial t} + \nabla \cdot (\rho k \bar{\mathbf{u}}) = \nabla \cdot \left[\frac{\mu_t}{\sigma_k} \nabla k \right] + P_k - c_\mu^{3/4} \rho \frac{k^2}{\phi} \quad (2.16a)$$

$$\frac{\partial(\rho \Phi)}{\partial t} + \nabla \cdot (\rho \Phi \bar{\mathbf{u}}) = \nabla \cdot \left[\frac{\mu_t}{\sigma_\Phi} \nabla \Phi \right] + \zeta_1 \frac{\Phi}{k} P_k - \hat{\zeta}_2 \mu_t S_{ij} |U''| \frac{\Phi^2}{k^{3/2}} - \zeta_3 \rho k \quad (2.16b)$$

where P_k , $\hat{\zeta}_2$, $|L'|$, and $|U''|$ are defined by equations 2.17a, 2.17b, 2.17c, and 2.17d respectively

$$P_k = 2\mu_t S_{ij} \cdot S_{ij} - \frac{2}{3} \rho k \frac{\partial \bar{u}_i}{\partial x_j} \delta_{ij} \quad (2.17a)$$

$$\hat{\zeta}_2 = \zeta_2 \max \left(c_{\text{SAS}}, \left| \frac{L'}{\kappa} \right| \right) \quad (2.17b)$$

$$|L'| = \sqrt{\frac{\partial L}{\partial x_j} \frac{\partial L}{\partial x_j}} \quad (2.17c)$$

$$|U''| = \sqrt{\frac{\partial^2 \bar{u}_i}{\partial x_j \partial x_j} \frac{\partial^2 \bar{u}_i}{\partial x_k \partial x_k}} \quad (2.17d)$$

The constants in equations 2.16a and 2.16b usually take the following values: $\zeta_1 = 0.8$, $\zeta_2 = 3.51$, $\zeta_3 = 0.0326$, $\sigma_k = 2/3$, $\sigma_\Phi = 2/3$, $C_\mu = 0.09$, $\kappa = 0.41$, $c_{\text{SAS}} = 0.5$.

The unique feature of this model is that the length scale L predicted is proportional to the size of the resolved eddies in a flow. On the other hand, the length scale of most other two equation models is proportional to the thickness of the shear layer. Thus it is claimed by Menter et al. [50] that the length scale in the SAS model can adjust to local flow topology where other models cannot. This results in the appearance of LES-like flow structures in unsteady parts of the flow field.

SAS-SST Formulation Menter and Egorov [48] provide SAS functionality to the SST model by reformulating equation 2.16b based on the identity $\Phi = c_\mu^{-1/4} k/\omega$. The resulting equation reads:

$$\frac{\partial(\rho \omega)}{\partial t} + \nabla \cdot (\rho \omega \bar{\mathbf{u}}) = \nabla \cdot \left[\frac{\mu_t}{\sigma_\omega} \nabla \omega \right] + \alpha \rho S^2 - \beta \rho \omega^2 + F_{\text{SST-SAS}} \quad (2.18)$$

where $F_{\text{SST-SAS}}$ is a function that imposes the SST model in steady parts of the flow while ensuring the SAS regime in unsteady flow regions:

$$F_{\text{SST-SAS}} = \rho \cdot F_{\text{SAS}} \max \left[\tilde{\zeta}_2 \kappa S^2 \frac{L}{L_{vK}} - \frac{2}{\sigma_\Phi} k \cdot \max \left(\frac{1}{\omega^2} \frac{\partial \omega}{\partial x_j} \frac{\partial \omega}{\partial x_j}, \frac{1}{k^2} \frac{\partial k}{\partial x_j} \frac{\partial k}{\partial x_j} \right), 0 \right] \quad (2.19)$$

The von Karman length scale, L_{vK} , in equation 2.19 is defined as follows:

$$L_{vK} = \kappa \left| \frac{\partial U / \partial y}{\partial^2 U / \partial y^2} \right| \quad (2.20)$$

The model constants for the above equations usually take the following values: $F_{\text{SAS}} = 1.25$, $\tilde{\zeta}_2 = \zeta_2 \cdot c_{\text{SAS}} = 1.755$, $\sigma_\Phi = 2/3$.

2.5.2 LES

LES involves a full deterministic DNS type analysis of the large scale fluctuations of the flow and a RANS type model applied to the smaller scales. This is justified by considering that since the energy cascade generally only goes in one direction i.e. from the largest scales to the smallest, applying a model to the smaller scales will not have an adverse effect on the accurate simulation of the larger scales. Thus there is no approximation of mass and momentum transfer since this mostly occurs in the larger scales of turbulence and satisfactory results are achieved without the expensive cost of DNS.

The concept of *filtering* determines which scales to resolve and which to model. A local average \bar{u}_i of velocity u_i in the vicinity of length coordinate x_i is shown in equation 2.21,

$$\bar{u}_i = \int_{-\infty}^{\infty} u_i(x_i - r) G(r) dr \quad (2.21)$$

where $G(r)$ is a filter function that smooths the local variations of velocity based on local spatial variable r .

There are a number of different forms of filter function, the two most common being the *box* filter and the *Gaussian* filter. The box filter is defined by equation 2.22,

$$\begin{aligned} G(r) &= 1/L & |r| < L/2 \\ G(r) &= 0 & |r| > L/2 \end{aligned} \quad (2.22)$$

where L is the length limit over which the averaging is performed. The Gaussian filter is defined by equation 2.23.

$$G(r) = \frac{\exp(-r^2/L^2)}{\pi^{1/2}L} \quad (2.23)$$

Whatever filter is used, L is commonly linked to the grid size when finite volume or finite element methods are employed. Thus the filter width is an additional consideration when creating a mesh for LES. With this in mind it is generally considered undesirable to use a mesh with irregularly sized cells. Fröhlich et al. [23] discuss the potential problems of turbulent eddies advecting through a mesh of varying resolution. In the tests that they carry out, they observe that as a flow travels from a region of coarse resolution to

a region of finer resolution, turbulent eddy dissipation is under-estimated and turbulent kinetic energy is over-estimated. Because of this it is considered better to introduce gradual variations rather than abrupt changes in filter width wherever possible. These problems do not occur in the case of eddies travelling from finely resolved regions to coarser regions, which is encouraging when considering the meshes that will be used in the wake of cylinders. Generally at high values of Reynolds number, turbulent eddies will form in the finely resolved boundary layer before travelling to a coarser mesh downstream.

The conservation of momentum member of the NSEs can be rewritten to include spatially averaged terms for velocity and pressure, as shown in equation 2.24. From this point forward, the overline in any equation indicates spatial averaging and not time averaging.

$$\frac{\partial(\rho\overline{u_i})}{\partial t} + \nabla \cdot (\rho\overline{u_i\mathbf{u}}) = -\frac{\partial\overline{p}}{\partial x_i} + \nabla \cdot (\mu\nabla\overline{u_i}) - \nabla \cdot (\rho[\overline{u_i\mathbf{u}} - \overline{u_i}\overline{\mathbf{u}}]) + S_i \quad (2.24)$$

This equation appears very similar to the equivalent formulation used for RANS models but it must be remembered that this equation consists of *spatial* averages whereas the RANS equivalent contain time averaged properties. The largest difference between them is the term that replaces the Reynolds Stresses. The new term now includes $\rho[\overline{u_i u_j} - \overline{u_i}\overline{u_j}]$ which are known as *residual stresses* or *sub-grid scale Reynolds stresses*. The application of models to represent these stresses is known as Sub Grid Scale (SGS) modelling.

Smagorinsky Model

The most popular way to account for the residual stresses τ_{ij} , is to use a form of eddy-viscosity model known as the *Smagorinsky model*. This is defined by equation 2.25,

$$\tau_{ij} - \frac{1}{3}\delta_{ij}\tau_{kk} = -2\mu_R\overline{S_{ij}} \quad (2.25)$$

where $\overline{S_{ij}}$ is defined by equation 2.26.

$$\overline{S_{ij}} = \frac{1}{2} \left(\frac{\partial\overline{u_i}}{\partial x_j} + \frac{\partial\overline{u_j}}{\partial x_i} \right) \quad (2.26)$$

The eddy viscosity of the residual motion (i.e. the motion of those eddies not explicitly modelled) μ_R is given by equation 2.27,

$$\mu_R = \rho(C_S L_S)^2 |\overline{S}| \quad (2.27)$$

where $\overline{S} = \sqrt{2\overline{S_{ij}}\overline{S_{ij}}}$, L_S is the filter width, and C_S is the *Smagorinsky Coefficient* which usually takes a value in the range 0.1 – 0.2. This model over-dissipates turbulence near walls [16] so to address this, variations on this model have been suggested where the model constant is allowed to be a function of position and time.

Dynamic Models

The limitations of the Smagorinsky model has led to the formulation of *dynamic models*, where the model constant is recalculated at each time step based on local field variables.

Germano Formulation The dynamic model proposed by Germano et al. [25] uses two spatial filters that follow the form of equation 2.21 on page 23. One is called the *grid filter*, where the filter width is based on the local grid dimension. The other is the *test filter*, whose filter width is larger than that used for the grid filter.

For all formulae in this section, a variable with an overline indicates that it has been passed through the grid filter and a variable in angle brackets indicates that it has been passed through the test filter.

If the grid filter and test filter are applied in succession, the equivalent to equation 2.24 on the preceding page would look like this:

$$\frac{\partial(\rho \langle \overline{u_i} \rangle)}{\partial t} + \nabla \cdot (\rho \langle \overline{u_i} \rangle \langle \overline{\mathbf{u}} \rangle) = -\frac{\partial \langle \overline{p} \rangle}{\partial x_i} + \nabla \cdot (\mu \nabla \langle \overline{u_i} \rangle) - \nabla \cdot (\rho [\langle \overline{u_i} \overline{\mathbf{u}} \rangle - \langle \overline{u_i} \rangle \langle \overline{\mathbf{u}} \rangle]) + S_i \quad (2.28)$$

The residual stress that results from equation 2.28 is:

$$T_{ij} = \rho [\langle \overline{u_i u_j} \rangle - \langle \overline{u_i} \rangle \langle \overline{u_j} \rangle]$$

If the residual stresses from equation 2.24, τ_{ij} are passed through the test filter, and then subtracted from T_{ij} , this results in a tensor, \mathcal{L}_{ij} , representing the stresses created from the turbulence whose length scales lie between the test filter width and the grid filter width.

$$\mathcal{L}_{ij} = T_{ij} - \langle \tau_{ij} \rangle = \rho [\langle \overline{u_i u_j} \rangle - \langle \overline{u_i} \rangle \langle \overline{u_j} \rangle] \quad (2.29)$$

This identity can be used to derive a value of model constant C_{dyn} most appropriate to the instantaneous state of flow in a local region. The Smagorinsky Model is applied to τ_{ij} as described by equation 2.25 on the preceding page (note that C_{dyn} is equivalent to C_S^2). Let m_{ij}^s represent the model applied to τ_{ij} , thus:

$$m_{ij}^s = -2L_S^2 |\overline{S}| \overline{S_{ij}} \quad (2.30)$$

In a similar way T_{ij} is modelled thus:

$$T_{ij} - \frac{1}{3} \delta_{ij} T_{kk} = -2C_{dyn} \rho L_t^2 |\langle \overline{S} \rangle| \langle \overline{S_{ij}} \rangle =: C_{dyn} m_{ij}^t \quad (2.31)$$

where $\langle \overline{S_{ij}} \rangle$ is defined by equation 2.32, $\langle \overline{S} \rangle = \sqrt{2 \langle \overline{S_{ij}} \rangle \langle \overline{S_{ij}} \rangle}$, and L_t is the length scale used for the test filter. m_{ij}^t is defined to give a terse expression of this model.

$$\langle \overline{S_{ij}} \rangle = \frac{1}{2} \left(\frac{\partial \langle \overline{u_i} \rangle}{\partial x_j} + \frac{\partial \langle \overline{u_j} \rangle}{\partial x_i} \right) \quad (2.32)$$

Thus by combining equations 2.30 and 2.31 with equation 2.29 one obtains:

$$\mathcal{L}_{ij}^a := \mathcal{L}_{ij} - \frac{1}{3} \delta_{ij} \mathcal{L}_{kk} = C_{dyn} m_{ij}^t - \langle C_{dyn} m_{ij}^s \rangle \quad (2.33)$$

where \mathcal{L}_{ij}^a is defined as the asymmetric part of \mathcal{L}_{ij} . By taking C_{dyn} out of the $\langle \dots \rangle$ filter and multiplying both sides by $\overline{S_{ij}}$ one obtains:

$$C_{dyn} = \frac{\mathcal{L}_{ij}^a \overline{S_{ij}}}{M_{ij} \overline{S_{ij}}} \quad (2.34)$$

where $M_{ij} = m_{ij}^t - \langle m_{ij}^s \rangle$.

Lilly Variation Lilly improves on the Germano Model by proposing a least-squares approach in calculating C_{dyn} that minimises error. Thus the new formulation for C_{dyn} is:

$$C_{dyn} = \frac{\mathcal{L}_{ij}^a M_{ij}}{M_{ij} M_{ij}} \quad (2.35)$$

Dynamic Models overcome most of the drawbacks with the fixed Smagorinsky Model, e.g. overdissipation in near-wall regions and length scale difficulties associated with anisotropic grids. However care has to be taken with its use. Observations by Breuer [11] appear to suggest that use of a Dynamic Model with an over-refined grid can lead to a poorer quality of prediction than is possible with a fixed Smagorinsky Model. Also for Dynamic Models, it is possible for negative values of eddy viscosity to appear indicating the occurrence of *backscatter*, i.e. a reverse of the energy cascade: eddies passing some of their energy to other eddies of a larger length scale. If a region of negative eddy viscosity is large it can introduce numerical stability problems. To counter this a lower limit of zero is introduced to C_{dyn} to prevent the appearance of any negative eddy viscosity in the flow field. Stability is further enhanced with relaxation techniques applied to C_{dyn} in time or space.

LES WALE Model

Nicoud and Ducros [58] had formulated this model to enable accurate modelling of transition in pipe flows. But their claim to guarantee a zero eddy viscosity for laminar flow in wall regions makes this model an attractive prospect for the prediction of the drag crisis.

Just as for the Smagorinsky model, the residual stresses τ_{ij} , and the rate-of-strain tensor for the resolved scale $\overline{S_{ij}}$, are accounted for by equations (2.25), and (2.26) respectively.

The Wall Adapting Local Eddy-viscosity model (LES WALE) differs from the Smagorinsky model in the definition of eddy viscosity μ_R , as shown by equation (2.36),

$$\mu_R = \rho(C_W L)^2 \frac{(S_{ij}^d S_{ij}^d)^{3/2}}{(\overline{S_{ij}} \overline{S_{ij}})^{5/2} + (S_{ij}^d S_{ij}^d)^{5/4}} \quad (2.36)$$

where S_{ij}^d is the traceless symmetric part of the square of the velocity gradient tensor:

$$S_{ij}^d = \frac{1}{2} \left[\left(\frac{\partial \overline{u}_i}{\partial x_j} \right)^2 + \left(\frac{\partial \overline{u}_j}{\partial x_i} \right)^2 \right] - \frac{1}{3} \delta_{ij} \left(\frac{\partial \overline{u}_k}{\partial x_k} \right)^2 \quad (2.37)$$

The important feature of this model is the author's claim for proper near-wall scaling of eddy viscosity which, according to them, is something the Smagorinsky model is unable to achieve.

2.5.3 DES

For high Reynolds number flows modelled using LES it was found that the amount of grid refinement necessary for boundary regions induced extra computational costs that were

prohibitive [82]. Detached Eddy Simulation (DES) addresses this problem by applying a RANS model, typically SST, to the boundary regions, thus reducing the mesh resolution requirements of these areas. Beyond the boundary regions, LES is used to fully resolve the time-dependent, large, three-dimensional eddies that develop in the wake of an object.

Very recently, Liaw [40] has used LES and DES for circular cylinders. His conclusions generally point towards LES being able to produce results that agree better with experimental work than DES. Thus DES is seen to be useful only in a qualitative sense since at least it produces flow features that cannot be captured by RANS models.

A problem in the use of DES is pointed out by Menter et al. [51]. The switch between the use of a RANS based model to an LES model is based on a comparison of the turbulence length scale produced by the RANS model with the local grid spacing. The potential risk is that the grid spacing can be overly refined in near-wall regions so as to cause the switchover to LES to occur within the boundary layer, not in separated regions as intended. This usually has the effect of producing separation prematurely.

2.6 Verification and Validation

A very important concept when using CFD is credibility. There has to be a way of determining whether the uncertainty and error in a model is at an acceptable level. No strong principle dictates how this is done and the degree of accuracy and credibility required depends on the purpose of the simulation. In fact there have been many guidelines put forward on this matter. The AIAA has published a guide [1] which defines *verification* as:

“The process of determining that a model implementation accurately represents the developer’s conceptual description of the model and the solution to the model.”

and *validation* as:

“The process of determining the degree to which a model is an accurate representation of the real world from the perspective of the intended uses of the model.”

Verification usually involves refinement of the grid size and time step on a trial and error basis to ascertain the discretisation error. This works on the principle of *convergence* where, generally speaking, the smaller the grid size and time step, the closer the solution of the numerical method will be to the exact solution of the conceptual model. This is called *consistency* in mathematics. The practical limit of this is where round-off errors in the calculations prevent any further improvement in accuracy. This limit can be pushed back by using more bytes to represent floating point numbers (e.g. variables in Fortran are declared as `real*8` as opposed to `real*4` to achieve this) if the further cost in terms of storage is acceptable.

Validation involves comparison of the CFD simulation results against experimental data. Important things to consider in this process are:

- that all the flow physics important to the problem are captured by the model
- that CFD simulation results and the experimental data to compare have been created independently.
- that an analysis of the uncertainty of the CFD simulation results and the experimental data is carried out.

The issue of verification and validation not only dictates the level of confidence in CFD now but also has a strong influence on how much CFD will be used in the future. It is therefore a very important concept which requires full consideration in any process that makes use of CFD.

2.7 Concluding Remarks

This chapter sets out the CFD theory and practice that is relevant to the thesis. It is clear from the complexity of the issues raised that to implement a satisfactory model is not a straightforward task. The user of CFD has to have sufficient knowledge of the underlying theory and experience to construct a model correctly. It is clear that the author needs to have sufficient practice using CFD software to be able to use CFD effectively throughout the project.

There are a variety of turbulence models available, each having advantages and disadvantages for the type of flows they can model. An early challenge of this project is to have a clear understanding of these pros and cons in terms of modelling cables, and thus know which type is the most suitable.

Chapter 3

Literature Review

This chapter contains a review of literature relating to fluid flows past a stationary cylinder and past a cylinder in motion. Each of these flow conditions fall within the scope of this thesis and so a review of experimental observations, and numerical work for each of these flow conditions is necessary. In the coverage of these subjects an introduction to relevant aspects of aeroelastic behaviour and cable dynamic behaviour is given. Furthermore, numerical methods and concepts unique to modelling this type of flow found in the literature are described.

3.1 Flow past a stationary cylinder

This section discusses experimental and numerical work related to flow past a static cylinder with particular focus on the drag crisis.

3.1.1 Experimental work

Flow characteristics

A large amount of literature exists that is devoted to the identification, classification and measurement of characteristics of the flow past a stationary cylinder.

Zdravkovich [92] reviewed in detail a large amount of literature on flow past stationary cylinders and gave a classification to describe a set of flow regimes. Each regime was observed within a particular range of Reynolds Number*, they are summarised here in order of increasing R_e value. A graphical depiction of some of these flow states can be found in Figure 3.1.

L Laminar ($0 < R_e < 180-200$)

Viscous forces are prevalent in all parts of the flow, preventing any transition to

* $R_e = DU/\nu$ where D is the cylinder diameter, U the free stream velocity, and ν the kinematic viscosity.

fashion, producing regular alternating swirls as they travel further downstream (see Figure 3.1 (c)). Note that these swirls are laminar.

TrW Transition in wake ($180-200 < R_e < 350-400$)

The transition-in-wake regime can be divided into two sub-categories:

TrW1 Transition of Laminar Eddies in the Wake ($180-200 < R_e < 220-250$)

The swirls formed from the free shear layers are laminar but become unstable and develop into turbulence further downstream. The point at which this occurs approaches the cylinder with increasing R_e .

TrW2 Transition of an Irregular Eddy During its Formation ($220-250 < R_e < 350-400$)

The transition to turbulence eventually reaches the point where the swirls form. At this stage there is a markedly different rate of swirl production. This is due to the swirls being partly turbulent before they are shed and carried downstream.

TrSL Transition in shear layers ($350-400 < R_e < 100k-200k$)

The transition in shear layers regime can be divided into three sub-categories:

TrSL1 Development of Transition Waves ($350-400 < R_e < 1k-2k$)

The free shear layers before the formation of the eddies start to undulate to form transition waves.

TrSL2 Formation of Transition Eddies ($1k-2k < R_e < 20k-40k$)

The transition waves become discrete swirls before becoming turbulent and roll up in alternate eddies.

TrSL3 Burst to Turbulence ($20k-40k < R_e < 100k-200k$)

Full turbulence occurs in the shear layers near the points of separation and eddies are formed close to the downstream side of the cylinder (see Figure 3.1 (d)).

TrBL Transition in boundary layers ($100k-200k < R_e < 300k-340k$)

The transition in boundary layers regime can be divided into five sub-categories:

TrBL0 Precritical Regime ($100k-200k < R_e < 300k-340k$)

This is the final flow condition before transition starts to occur in the boundary layers on the cylinder surface. The point of separation begins to move towards the rear side of the cylinder. This reduces the size of the wake region and thus the value of drag starts to fall.

TrBL1 One-bubble Regime ($300k-340k < R_e < 380k-400k$)

At a certain point in increasing R_e , the TrBL0 state abruptly changes. A “separation bubble” appears on one side of the cylinder where there has been sufficient transition in the free shear layer to re-attach. This results in an

asymmetric pressure distribution, a smaller wake and a discontinuous drop in drag force.

TrBL2 Two-bubble Regime ($380k-400k < R_e < 0.5M-1M$)

A “separation bubble” appears on the other side of the cylinder making the flow regime symmetric again. This results in another discontinuous drop in the drag force and a change in the shedding frequency (see Figure 3.1 (e)).

TrBL3 Supercritical Regime ($0.5M-1M < R_e < 3.4M-6M$)

Periodic eddy shedding stops as the line of separation along the span of the cylinder breaks up causing disruption and fragmentation of the separation bubbles.

TrBL4 Post-critical regime ($3.5M-6M < R_e < ?$)

The transition to turbulence occurs in the boundary layer before the point of separation all along the span of the cylinder. Seeing as the separation lines are no longer disrupted, periodic eddy shedding reappears.

As R_e further increases the transition point moves towards the stagnation point. An upper value of R_e for this state is not yet known.

T Turbulent ($? < R_e < \infty$)

This is the condition when all flow regions around the cylinder are turbulent. It is not yet known for which value of R_e this condition starts to occur. The theoretical upper limit of R_e for this state is infinity.

The main focus of Zdravkovich’s classification was to recognise where the transition to turbulence occurred for each flow state. The position of the transition point was seen to determine the flow behaviour in the wake of the cylinder.

Sung and Yoo [78] describe in detail the wake behaviour and observe the secondary vortices that occur in the immediate wake of the cylinder.

Wind Tunnel Size

Constraints on the width of the wind tunnel lead to undesired effects on the observed flow. Some literature is devoted to measurement of these effects.

Any bluff object placed within a confined flow can be considered to be a partial blockage. The flow past the object will accelerate due to the narrowing of cross-sectional space of the wind tunnel at the location of the object. This would not be the case for field observations of flow past cables since the flow is not confined.

Blockage is a term often found in the literature to mean confinement ratio, i.e. the ratio of cylinder diameter to the cross section dimension of the wind tunnel. Richter and Naudascher [64] investigated blockage effects on a long circular cylinder placed in a narrow wind tunnel. They published data including mean drag coefficient, Root Mean Square (RMS) values of the drag and lift fluctuations, the Strouhal Number[†] of the

[†]see § 3.2.1 for definition of Strouhal Number

dominant vortex shedding, and the value of Reynolds Number for which the drag crisis occurs. They find that as the confinement ratio increases:

- the Reynolds number for which drag crisis occurs decreases,
- the values of drag before and after the drag crisis increase and the difference between them increases,
- the Strouhal number of the lift oscillations before and after the drag crisis increase and the difference between them increases.

The experimental evidence produced by Richter and Naudascher [64] would suggest that blockage is not an issue that would impede the onset of a drag crisis in a numerical simulation. However Blackburn [8] has highlighted that spanwise correlation lengths become longer with increasing blockage.

Anthoine [6] presents a method of blockage effect correction that can be applied to drag coefficient measurements of circular cylinders in wind tunnels. This is based on theory developed by Maskell [45].

Trip Wires and Surface Roughness

A number of papers confirm the effect that cylinder surface roughness has on the flow. In all cases the higher the roughness is, the lower the range of Reynolds Number for which the drag crisis is observed. Some authors (Kareem and Cheng [36], Shih et al. [72]) achieve early transition to turbulence by placing tripping wires at locations to encourage transition to turbulence and to delay separation of the boundary layer. The optimum locations each paper reports is in general agreement. Mahbub Alam et al. [2] measured the reduction of forces acting on a cylinder (and two cylinders) by using tripping rods at a variety of locations on the circumference of the cylinder. They thus infer the influence of surface roughness on the flow characteristics past a stationary cylinder.

Approaching Flow Conditions

A recognised influence on the transition to turbulence is the level of turbulence intensity in the approaching flow. Higher turbulence intensity means more fluctuations in the flow approaching the cylinder that can persist within the boundary layer. This increases the probability of transition to turbulence, and thus early onset of the drag crisis and turbulence occurs. Kareem and Cheng [36], and Konstantinidis et al. [39] are but a couple of examples of this concept shown in experimental literature.

The other variable in approaching flow conditions prominent in literature is shear flow i.e. where the velocity profile varies linearly in one cross sectional direction. In the case of cross diameter sheared flow, Sumner and Akosile [75] is an example.

Force measurements

A large amount of literature can be found providing force measurement data. Norberg [59] carried out some force measurements and proposed empirical formulae to describe the variation of Strouhal frequencies with Reynolds number. Norberg [59] emphasises the importance of correlation length to capture the correct displacement response. Schewe [69] carried out some force measurements and produced spectral frequency plots of lift force at a range of flow regimes through the initial stages of the drag crisis. ESDU presents data that has been compiled from a range of experimental literature. The experimental data included in their publication [83] comes from a wide range of sources, each having a unique set of boundary conditions that influences the recorded data. The ESDU publication [83] identifies which of the boundary conditions have the most significant influence and presents a method of normalising data to account for these effects. This method is discussed in more detail in Chapter 4.

3.1.2 Numerical Work

Large Eddy Simulations

A variety of implementations of LES for the simulation of flows past stationary cylinders can be found in the literature. A survey of this literature can provide an understanding of the important features of LES necessary to successfully capture drag crisis effects.

Catalano et al. [14] develop a wall model used with a Smagorinsky SGS model to attempt to numerically simulate the drag crisis. The wall model alleviates the high resolution requirements near to the surface of the cylinder for high Reynolds Number flows. By comparison with similar work carried out using RANS models, they identify that a delayed point of separation is a feature that must be captured by a turbulence model if it is to be useful for this task. It should be noted that their wall stress model produces a reasonably accurate level of drag for only a short range of Reynolds Number beyond the drag crisis. They do not successfully capture the drag crisis itself, however.

Near wall resolution is an important issue to address. Ma et al. [42] make a comparison of DNS simulations at low Reynolds number (3900) with a number of LES simulations with different levels of resolution. They emphasise how effective dynamic models are at capturing vortex dynamics.

Selvam [71] attempts to numerically simulate the drag crisis using an FEM based solver using an LES Smagorinsky model. On comparison with experimental data he finds that the drag is overpredicted in his simulation. It is interesting to note that his review of similar work carried out by others states that overprediction of drag is commonplace. In fact only the 3D numerical simulation by Tamura et al. [79] gives an accurate drag value.

Nakayama and Vengadesan [55] have carried out simulation of flow past a square cylinder using a variety of combinations of subgrid stress models and finite difference (advection) schemes. They show that the performance of the SGS model is highly de-

pendant on the advection scheme used with it. It is worth noting that the commercial software used for this thesis (ANSYS CFX) recommends the use of the central differencing scheme with all of their LES models for best performance.

Domain Size

Just as constraints on the width of the wind tunnel lead to undesired effects in experimental work, the same principle applies to the domain size in numerical work.

Work by Okajima et al. [61] can be said to be the numerical equivalent of the Richter and Naudascher [64] experimental work investigating blockage. It highlights effects blockage has on results, which are qualitatively the same as those found by Richter and Naudascher [64]. For practical purposes, blockage cannot be eliminated completely. Work produced by Okajima et al. [61] and Richter and Naudascher [64] give an impression of what kind of error and of what magnitude to expect with blockage.

Effects caused by restriction of the spanwise domain dimension have been investigated by Selvam [71]. Having carried out a LES 2D simulation of the drag crisis, he found that he did not encounter as big a drop in drag as that found by experiment. The limitations of 2D LES has been looked at in detail by Breuer [10] along with other numerical and modelling aspects. This had been done for a Reynolds number of 3900, far below the drag crisis range. Noting that the time averaged streamlines in the wake produced for a 2D LES is non-symmetrical and significantly different to that produced by a similar 3D simulation, Breuer [10] concludes that three-dimensional effects are crucial to a simulation capturing the correct wake characteristics.

Small Scale Resolution Catalano et al. [14] identify the need for high grid resolution close to the cylinder wall. In order to address this they use a wall stress model which produces a reasonably accurate level of drag for only a short range of Reynolds Number.

Kemenov and Menon [37] deal with this issue when they introduce a novel two level simulation approach. No-one else has continued this work however.

3.2 Aeroelastic Behaviour of Structures

Up until the middle of the 20th century, wind load effects on structures were represented in the design process as static loads of a certain assumed magnitude [68]. This was considered to be a sufficiently safe assumption to make until the collapse of the Tacoma Narrows Bridge in 1940. From the time it was opened, the deck of this bridge suffered significant vertical movement caused by local winds blowing across it causing it to be nicknamed “Galloping Gertie” by local people. Although this movement was uncomfortable for anyone crossing the bridge it was not considered to be serious enough for the bridge to be closed. Barely six months after it was opened, a storm blew up around the bridge which was to cause its catastrophic failure. The vertical movement of the deck which was by then familiar to regular users of the bridge was replaced by a lon-

gitudinal twisting mode of vibration that had never been seen before. This movement became so intense that the bridge had to be evacuated. Eventually the intensity of this vibration caused the failure of some of the cable tendons and the deck fell away. The event was filmed by local media and so the unique nature of the collapse could be seen by generations of engineers to come.

Thus it came to be a turning point in the approach to designing long-span bridges as it gave a clear warning of the risks in ignoring aeroelastic effects in a potential design. From that time, wind loads on civil engineering structures began to be treated as a form of bluff-body aerodynamics.

The definition of an aeroelastic phenomenon is where a structure is moved by a flow in such a way that it suffers significant additional forces. The various classifications of this phenomenon are discussed in the following subsections.

3.2.1 Vortex Induced Vibration

Fluid flowing past a bluff object can be broken up into vortices that trail into the wake. For a wide range of Reynolds numbers, the shedding of these vortices is periodic, which itself applies a periodic loading on the structure. Vortex Induced Vibration (VIV) problems exist in water flows around pilings, piers, offshore tower legs, and deep-sea cables. In wind flows, VIV occurs on overhead power cables, flagpoles, chimneys, structural members, bridge decks and cable tendons used in bridges.

Strouhal Number When a bluff object is stationary, the rate at which vortices are shed is defined by a dimensionless coefficient known as the Strouhal Number, S_t , as defined by equation 3.1,

$$S_t = \frac{f_v D}{U} \quad (3.1)$$

where f_v , D , and U are the shedding frequency, the diameter of the bluff object, and free-stream velocity respectively. The Strouhal number is found by experiment to be about 0.2 for a circular section, across a wide range of Reynolds number. Norberg [59] proposes a set of empirical formulae to represent the variation of S_t with Re , reproduced here in Table 3.1 on page 38 and plotted in Figure 3.2.

Lock-In When a bluff object is free to move, the *lock-in* phenomenon can occur. At most flow speeds the shedding frequency, f_v , can be predicted by equation 3.1. If, however, the flow velocity reaches a point where the shedding frequency is close to the natural frequency of the bluff object, resonance occurs. This causes an increase in the object's oscillation to enough of an extent to allow the rate of vortex shedding to be controlled by the rate of oscillation. This is the beginning of the *lock-in* effect, as shown by the flat region in figure 3.3 on the following page. In the literature this phenomenon is also referred to as *lock-on*, *vortex capture*, and *frequency capture*, depending on the preference of the author. If the flow speed increases further, the rate of vortex shedding persists at the natural frequency of the object. This is combined with large oscillations. At a wind

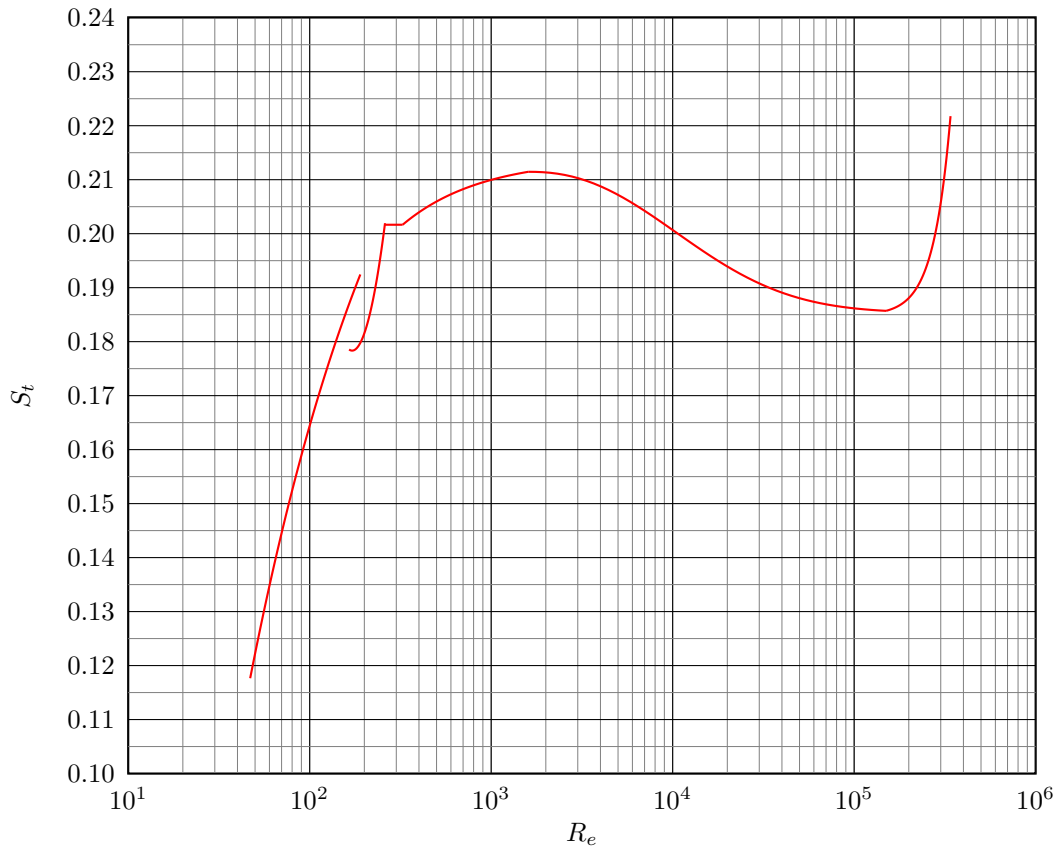


Figure 3.2: Empirical variation of S_t with R_e given by formulae in Table 3.1

speed a few percent higher than the value where *lock-in* begins, the flow field disrupts the oscillations to enough of an extent to cease *lock-in*, and the shedding frequency reverts back to the Strouhal relationship (equation 3.1 on the previous page).

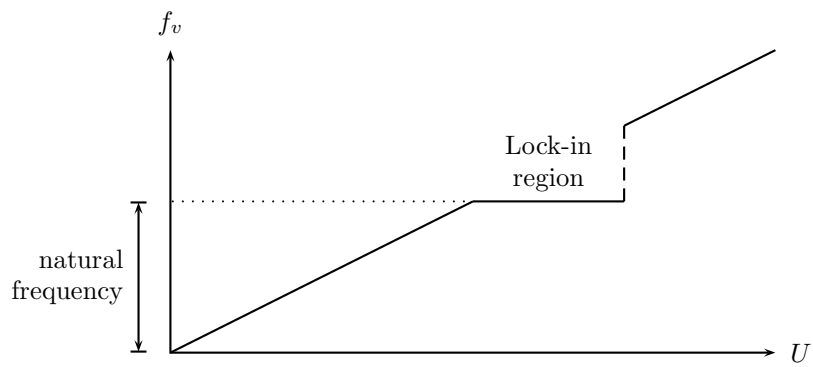


Figure 3.3: Plot of Vortex Shedding Frequency against Flow Velocity

Table 3.1: Empirical formulae for S_t variation with R_e

R_e	S_t
47 – 190	$0.2663 - \frac{1.019}{\sqrt{R_e}}$
165 – 260	$-0.089 + \frac{22.9}{R_e} + 7.8 \times 10^{-4} \times R_e$
260 – 325	0.2016
325 – 1.6×10^3	$0.2139 - \frac{4}{R_e}$
$1.6 \times 10^3 - 1.5 \times 10^5$	$0.1853 + 0.0261 \times \exp[-0.9 \times x^{2.3}]$
$1.5 \times 10^5 - 3.4 \times 10^5$	$0.1848 + 8.6 \times 10^{-4} \times \left(\frac{R_e}{1.5 \times 10^5}\right)^{4.6}$

Hysteresis The extent of oscillation in the resonant range depends on how it was approached i.e. from a higher or from a lower velocity. This *hysteresis* behaviour results in two branches of amplitude variation being seen within the lock-in region.

This has been observed by Carberry et al. [12] in their experiments using a cylinder in cross flow subject to a forced vibration at a fixed amplitude. They note that there were two distinct types of vortex shedding behaviour in the near-wake associated with a particular phase level between lift force and cylinder displacement (both varying sinusoidally in time). They present evidence that associated with a jump between one wake state to the other are a range of effects including a phase jump between lift force and cylinder displacement of approximately 180° . In a subsequent paper [13], they describe how their observations apply to cylinders allowed to oscillate freely in a cross flow. Similar observations have been made by Hover et al. [30] who investigated flow past cylinders allowed to freely oscillate and subjected to forced oscillations. Additionally, in a subsequent paper, Hover et al. [31], observe the breakdown in spanwise correlation of the lift force during the phase transition.

Mass Parameter Vandiver [85], who has produced a large body of work focusing on VIV and lock-in behaviour of marine cables over many years, introduces a number of dimensionless parameters important to predicting lock-in for deep-sea cables. These include the mass ratio and the reduced damping parameter. The mass ratio, m^* , is given by equation 3.2,

$$m^* = \frac{m_c}{\rho D^2} \quad (3.2)$$

where m_c is mass of cable per unit length, ρ is density of fluid, and D is the diameter of the cable. The lower the value of m^* gets, the broader the range of velocities for which lock-in occurs.

Reduced Damping Parameter The reduced damping parameter is usually represented by the Scruton number S_c , defined by equation 3.3 [24],

$$S_c = \frac{4\pi m_c \zeta}{\rho D^2} \quad (3.3)$$

where ζ is the critical damping ratio, a dimensionless measure of damping in the system. ζ is defined as the ratio of damping to the level of critical damping (i.e. the minimum value of damping at which no oscillations can occur).

As the value of S_c increases the lock-in behaviour decreases, i.e. smaller amplitudes and narrower range of velocities. An empirical model that links the maximum response amplitude y_0 , to the Strouhal and Scruton numbers is given by equation 3.4 [73].

$$\frac{y_0}{D} = \frac{1.29}{[1 + 0.43 (8\pi^2 S_t^2 S_c)]^{3.35}} \quad (3.4)$$

Shear Flow Parameters In the context of deep-sea cables, Vandiver et al. [86] describe two more parameters that may be useful for prediction of lock-in. These are specific to sheared flows, i.e. flows where the velocity varies in the span direction. The first is N_s , the number of potentially responding modes of cable vibration within a range of vortex-shedding frequencies generated by the flow. The second is $\Delta V/V_{ave}$, known as the shear parameter is the ratio of change in velocity over the length of the cable to the spatially averaged velocity. A number of experiments are carried out to ascertain values of these parameters for which lock-in occurs.

Experimental Work

Comprehensive reviews of the progress of experimental work related to VIV are given by Sarpkaya [67], Gabbai and Benaroya [24], and Williamson and Govardhan [90]. A large portion of the experimental literature is devoted to the investigation of methods of vortex suppression (e.g. Bearman and Branković [7]) because there is high demand for the control of VIV on risers used in offshore drilling. In these environments VIV is often the main cause of fatigue which determines the design life of a riser, and consequently whether or not a new field discovery is worth developing.

Numerical Work

Twenty five years ago, Scanlan [68] reported that the state of predictive theory for VIV was poor. Wind tunnel experiments alone do not sufficiently answer this challenge as the achievable Reynolds number does not correspond to real world situations and so the Strouhal number predicted may not be the same as that for full scale. This, coupled with the fact that powerful computing is becoming more affordable in general, is why there is interest in the use of CFD by the civil engineering community.

Unfortunately the range of Reynolds Number currently achievable by CFD falls short of the range observed in the real world. Nevertheless, it is easier with CFD to observe the

characteristics of the immediate wake and gain a better understanding of the processes causing VIV. Thus much attention has been given on this matter as exemplified by [56], [57], [18], [85], and [86].

Newman and Karniadakis [56], [57] simulate VIV of a flexible cable using DNS. They achieve Reynolds numbers up to 300 and use a domain of a spanwise length up to 45 cable diameters. The movement of the cable was taken into account by using a body-fitted coordinate system. Evangelinos and Karniadakis [18] continue this work further and present results for VIV of a long flexible cylinder simulated using spectral methods. Their simulations were for a Reynolds number of 1000 and they limited the cylinder span to depth ratio to 4π . The maximum amplitudes they observed was about one cylinder diameter. The body-fitted coordinate system which they use may be appropriate to accommodate this amount of deflection but for larger deflections may be problematic (as discussed in section 3.4.2).

3.2.2 Flutter

A number of types of flutter exist. The first type of flutter observed is known as *classical flutter*, which occurs where vibration frequencies in two degrees of freedom, torsional and pitching, are forced together by the flow to form a coupled motion. This is most commonly seen in flat plates and airfoils. Classical flutter occurs rarely in civil engineering structures.

A more commonly observed form of flutter on bluff bodies is known as *stall* or *separated-flow flutter*, where a single degree of freedom (notably torsion) is excited aeroelastically. This is a prominent form of flutter found in bridge decks and can clearly be seen in footage of the Tacoma Narrows bridge collapse.

As far as cables are concerned, torsional stability is not an issue and other types of aeroelastic behaviour are more prominent. So flutter is not discussed any further in this report, but the interested reader is referred to Frandsen [22], Robertson et al. [65], and Simiu and Scanlan [73].

3.2.3 Galloping

Galloping is a form of aeroelastic behaviour most commonly associated with very slender structures. A number of types of galloping exist. They are typically oscillations of very large amplitude i.e. many times the diameter of a bluff object, and of low frequency.

Cross-wind galloping is where the direction of oscillation is normal to wind flow direction. A common example of this is power-line cables with an ice coating produced by sleet. The effective section of the cable is changed with the addition of the ice making it more susceptible to this kind of vibration. Because of the low frequency of vibration in comparison to frequencies associated with VIV, local pressure fluctuations can be ignored in this context and this kind of behaviour is analysable in terms of steady or average aerodynamic coefficients.

Den Hartog [73] formulated a criterion to predict *cross-wind galloping* instability given by equation 3.5,

$$\frac{dC_L}{d\alpha} + C_D < 0 \quad (3.5)$$

where C_L is the steady lift coefficient, C_D is the steady drag coefficient, and α is the angle of attack of the wind. For circular sections $dC_L/d\alpha$ is zero so cross-wind galloping can never occur unless the circular profile of a cable is modified. This is why the formation of ice on the cable surface produces this type of vibration.

The Den Hartog condition, however, does not take into account skew winds, i.e. it only considers wind directions in a plane normal to the cylinder axis. When the wind has a longitudinal component relative to the cable axis, another type of excitation known as *dry inclined cable galloping* can occur. The inclusion of “dry” in the name is because this type of excitation has been observed for circular sections, i.e. there does not need to be any precipitation of any kind for this to happen.

Macdonald and Larose [43, 44] offer a complete theoretical model of this behaviour. Not only do they take into account the variety of wind direction but also the fact that the force coefficients vary with Reynolds number. This is particularly important as the drag crisis comprises of a significant drop in drag force over a range of Reynolds number achievable in cable structures. They observe that along-wind as well as cross-wind vibrations can occur especially in the case of perfectly tuned systems, i.e. cables whose natural frequencies in both orthogonal directions are the same. With this in mind, a two-degree-of-freedom formulation is presented. In situations where this is not the case, i.e. where the orthogonal frequencies vary by more than a few per cent, the vibration can be idealised as a one degree of freedom problem.

Another type of galloping occurs where two slender structures are close to each other, with one upstream of the other. The first structure encountered by the wind disrupts the flow approaching the second inducing *wake galloping*. A typical example is found with bundled power-line cables. This phenomenon usually shows itself as a coupled two-degree-of-freedom movement in the downstream cable in the along-wind and cross-wind directions, oscillating in an elliptical orbit with the long axis of the ellipse oriented approximately in the flow direction. The direction of the oscillation is such that the cable moves downstream near the outer edges of the wake and upstream near the centre of the wake. This phenomenon has been investigated experimentally by Bokaian and Geoola [9].

3.2.4 Buffeting

Buffeting is the unsteady loading on a structure caused by velocity fluctuations in the flow. If the fluctuations are due to turbulence shed in the wake of an upstream body, the phenomenon is referred to as *wake buffeting*. At the moment no analytical model of wake buffeting exists.

3.2.5 Rain-Wind Excitation

As the name suggests, this form of excitation will only occur in rainy weather. Droplets of water fall onto the cable surface to form rivulets that temporarily change the shape of the cross section. The alteration of this shape can lead to galloping effects in a similar way to ice formations on power lines as mentioned in section 3.2.3. Due to the rivulet being very light, its position on the cable is very susceptible to change by the combined effects of gravity, wind and the motion of the cable itself.

Although this form of excitation has only recently been identified it is considered in industry to be the one that causes the most problems for cables. Irwin [35] has proposed empirical limits to the damping of cables to protect against this phenomenon. This is due to the fact that a thorough numerical simulation of rain-wind excitation has not yet been performed.

Seidel and Dinkler [70] have likened the effect of the rivulet to the effect of the tripwire in a famous experiment by Prandtl where the drag force on a spherical object was seen to be significantly reduced by the tripwire inducing supercritical flow. Thus if rain-wind vibration is to be modelled correctly, then the ability to numerically model the ‘drag crisis’ on a cable section is very important.

3.3 Cable Dynamics

The suspended cable is a basic element of theoretical interest in applied mechanics and so it has a long history as documented by Irvine [34]. Early work on cable dynamics began in the eighteenth century where models for the vibration of taut strings and inextensible cables carrying lumped masses were developed. This continued through to the nineteenth century where equations of motion were developed to obtain natural frequencies for small oscillations of an inextensible bare cable.

Cable dynamics obtained renewed interest after the Tacoma Narrows Bridge collapse but it wasn’t until 1974 when Irvine and Caughey [33] introduced the effect of cable elasticity and proposed a parameter, λ^2 , which is fundamental to predicting cable behaviour. This parameter is detailed in § 3.3.3 and § 3.3.4.

3.3.1 The Catenary Profile

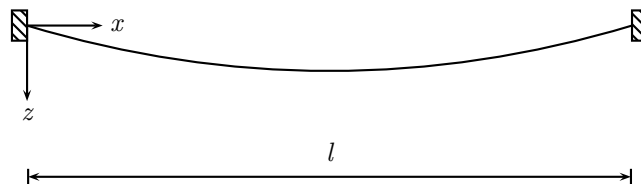


Figure 3.4: Coordinate system used for cable equations

Considering a suspended uniform inextensible cable of no flexural rigidity, hanging from two fixed points at the same level as shown in figure 3.4 on the preceding page, the vertical coordinate of any point z is given by equation 3.6,

$$z = \frac{H}{mg} \left\{ \cosh \left(\frac{mgl}{2H} \right) - \cosh \left(\frac{mg}{H} \left(\frac{l}{2} - x \right) \right) \right\} \quad (3.6)$$

where H is the horizontal component of the cable tension, mg is the self-weight of the cable per unit length, l is the cable span, and x is the length coordinate along the span.

If mg , l , and cable length L_0 are known then H can be found by equation 3.7.

$$\sinh \left(\frac{mgl}{2H} \right) = \frac{mgL_0}{2H} \quad (3.7)$$

3.3.2 The Parabolic Profile

In the equations of section 3.3.1, mgl/H is small when the cable length is only fractionally longer than the span. In such cases, the hyperbolic functions can be approximated by a power series to represent a parabola. By doing so, the derivation of parameters related to cable dynamic behaviour is made much easier without significant loss of accuracy provided the sag to span ratio is not excessive.

In their work leading up to the derivation of the λ^2 parameter, Irvine and Caughey [33] approximate the cable profile by equation 3.8.

$$z = \frac{mgl^2}{2H} \left\{ \frac{x}{l} - \left(\frac{x}{l} \right)^2 \right\} \quad (3.8)$$

In this case, H is related to d , the sag of the cable, by equation 3.9.

$$H = \frac{mgl^2}{8d} \quad (3.9)$$

Irvine and Caughey [33] propose that the cut-off in ratio of sag to span for which the parabolic assumption is valid is 1:8, for then $H \geq mgl$. However, a few years later Irvine [34] claims that independent finite element analyses have shown this assumption to retain accuracy even with profiles as deep as 1:4.

3.3.3 The λ^2 Parameter

An important parameter relating to cable statics and dynamics is λ^2 , as proposed by Irvine and Caughey [33]. The λ^2 parameter is a measure of the relative importance of the cable's elastic stiffness and geometric stiffness.

When the ends of a sagging cable are stretched apart, some of the resistance supplied is geometric because the sag of the cable is being reduced. The rest of the resistance is supplied by the axial strength of the cable. λ^2 accounts for both of these effects in equation 3.10,

$$\lambda^2 = \frac{(mgl/H)^2}{H/EA} \quad (3.10)$$

where E is the cable Young's modulus, and A is the cable cross-sectional area. Small values of λ^2 relate to taut flat cables, larger values relate to heavier cables such as those seen in suspension bridges.

3.3.4 Relationship Between λ^2 and Modes of Vibration

The out of plane modes of vibration of a small sag cable are the same as those of a taut string and their natural frequencies, ω_n are given by equation 3.11.

$$\omega_n = \frac{n\pi}{l} \sqrt{\frac{H}{m}} \quad n = 1, 2, 3, \dots \quad (3.11)$$

The frequency of the first transverse horizontal mode (i.e. $n = 1$) is the lowest natural frequency of any given parabolic cable.

The way that in-plane modes of vibration are influenced by λ^2 is described by Irvine [34] in terms of *crossover points*. These *crossover points* are values of λ^2 for which the natural frequency of a symmetrical mode of vibration matches that of a nearby antisymmetrical (with respect to the centre point of the span) mode of vibration. Consider first the case where $\lambda^2 \approx 0$. The cable is practically a taut string and the modes and natural frequencies of the in-plane vibrations will match those of the out-of-plane vibrations. As the value of λ^2 increases away from zero, the natural frequency of the first symmetric mode of vibration increases. The associated mode shape is symmetric with no internal nodes along the span (see Figure 3.5a). When $\lambda^2 = 4\pi^2$, the frequencies of the

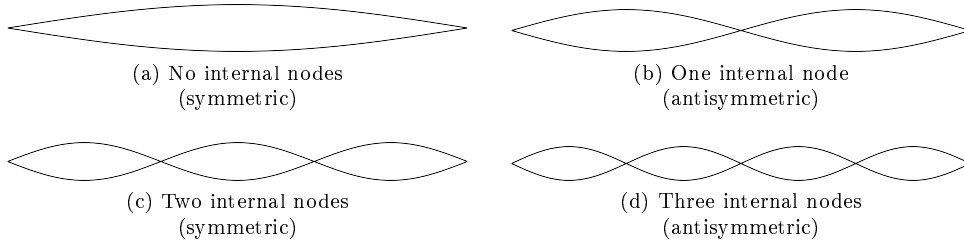


Figure 3.5: Mode shapes

first symmetric and antisymmetric modes are equal. The shape of the symmetric mode at this point will be such that the curve at the supports will be tangential to the static profile. As λ^2 goes above $4\pi^2$ the frequency of the symmetric mode will be above that of the first antisymmetric mode. The associated symmetric mode shape at this point will have 2 nodes along the span (see Figure 3.5c). A similar process can be observed for higher values of λ^2 with symmetric/antisymmetric mode shapes of higher order. The crossover point at each of these transitions is given by equation 3.12.

$$\lambda^2 = 4j^2\pi^2 \quad j = 2, 3, \dots \quad (3.12)$$

3.4 Numerical Modelling

This section briefly discusses numerical simulations carried out that bear some relevance to this project, and the numerical techniques involved. As will be seen, the variety of numerical techniques employed by different authors demonstrates that there is a large number of choices to be made when selecting a methodology.

An early choice to consider is whether the fluid and solid domain can be modelled together in one algorithm employing one numerical method. Certainly early examples of FSI simulations take this approach, such as the piston problem as described by Dowell and Hall in their review [17]. These early examples are simple in that the number of degrees of freedom of the structure are few, the degree of movement is limited and the shape of the structure itself does not deform. FSI tutorials given in the literature of commercial CFD software falls into this category [4], where the movement of the structure is easily modelled by user routines allowed by the software. Thus the solution is *monolithic* with no significant increase in complexity from normal CFD problems.

When the movement of the structure is not so limited and there are many degrees of freedom, as is the case for cables in general, a *partitioned* approach is more suitable, i.e. a separate algorithm for the fluid and the structure domain with a numerical method that is suitable for each. The fluid problem and the structural problem will have different requirements for meshing and time stepping so it would be difficult to justify using a monolithic solver.

The additional challenge that is introduced when using separate solvers is to ensure compatibility between them. Compatibility in the sense that the shape of the common interface between the fluid and solid domains match and that conservation of mass and energy is maintained.

3.4.1 Discrete Vortex Method

The Discrete Vortex Method (DVM) is a numerical method in CFD that has received increasing attention recently. For example Taylor and Vezza [80] have developed a DVM solver and used it to model stationary and oscillating bridge decks. It works by modelling the transport of vortices through the fluid domain. Saltara et al. [66] use DVM to model flow around an elastically mounted cylinder and compare their results against published experimental results. The amplitude of vibration from their numerical model tends to be far less than what had been observed experimentally but they suggest this is due to different flow histories with regard to the way the velocity was incremented. It appears the hysteretical behaviour of the cylinder motion (as also mentioned by Gabbai and Benaroya [24]) is due further investigation. Yamamoto et al. [91] and Meneghini et al. [47] arrive at a similar conclusion when they do a numerical experiment that is similar except that it extends in the spanwise direction to simulate deep-sea riser cables.

Morgenthal and McRobie [53] discuss the potential benefits of DVM as compared to the Finite Volume Method (FVM) to analyse the decks of long span bridges. They conclude

that the main advantage of DVM is that it's computationally inexpensive compared to FVM and for this reason is more likely to be used in industry. However they also point out that FVM is better suited for changes in body shape. As discussed in section 3.2, rain or sleet conditions can produce aeroelastic behaviour in cables based on effective shape changes of the cable cross-section. So to simulate galloping and rain-wind excitation, FVM is the better option.

Another big drawback in DVM is that it is currently only well suited to modelling 2-dimensional flows. Gabbai & Benaroya [24] and Zdravkovich [92] discuss in their respective texts the spanwise variation of vortices and therefore the three-dimensional nature of turbulence in cable problems. Hence DVM requires further development so that it can model three-dimensional vortices before it can be used with any confidence for numerical simulations of flow around cables.

3.4.2 Arbitrary Lagrangian Eulerian Formulation

The Arbitrary Lagrangian Eulerian (ALE) formulation is a way of reconciling the conflicting characteristics of the reference frames commonly used in fluid and structural solvers. Usually numerical methods used for solving fluids problems use an *Eulerian* reference frame, i.e. a grid that is fixed in space through which the material passes. On the other hand, numerical methods commonly used for structural problems use a *Lagrangian* reference frame, i.e. a grid that moves with the material so that the displacement of the material is given by the displacement of the grid.

One way to accommodate the change in position of the fluid-solid boundary as the structure moves is to remesh the fluid domain at each time step and interpolate the fluid variables from the old mesh onto the new mesh. This is referred to by Souli et al. [74] as “rezoning and remap” and they claim that it is first-order accurate, unlike the ALE approach which is second-order accurate. In addition it is more computationally expensive than ALE.

The ALE approach maintains the topology of the mesh between time steps by allowing the fluid mesh to move and making a correction to the NSEs to allow for this movement. Thus the conservation of momentum member of the NSEs includes an extra term for grid velocity, w_i , as shown in equation 3.13.

$$\frac{\partial(\rho u_i)}{\partial t} + (u_i - w_i)\nabla \cdot (\rho \mathbf{u}) = -\frac{\partial p}{\partial x_i} + \nabla \cdot (\mu \nabla u_i) + S_i \quad (3.13)$$

With the ALE formulation a variety of meshing strategies is possible. Sun et al. [77] implement this on their simulation of a bridge deck by allowing the mesh close to the fluid-solid boundary to move but keeping the mesh in the far-field rigid. Thus in a translation of the structure the fluid cells on one side of the structure will compress and on the other side will expand. With this approach some *a priori* knowledge of the range of displacements possible is required because if the ALE region around the deck section is not sufficiently large there will be problems of mesh quality to the extent that some fluid elements could even invert at the upper limits of displacement. In the case of cables,

large displacements many times the diameter are possible in some examples of aeroelastic phenomena [35] and so this meshing strategy is not suitable.

Newman and Karniadakis [57] employ a different approach in their DNS model of a cable at low Reynolds number flows. Their fluid solver uses a frame of reference that remains fixed throughout the whole solution time so there is no question of compromising mesh quality. The ALE formulation is applied throughout the entire fluid domain so that in effect the fluid frame of reference is following the cable. This approach would only work well if the variation of the displacements along the span of the cable is not large. One could envisage a large loss of accuracy in the solution if the deflected shape deviated largely from the shape used in the fluid solver frame of reference.

3.4.3 Coupling

When using a partitioned approach for an FSI simulation, the coordination of the running of separate solvers and the exchange of information between them is controlled by a *coupling* algorithm.

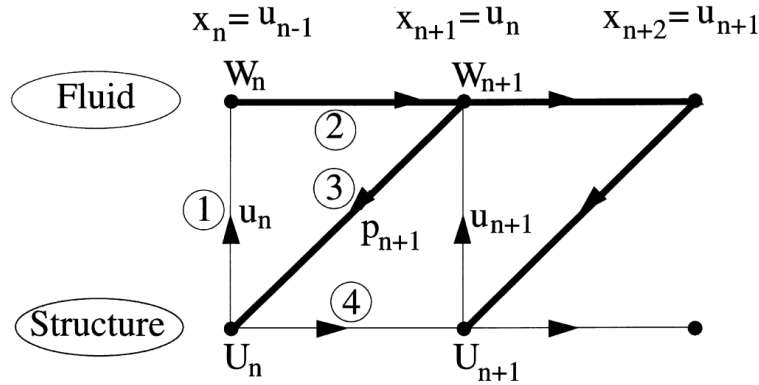
Explicit Methods

The simplest form of coupling is to run the fluid and structural solvers on a staggered basis. This is known as *explicit* coupling. When the fluid solver completes a time step, the pressure/force at the fluid-solid interface is interpolated to the structural grid and supplied as an input to the structural solver. The structural solver in turn will supply updated displacements to the fluid solver. Due to the different physics and numerical methods employed by each solver, it is possible for the time step requirements to be different. Because of this and the fact that there is no attempt to conserve energy and momentum at the interface, explicit coupling is unstable.

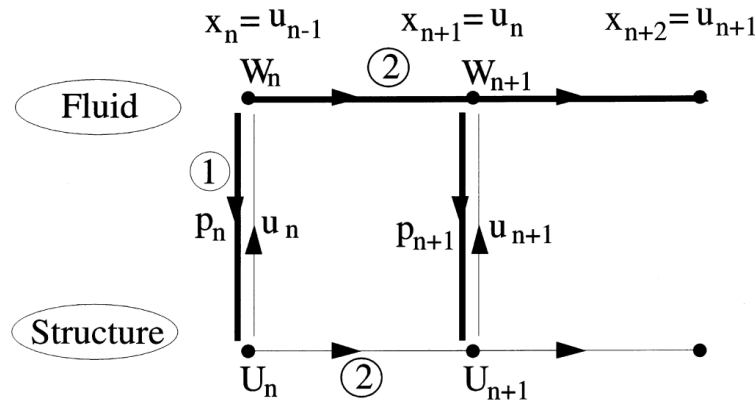
A good introduction to the variety of explicit methods is given by Farhat and Lesoinne [19]. In this paper they describe the Conventional Serial Staggered (CSS) procedure and the Conventional Parallel Staggered (CPS) procedure before suggesting improvements to these, calling them the Improved Serial Staggered (ISS) procedure and the Improved Parallel Staggered (IPS) procedure respectively. Their sketches of the “conventional” and the “improved” procedures are reproduced in Figures 3.6 and 3.7 respectively. Each sketch shows the communication steps between the fluid and structure solvers as they advance by a single cycle through the solution. The subscript n designates the n^{th} time station, incrementing from left to right in the sketch. The top row indicates the state of the “wetted” boundary where the fluid and structure domains intersect. On this common boundary x indicates the position of a fluid grid point, u denotes the displacement of the structure, and p denotes fluid pressure. The subsequent rows indicate the time dependent state (in terms of displacement and velocity) of the fluid and structure domains, denoted by W and U respectively.

CSS Procedure

Figure 3.6a shows the steps involved in each cycle of the CSS procedure. This is a very straightforward procedure but is only first order accurate in time and violates the Geometric Conservation Law (GCL) which is the main motivation for the authors to propose an improved procedure.



(a) Conventional Serial Staggered



(b) Conventional Parallel Staggered

Figure 3.6: “Conventional” coupling schemes presented by Farhat and Lesoinne [19]

CPS Procedure

Figure 3.6b shows the steps involved in each cycle of the CPS procedure. This allows the fluid and structural solver to operate in parallel but the main limitation is that the time step size has to be kept small for a stable solution to be possible.

ISS Procedure

The ISS Procedure is an improvement on the CSS Procedure that ensures continuity of velocity as well as position of the fluid and structure meshes on the common boundary.

The main feature is that the timing of both solvers are offset by half a time step. Figure 3.7a gives a graphical depiction of this idea. A dot denotes a derivative with respect to time. A description of the procedure in step-by-step form goes as follows.

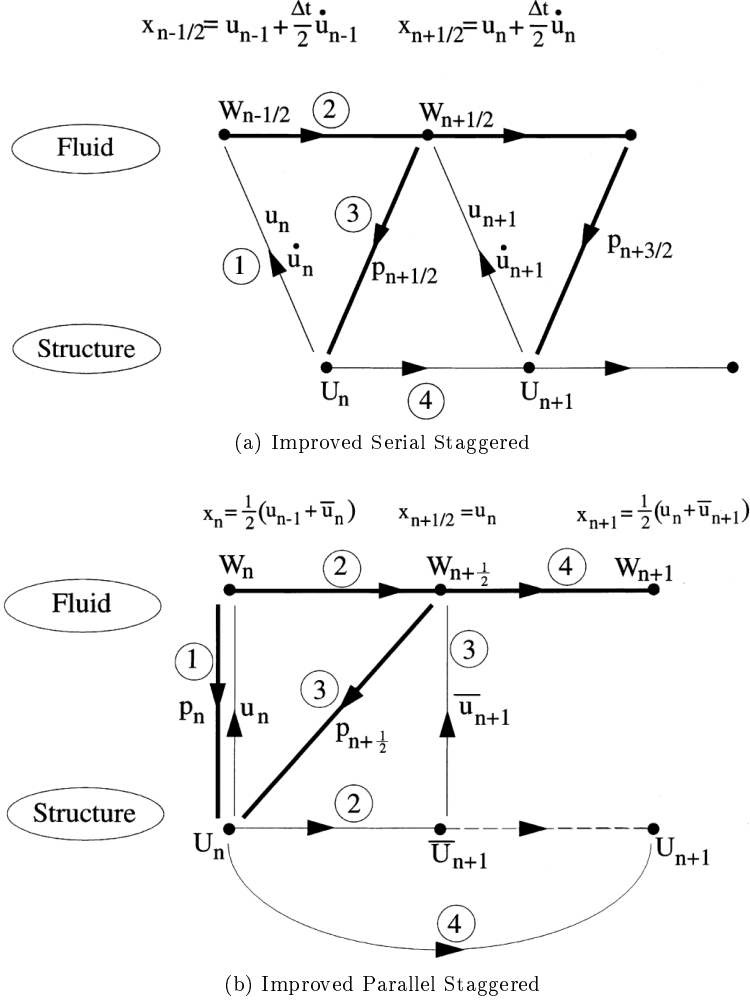


Figure 3.7: “Improved” coupling schemes presented by Farhat and Lesoinne [19]

1. Given initial conditions W_0 , u_0 and \dot{u}_0 initialise the fluid mesh as follows

$$x_{-\frac{1}{2}} = u_0 - \frac{\Delta t}{2} \dot{u}_0 \tag{3.14}$$

For $n = 1, \dots$

2. Set $\dot{x}_n = \dot{u}_n$ and update the fluid dynamic mesh as follows

$$x_{n+\frac{1}{2}} = x_{n-\frac{1}{2}} - \Delta t \dot{x}_n \tag{3.15}$$

3. Solve the flow problem to obtain the fluid state vector $W_{n+\frac{1}{2}}$

4. Extract the pressure field on the common boundary and convert it into a structural load
5. Advance the structural system using the second-order time accurate midpoint rule

This procedure has been adopted in a recent paper by Relvas and Suleman [63].

IPS Procedure

The IPS Procedure is an improvement on the CPS Procedure that ensures greater accuracy by introducing feedback between the fluid and structural fields within a time step. This is done at the expense of an extra half-step taken by the fluid solver. Figure 3.7b on the preceding page gives a graphical depiction of this idea. An overbar denotes predicted quantities at the half time step.

Implicit Methods

Implicit coupling involves the exchange of information between the separate solvers at each iteration to ensure conservation of energy and momentum. Both solvers are run concurrently which according to Matthies and Steindorf [46] is just as efficient as a monolithic approach.

Block-Jacobi and Block-Gauss-Seidel Methods

Cervera et al. [15] provide an introduction to Block-Jacobi and Block-Gauss-Seidel Methods. These methods are improved on by Matthies and Steindorf [46] introducing a Block-Newton Method which has superior stability and convergence properties. Fernández and Moubachir [20] improve the Block-Newton method further by introducing expressions to evaluate the exact Jacobians that were only approximated in [46]. Symbols and terminology used in the following sections are as defined in § 3.4.3.

Assuming that the fluid and the structural problems are discretised appropriately we have two sets of discrete equilibrium equations to solve for each time step. There are the Navier-Stokes equations for the fluid domain (see eq. 3.16) and an appropriate set of equations for the structural domain (see eq. 3.17).

$$N(W^{n+1}, U^{n+1}) = 0 \quad (3.16)$$

$$S(U^{n+1}) = h(W^{n+1}) \quad (3.17)$$

The fluid solver operates on an iterative basis performing a few subcycles for each time step until a convergence criteria has been reached. The structural solver may or may not operate on an iterative basis given the complexity of the structural model. For our purposes however we can regard a simple structural solver as a very efficient iterative solver requiring just one iteration. With this in mind we can restate eqs. 3.16 and 3.17

as fixed point iterations as seen in eqs. 3.18 and 3.19 respectively.

$$W_{k+1} = F(W_k, U_k) \quad (3.18)$$

$$U_{k+1} = G(W_{k+1}, U_k) \quad (3.19)$$

Assuming eq. 3.18 is solved first, eqs. 3.18 and 3.19 represent one stage of either the Block-Jacobi Method or the Block-Gauss-Seidel Method, depending on whether the fluid variable term in eq. 3.19 is W_k or W_{k+1} respectively. Cervera et al. [15] point out that of the two methods, the Block Gauss Seidel method has the higher convergence rate.

Sun et al. [76] implement the Block Gauss Seidel Method in the FSI simulations that they carry out. A flow diagram depicting the steps carried out in this process is shown in fig. 3.8.

Block-Newton Method

Matthies and Steindorf [46] criticise the block Gauss-Seidel method of iteration as being often too slow and sometimes not convergent at all. They propose the use of a Newton-Raphson type of iteration where the derivatives are approximated by finite differences. Called the *block-Newton* method, they formulate a linear system to be solved at each step given in equation 3.20.

$$\begin{pmatrix} D_W f(w_k, u_k) & D_U f(w_k, u_k) \\ D_W g(w_k, u_k) & D_U g(w_k, u_k) \end{pmatrix} \begin{pmatrix} \Delta w_k \\ \Delta u_k \end{pmatrix} = - \begin{pmatrix} f(w_k, u_k) \\ g(w_k, u_k) \end{pmatrix} \quad (3.20)$$

where,

$$\begin{aligned} \Delta w_k &= w_{k+1} - w_k \\ \Delta u_k &= u_{k+1} - u_k \\ f(w_k, u_k) &= w_k - F(w_k, u_k) \\ g(w_k, u_k) &= u_k - G(w_k, u_k) \end{aligned}$$

By using only existing solvers for the structure and the fluid, there is no direct access to the partial derivatives in equation 3.20, but Matthies and Steindorf propose an iterative algorithm that approximates them. In the illustrative examples in their paper they demonstrate that the block-Newton method requires fewer iterations than a block Gauss-Seidel method to reach the same solution. However seeing as this is a Newton-Raphson based scheme, it may be prone to convergence problems characteristic of Newton-Raphson methods in general.

A flow diagram of the process followed to obtain Δw_k and Δu_k is given in fig. 3.9. For further understanding of the underlying mathematics the reader is referred to [46].

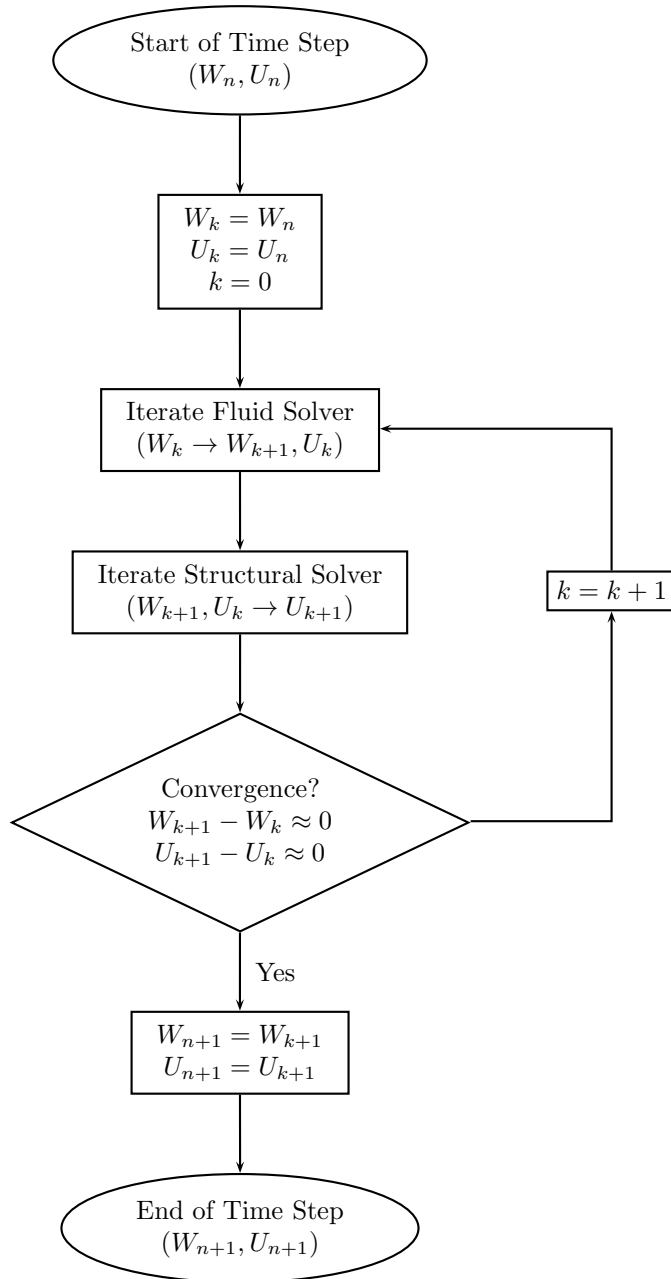


Figure 3.8: Flow diagram of Block Gauss Seidel Method

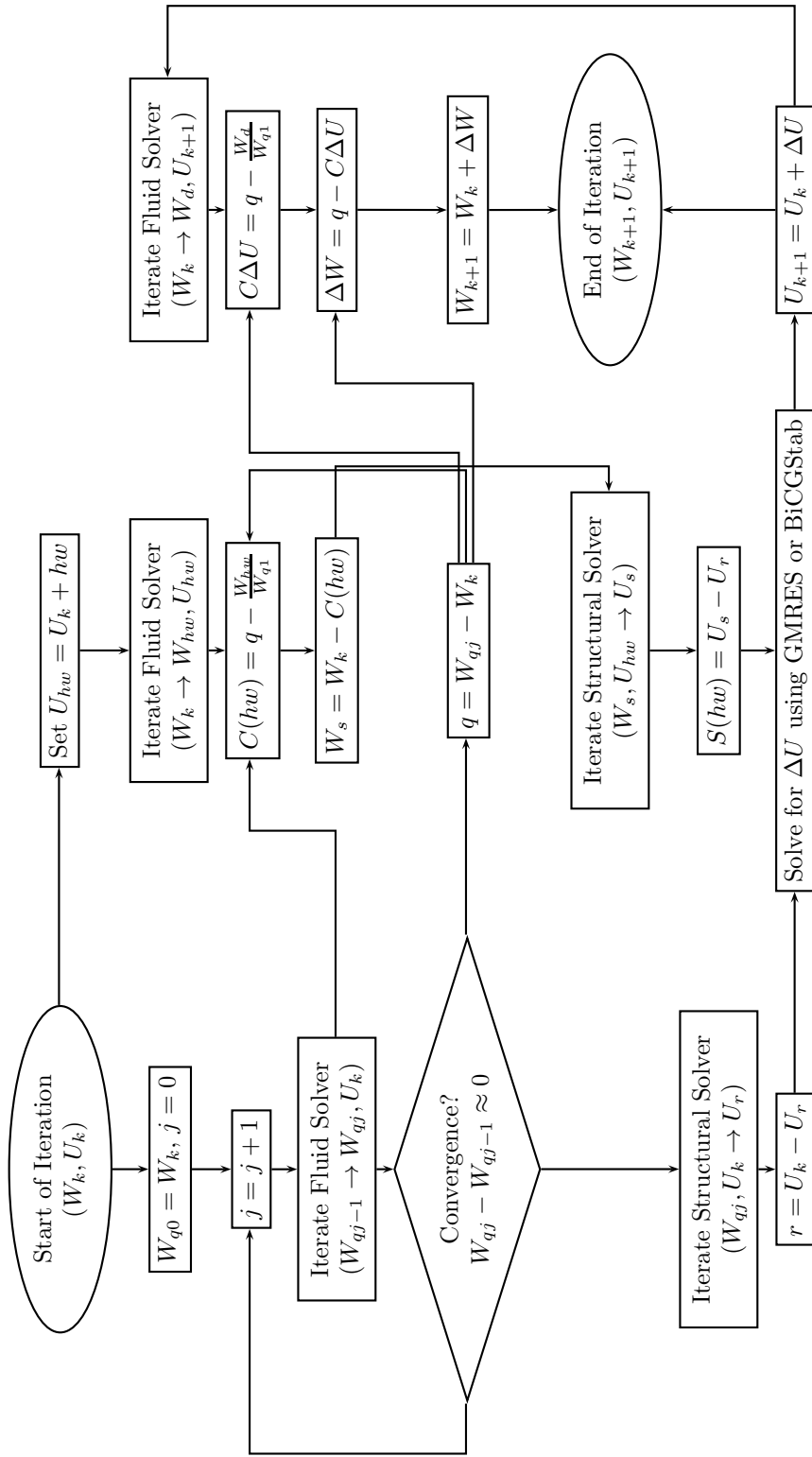


Figure 3.9: Flow diagram of Block Newton Method

Chapter 4

Static Cylinder

4.1 Introduction

The aim of the work presented in this chapter is to find a reliable and effective way to numerically simulate cross-flow past a stationary circular cylinder for a range of Reynolds Numbers that capture the drag crisis. There are important issues that have been encountered in the course of this work which are important to the subsequent work in the thesis. Each of these challenges are presented and discussed in detail. The chapter closes with a review of the effectiveness of all approaches investigated and chooses which is the most appropriate for use in the work presented in later chapters.

4.2 Simulation description

All simulations were carried using a commercial software supplied by ANSYS called CFX-10.0. The following subsections give a terse list of the salient features of these.

Domain geometry

Figure 4.1 on the next page shows the typical geometry used for the simulations.

STREAMWISE LENGTH OF DOMAIN:	18·0 m
TRANSVERSE LENGTH OF DOMAIN:	8·0 m
SPANWISE LENGTH OF DOMAIN:	2·5 m
DISTANCE OF CYLINDER FROM INLET:	4·0 m
DIAMETER OF CYLINDER:	1·0 m
BLOCKAGE AREA RATIO :	0·125
MASKELL BLOCKAGE CORRECTION (SEE § 4.5.2):	0·8275

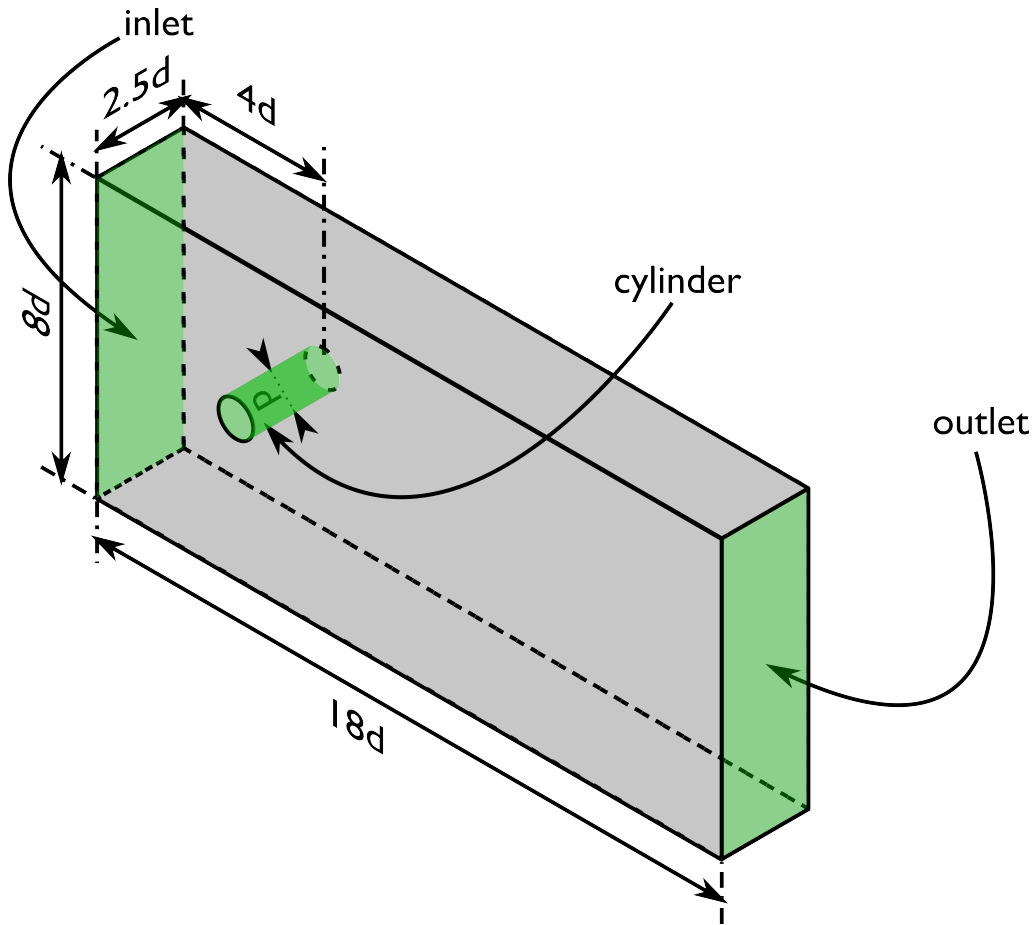


Figure 4.1: Domain Geometry

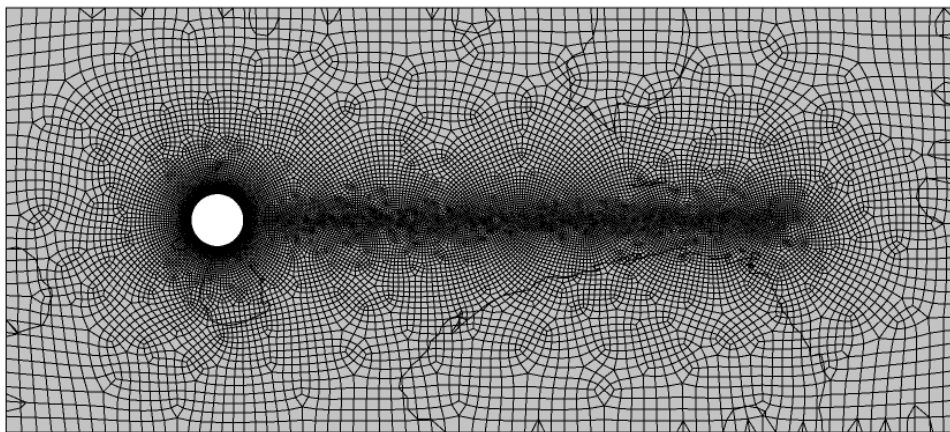


Figure 4.2: Domain cross-section of mesh

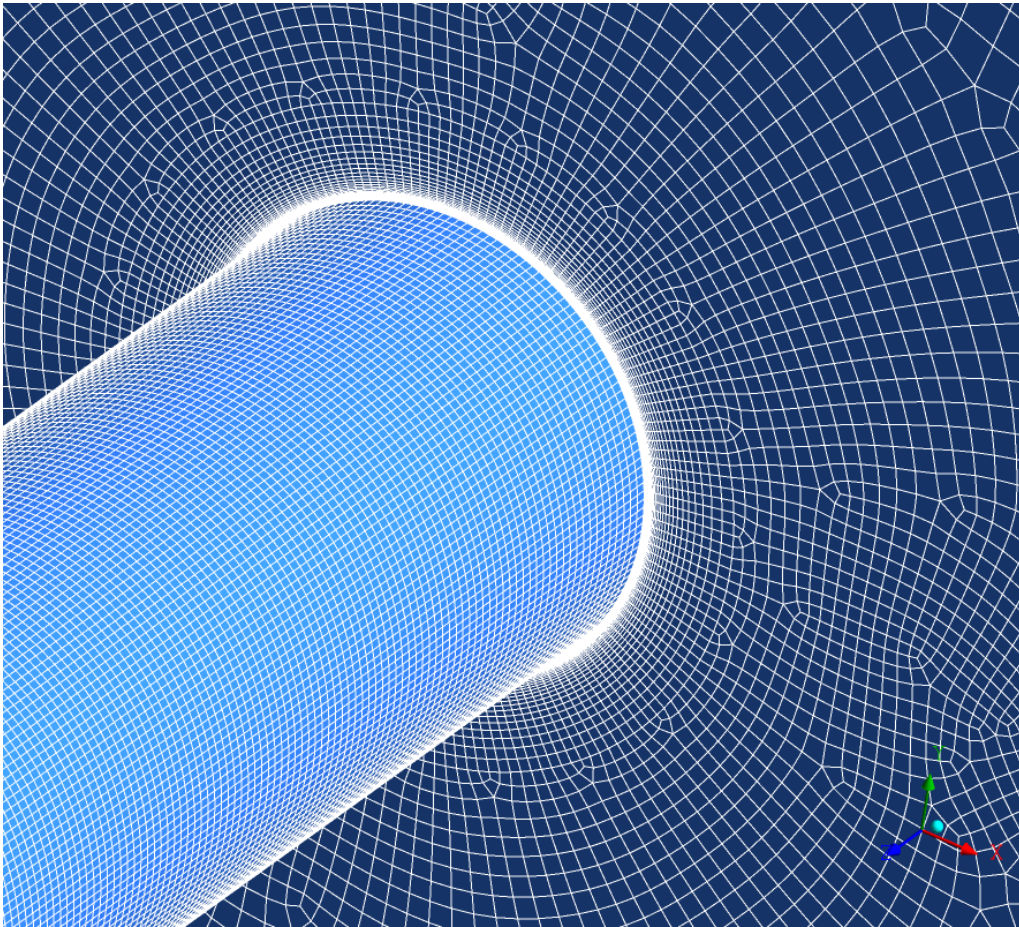


Figure 4.3: Close up view of mesh in cylinder region

Fluid properties

DEFINED MATERIAL:	Air at 25 °C
DENSITY:	1.185 kg/m ³
DYNAMIC VISCOSITY:	1.831 × 10 ⁻⁵ kg/m/s
KINEMATIC VISCOSITY:	1.54515 × 10 ⁻⁵ m ² /s
TURBULENCE MODEL:	LES
SUBGRID SCALE MODELS TESTED:	Dynamic (Germano and Lilly) Smagorinsky

Boundary conditions

INLET BOUNDARY CONDITION:	Normal speed (no turbulence)
---------------------------	------------------------------

Defined Re	Inlet velocity ($\frac{m}{s}$)
30000	0.463
50000	0.773
60000	0.927
70000	1.082
80000	1.236
90000	1.391
100000	1.545
150000	2.318

OUTLET BOUNDARY CONDITION:	Opening pressure and direction Pressure maintained at 0 Pa (relative to reference pressure 1 atm) Direction maintained as normal to boundary face
CYLINDER BOUNDARY CONDITION:	No slip wall (smooth)
TRANSVERSE SIDE WALLS (PARALLEL TO CYLINDER AXIS):	Free slip wall
SPANWISE SIDE WALLS (NORMAL TO CYLINDER AXIS):	Periodic with opposite side (conservative interface flux)

Mesh details (for $Re \leq 100000$ simulations)

CELL TYPE:	Hexahedral throughout
NO. OF CELLS:	2521100
NO. OF FACES:	89222
NO. OF NODES:	2565905
FIRST NODE DISTANCE AT CYLINDER SURFACE:	5.75×10^{-5} m
NO. OF CELL LAYERS IN CYLINDER BOUNDARY REGION:	46
NO. OF CELLS AROUND CIRCUMFERENCE OF CYLINDER BOUNDARY REGION:	176
GEOMETRIC GROWTH RATE OF CELL LAYER THICKNESS IN CYLINDER BOUNDARY REGION:	1.15
TOTAL THICKNESS OF CYLINDER BOUNDARY REGION:	0.2062 m
CELL SIZE IN SPANWISE DIRECTION:	0.025 m

In the mesh generation, a surface is placed in the wake region behind the cylinder, in the same plane as the cylinder axis and extending 10 m downstream. The purpose of this surface is to attach a size function to it as well as the outer surfaces of the cylinder boundary region. This results in the cell size being small in the wake compared to the free stream areas of the domain (as can be seen in Figure 4.2), and ensures an appropriate gradual growth in cell size going away from the cylinder boundary and wake regions (as can be seen in Figure 4.3).

GEOMETRIC GROWTH RATE IN CELL SIZE FROM SOURCE FACES:	1.06
CELL SIZE AT SOURCE FACES:	0.025 m
SIZE LIMIT IN CELL GROWTH FROM SOURCE FACES:	0.4 m

Mesh details (for $Re = 150000$ simulations)

The overall geometry including source faces for the $Re = 150000$ simulations is the same as for the $Re \leq 150000$ simulations.

CELL TYPE:	Hexahedral throughout
NO. OF CELLS:	3443300
NO. OF FACES:	116866
NO. OF NODES:	3501973
FIRST NODE DISTANCE AT CYLINDER SURFACE:	2.30×10^{-5} m
NO. OF CELL LAYERS IN CYLINDER BOUNDARY REGION:	52
NO. OF CELLS AROUND CIRCUMFERENCE OF CYLINDER BOUNDARY REGION:	176
GEOMETRIC GROWTH RATE OF CELL LAYER THICKNESS IN CYLINDER BOUNDARY REGION:	1.15
TOTAL THICKNESS OF CYLINDER BOUNDARY REGION:	0.2196 m
CELL SIZE IN SPANWISE DIRECTION:	0.025 m
GEOMETRIC GROWTH RATE IN CELL SIZE FROM SOURCE FACES:	1.04
CELL SIZE AT SOURCE FACES:	0.025 m
SIZE LIMIT IN CELL GROWTH FROM SOURCE FACES:	0.2 m

Solver settings

TIME STEP SIZE:																			
	<table border="1"> <thead> <tr> <th>Defined Re</th> <th>Time step Δt (s)</th> </tr> </thead> <tbody> <tr> <td>30000</td> <td>0.0060</td> </tr> <tr> <td>50000</td> <td>0.0040</td> </tr> <tr> <td>60000</td> <td>0.0035</td> </tr> <tr> <td>70000</td> <td>0.0035</td> </tr> <tr> <td>80000</td> <td>0.0020</td> </tr> <tr> <td>90000</td> <td>0.0015</td> </tr> <tr> <td>100000</td> <td>0.0015</td> </tr> <tr> <td>150000</td> <td>0.0010</td> </tr> </tbody> </table>	Defined Re	Time step Δt (s)	30000	0.0060	50000	0.0040	60000	0.0035	70000	0.0035	80000	0.0020	90000	0.0015	100000	0.0015	150000	0.0010
Defined Re	Time step Δt (s)																		
30000	0.0060																		
50000	0.0040																		
60000	0.0035																		
70000	0.0035																		
80000	0.0020																		
90000	0.0015																		
100000	0.0015																		
150000	0.0010																		
ADVECTION SCHEME:	Central difference																		
RMS RESIDUAL TARGET:	1×10^{-4}																		
TRANSIENT SCHEME:	Second order backward Euler																		

4.3 Pre-processing recommendations

The following sections discuss recommendations, encountered in the literature and from direct experience, in the setting up and definition of simulations where the main objective is to simulate the drag crisis.

4.3.1 Turbulence Model

An important aspect in a numerical simulation is the way in which turbulence is modelled, the choice of which is made here based on what expected flow features are important to capture. Zdravkovich's [92] summary of all flow conditions that are physically possible for a circular cylinder, presented earlier, can be used to eliminate some candidates for turbulence methods. In the range of flow conditions of interest, unsteadiness exists that forms important features that must be captured in the simulations. Traditional RANS models are considered unsuitable because of their inability to capture transient turbulent features. Although there are some notionally unsteady RANS (URANS) models available, these are not appropriate because it is still only the mean effects of turbulence, albeit in a transient framework, that are modelled, not the unsteadiness of the flow. Another feature of RANS models to consider is that they are relevant to situations where turbulence is present in the entire flow field. At the Reynolds numbers of interest in this work, part of the cylinder will have a laminar boundary layer. Unless there is a specific formulation included in the RANS model to handle laminar to turbulent transition, it would be difficult to reproduce proper behaviour in this region.

The ratio between the largest to the smallest length scales of turbulence is such that the number of grid nodes required to resolve a turbulent flow is a function of $Re^{9/4}$, where Re is Reynolds number.

For the range of Re of interest this makes DNS prohibitively expensive. The turbulence formulations that remain available in commercial CFD products, between RANS models and DNS, are the LES and DES approach. Of these, DES can be dismissed due to time filtering effects that damp the development of resolved turbulence in the region of shear layers close to the cylinder wall. The unsteadiness that is considered important occurs in the near wall regions to which DES assigns a RANS method. That leaves LES, which is the turbulence method employed for the work in this chapter. There are numerous SGS models available for LES. This chapter will focus on two candidate methods: the Smagorinsky model and the Dynamic (Germano and Lilly [41]) model.

4.3.2 Discretisation - time step requirements

Since the aim is to capture the drag crisis, a high level of discretisation is needed at the cylinder surface. The time step size needs to be small enough to capture the development of flow instability which develops into turbulence at the boundary layer, however not so small that superfluous solution steps are produced. For this reason and because

of guidance related to the LES Dynamic model given in the ANSYS CFX user documentation [5], the target Courant number (a dimensionless measure of residence time in a cell) is just below 1. The actual values of Courant number that occur in the simulations are summarised in Table 4.1.

Table 4.1: Courant number encountered in simulations

Defined Re	Courant number	
	(rms)	(max)
30000	0.12	1.53
50000	0.14	1.70
60000	0.14	1.70
70000	0.17	2.06
80000	0.11	1.31
90000	0.09	1.11
100000	0.11	1.24
150000	0.11	1.61

4.3.3 Discretisation - meshing requirements

As mentioned in a previous chapter, the y^+ statistic is a dimensionless number indicating the distance of the first node from a boundary. According to guidance information, for the LES models used the target value of y^+ is less than 1. In addition to this requirement, the mesh must be refined in the near cylinder boundary and wake to capture a high-gradient of velocity and eddy viscosity. Table 4.2 shows mean y^+ statistics for all simulations considered.

Table 4.2: Maximum y^+ encountered

Defined Re	y^+
30000	0.339
50000	0.598
60000	0.761
70000	0.773
80000	0.914
90000	1.181
100000	1.129
150000	0.854

4.3.4 Domain dimensions

If the dimensions in the spanwise (i.e. parallel to cylinder axis), streamwise (i.e. normal to inlet and outlet boundaries), and transverse (i.e. orthogonal to spanwise and streamwise) directions are too short, it can have a dramatic effect on the quality of results obtained. On the other hand if they are too long it can lead to superfluous use of computing

resources. It is important to strike the correct balance in determining the most economic yet effective length of dimension in each direction, and to have an appreciation of the effects of varying each dimension.

In terms of spanwise dimension, the length required is determined by the likely "correlation length" that will occur. This is explored and discussed in further detail in the next chapter, but it is worth noting here that, according to data compiled and presented by Norberg [59], a spanwise dimension of at least two cylinder diameters is seen as sufficient for the range of Reynolds number considered.

Regarding the streamwise direction, there has to be sufficient domain to capture the wake that has an effect on the flow at the cylinder and upstream. Also, as will be discussed in the next section, there has to be sufficient upstream area to see development of turbulence in the flow approaching the cylinder.

The transverse dimension determines the amount of blockage i.e. the measure of how much of the domain cross-section is occupied by the bluff object in the direction of flow. Blockage is an effect common to wind tunnel experiments and numerical simulations with flow domains of the type shown above. It is undesired because of the often appreciable level of error introduced to the results when compared to unconfined flows. The effect of blockage can be reduced by using a flow domain of a larger transverse dimension, but for most flow domains of a practical size, it is never entirely eliminated. Thus the common approach is to introduce a correction for blockage in the results. The Engineering Sciences Data Unit has produced a publication that discusses blockage in detail and gives advice on blockage correction methods [84]. The correction method employed for the simulations considered in this chapter is discussed in more detail in the next section.

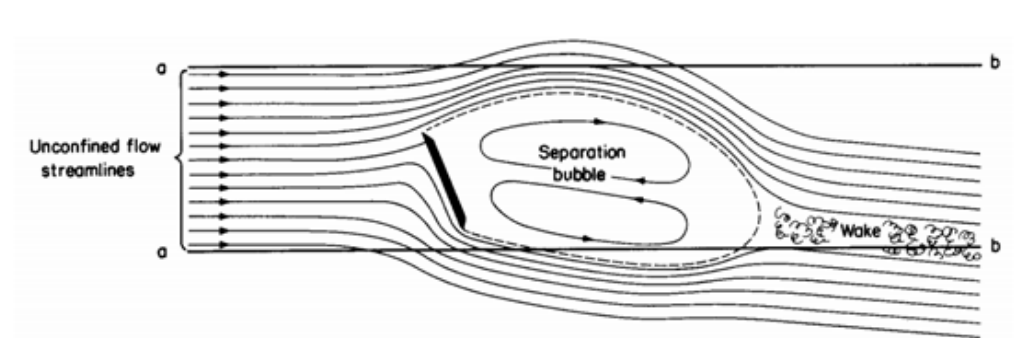


Figure 4.4: Unconfined Flow Streamlines

Figure 4.4 shows a drawing taken from [84] showing unconfined flow streamlines superimposed over the walls of a domain with high blockage. It is easy to see from this diagram how the flow can be changed by the presence of the walls of the domain. The wake would be moved upwards to be within the domain and the separation bubbles would be constricted. The streamlines would be further constricted at the sides of the bluff object and so the mean velocity in this region would be increased. Consequently the acceleration of flow and the drop in pressure from upstream would be greater. These

concepts are shown by the representative graphs reproduced in Figure 4.5.

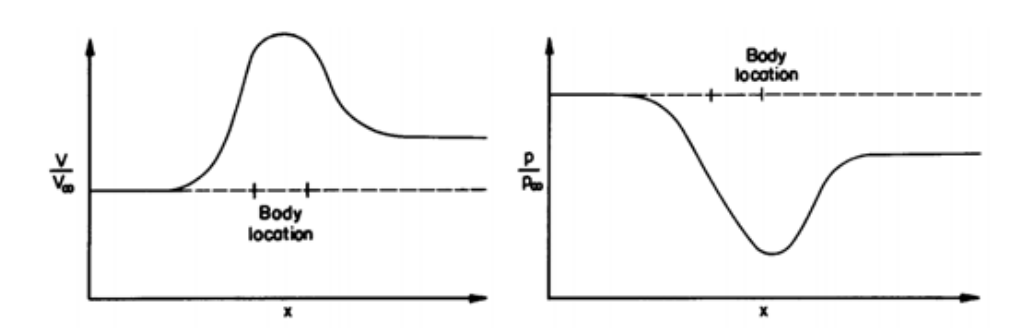


Figure 4.5: Blockage effects on streamwise velocity and pressure

Richter and Naudascher [64] have long ago investigated the effects of blockage specifically on flows past circular cylinders in the region of the drag crisis. Some figures from their paper are reproduced below (figures 4.6, 4.7, 4.8, 4.9). In order of appearance they represent Strouhal Number, Mean Drag Coefficient, Fluctuating Drag, and Fluctuating Lift.

In all graphs reproduced from [64] the amount of blockage is reproduced by d/h where d is the dimension of the bluff object and h is the wind tunnel dimension. The relevant d/h value for the present work is $\frac{1}{8}$.

It can be seen by the reproduced graph in Figure 4.6 that the Strouhal number jumps to an increased value as the Reynolds number increases through the drag crisis. The level of blockage affects all points of this graph.

The jump in Strouhal number at the drag crisis is seen to occur at lower values of Reynolds number as blockage increases. The height of the jump (i.e. difference between maximum and minimum values of Strouhal number) increases from $d/h = 0$ to $d/h = 1/4$, beyond which it appears to remain constant.

All values of Strouhal number are raised with increasing blockage. No data is plotted for $d/h = 1/8$ but nonetheless it can be seen that the Strouhal number St for flows with Reynolds numbers lower than the critical range would be in the range $0.19 \leq St \leq 0.21$

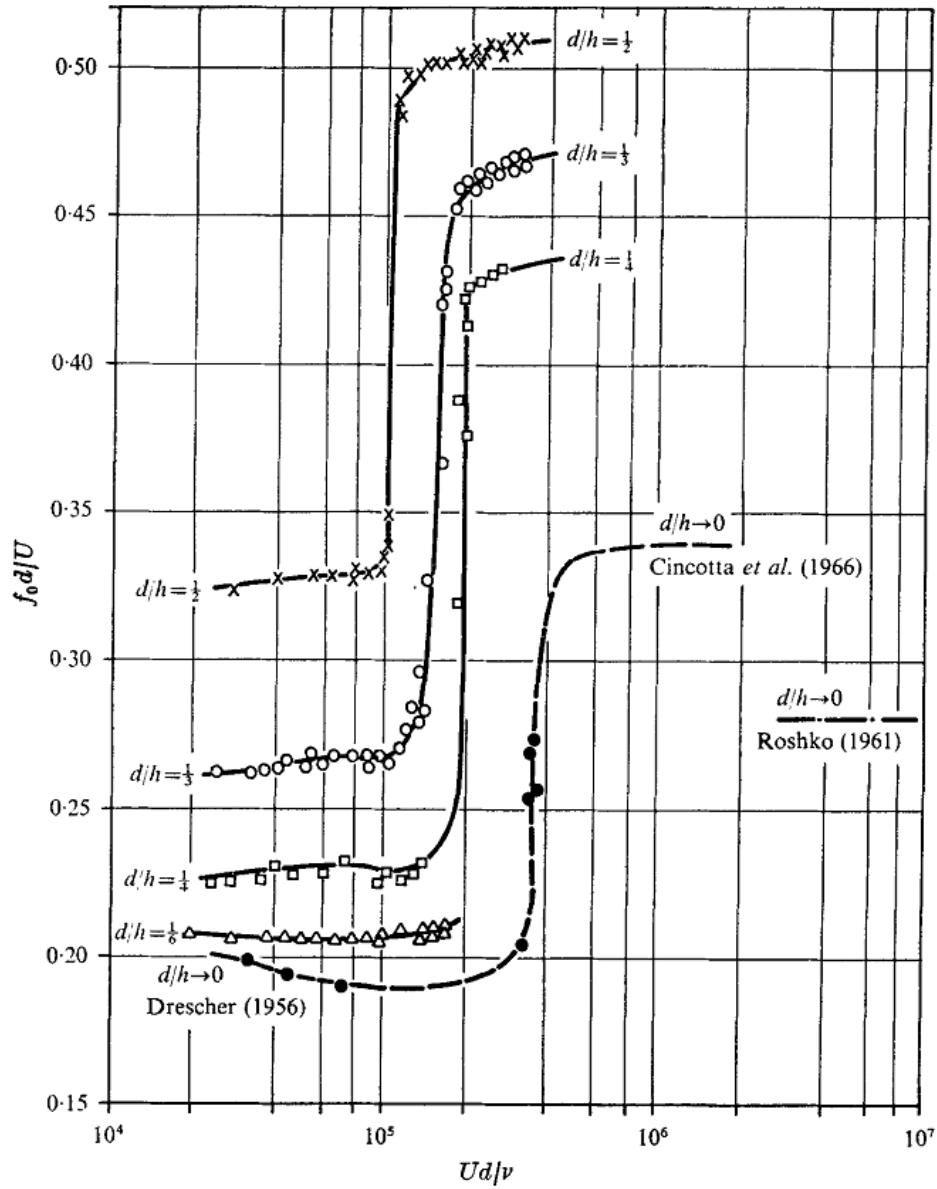


Figure 4.6: Strouhal number $f_0 d/U$ for various confinement ratios d/h vs. Reynolds number Re for $10^4 < Re < 10^7$, reproduced from [64]

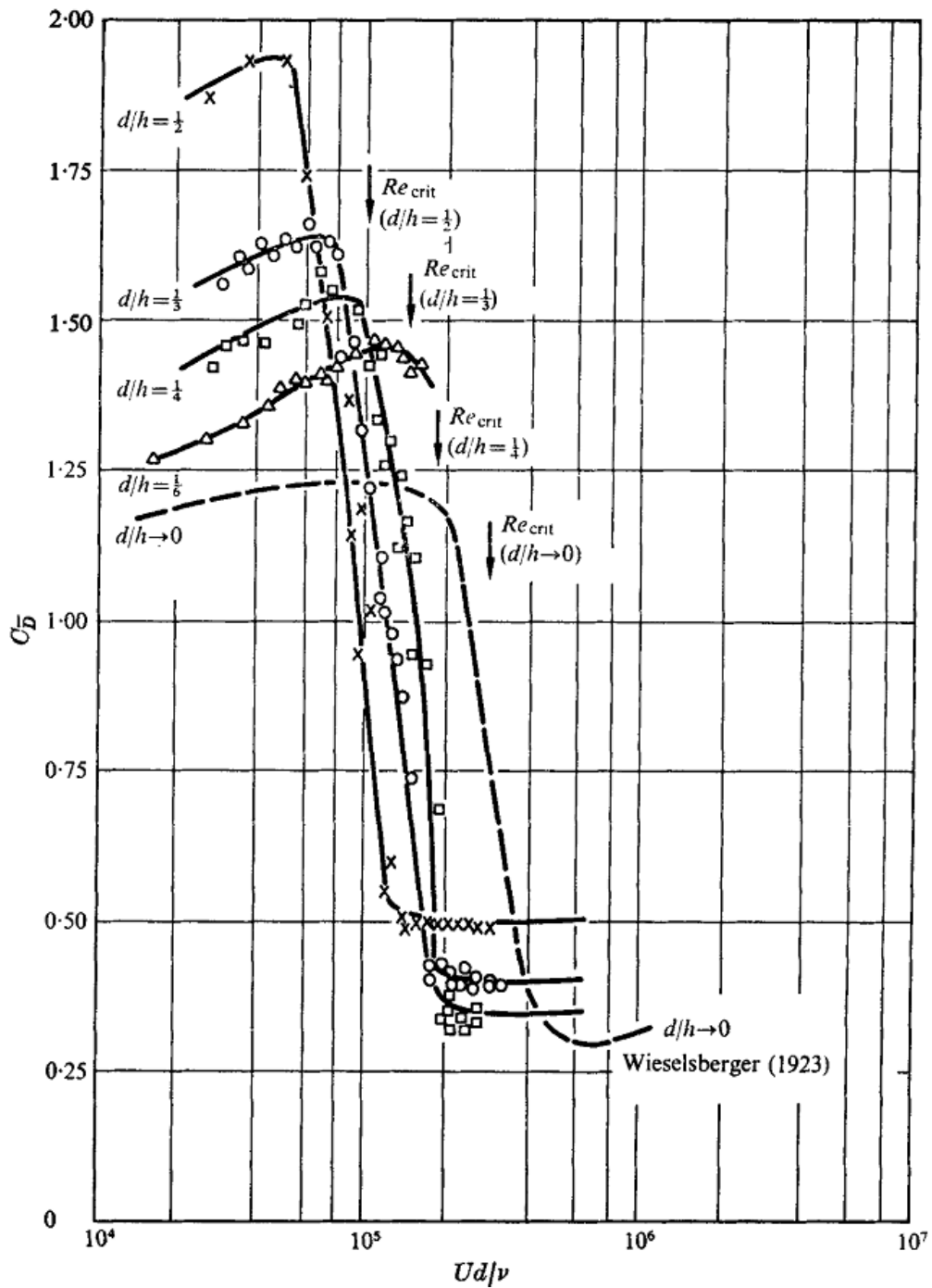


Figure 4.7: Mean drag C_D for various confinement ratios d/h vs. Reynolds number Re for $10^4 < Re < 10^7$, reproduced from [64]

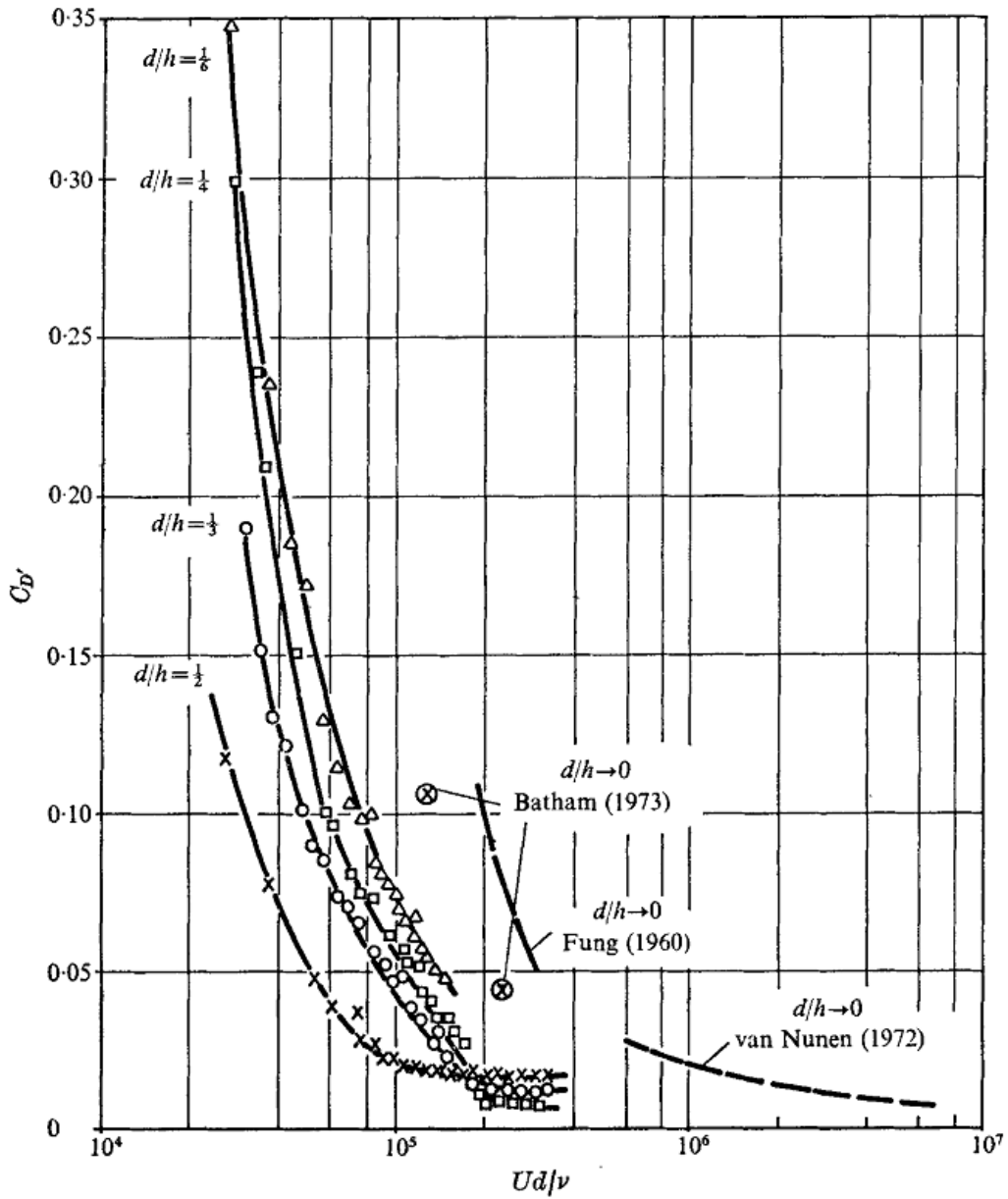


Figure 4.8: Fluctuating drag C_D for various confinement ratios d/h vs. Reynolds number Re for $10^4 < Re < 10^7$, reproduced from [64]

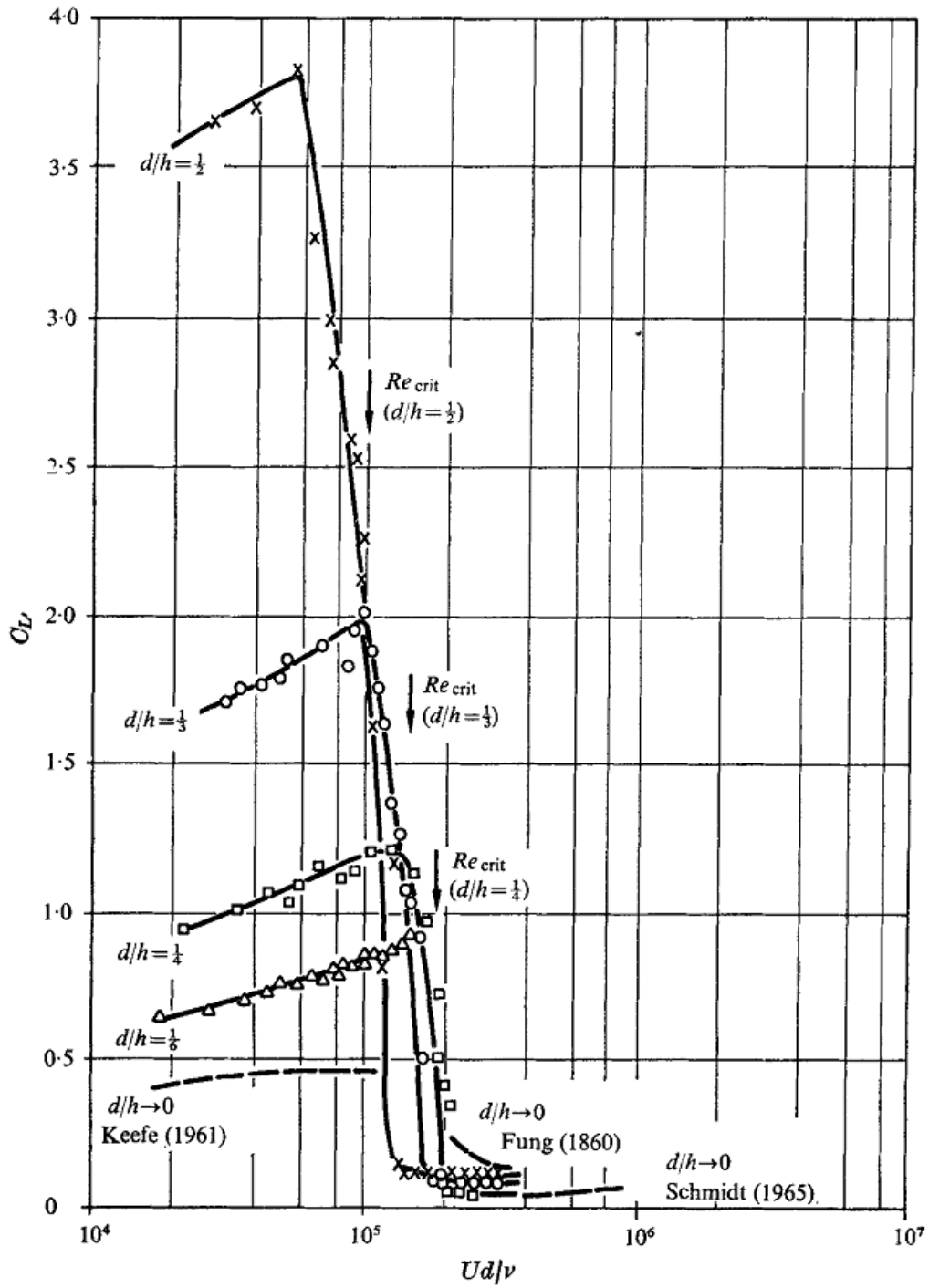


Figure 4.9: Fluctuating lift C_D for various confinement ratios d/h vs. Reynolds number Re for $10^4 < Re < 10^7$, reproduced from [64]

4.4 Runtime of simulations

Table 4.3 shows data associated with the length of time that each simulation has covered.

Transit times shown are simply the streamwise length of domain divided by the inlet velocity for each simulation. This figure divided by the timestep size will give the minimum number of timesteps required to simulate a fluid particle travelling from the inlet boundary to the outlet boundary. Most of the simulations at each defined Re have used an initial flowfield from a simulation of a different value of Re as a starting point. Thus the transit time has been useful when a change to Re has been introduced because it can indicate the earliest point from which to record data for post-processing.

The number of shed cycles shown for each simulation is the product of the shedding frequencies given further on in this chapter and the total simulation time for which significant data is recorded.

A natural concern about run time of simulations is how long would be sufficient for the purpose at hand. This is explored in § 4.4.1 with a discussion on stationarity.

Table 4.3: Runtimes for all static cylinder simulations

Defined Re	Minimum transit time (s)	Total time covered (s)	Shedding frequency (Hz)	No. of shed cycles
30000	38.83	260.64	0.094	24.5
50000	23.30	252.30	0.176	44.4
60000	19.42	157.83	0.221	34.8
70000	16.64	137.36	0.265	36.4
80000	14.56	106.04	0.304	32.2
90000	12.94	111.95	0.352	39.4
100000	11.65	71.75	0.397	28.5
150000	7.77	117.09	0.596	67.4

4.4.1 Stationarity

For the purpose of these simulations, stationarity is defined by the variation of mean and variance of a physical property with time. A process with a constant mean and variance and can be described as stationary or random. This is a property which is described in terms of probability. An infinite number of tests for randomness is possible, each testing for a specific unique pattern. Therefore the application of a finite number of tests can never be considered to give a definitive result. Thus the tests follow the concept of statistical hypothesis testing, where a *null hypothesis* (H_0) and *alternate hypothesis* (H_a) is considered.

The null hypothesis is a statement of the assumed default property of the signal until proved otherwise. The alternative hypothesis is a statement which is considered true on the occasions when the null hypothesis is determined to be false. Thus there are only

two possible conclusions from hypothesis testing, this is set out in Table 4.4 as a 2×2 array against the true unknown status of the data analysed.

Table 4.4: Possible error outcomes of hypothesis testing

True situation	Conclusion	
	Accept H0	Accept Ha (reject H0)
Data is random (H0 is true)	No error	Type I error
Data is not random (Ha is true)	Type II error	No error

It is possible in hypothesis testing that the wrong conclusion can be reached. As shown in Table 4.4, a situation where the data is truly random but the null hypothesis is rejected is known as a Type I error. A situation where the null hypothesis is accepted but the data is truly non-random is known as a Type II error.

The probability of a Type I error is called the *level of significance* of the test, and is denoted by α . This is the probability of falsely rejecting a null hypothesis, and its value can be chosen by the tester.

The probability of a Type II error, denoted by β , is more difficult to determine. It is the probability that a test will indicate that the data sequence is random when in fact it is non-random. This can take on many different values because there are many different ways that a sequence can be non-random, each relating to a unique value of β .

The tests undertaken minimise the probability of a Type II error by following the procedures described in NIST Special Publication 800-22 Revision 1 [60]. Each test described therein focusses on a particular randomness statistic which is used to determine acceptance or rejection of the null hypothesis. For all tests presented, the null hypothesis (H0) is that the drag signal is random. The alternate hypothesis (Ha) is that the drag signal is non-random. With randomness assumed, this statistic will have a distribution of possible values. A theoretical reference distribution is determined by mathematical methods. From this reference distribution a *critical value* is determined. This value is usually at the extreme tail ends of the distribution (e.g. at the 99% point). During a test, a test statistic value is calculated on the data sequence, and compared against the critical value. If the critical value is exceeded the null hypothesis for randomness is rejected. Otherwise the null hypothesis is accepted.

For each test in NIST Special Publication 800-22 Revision 1 [60], the test statistic is used to calculate a *P-value* that indicates the strength of evidence against the null hypothesis. The *P-value* is the probability that a theoretically perfect random number generator would have produced a less random signal than the sequence tested. If the P-value is 1, this indicates that the sequence appears to have perfect randomness. A P-value of zero indicates complete non-randomness.

The threshold P-value that determines the test conclusion is α , the significance level. If $P\text{-value} \geq \alpha$, then the null hypothesis is accepted, i.e. the data appears to be random. If $P\text{-value} < \alpha$, then the null hypothesis is rejected, i.e. the data appears to be non-random.

The tests in [60] used for the simulations in this chapter are the *Frequency (monobit) test* and the *Runs Test* on the cylinder drag signal over time. The value of α chosen for the tests is 0.01, which indicates that one would expect one sequence in 100 to be rejected by the test if the sequence was random. A P-value ≥ 0.01 would mean that the data would be considered to be random with a confidence level of 99%. A P-value < 0.01 would mean that the data would be considered to be non-random with a confidence of 99%.

The input for each test described below is a sequence of ones and zeros, ϵ , consisting of n observations, that has been derived from drag coefficient vs. time data. For reasons discussed further on, the drag coefficient vs. time signal is split up into a number of segments. A segment whose mean value is greater than the median value of the entire sequence is represented by a 1 in the ϵ sequence. Conversely, a 0 appears in the ϵ sequence, where the mean value of a segment is not greater than the median for the entire sequence.

To compute the P-value in each test, the complimentary error function (erfc) is used. This is defined as follows:

$$\text{erfc}(z) = \frac{2}{\sqrt{\pi}} \int_z^{\infty} e^{-u^2} du \quad (4.1)$$

Frequency (monobit) test

The focus of this test is the proportion of zeros and ones for the whole sequence. The purpose of this test is to determine whether this proportion is the same as would be expected for a truly random sequence.

The steps undertaken for the frequency (monobit) test are as follows:

1. Conversion to ± 1 : Zeros and ones of input sequence ϵ are converted to values of -1 and $+1$ respectively. The converted sequence is summed together, i.e. $S_n = X_1 + X_2 + \dots + X_n$, where $X_i = 2\epsilon_i - 1$.
2. Compute the test statistic $s_{obs} = \frac{|S_n|}{\sqrt{n}}$.
3. Compute $P\text{-value} = \text{erfc}\left(\frac{s_{obs}}{\sqrt{2}}\right)$.
4. If P-value < 0.01 , then the sequence is non-random. Otherwise, conclude that the sequence is random.

Runs test

The focus of the runs test is the total number of runs in a sequence. A run is a sequence of identical bits. The purpose of this test is to determine whether the number of runs is as expected for a random sequence.

The steps undertaken for the runs test are as follows:

1. Perform the frequency (monobit) test described above. Only proceed to the next step if the sequence passes this test. Otherwise the runs test is not applicable and the conclusion should be that the sequence is non-random.

2. Compute the proportion of ones in the sequence: $\gamma = \frac{\sum_j \epsilon_j}{n}$.

3. Compute the test statistic,

$$V_n = \sum_{k=1}^{n-1} r(k) + 1$$

where $r(k) = 0$ if $\epsilon_k = \epsilon_{k+1}$, and $r(k) = 1$ otherwise.

4. Compute

$$P - value = \operatorname{erfc} \left(\frac{|V_n - 2n\gamma(1 - \gamma)|}{2\sqrt{2n\gamma(1 - \gamma)}} \right)$$

5. If P-value < 0.01, then the sequence is non-random. Otherwise, conclude that the sequence is random.

It is recommended in [60] that the sequence tested should have a minimum size of 100 bits, i.e. $n \geq 100$.

Application of runs test

The runs test described above was applied to the drag coefficient vs. time signal for all simulations. The result from converting every value of drag coefficient (i.e. no segmentation and averaging) into ϵ was “non-random” for all simulations tested.

This would appear to suggest that all the simulations should be run further to achieve stationarity in the drag coefficient. The runs test is essentially a test of independence, thus it is apt to pose the question: are successive observations independent of one another or are they correlated? It is reasonable to consider that a flow variable has dependence to some extent on the state of the flowfield over previous timesteps. When viewed in this light, it is unsurprising to encounter that a “non-random” conclusion for all simulations tested since this indicates that the drag coefficient at any instant is dependent on its value in the previous timestep. The extent of dependence is found by splitting the sequence of drag coefficient observations into blocks of an optimal size, where the conclusion is “random” but would be “non-random” for any smaller block.

Table 4.5: Runs test results for segmented drag observations

Defined Re	Period of independence [s]	Shedding period [s]
30000	7.04	10.63
50000	5.86	5.68
60000	3.76	4.53
70000	3.61	3.77
80000	2.41	3.29
90000	2.73	2.84
100000	2.05	2.52
150000	1.53	1.68

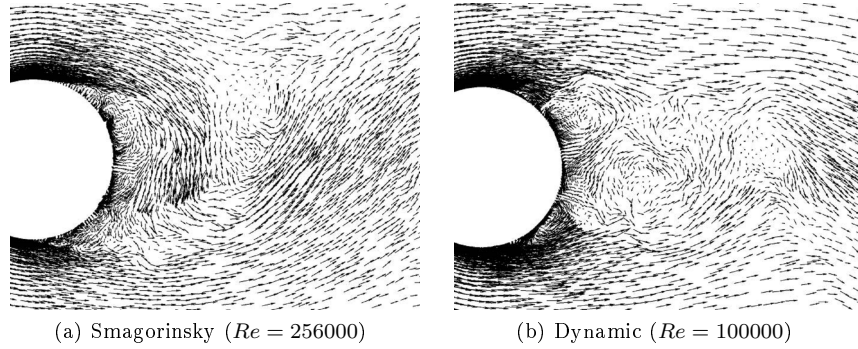


Figure 4.11: Typical velocity flowfield vector plot at the downstream cylinder side

occurs closer to the rearward face of the cylinder as the Reynolds number increases. At a Reynolds number just below that for the drag crisis two transition points can be observed, one in each shear layer just beyond the point of separation on either side of the cylinder. An increase in Reynolds number causes these points to move causing one or both separation points to jump from a position at roughly 90° to a position 120° on the perimeter measured from the upstream stagnation point. This results in a drop in drag caused by the narrowing of the wake behind the cylinder. This happens, to an extent, with the Dynamic model, Figure 4.11b, but it does not materialise with the Smagorinsky model, Figure 4.11a. Plotting the turbulence viscosity in the first part of the boundary layer, Figure 4.12, reveals why this is the case. The Smagorinsky closure does not recover a sensible asymptotic behaviour of the sub-grid viscosity at the wall.

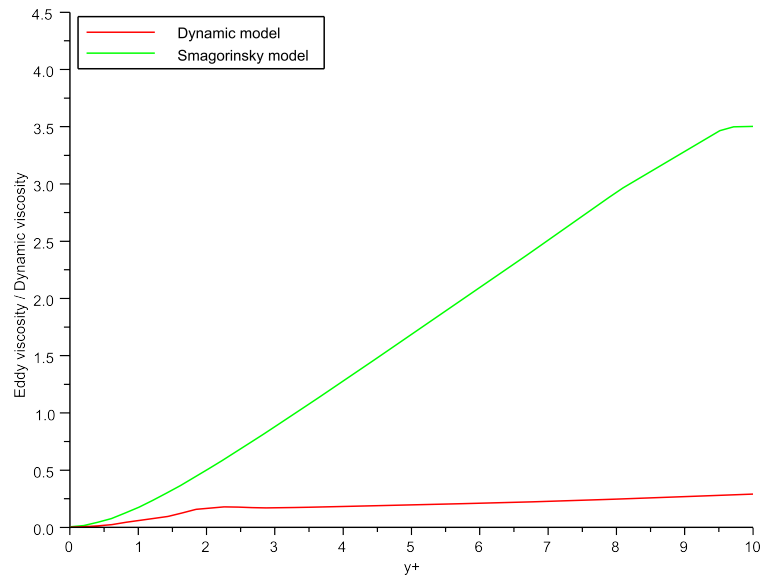


Figure 4.12: Plot of eddy viscosity ratio against y^+ at cylinder wall normal

It can be seen that in the same location of the domain, for the same initial flow con-

ditions, the Smagorinsky model predicts a far greater amount of eddy viscosity than that predicted by the Dynamic model. In fact the Smagorinsky model is commonly criticised in the literature for over prediction of eddy viscosity in near-wall regions (cf. Nicoud and Ducros [58] in their WALE model proposal). A way of addressing the problem in the Smagorinsky model is the application of Van Driest damping. This was attempted for the simulations above but was found to produce little difference in mean drag. Van Driest damping has been criticised by in the literature as being a somewhat arbitrary correction with no physical basis. Certainly it has not been useful in this case. If a model generally predicts too much eddy viscosity in near wall regions, it is likely that small scale disturbances at the cylinder wall are effectively damped out in these simulations. These small scale disturbances would otherwise lead to transition to turbulence in the boundary layer which, by the description of the drag crisis given earlier, would be a necessary feature to capture in the simulations. The origin of the difference in eddy viscosity prediction is the model constant. For the Smagorinsky model it is a constant value defined as part of the initial conditions. The Dynamic model calculates the model constant, so that it can have a varying value throughout the domain, dependent on local conditions. Thus for near-wall regions the model constant it calculates is lower than the value used for the Smagorinsky model. Although the Dynamic model has more computing overhead than the Smagorinsky model, it can be seen from the above that it is necessary for the work in this thesis. All discussions of results from here to the end of this chapter shall relate to the Dynamic model.

4.5.2 Blockage correction

It has been mentioned earlier that it is necessary to consider how blockage will affect the results obtained from the simulations. ESDU publication 80024 discusses in detail the effects of blockage and a variety of correction methods. The correction method used for the simulation results presented here is presented in section 4.1 of this reference, the Maskell/Cowdrey correction.

$$\frac{C_{Ff}}{C_F} = 1 - mS/A \quad (4.2)$$

where C_F is a force parameter in confined flow conditions, C_{Ff} is the equivalent force parameter in free flow conditions, S/A is the amount of blockage (12.5% for the simulations considered here), and m is an empirical factor whose value depends on the shape of the bluff object (1.38 for circular sections). In the case of the simulations presented here, the ratio $\frac{C_{Ff}}{C_F}$ is calculated to be 0.8275.

It should be noted that the above method is recommended for flows where the point of separation occurs at or upstream of the maximum cross-sectional area of the body. Another method is presented in 80024, the Quasi-streamlined flow method, recommended for flows where separation occurs downstream of the maximum cross-sectional area of the body.

4.5.3 Mean Drag

The drag data produced by the simulations is compared to data presented in ESDU publication 80025 [83]. This publication compiles experimental data from a range of literature. Each item of experimental literature will tend to have a level of free-stream turbulence and cylinder surface roughness that is unique. Both turbulence and roughness have an observable effect on drag, so the ESDU publication presents a method to normalise the Reynolds number according to turbulence and roughness, thereby unifying all experimental observations reviewed.

The method to calculate 'effective' Reynolds number Re_e is summarised as follows:

1. Obtain a value of the surface roughness parameter, ϵ , from Table 10.1 in ESDU publication 80025 [83] and evaluate ϵ/D , where D is cylinder diameter.
2. Determine λ_R from Figure 2 in ESDU publication 80025 [83].
3. Evaluate $Re = V_\infty D/\nu$, where V_∞ is free-stream velocity and ν is kinematic viscosity. If $Re > 2 \times 10^6$ then the factor $\lambda_T \approx 1.0$ and steps 4 to 8 can be ignored.
4. Obtain typical values of the intensity I_u and scale of turbulence rL_u from Table 10.2 in ESDU publication 80025 [83] and evaluate $I_u(D/{}^rL_u)^{1/5}$.
5. Determine λ_{Tcrit} from Figure 3a in ESDU publication 80025 [83].
6. Evaluate $Re_{crit} = 4.5 \times 10^5 / (\lambda_{Tcrit} \lambda_R)$.
7. Evaluate Re/Re_{crit} .
8. Determine $(\lambda_T - 1)/(\lambda_{Tcrit} - 1)$ from Figure 3b in ESDU publication 80025 [83] and hence evaluate λ_T .
9. Evaluate $Re_e = \lambda_T \lambda_R Re$.

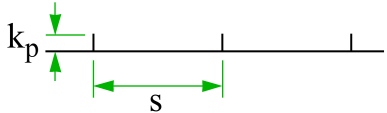
The following paragraphs describe how the above method was applied to the simulation results.

Roughness parameter

Typical values of ϵ for various materials (e.g. metal, brickwork, glass, \check{E}) are given in table 10.1 of ESDU publication 80025 [83]. In the case of the simulations presented here, none of these typical values can be used with confidence since the cylinder surface is defined as a smooth wall. There is a roughness to consider however, introduced by the fact the mesh consists of cells with only planar facets, resulting in ridges formed by the positions where cell faces meet together on the cylinder surface (see Figure 4.13).

The mesh used for all simulations has 176 nodes around the entire circumference, thus the ridge height k_p is determined in the following way: $k_p = r(1 - \cos(\pi/n)) = 0.5 \times (1 - \cos(\pi/176)) = 7.96531 \times 10^{-5}m$. Although k_p is known, no clear relationship between ϵ and k_p exists. ESDU publication 80025 [83] gives a table of ϵ/k_p ratios for a

Table 4.6: Surface roughness parameters from ESDU publication 80025 [83]

Description	Sketch	s/k_p	ϵ/k_p
Rounded grooves		40	0.04
Fences		2.5	2

variety of types of surface finish. Although none of the surface finish types match exactly, it is considered unlikely that the ϵ/k_p ratio for the surface in the figure below will be less than 0.04 or greater than 2. The corresponding surfaces shown in table B.3 in ESDU publication 80025 [83] are given here in Table 4.6.

It is considered unlikely that the cylinder surface in our simulations would perturb the boundary flow to a lesser extent than the rounded grooves shown in in Table 4.6, nor would it perturb the boundary flow to a greater extent than the fences shown in Table 4.6.

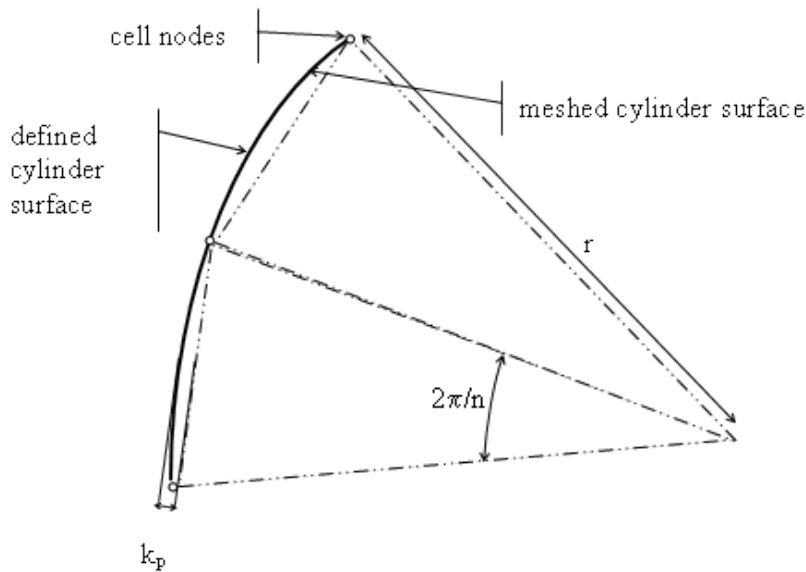


Figure 4.13: Sketch showing surface facets of cylinder due to meshing

Effective Reynolds numbers for a smooth condition, a 'least rough' condition, and a 'most rough' condition are calculated. Table 4.7 shows the difference between the smooth and the 'most rough' condition.

It is clear from Table 4.7 that the effect of roughness diminishes as the Reynolds

Table 4.7: Difference in corrected Re between smooth and 'most rough' condition

Defined Re	Difference
60000	11-14%
70000	10-12%
80000	9-11%
90000	8-10%
100000	8%

Table 4.8: Re values corrected for blockage

Defined Re	Re corrected for blockage
60000	65957.97
70000	76950.96
80000	87943.95
90000	98936.95
100000	109929.90

number increases. This is expected since the boundary flow would be less susceptible to perturbation as the momentum carrying the flow over the ridges increases.

λ_R parameter

In ESDU publication 80025 [83], λ_R is determined from Figure 2, which is defined by the following equations:

$$\lambda_R = 1 + (\lambda'_R - 1)\{1 - \exp[-5(Re_e \times 10^{-4})^2]\} \quad (4.3)$$

$$\text{where } \lambda'_R = \lambda_R \text{ for } Re_e > 10^4 \text{ and is given by} \quad (4.4)$$

$$\lambda'_R = 7 - 6 \exp[-0.11E] \quad (4.5)$$

$$(4.6)$$

The above equations require the value of Re_e to be known if it is less than 10^4 . The effective Reynolds number calculated by this procedure will always be above the input value of Re determined at step 3, so for our purposes we can safely assume $\lambda_R = \lambda'_R$ in for all simulations considered.

Re evaluation

The input value of Reynolds number is the value defined in the simulation but corrected for blockage. Table 4.8 presents the corrected values used.

Turbulence intensity and length scale

No turbulence or length scale is defined at the inlet. Nonetheless turbulence still develops upstream of the cylinder. The evidence for this is given by velocity data obtained from

monitor points located upstream of the cylinder as shown in the sketch in Figure 4.14.

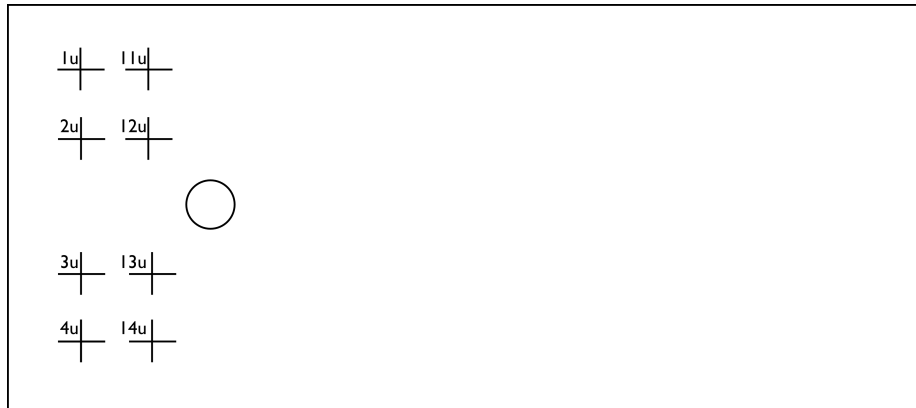


Figure 4.14: Monitor point positions (marked +) upstream of cylinder

A plot of velocity at a time instant for one of the $Re = 60000$ simulations in a plane normal to the cylinder axis at mid span is shown in Figure 4.15. The scale ranges from the defined inlet velocity to the blockage velocity determined by the Maskell/Cowdrey correction defined earlier.

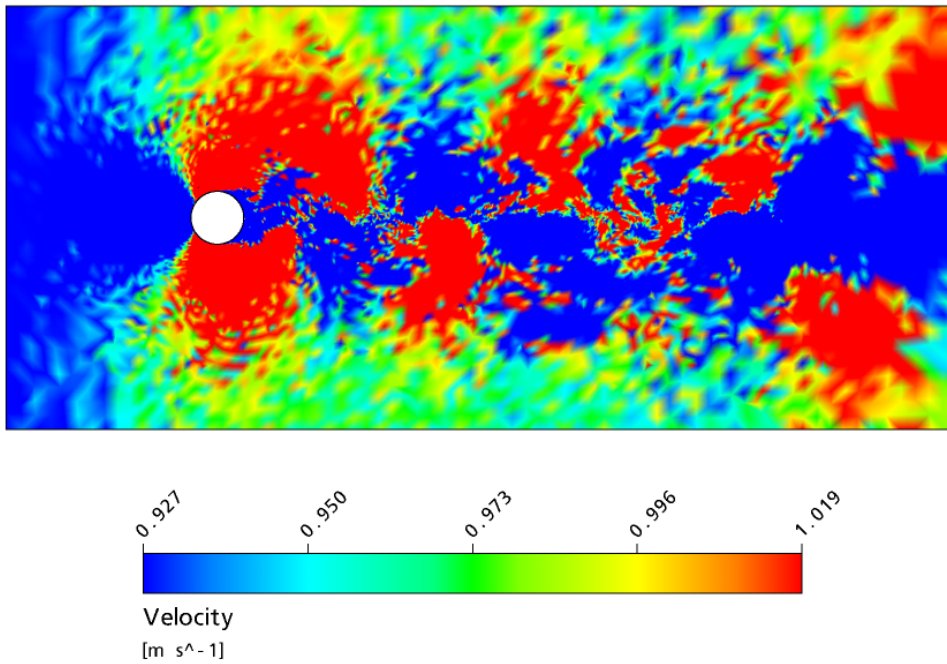


Figure 4.15: Instantaneous snapshot of velocity field for ($Re = 60000$) simulation

A flow parameter corrected for blockage effectively uses a reference velocity that is linked to where the wake occupies the largest cross section of domain instead of the velocity at the inlet. If this reference velocity is considered to be the freestream velocity,

Figure 4.15 shows that there is a large area upstream of the cylinder where the flow is retarded.

Figure 4.16 shows a sketch from Zdravkovich [92] that indicates how the flow field looks in a typical unconfined cross-flow.

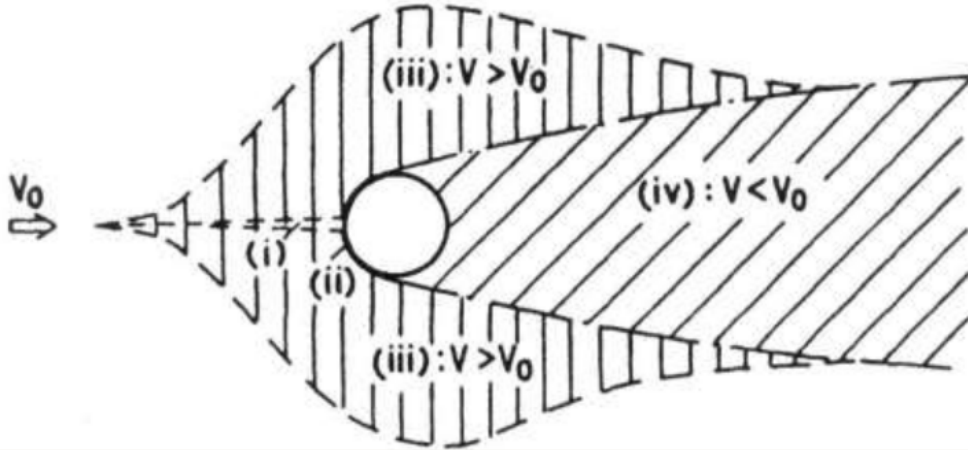


Figure 4.16: Sketch of typical flow field from Zdravkovich [92]

The enumerated regions in Figure 4.16 are described (quoted directly) as follows:

- (i) one narrow region of retarded flow
- (ii) two boundary layers attached to the surface of the cylinder
- (iii) two sidewise regions of displaced and accelerated flow
- (iv) one wide downstream region of separated flow called the wake

It can be seen that the upstream flow region for the simulations is different to a cylinder in unconfined cross-flow. The narrow region of retarded flow shown in the Zdravkovich sketch (Figure 4.16) is replaced by region of retarded flow that is narrow at the stagnation point but widens travelling upstream until it covers the entire domain cross section at the inlet. The flow in this region has instability introduced by the variation in pressure caused by blockage. The upstream pressure includes a transient element caused by vortex shedding, with a relatively higher pressure alternating from one side of the cylinder to the other at the vortex shedding frequency. This has the effect of causing the upstream flow to have a randomly fluctuating element (u') as can be seen in a typical plot against time of streamwise velocity at one of the monitor points (Figure 4.17).

The turbulence intensity at each of the monitor points is calculated from the streamwise velocity trace according to the following formula:

$$I_u = \sigma_u / V_u \quad (4.7)$$

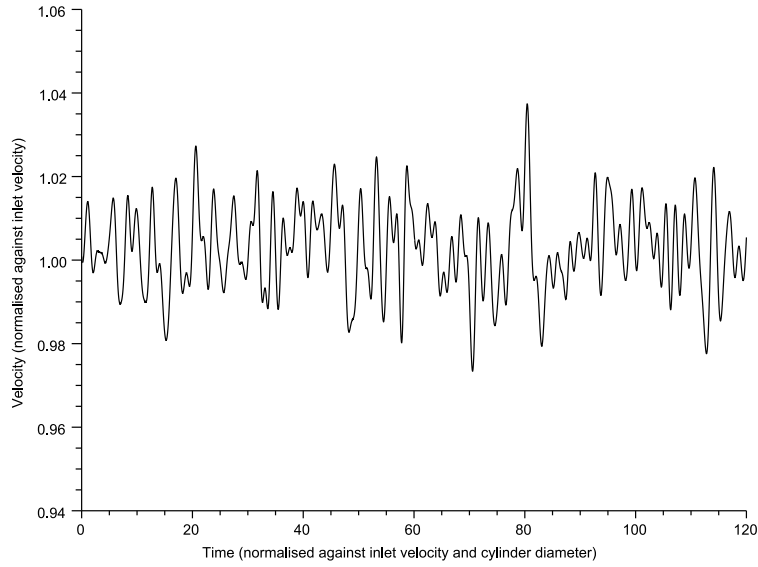


Figure 4.17: Velocity-time plot recorded at monitor point 1u for ($Re = 60000$) simulations

where σ_u is the standard deviation of the streamwise velocity, and V_u is the mean of the streamwise velocity.

Table 4.9 presents the distribution of upstream turbulence intensities for all simulations considered.

Table 4.9: Turbulence intensities

Label	Position		I_u [%] per defined Re [$\times 10^3$]				
	x [m]	y [m]	60	70	80	90	100
1u	-2.5	-3.0	0.97	0.96	0.83	0.82	0.86
2u	-2.5	-1.5	1.19	1.18	1.02	0.98	0.98
3u	-2.5	1.5	0.99	0.99	0.96	0.88	0.87
4u	-2.5	3.0	0.82	0.84	0.71	0.69	0.74
11u	-1.0	-3.0	1.50	1.34	1.35	1.17	1.03
12u	-1.0	-1.5	2.37	2.43	2.09	1.88	1.85
13u	-1.0	1.5	2.80	2.72	2.55	2.31	2.52
14u	-1.0	3.0	1.39	1.53	1.39	1.24	1.07

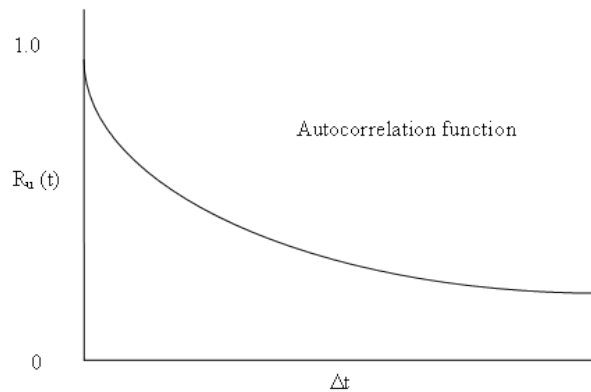
It can be seen in Table 4.9 that the turbulence intensity increases as the flow progresses downstream. Also the central monitor points report higher levels of turbulence intensity than the outer monitor points, i.e. $2u, 3u > 1u, 4u$ and $12u, 13u > 11u, 14u$.

It is worth noting that the common method of blockage correction, i.e. a factor applied to the velocity, will not account for the variation of turbulence intensities shown above. It can be seen from the formula for turbulence intensity that any factor applied to velocity will divide out to unity. The above statistic is therefore solely a measure of the effect of instability caused by vortex shedding and not the acceleration caused by blockage.

The lateral integral length scale, rL_u , is determined for each monitor point using an

autocorrelation function on the fluctuating component of the streamwise velocity, u , vs. time, t , signal. The procedure for this calculation is as follows:

1. Evaluate autocovariance. This is obtained by taking the mean value of the product of pairs of u at time t and $t + \Delta t$, i.e. $\overline{u_t u_{t+\Delta t}}$. When the time lag, Δt , is zero the autocovariance is equal to the variance $\sigma^2(u)$.
2. Normalise the autocovariance by dividing by the variance, the resulting quantity is called the autocorrelation coefficient, $R_u(t)$, i.e. $R_u(t) = \overline{u_t u_{t+\Delta t}} / \sigma^2(u)$.
3. Repeat steps 1 and 2 for a range of time lags. The variation of $R_u(t)$ with t is called the autocorrelation function.



4. Integrate over the entire length of the graph and multiply by the mean free-stream velocity, U . This will produce the longitudinal integral length scale L_x , i.e. $L_x = U \int_0^\infty R_u(t) dt$.
5. Assuming the turbulence is isotropic at the monitor point, the lateral integral length scale will be $\frac{1}{2}L_x$ (this assumption is based on the ESDU 71012 definition). The isotropic assumption is made to enable the determination of rL_u using a single point. It should be noted that the isotropic assumption is difficult to justify if the monitor point is situated close (i.e. of the same order as L_x) to a boundary.

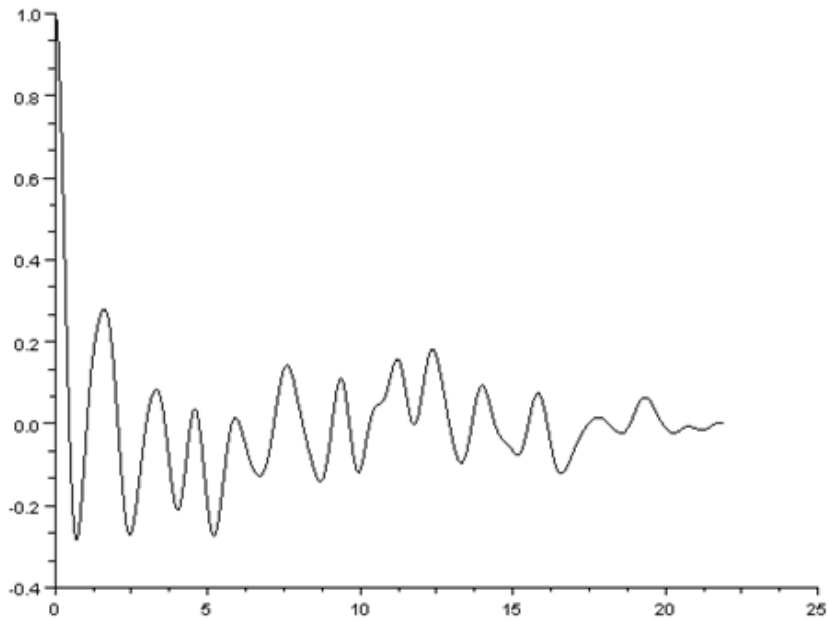
Following the above method, Table 4.10 summarises the length scales evaluated.

It can be seen in Table 4.10 that there is no obvious trend in the figures for length scale as exists for the turbulence intensities. This may be due in part to the length of integration used. A typical plot of the autocorrelation function is shown in Figure 4.18.

It can be seen that there is a sinusoidal element to the autocorrelation plot in Figure 4.18 which signifies the influence of the vortex shedding on the upstream flow. An integral summation over the entire graph results in a negligible value of length scale calculated, consequently resulting in an over-estimated figure for corrected Re (of the order 600000 and beyond). The figures in the table above are based on a integration from zero time lag to the first zero crossing. It can be argued that as the time lag increases, the autocorrelation function becomes less statistically significant because it is based on

Table 4.10: Lateral integral length scales [m]

Label	Position		rL_u [m] per defined $Re[\times 10^3]$				
	$x[m]$	$y[m]$	60	70	80	90	100
1u	-2.5	-3.0	0.245369	0.265429	0.221137	0.259044	0.209989
2u	-2.5	-1.5	0.141673	0.136743	0.119430	0.135612	0.141852
3u	-2.5	1.5	0.148879	0.157505	0.138510	0.142517	0.136292
4u	-2.5	3.0	0.193210	0.199530	0.182125	0.202706	0.184904
11u	-1.0	-3.0	0.178378	0.167887	0.152913	0.144729	0.143195
12u	-1.0	-1.5	0.205296	0.194253	0.115945	0.127051	0.199945
13u	-1.0	1.5	0.097543	0.102750	0.093275	0.103567	0.094095
14u	-1.0	3.0	0.156536	0.162056	0.153909	0.154917	0.165931

Figure 4.18: Autocorrelation plot for monitor point 1u for ($Re = 60000$) simulations

fewer products in a given data sample. There is no clear principle in determining to what extent to integrate, although there is one paper that makes a few suggestions and discusses their effectiveness O'Neill et al. [62]. The integration method employed here reflects one of the possibilities mooted in this reference.

λ_{Tcrit} evaluation

In ESDU publication 80025 [83], λ_{Tcrit} is determined from Figure 3a, which is defined by the following equations:

$$\lambda_{Tcrit} = 13 - 12 \exp[-11.5 I_u (D/r L_u)^{1/5}] \quad (4.8)$$

λ_T evaluation

In ESDU publication 80025 [83], λ_T is determined from Figure 3b, which is defined as follows:

For $Re/Re_{crit} \leq 0.5$,

$$\frac{\lambda_T - 1}{\lambda_{Tcrit} - 1} = 1.28 \exp[-20(-R_1)^{2.8}]$$

where $R_1 = \log_{10}(2Re/Re_{crit})$.

For $Re/Re_{crit} \geq 0.5$,

$$\frac{\lambda_T - 1}{\lambda_{Tcrit} - 1} = 1.28 \exp[-1.3(-R_1)^{1.4} - 0.1(-R_1)^4]$$

Re_e evaluation

The normalised values of Reynolds number Re_e , for all simulations considered as reported in Tables 4.11, 4.13, and 4.15. Three sets of figures are reported due to the variability of the roughness parameter, which indicates the sensitivity of Re_e to roughness, and the range of Re_e possible for each simulation.

Table 4.11: Re_e at monitor points for 'most rough' condition ($E = 0.159306$)

Label	Position		Re_e per defined $Re [\times 10^3]$				
	x [m]	y [m]	60	70	80	90	100
1u	-2.5	-3.0	224643.7	259774.2	276741.4	297861.7	339740.1
2u	-2.5	-1.5	276557.4	314056.9	327810.0	347071.8	373648.3
3u	-2.5	1.5	240621.0	276502.3	290982.5	316224.8	353829.5
4u	-2.5	3.0	232223.7	269026.1	282601.2	305297.3	343842.5
11u	-1.0	-3.0	234781.9	274484.4	287937.2	315741.0	352197.7
12u	-1.0	-1.5	263963.0	302506.9	328790.9	349256.9	361995.9
13u	-1.0	1.5	254598.5	290099.7	303346.2	326370.8	366230.9
14u	-1.0	3.0	238993.9	275601.6	287738.2	313611.1	347363.3

Table 4.12: Descriptive statistics for Table 4.11

Range	Statistic	Defined Re [$\times 10^3$]				
		60	70	80	90	100
1 – 4u	<i>mean</i>	243511.4	279839.9	294533.8	316613.9	352765.1
11 – 14u	<i>mean</i>	248084.3	285673.1	301953.1	326245.0	356947.0
<i>overall</i>	<i>mean</i>	245797.9	282756.5	298243.4	321429.4	354856.0
<i>overall</i>	<i>stdev</i>	17646.42	18123.22	20034.55	18487.71	11634.71

Table 4.13: Re_e at monitor points for 'least rough' condition ($E= 0.003186$)

Label	Position		Re_e per defined Re [$\times 10^3$]				
	x [m]	y [m]	60	70	80	90	100
1u	-2.5	-3.0	199745.6	235075.5	252350.4	274044.7	314749.2
2u	-2.5	-1.5	251446.2	290211.7	303586.4	322175.0	347770.9
3u	-2.5	1.5	215840.6	251767.5	267198.1	292055.4	328461.5
4u	-2.5	3.0	207396.1	244108.9	258456.6	281355.2	318740.9
11u	-1.0	-3.0	209973.5	249683.2	264090.9	291582.4	326872.9
12u	-1.0	-1.5	238862.7	278740.3	304547.9	324307.9	336414.5
13u	-1.0	1.5	229736.3	266124.9	279528.5	301968.6	340540.6
14u	-1.0	3.0	214208.3	250835.7	263884.8	289499.1	322167.1

Table 4.14: Descriptive statistics for Table 4.13

Range	Statistic	Defined Re [$\times 10^3$]				
		60	70	80	90	100
1 – 4u	<i>mean</i>	218607.1	255290.9	270397.9	292407.6	327430.6
11 – 14u	<i>mean</i>	223195.2	261346.0	278013.0	301839.5	331498.8
<i>overall</i>	<i>mean</i>	220901.2	258318.5	274205.4	297123.5	329464.7
<i>overall</i>	<i>stdev</i>	17539.51	18557.98	19985.13	18070.62	11330.21

Table 4.15: Re_e at monitor points for smooth condition ($E= 0$)

Label	Position		Re_e per defined Re [$\times 10^3$]				
	x [m]	y [m]	60	70	80	90	100
1u	-2.5	-3.0	199198.5	234546.6	251815.3	273532.1	314218.6
2u	-2.5	-1.5	250903.2	289698.4	303068.8	321645.3	347221.8
3u	-2.5	1.5	215298.4	251229.3	266674.8	291539.3	327923.1
4u	-2.5	3.0	206851.2	243576.4	257912.9	280842.2	318208.0
11u	-1.0	-3.0	209429.4	249146.8	263552.7	291066.5	326335.4
12u	-1.0	-1.5	238324.1	278224.3	304029.9	323777.1	335871.6
13u	-1.0	1.5	229197.5	265566.5	279015.0	301448.5	339995.5
14u	-1.0	3.0	213665.5	250298.3	263342.8	288983.9	321632.3

Table 4.16: Descriptive statistics for Table 4.15

Range	Statistic	Defined Re [$\times 10^3$]				
		60	70	80	90	100
1 – 4u	mean	218062.8	254762.7	269867.9	291889.7	326892.9
11 – 14u	mean	222654.1	260809.0	277485.1	301319.0	330958.7
overall	mean	220358.5	257785.8	273676.5	296604.4	328925.8
overall	stdev	17541.43	18563.94	19994.42	18063.54	11323.86

It can be seen from the descriptive statistics given in Tables 4.14, 4.12, and 4.16 that the variation of Re_e follows similar trends to those shown in the figures for I_u . This occurs even though the length scales used in the calculations above appear to be randomly distributed. Given the distribution of Re_e across the monitor points, it is tempting to suggest an extrapolation of the measured values to obtain a figure relevant to near the cylinder surface. In order to do this, however, it would be necessary to gain a more detailed view of the upstream variation of Re_e which would require collection of data from more monitor locations. The following graphs summarise the corrected mean drag for all simulations considered:

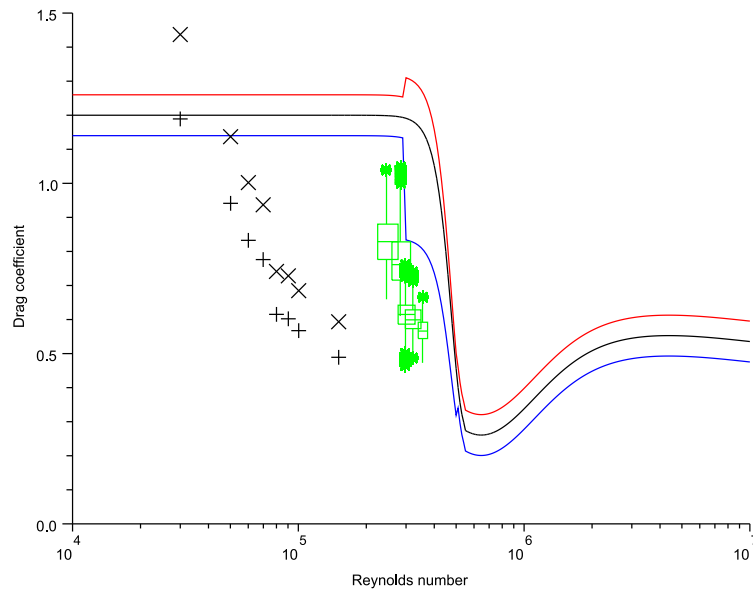


Figure 4.19: Drag results comparison with ESDU publication 80025 [83]

The graph in Figure 4.19 shows the raw data obtained from the simulations (plotted as X's), the same data corrected for blockage (plotted as +'s), and the same data corrected for blockage and normalised following ESDU recommendations (plotted as boxplots). For clarity, solely the data for the 'most rough' condition has been plotted. It can be seen that the corrections move the points closer to the ESDU data as expected. The corrected data, however, does not fall within the margin of error specified for the ESDU data. Given

the uncertainty in the calculation of roughness parameters, turbulent length scales and turbulence intensities mentioned above, it is possible that the correction parameters for turbulence and/or roughness have been underestimated. Of the two, it is more likely that it is the turbulence normalisation parameter that needs further attention. The entire bandwidth of possible values for λ_R has been determined, although the same could not be said for λ_T . The accuracy of λ_T could be improved by using an extrapolated value of turbulence intensity closer to the point of maximum blockage, although a fuller description of the upstream turbulence and length scale produced by more monitor points would be required. Also a longer interval of integration in the length scale calculation could lead to smaller calculated length scales and consequently larger values of normalised Re . However there needs to be a justification for choosing one integration interval policy over others beyond a desire to make the figures agree nicely with published data.

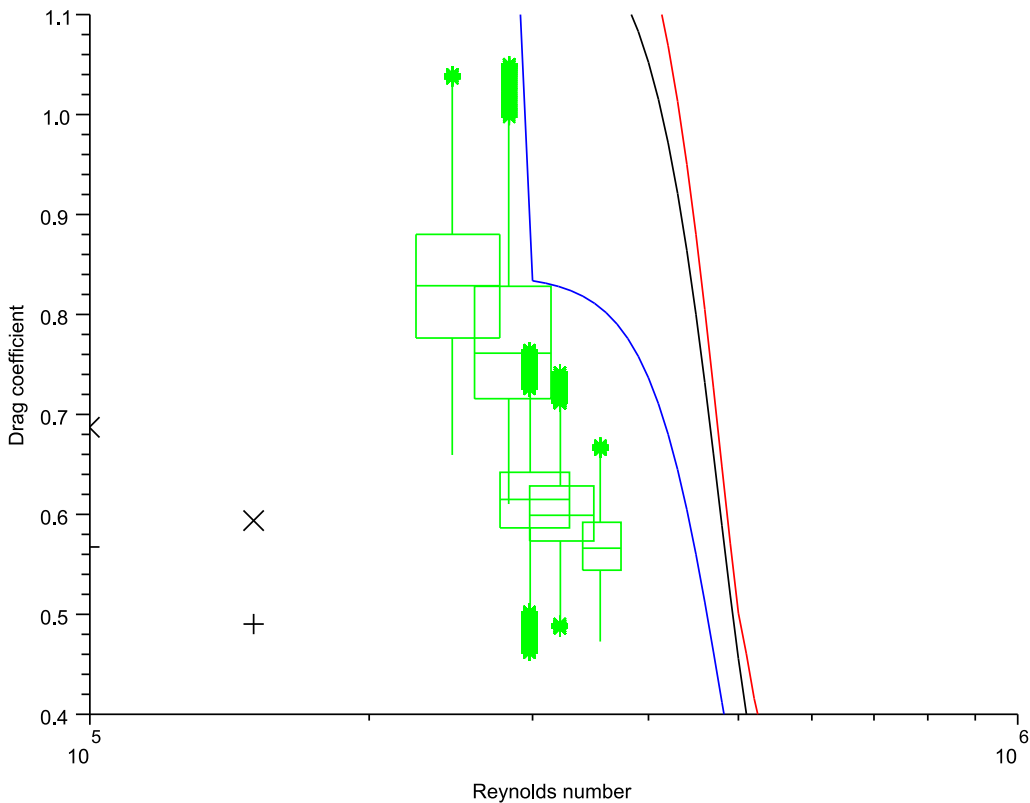


Figure 4.20: Comparison of results with drag data in ESDU publication 80025 [83]

The box and whiskers plots shown in the close-up in Figure 4.20 are drawn as follows:

- the median drag as a horizontal line,
- the upper and lower quartiles of drag drawn as a box
- the width of the quartile box and median line corresponds to the maximum to minimum range of normalised Reynolds number evaluated at the monitor points

- the whiskers are located horizontally at the mean normalised Reynolds number Re_e , the vertical length of them correspond to either maxima/minima in the data range or $1.5 \times$ interquartile range (IQR) from the box, whichever is the lesser
- any outliers (i.e. data points beyond $1.5 \times$ IQR from the nearest quartile) are plotted as individual points

To illustrate the influence that the choice of integration limits in the length scale calculation has on the normalised Reynolds number, Figure 4.21 is the same close-up as shown in Figure 4.20 but using an integration from zero time lag up to the value where the autocorrelation function is a minimum in the negative region.

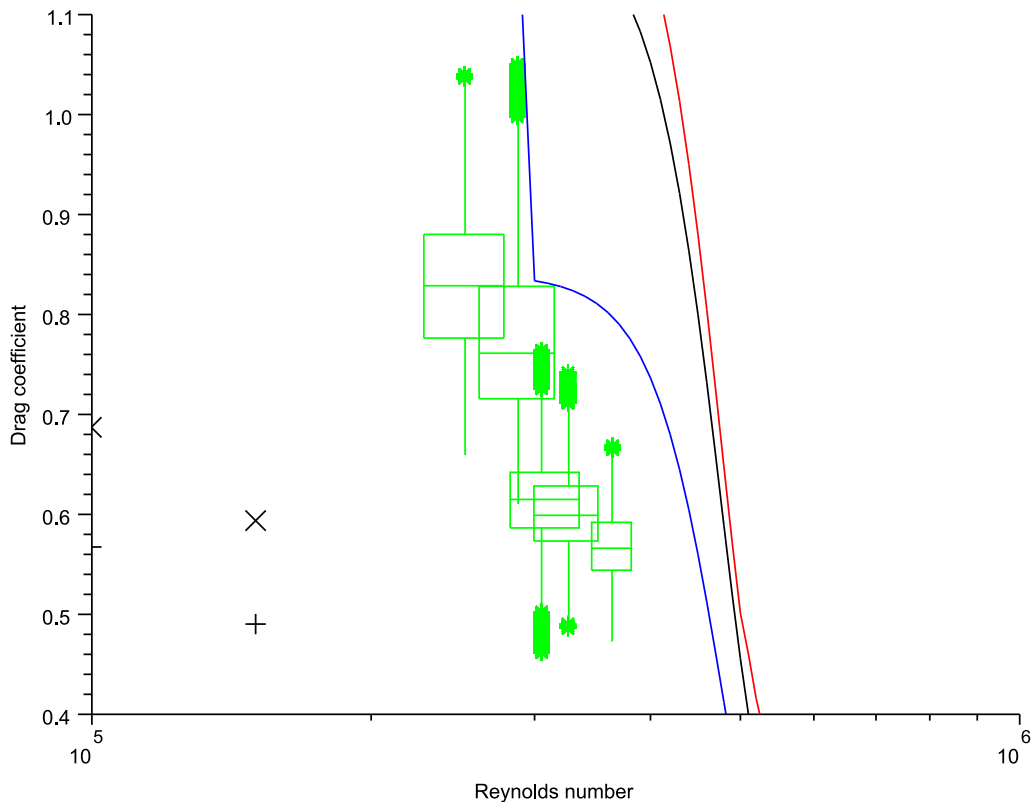


Figure 4.21: Influence of integration method on results

4.5.4 Separation

A common observation in experimental literature [92] about the drag crisis is the movement of the separation points in the downstream direction, further towards the rear of the cylinder. It is worth seeing if the simulation results show the same trend. Earlier in the thesis, separation points have been defined as the point where the boundary layer leaves the surface of the cylinder to form shear layers that roll up into vortices. A more precise definition of separation point used in the processing of simulation results is the point on

the cylinder surface where the velocity gradient is zero. Graphs showing the spanwise averaged separation point through several shedding cycles for some of the simulations are shown in Figure 4.22. The value of the separation point is the angle measured from the upstream stagnation point of the cylinder. The time axis is non-dimensionalised by cylinder diameter and free-stream velocity. On each graph the red and blue lines show the separation points on either side of the cylinder, the black line is the average of both separation points, and the green line is the time-average of both separation points.

Table 4.17: Time-average separation angles

Defined Re	Mean Angle [degrees]	Recorded Time Range [tU/D]
50000	85.59	6.21
60000	87.29	135.80
70000	88.43	136.21
80000	88.90	103.69
90000	90.47	91.66
100000	91.23	33.72
150000	93.47	5.04

Zdravkovich [92] has noted that the separation points move towards the back of the cylinder with increasing Re through the drag crisis. The time period over which the above data is sampled varies between simulations and are comparatively very short for some values of Reynolds number. Thus the averaged values for separation angles must be accepted with varying degrees of confidence. Despite this it can be seen that the average separation angle increases with Reynolds number as expected following the observations by Zdravkovich [92].

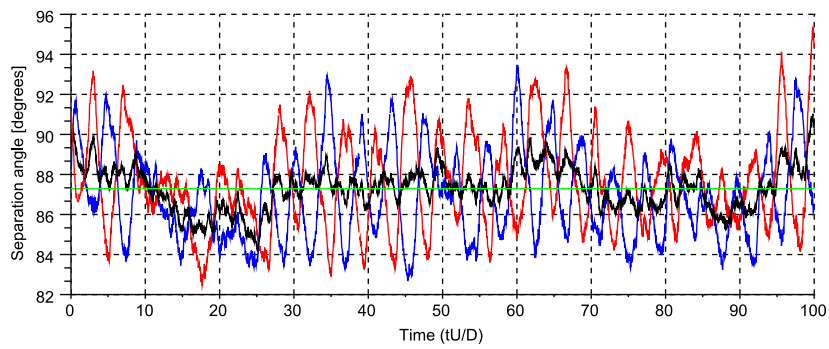
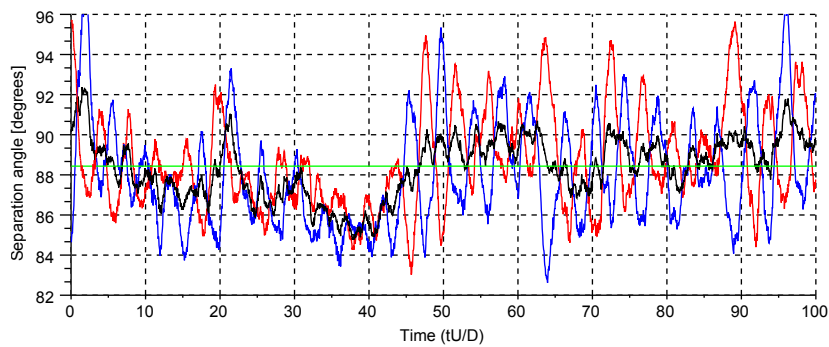
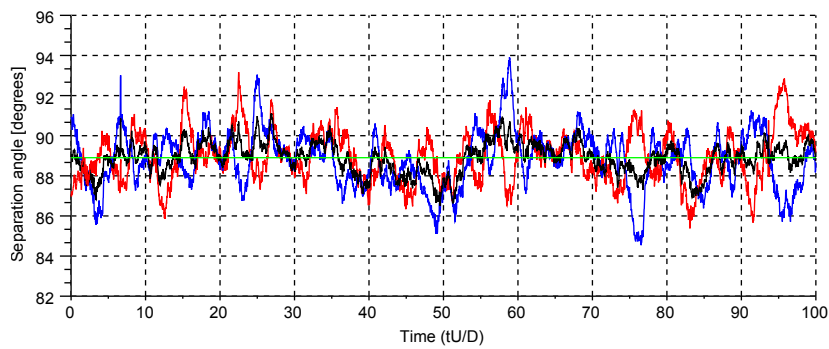
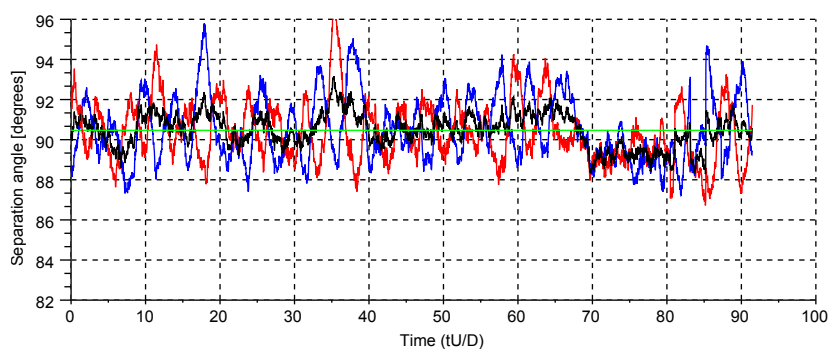
(a) $Re = 60000$ (b) $Re = 70000$ (c) $Re = 80000$ (d) $Re = 90000$

Figure 4.22: Separation point vs. time plots

4.5.5 Base Pressure

In a review of experimental data, Williamson [89] produced a compiled plot of the variation of base pressure, C_{pb} , (i.e. pressure at a point 180° from the upstream stagnation point) with Re . The time averaged base pressure coefficients obtained in the simulations are summarised in Table 4.18.

Table 4.18: Base Pressure Coefficients

Defined Re	C_{pb}
50000	-0.886
60000	-0.764
70000	-0.695
80000	-0.533
90000	-0.550
100000	-0.528
150000	-0.476

If these coefficients are included in Williamson's plot, using overall mean figures in Table 4.11 for values of Re , fairly close agreement to experimental data can be observed, as can be seen in Figure 4.23.

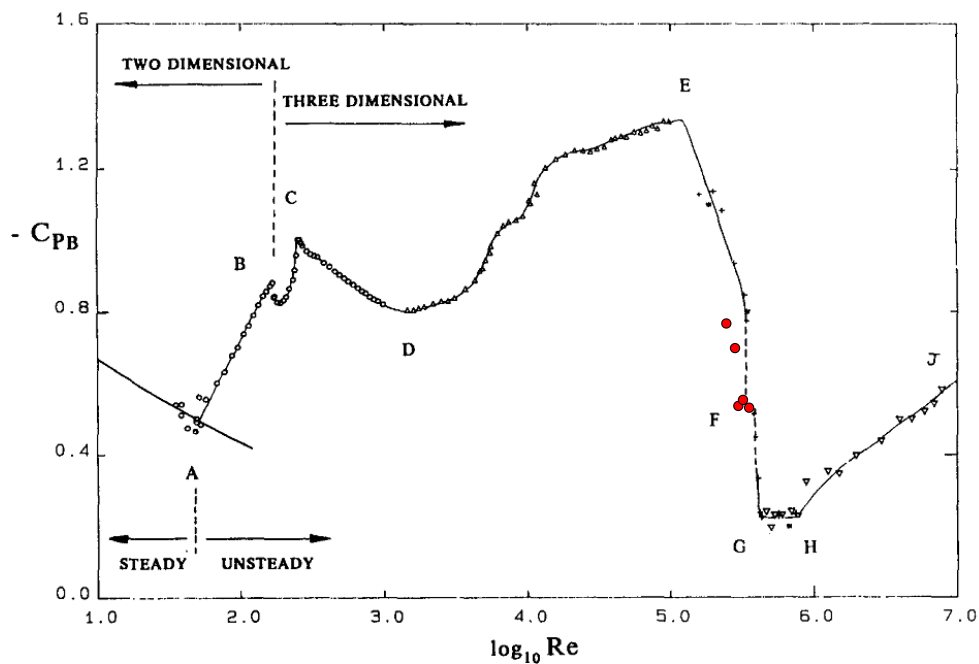


Figure 4.23: Comparison of base pressures with Williamson [89] data

Graphs showing the spanwise and time averaged pressure coefficient C_p are given in Figure 4.24. The red line shows the maxima and the blue line shows the minima of the data sample analysed.

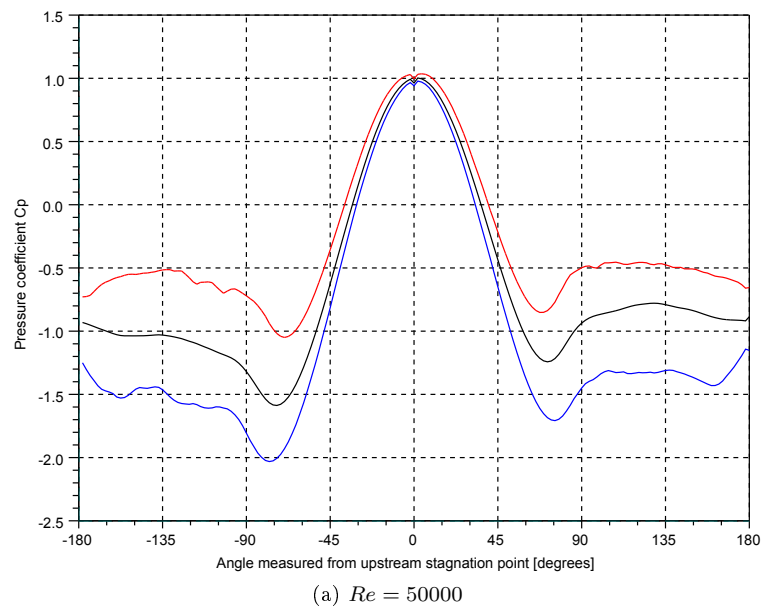


Figure 4.24: Cylinder surface pressure plots

It can be seen from the above data that C_{pb} decreases with increasing Re , in accordance with Zdravkovich's [92] observation. It can be observed from the above plots that all the minima occur in a circumferential position less than 90° .

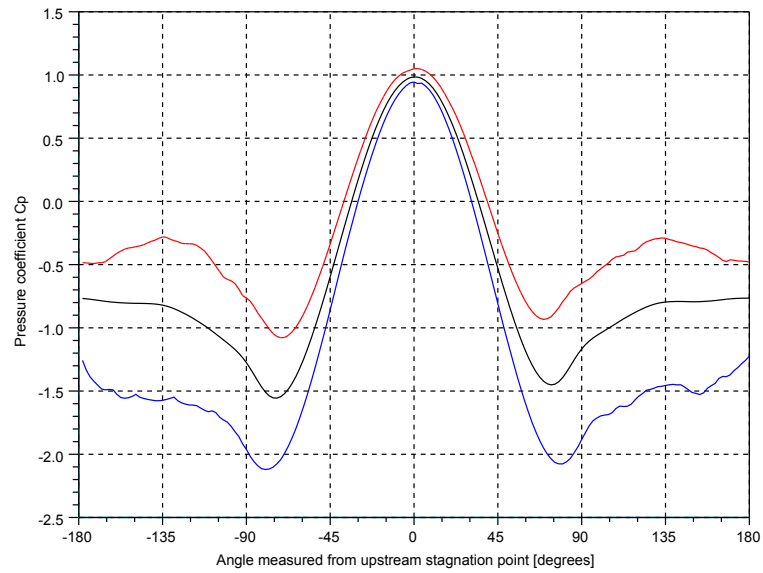
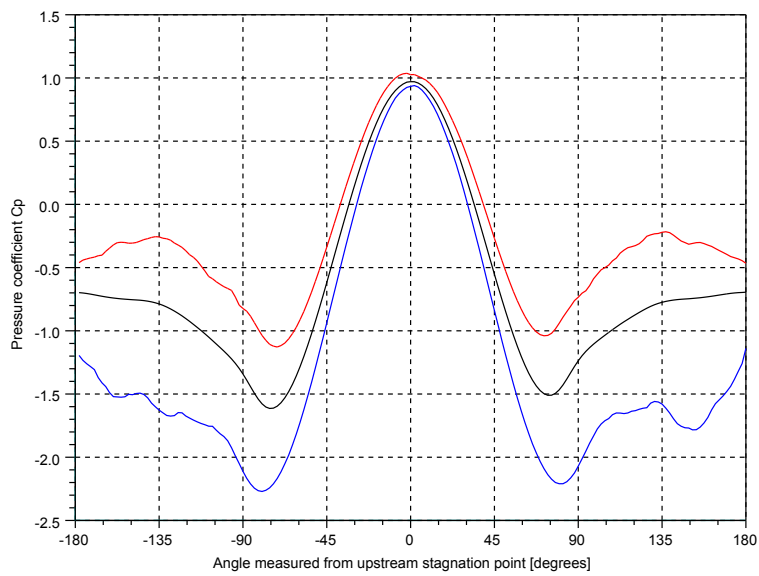
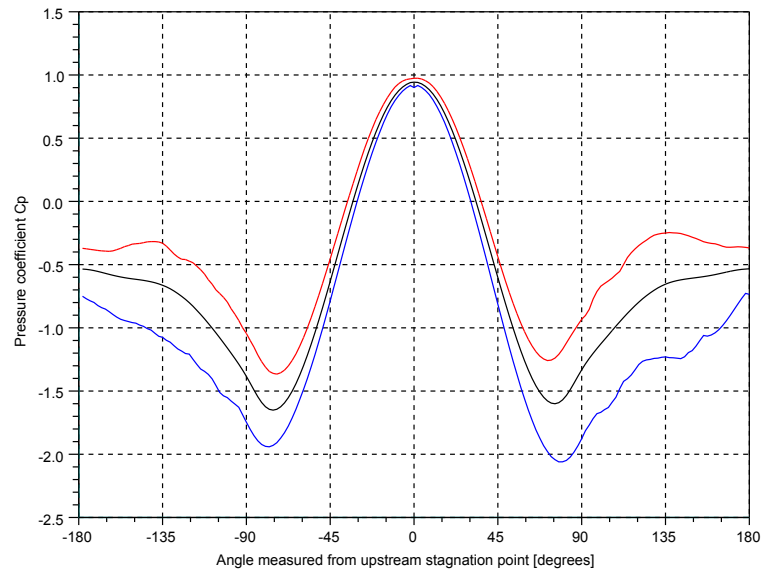
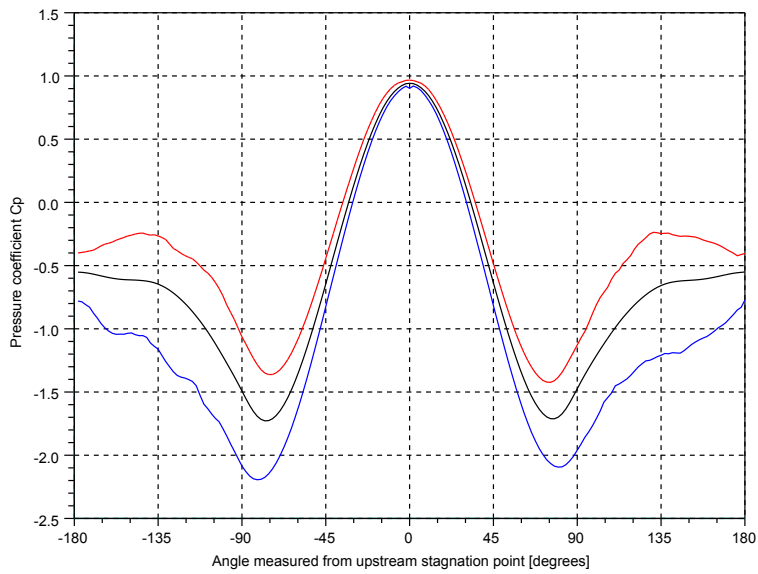
(b) $Re = 60000$ (c) $Re = 70000$

Figure 4.24: Cylinder surface pressure plots (cont.)



(d) $Re = 80000$



(e) $Re = 90000$

Figure 4.24: Cylinder surface pressure plots (cont.)

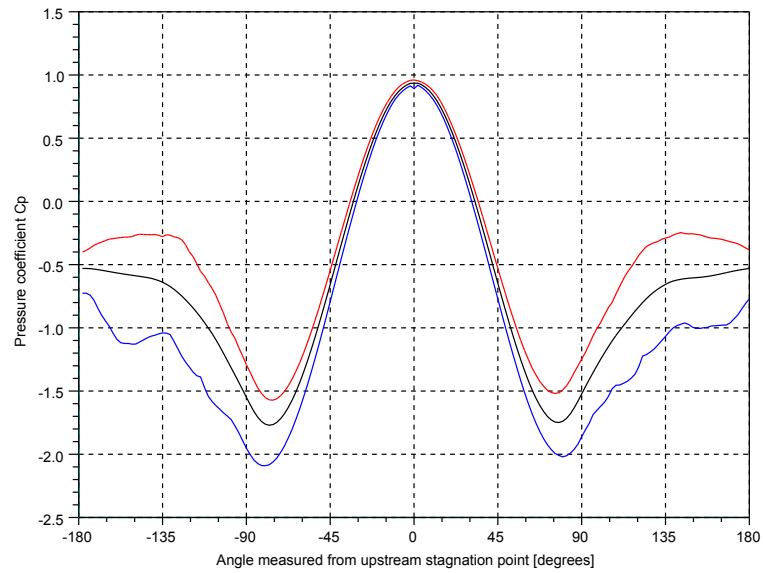
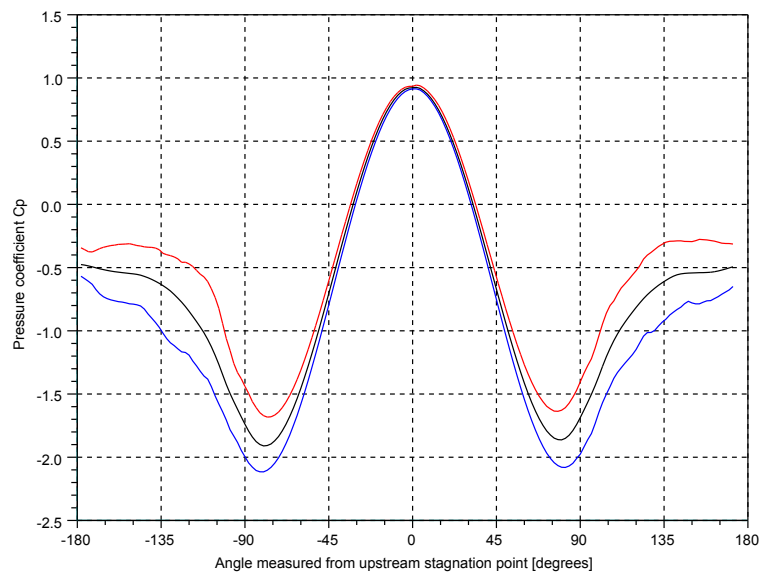
(f) $Re = 100000$ (g) $Re = 150000$

Figure 4.24: Cylinder surface pressure plots (cont.)

4.5.6 Strouhal Number

In addition to the dramatic drop in drag, the drag crisis is marked by a change in strouhal number. There is literature including Zdravkovich [92] and Schewe [69] that discusses a discontinuous change in Strouhal number. However to obtain a clearer view of the change in nature of vortex shedding, it is worth observing spectral frequency plots as shown in Figure 4.25. These plots were created using Scilab, a numerical computational package originally produced by researchers from Institut national de recherche en informatique et en automatique (INRIA) and École nationale des ponts et chaussées (ENPC). This software was chosen because of its free availability and capability to carry out Fast Fourier Transforms (FFTs).

Table 4.19: Dominant Frequencies

Defined Re	Frequency [fD/U]	Recorded Time Range [tU/D]
30000	0.203	120-81
50000	0.228	194-92
60000	0.238	146-32
70000	0.245	148-58
80000	0.246	131-05
90000	0.253	155-74
100000	0.257	110-94
150000	0.257	262-04

In the experimental literature, Schewe [69] provides a description of what to expect for frequency spectra plots through the progression of Re in the realm of the drag crisis. Initially, there is a strong single frequency (non-dimensionalised by diameter and free-stream velocity) of approximately 0.2 in increasing Re leading up to the drag crisis. As the Reynolds number increases through the drag crisis itself the strength of the non-dimensional frequency of 0.2 gradually dies to be replaced by a non-dimensional frequency of 0.3. The figures above showing frequency domain plots of the lift observed in the simulations present a gradual change of non-dimensional frequency from approximately 0.203 to 0.257, as presented in Table 4.19 which lists the frequencies of greatest FFT amplitude. For some of the plots presented in Figure 4.25 there is no single dominant frequency. For example in the case of Figures 4.25g and 4.25h, there are significant peaks at frequencies above those given in Table 4.19.

Experimental observations show the switch from 0.2 to 0.3 to be a discontinuous switch that relates to the appearance of a nearly turbulent boundary layer separating from the surface, quickly becoming turbulent and reattaching to the cylinder surface - the so-called “one-bubble” regime. This is followed by a “two-bubble” regime when the same thing occurs on the other side of the cylinder and the frequency then discontinuously jumps to 0.4. The reason that these discontinuous jumps are not seen in the above results is because of spatial averaging in the spanwise direction. A black and white shaded plot of the separation on one side of the cylinder at $Re = 50000$ is given in Figure 4.26.

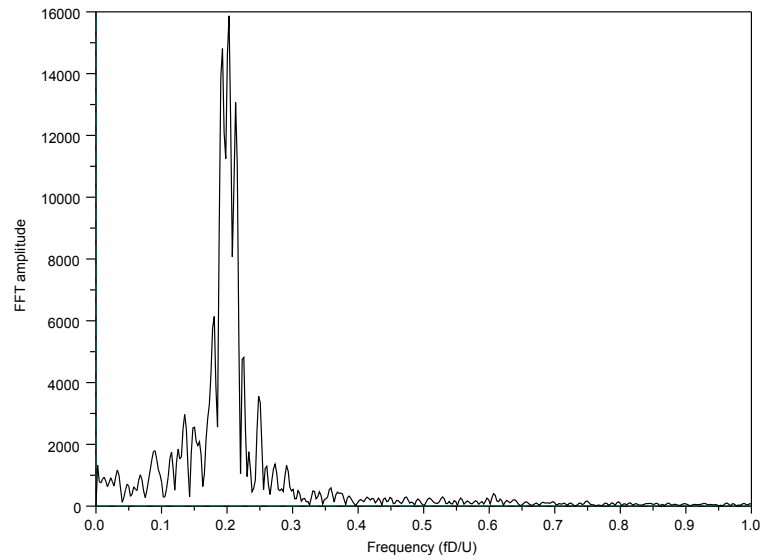
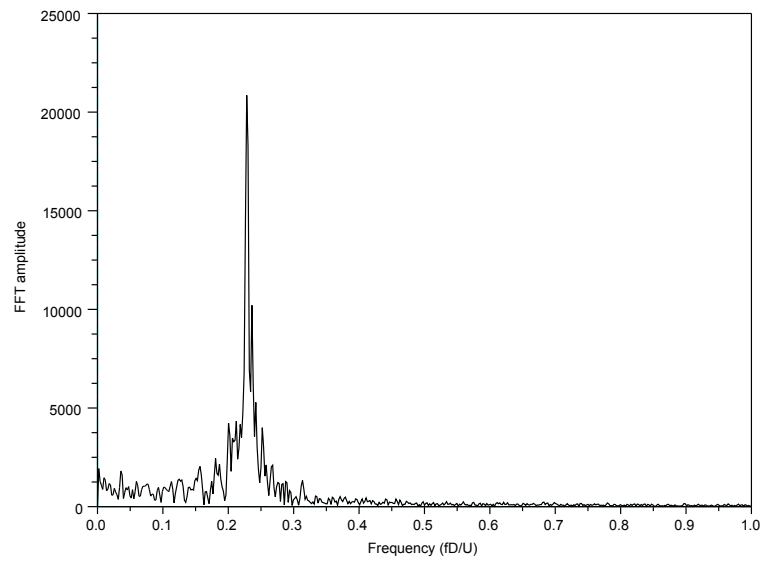
(a) $Re = 30000$ (b) $Re = 50000$

Figure 4.25: Spectral frequency plots

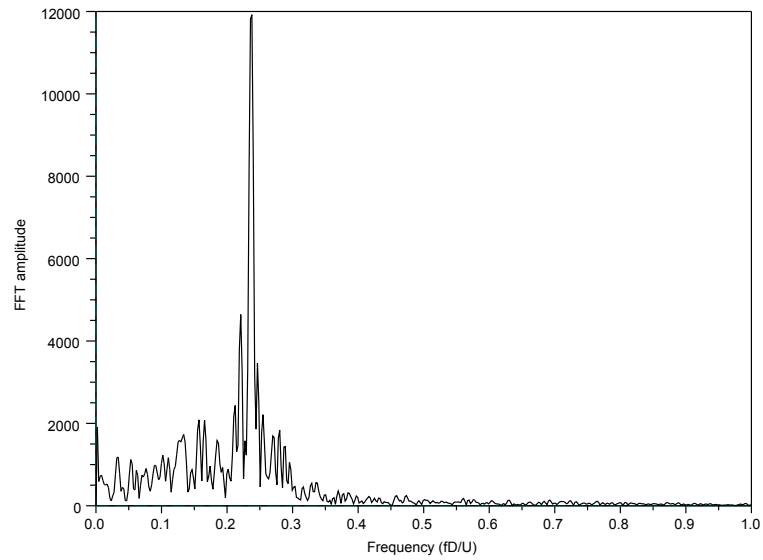
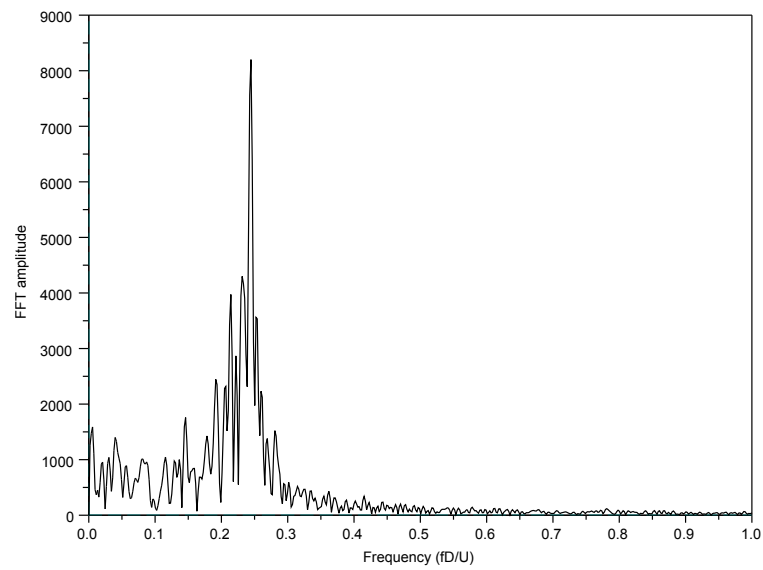
(c) $Re = 60000$ (d) $Re = 70000$

Figure 4.25: Spectral frequency plots (cont.)

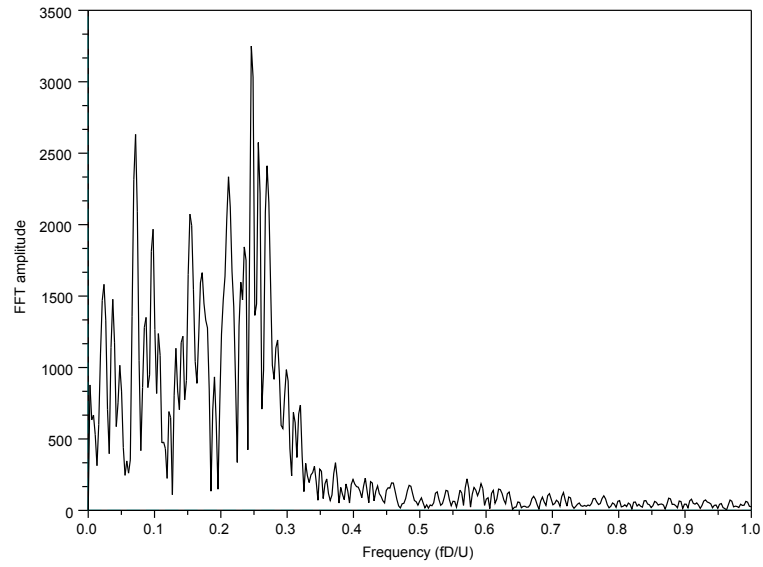
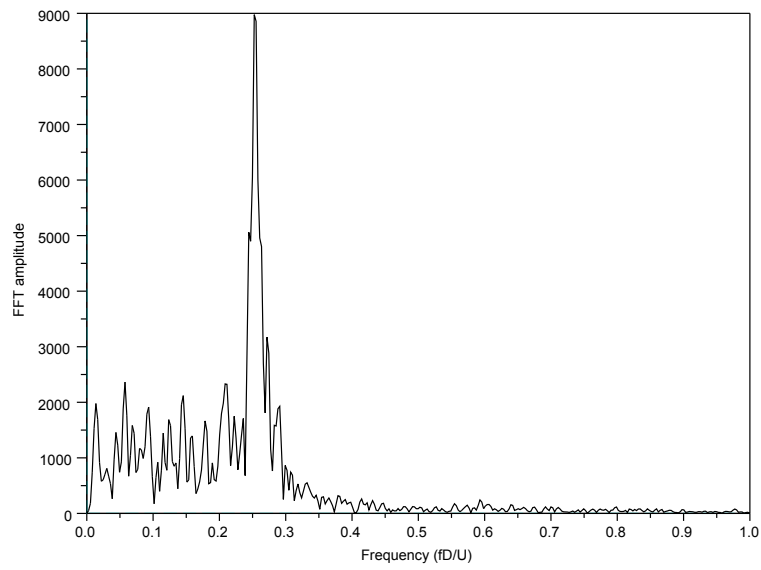
(e) $Re = 80000$ (f) $Re = 90000$

Figure 4.25: Spectral frequency plots (cont.)

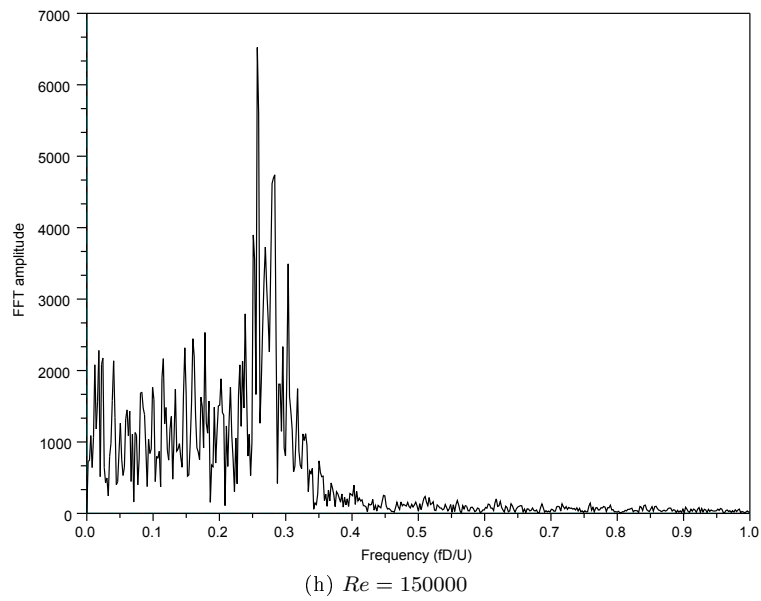
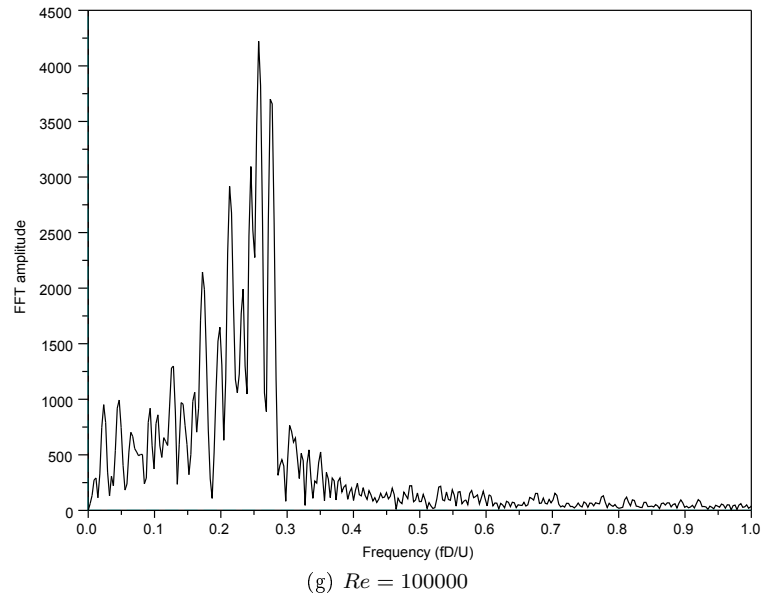


Figure 4.25: Spectral frequency plots (cont.)

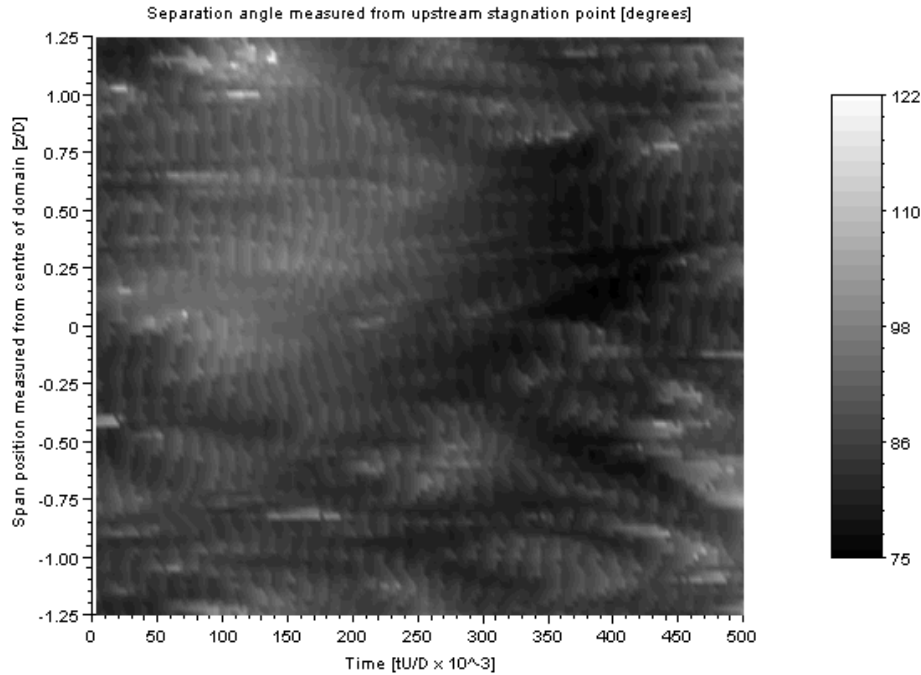


Figure 4.26: Timewise and Spanwise Variation of Lower Separation Angle Over a Shedding Cycle ($Re = 50k$)

These plots show raw data without having been averaged and indicate how the separation angle can vary across the span and with time. From this it is easy to see how there can be locally discontinuous jumps in data which can be somewhat masked by the averaging process.

4.6 Conclusions

The aim of this chapter has been to simulate numerically the onset of the drag crisis. The work presented here represents an initial attempt using LES. This has been achieved to some degree of success as the results presented have been shown to follow traits consistent with experimental observations made of the drag crisis.

Challenges however do come about, as have been identified above. The two main challenges in this work has been selection of an appropriate approach to deal with turbulence, and selection of appropriate input parameters which keep resource costs low while still enabling production of results of an acceptable quality. The latter challenge includes domain and mesh geometry and size of time step integration as factors. The requirement for smallness of time step and fineness of mesh resolution in the boundary region of the cylinder has meant that long run times with appreciably large computing

resources, at least in comparison with those found in industry, have been necessary. It is the author's view that at the time of writing this chapter, it is possible with commercially available software and computing resources to produce acceptable numerical simulation of the drag crisis, albeit at a high cost.

The results presented and discussed in this chapter represent a small part of what could be obtained from the simulations carried out. Further post-processing would likely produce further interesting observations. Notably an investigation into the spanwise variation of the lift force would be worthwhile to gain an insight into spanwise correlation effects.

Chapter 5

Fluid Structure Interaction

5.1 Introduction

This chapter describes how the commercial solver used for the thesis is adapted to be capable of numerical simulation of cylinders that are free to move in all directions perpendicular to its axis. The objective is to implement a Fluid Structure Interaction capability that is efficient and reliable for the work presented in the final chapter of the thesis. The importance of selecting the best coupling strategy is highlighted by a number of tests that demonstrate the capability of the FSI implementation used.

5.2 Implementation

5.2.1 Solver modification

The FSI implementation presented in this chapter makes use of the user defined routine capabilities of ANSYS CFX. Two methodologies are available for the customisation of the solver: CFX Expression Language (CEL) functions and Junction Box routines. Either can be used on its own in a numerical simulation, or both can be used together. Their comparative capabilities are set out in Table 5.1.

In comparison to Junction Box routines, CEL functions are relatively straightforward to use because they can be set in the pre-processing Graphical User Interface (GUI) tool supplied with the product and its use is covered comprehensively in the supporting documentation. References to CEL functions can be made where any numerical value can be entered in the GUI. During the solution process, whenever the solver would encounter a CEL function reference instead of an input value, the CEL function would be executed and its numerical result would be used. A feature of this method is that the user either does not know or has only at best a conceptual sense of when the CEL functions will be called by the solver. This can be seen as both a positive and negative feature. On the positive side the user does not need an extensive knowledge of the internal workings of

Table 5.1: Comparison of CEL functions with Junction Box Routines

CEL functions	Junction Box routines
Used by the fluid solver on a variety of unspecified occasions during the run process	Invoked by the fluid solver at a specified point during the run process
Argument lists are passed in by the fluid solver. A return value (or list of values) is expected, the type of which depends on the context in which the function is called.	No argument lists are used and no return value is expected.
Limited access to data structure	Full access to data structure

the solver. Conversely the limitation of control over when the CEL functions are invoked can be seen as a negative aspect.

Junction Box routines derive their name from the concept that they are executed by the solver at predetermined points throughout the solution process, referred to by the supporting documentation as “junction boxes”. The flow diagram shown in Figure 5.1 shows the full list of predetermined points available throughout the solver process where junction box routines can be placed. Knowledge of programming languages is required by the user to create a junction box routine. The user documentation suggests there are two main choices: C and FORTRAN, with a preference expressed for FORTRAN77 in particular. Macros are supplied by the software vendor to help in the process of compiling the code into a format that is compatible with the solver. An advantage that Junction Box routines have over CEL functions is that they offer a wider access to the solver internal data structure that stores variables in a hierarchical structure similar to directories found in a modern computer file storage system. In the case of ANSYS CFX, the internal data structure is not well documented. An important reason against good documentation is the internal architecture being likely to sufficiently change with each release to cause difficulties. In this case there would be an expensive overhead in documentation costs and users would be likely to suffer compatibility issues with code that they had developed for prior releases. So users are discouraged from producing code that accesses the internal data structure directly with a lack of sufficient detail given in the documentation. Instead utility routines are supplied, collectively known as the Memory Management System (MMS), with the software which provides a permanent way of addressing the internal data structure.

Both junction box routines and CEL functions are used for work in this thesis in order to benefit from the best advantages of each approach. The full list of routines written alongside a short description is given in Table 5.2 on page 106.

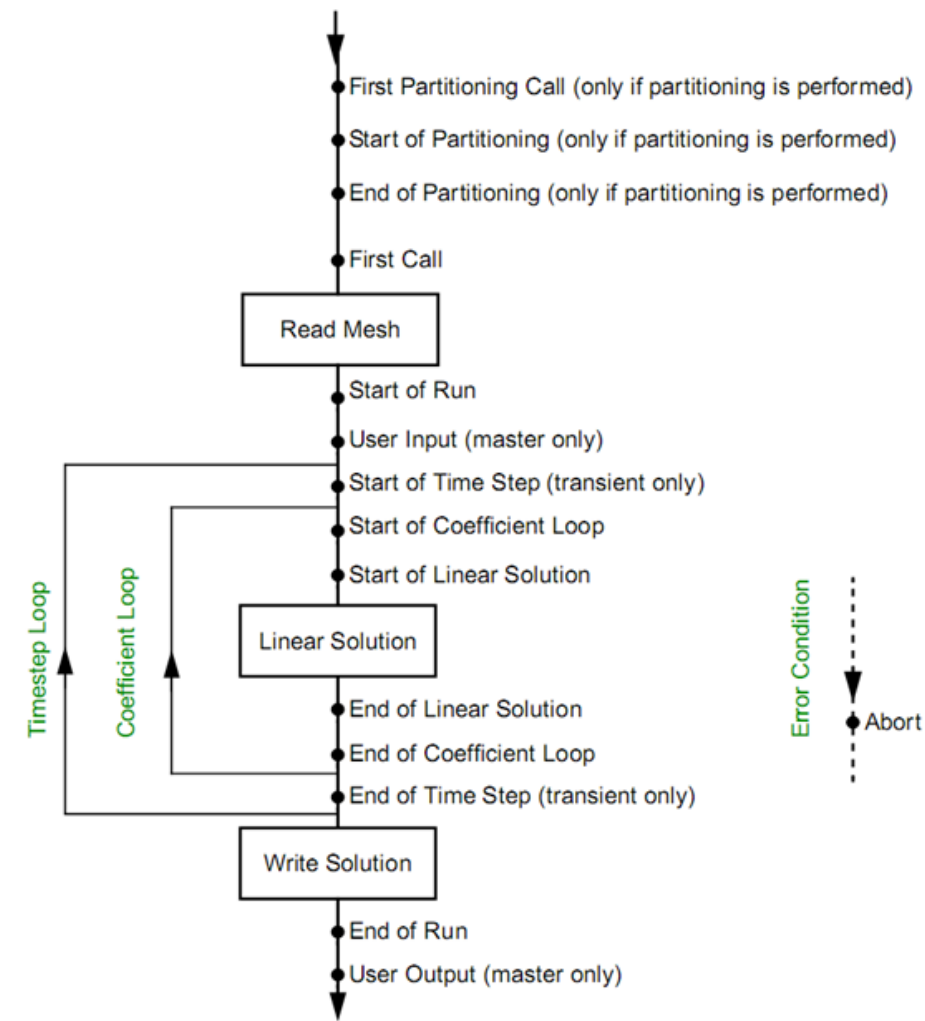


Figure 5.1: Flow diagram of a typical ANSYS CFX solver run taken from the ANSYS CFX user manual [5]

5.2.2 Flow Diagrams

The way that the user defined routines fit into the overall solver run process is shown in Figure 5.2.

The important data produced by the user code is stored in the `/USER_DATA` area of the data structure. Figure 5.3 shows how it is handled by the solver and user code.

5.2.3 Integration methods

The following subsections describe a range of integration methods examined and a closed solution found in Harris and Piersol [27] that is used for validation purposes.

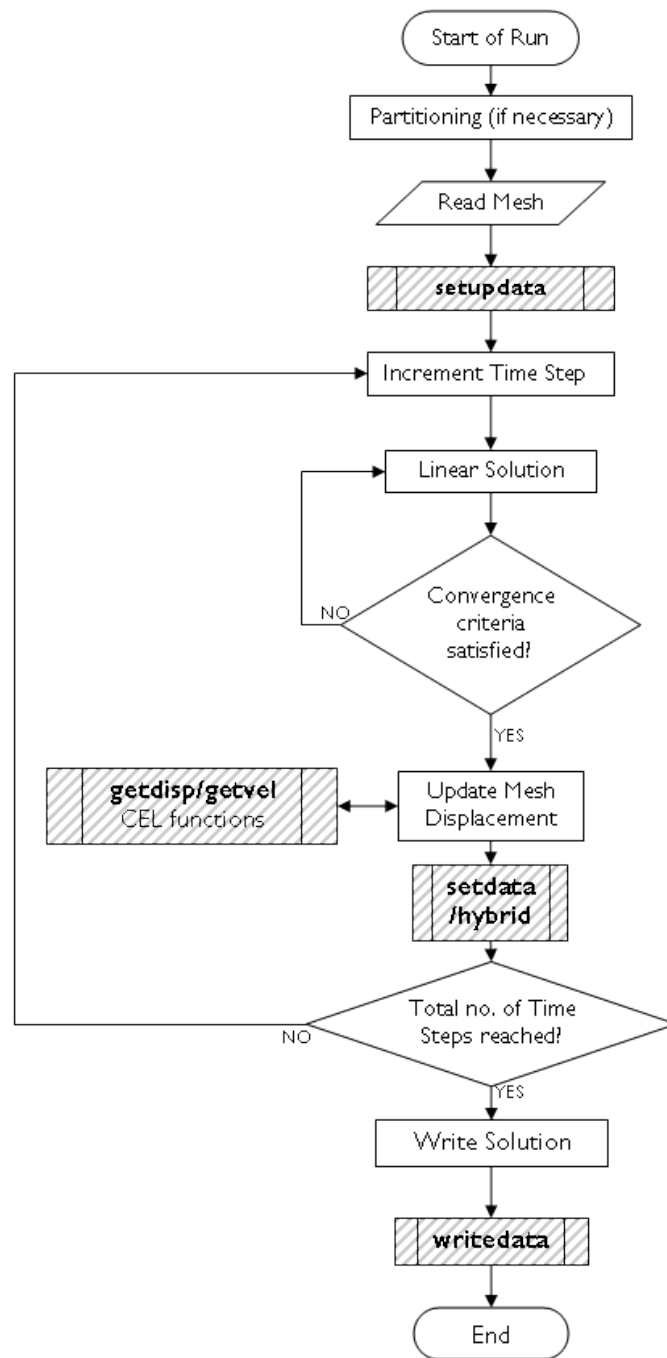


Figure 5.2: Flow chart of overall solver process including user-routines

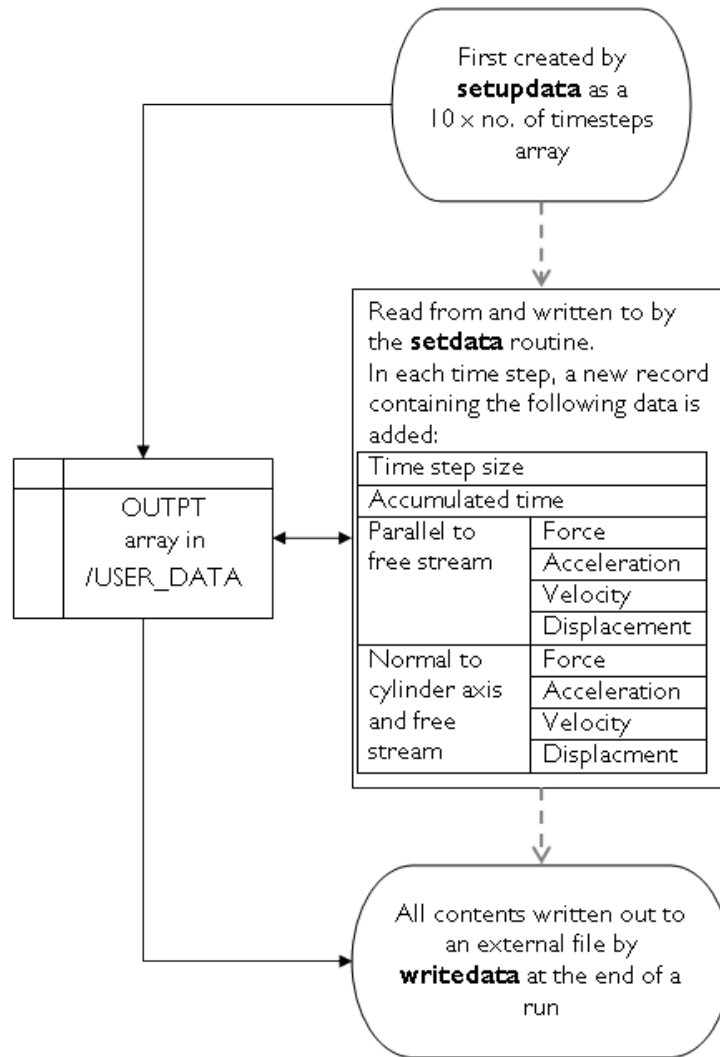


Figure 5.3: Flow chart of user code interaction with data structure

Table 5.2: Routines of the coupler program

Name(s)	Type	Description
convcheck	Junction Box routine	Routine invoked at the end of each coefficient loop to determine whether or not to continue iterating
getdisp_x getdisp_y	CEL functions	Used by the fluid solver to look up the latest calculated values of displacement
hybrid	internal routine	Low level routine that performs an integration to obtain the latest values of displacement
setdata	Junction Box routine	High level routine invoked at the start of each coefficient loop to calculate the latest displacement
setupdata	Junction Box routine	Routine invoked at the start of run to initialise variables and data areas
writedata	Junction Box routine	Routine invoked at the end of run to write output

Closed solution

The standard single degree of freedom equation of a lumped mass with damping is given in equation (5.1).

$$m\ddot{x} + c\dot{x} + kx = F \quad (5.1)$$

where m is mass, c is damping constant, k is stiffness, F is the applied forcing function, and x is displacement. If the forcing function for equation (5.1) is taken to be a sinusoid varying with time, and if the damping is taken to be negligible, the closed solution is as follows:

$$x = A \sin \omega_n t + B \cos \omega_n t + \frac{F_0/k}{1 - \omega^2/\omega_n^2} \sin \omega t \quad (5.2)$$

where t is time, k is stiffness, ω_n is undamped angular natural frequency $\sqrt{\frac{k}{m}}$, ω is angular frequency of forcing function, F_0 is the amplitude of the forcing function, A is a coefficient derived from velocity at time $t = 0$ (see equation (5.3)), and B is a coefficient equal to displacement at time $t = 0$.

$$\dot{x}(0) = A\omega_n + \frac{\omega \frac{F_0}{k}}{1 - \frac{\omega^2}{\omega_n^2}} \quad (5.3)$$

Backward Euler method

For equation (5.1), a backward Euler approximation is taken for acceleration and velocity, as follows:

$$\ddot{x}_{n+1} = \frac{1}{h}(\dot{x}_{n+1} - \dot{x}_n) \quad (5.4a)$$

$$\dot{x}_{n+1} = \frac{1}{h}(x_{n+1} - x_n) \quad (5.4b)$$

where h is time step size, the $_{n+1}$ suffix indicates a variable from the current time step, and the $_n$ suffix indicates a variable from the previous time step. Inserting these approximations into equation (5.1) produces the following:

$$\frac{m}{h} \left(\frac{1}{h} (x_{n+1} - x_n) - \dot{x}_n \right) + c \frac{1}{h} (x_{n+1} - x_n) + kx_{n+1} = F_{n+1}$$

or after rearrangement:

$$x_{n+1} = \frac{F_{n+1} + \dot{x}_n \frac{m}{h} + x_n \frac{1}{h} \left(\frac{m}{h} + c \right)}{\frac{1}{h} \left(\frac{m}{h} + c \right) + k} \quad (5.5)$$

Trapezoidal method

For this method the following two approximations are used:

$$x_{n+1} - x_n = \frac{h}{2} (\dot{x}_{n+1} + \dot{x}_n) \quad (5.6a)$$

$$\dot{x}_{n+1} - \dot{x}_n = \frac{h}{2} (\ddot{x}_{n+1} + \ddot{x}_n) \quad (5.6b)$$

By rearranging equation (5.1) into an expression for acceleration we can substitute the following two equations into equation (5.6b) above,

$$\ddot{x}_{n+1} = \frac{1}{m} (F_{n+1} - c\dot{x}_{n+1} - kx_{n+1})$$

$$\ddot{x}_n = \frac{1}{m} (F_n - c\dot{x}_n - kx_n)$$

thus

$$\dot{x}_{n+1} - \dot{x}_n = \frac{h}{2m} [(F_{n+1} - c\dot{x}_{n+1} - kx_{n+1}) + (F_n - c\dot{x}_n - kx_n)] \quad (5.7)$$

Substituting in equation (5.6a) into equation (5.7), we are left with only one unknown,

$$\begin{aligned} \dot{x}_{n+1} - \dot{x}_n &= \frac{h}{2m} [(F_{n+1} - c\dot{x}_{n+1} - k\{(\dot{x}_{n+1} + \dot{x}_n)\frac{h}{2} + x_n\}) \\ &\quad + (F_n - c\dot{x}_n - kx_n)] \end{aligned}$$

or by rearrangement,

$$\dot{x}_{n+1} = \frac{h \left(\frac{F_{n+1} + F_n}{2} - kx_n \right) + \dot{x}_n \left(m - \left(c + \frac{kh}{2} \right) \frac{h}{2} \right)}{\left(m + \left(c + \frac{kh}{2} \right) \frac{h}{2} \right)} \quad (5.8)$$

Runge Kutta Method

The standard formulae for a 4th order Runge-Kutta integration are as follows:

$$y_{n+1} = y_n + \frac{h}{6} (k_1 + 2k_2 + 2k_3 + k_4) \quad (5.9a)$$

$$k_1 = f(t_n, y_n) \quad (5.9b)$$

$$k_2 = f\left(t_n + \frac{h}{2}, y_n + \frac{h}{2}k_1\right) \quad (5.9c)$$

$$k_3 = f\left(t_n + \frac{h}{2}, y_n + \frac{h}{2}k_2\right) \quad (5.9d)$$

$$k_4 = f(t_n + h, y_n + hk_3) \quad (5.9e)$$

Two instances of equation (5.9) are used. In one case y_n is the displacement and $f(\cdot, \cdot)$ is velocity. In the other case y_n is the velocity and $f(\cdot, \cdot)$ is the acceleration. In the latter case, the acceleration is calculated by equation (5.1). In both cases a trapezoidal approximation is used for the k_2 and k_3 coefficients.

$$x_1 = \dot{x}_n h \quad (5.10a)$$

$$\dot{x}_1 = \frac{h}{m}(F_n - c\dot{x}_n - kx_n) \quad (5.10b)$$

$$x_2 = h(\dot{x}_n + \frac{1}{2}\dot{x}_1) \quad (5.10c)$$

$$\dot{x}_2 = \frac{h}{m} [\frac{1}{2}(F_n + F_{n+1}) - c(\dot{x}_n + \frac{1}{2}\dot{x}_1) - k(x_n + \frac{1}{2}x_1)] \quad (5.10d)$$

$$x_3 = h(\dot{x}_n + \frac{1}{2}\dot{x}_2) \quad (5.10e)$$

$$\dot{x}_3 = \frac{h}{m} [\frac{1}{2}(F_n + F_{n+1}) - c(\dot{x}_n + \frac{1}{2}\dot{x}_2) - k(x_n + \frac{1}{2}x_2)] \quad (5.10f)$$

$$x_4 = h(\dot{x}_n + \frac{1}{2}\dot{x}_3) \quad (5.10g)$$

$$\dot{x}_4 = \frac{h}{m} [F_{n+1} - c(\dot{x}_n + \dot{x}_3) - k(x_n + x_3)] \quad (5.10h)$$

$$x_{n+1} = x_n + \frac{1}{6}(x_1 + 2(x_2 + x_3) + x_4) \quad (5.10i)$$

$$\dot{x}_{n+1} = \dot{x}_n + \frac{1}{6}(\dot{x}_1 + 2(\dot{x}_2 + \dot{x}_3) + \dot{x}_4) \quad (5.10j)$$

Of all the methods tested, this routine was shown to produce the least error. Initially the `setdata` routine was placed at the “End of Coefficient Loop” time step and a test at the end of each loop for balance of energy was introduced. Unfortunately run times were extended significantly because of this and so a quicker method ensuring balance of energy had to be found. The Geometric Conservation Law mentioned by Farhat and Lesoinne [19] (mentioned in Chapter 3) ensures energy balance if it is obeyed. Their “Improved Staggered Serial” method of coupling obeys the GCL thus obviating the need for a calculation at the end of each coefficient loop. In order for it to work the extrapolation method for displacement has to be second order accurate. Thus the `setdata` routine is placed at the end of time step junction box and the extrapolation method modified as described in the following section.

Hybrid Method

This method is thus named because the velocity integration follows the Runge-Kutta method described above which is 4th order accurate whereas the displacement extrapolation follows the trapezoidal method which is 2nd order accurate in order to obey the

Geometric Conservation Law.

$$x_1 = \dot{x}_n h \quad (5.11a)$$

$$\dot{x}_1 = \frac{h}{m} (F_n - c\dot{x}_n - kx_n) \quad (5.11b)$$

$$\dot{x}_2 = \frac{h}{m} \left[\frac{1}{2}(F_n + F_{n+1}) - c \left(\dot{x}_n + \frac{1}{2}\dot{x}_1 \right) - k \left(x_n + \frac{1}{2}x_1 \right) \right] \quad (5.11c)$$

$$\dot{x}_3 = \frac{h}{m} \left[\frac{1}{2}(F_n + F_{n+1}) - c \left(\dot{x}_n + \frac{1}{2}\dot{x}_2 \right) - k \left(x_n + \frac{1}{4}x_1 \right) \right] \quad (5.11d)$$

$$x_4 = h \left(\dot{x}_n + \frac{1}{2}\dot{x}_3 \right) \quad (5.11e)$$

$$\dot{x}_4 = \frac{h}{m} \left[F_{n+1} - c(\dot{x}_n + \dot{x}_3) - k \left(x_n + \frac{1}{2}x_1 \right) \right] \quad (5.11f)$$

$$x_{n+1} = x_n + \frac{h}{2}(\dot{x}_n + \dot{x}_{n+1}) \quad (5.11g)$$

$$\dot{x}_{n+1} = \frac{\dot{x}_n + \frac{1}{6}(\dot{x}_1 + 2(\dot{x}_2 + \dot{x}_3) + \dot{x}_4)}{1 + \left(2 - \frac{ch}{2m}\right) \frac{kh^2}{12m}} \quad (5.11h)$$

From the above formulae, it can be seen that the velocity extrapolation has had to be adapted to contain the 2^{nd} order formula for the displacement expression. The mathematical background to this is given here: In the original 4^{th} order Runge-Kutta (RK4) scheme the displacement expression included four intermediate displacement variables x_1 , x_2 , x_3 , and x_4 , viz. $x_{n+1} = x_n + \frac{x_1}{6} + \frac{x_2}{3} + \frac{x_3}{3} + \frac{x_4}{6}$. For compatibility, the intermediate variables take on the following values:

$$x_1 = \dot{x}_n h$$

$$x_2 = \frac{h}{2}(\dot{x}_n + \dot{x}_{n+1})$$

$$x_3 = \frac{h}{2}(\dot{x}_n + \dot{x}_{n+1})$$

$$x_4 = \dot{x}_{n+1} h$$

Proof of compatibility follows:

$$x_{n+1} = x_n + \frac{1}{6}(x_1 + 2(x_2 + x_3) + x_4)$$

$$x_{n+1} = x_n + \frac{h}{6}(\dot{x}_n + 2(\dot{x}_n + \dot{x}_{n+1}) + \dot{x}_{n+1})$$

$$x_{n+1} = x_n + \frac{h}{2}(\dot{x}_n + \dot{x}_{n+1})$$

A reminder of how the equivalent velocity expressions are defined in RK4:

$$\dot{x}_{n+1} = \dot{x}_n + \frac{1}{6}(\dot{x}_1 + 2(\dot{x}_2 + \dot{x}_3) + \dot{x}_4)$$

$$\dot{x}_1 = \frac{h}{m}(F_n - c\dot{x}_n - kx_n)$$

$$\dot{x}_2 = \frac{h}{m} \left[\frac{1}{2}(F_n + F_{n+1}) - c \left(\dot{x}_n + \frac{1}{2}\dot{x}_1 \right) - k \left(x_n + \frac{1}{2}x_1 \right) \right]$$

$$\dot{x}_3 = \frac{h}{m} \left[\frac{1}{2}(F_n + F_{n+1}) - c \left(\dot{x}_n + \frac{1}{2}\dot{x}_2 \right) - k \left(x_n + \frac{1}{2}x_2 \right) \right]$$

$$\dot{x}_4 = \frac{h}{m} [F_{n+1} - c(\dot{x}_n + \dot{x}_3) - k(x_n + x_3)]$$

Inserting x_3 into \dot{x}_4 :

$$\dot{x}_4 = \frac{h}{m} [F_{n+1} - c(\dot{x}_n + \dot{x}_3) - k(x_n + \frac{h}{2}(\dot{x}_n + \dot{x}_{n+1}))]$$

Separate out \dot{x}_{n+1} :

$$\dot{x}_4 = \frac{h}{m} [F_{n+1} - c(\dot{x}_n + \dot{x}_3) - k(x_n + \frac{h}{2}\dot{x}_n)] - \frac{h^2k}{2m}\dot{x}_{n+1}$$

Inserting x_2 into \dot{x}_3 :

$$\dot{x}_3 = \frac{h}{m} \left[\frac{1}{2}(F_n + F_{n+1}) - c(\dot{x}_n + \frac{1}{2}\dot{x}_2) - k(x_n + \frac{h}{4}(\dot{x}_n + \dot{x}_{n+1})) \right]$$

Separate out \dot{x}_{n+1} :

$$\dot{x}_3 = \frac{h}{m} \left[\frac{1}{2}(F_n + F_{n+1}) - c(\dot{x}_n + \frac{1}{2}\dot{x}_2) - k(x_n + \frac{h}{4}\dot{x}_n) \right] - \frac{h^2k}{4m}\dot{x}_{n+1}$$

Simplify with the definition of a new variable, \dot{x}_{3m} :

$$\dot{x}_3 = \dot{x}_{3m} - \frac{h^2k}{4m}\dot{x}_{n+1}$$

Inserting this back into \dot{x}_4 :

$$\dot{x}_4 = \frac{h}{m} [F_{n+1} - c(\dot{x}_n + \dot{x}_{3m} - \frac{h^2k}{4m}\dot{x}_{n+1}) - k(x_n + \frac{h}{2}\dot{x}_n)] - \frac{h^2k}{2m}\dot{x}_{n+1}$$

Separate out \dot{x}_{n+1} :

$$\dot{x}_4 = \frac{h}{m} [F_{n+1} - c(\dot{x}_n + \dot{x}_{3m}) - k(x_n + \frac{h}{2}\dot{x}_n)] - \frac{h^2k}{4m}\dot{x}_{n+1} \left(2 - \frac{ch}{m} \right)$$

Simplify with the definition of a new variable, \dot{x}_{4m} :

$$\dot{x}_4 = \dot{x}_{4m} - \frac{h^2k}{4m}\dot{x}_{n+1} \left(2 - \frac{ch}{m} \right)$$

Thus the expression for \dot{x}_{n+1} can be written as follows:

$$\dot{x}_{n+1} = \dot{x}_n + \frac{1}{6}\dot{x}_1 + \frac{1}{3}\dot{x}_2 + \frac{1}{3}\dot{x}_{3m} + \frac{1}{6}\dot{x}_{4m} - \frac{h^2k}{12m}\dot{x}_{n+1} \left(2 - \frac{ch}{2m} \right)$$

Rearranging:

$$\dot{x}_{n+1} = \frac{\dot{x}_n + \frac{1}{6}(\dot{x}_1 + 2(\dot{x}_2 + \dot{x}_{3m}) + \dot{x}_{4m})}{1 + \frac{h^2k}{12m} \left(2 - \frac{ch}{2m} \right)}$$

5.2.4 Verification

To help in the choice of integration method, and in order to verify that it is implemented correctly, a simple test of the above methods is carried out. A spreadsheet simulating the integraton methods is set up and compared against the closed solution described in § 5.2.3. A terse summary of test values of important variables follows:

MASS, m :	0.2420 kg
DAMPING, c :	4.631×10^{-4} Ns/m

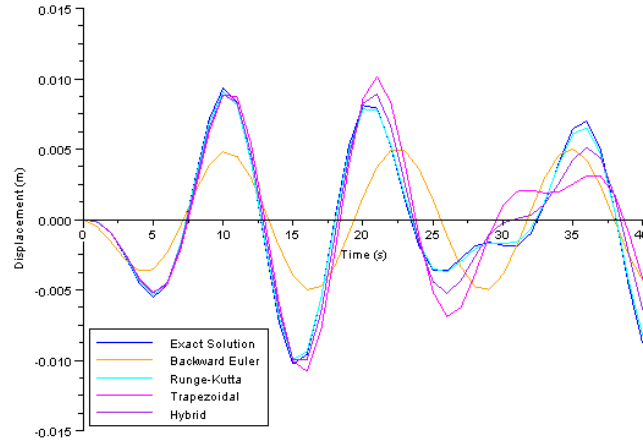


Figure 5.4: Range of displacements produced by all integration methods tested

STIFFNESS, k :	0.1268 N/m
AMPLITUDE OF FORCING FUNCTION, F_0 :	$4 \times 10^{-4} \text{ N}$
ANGULAR FREQUENCY OF FORCING FUNCTION, ω :	$\frac{2\pi}{12.4 \text{ s}} = 0.5067 \text{ rad/s}$
UNDAMPING ANGULAR NATURAL FREQUENCY, ω_n :	$\sqrt{k/m} = 0.7239 \text{ rad/s}$
TIMESTEP SIZE, Δt :	1 s

The plot in Figure 5.4 shows the development of displacement with time following the above integration methods in a spreadsheet. Divergence in displacement caused by error inherent in each extrapolation scheme can clearly be seen as time increases. In order to make the differences between each very apparent the time step used is larger than that would be used in practice. It can be seen that judging by this graph alone the RK4 scheme gives the best performance out of all the extrapolation schemes tested. However this comes with an increased runtime cost because extra iterations for each time step are necessary to ensure energy balance. This can be avoided by employing the ISS coupling method recommended by Farhat and Lesoinne [19]. In order to make this possible however, the extrapolation scheme for displacement has to be second order which the RK4 is not in its traditional form. Thus it is modified to a “hybrid” of the trapezoidal method of extrapolation for the displacement and the RK4 method for velocity. There follows a validation of this scheme with a simple One Degree of Freedom (1DOF) problem run in ANSYS CFX. The solver settings are chosen to enable a forcing function that follows $F_0 \sin(t)$ as closely as possible. Equivalent properties are entered into a spreadsheet application which simulates the algorithms and the trace of displacement compared. If the two sets of results match closely, this indicates that the hybrid extrapolation scheme is valid.

5.3 Validation

A set of 1DOF problems are run with varying parameters for stiffness and damping to construct response curves of the sort found in Harris and Piersol [27].

5.3.1 Simulation description

All simulations were carried using a commercial software supplied by ANSYS Inc. called CFX-10.0.

The domains of all models used for the purposes of this verification have a short spanwise dimension to the extent that they can be considered two dimensional. Also the flow conditions and turbulence selected produce the most consistent and regular sinusoidal load pattern possible on the cylinder object.

The following subsections give a terse list of the salient features of the simulations.

Domain geometry

STREAMWISE LENGTH OF DOMAIN:	2.3 m
TRANSVERSE LENGTH OF DOMAIN:	1.0 m
SPANWISE LENGTH OF DOMAIN:	0.05 m
DISTANCE OF CYLINDER FROM INLET:	0.5 m
DIAMETER OF CYLINDER:	0.1 m

Fluid properties

DEFINED MATERIAL:	Air at 25°C
DENSITY:	$1.185 \frac{\text{kg}}{\text{m}^3}$
DYNAMIC VISCOSITY:	$1.831 \times 10^{-5} \frac{\text{kg}}{\text{ms}}$
KINEMATIC VISCOSITY:	$1.54515 \times 10^{-5} \frac{\text{m}^2}{\text{s}}$
TURBULENCE MODEL:	SST

Boundary conditions

INLET BOUNDARY CONDITION:	Normal speed = 0.1545 m/s This speed ensures a defined Reynolds number of 1000, ensuring a flow regime where the lift force exerted has a sinusoidal shape when plotted against time. Turbulence intensity = 5% Eddy viscosity ratio (μ_t/μ) = 10
OUTLET BOUNDARY CONDITION:	Average static pressure 0 Pa (relative to reference pressure 1 atm)
CYLINDER BOUNDARY CONDITION:	No slip wall (smooth) Specified mesh displacement: Mesh motion X component = 0 m Mesh motion Y component = getdispY

Mesh motion Z component = 0 m

Axes convention:

X is streamwise direction,

Y is transverse direction,

Z is spanwise direction.

TRANSVERSE SIDE WALLS

(PARALLEL TO CYLINDER AXIS):

Free slip wall

SPANWISE SIDE WALLS

(NORMAL TO CYLINDER AXIS):

Free slip wall

Mesh details

CELL TYPE:	Hexahedral throughout
NO. OF CELLS:	107536
NO. OF FACES:	22676
NO. OF NODES:	119016
FIRST NODE DISTANCE AT CYLINDER SURFACE:	1×10^{-3} m
NO. OF CELL LAYERS IN CYLINDER BOUNDARY REGION:	9
NO. OF CELLS AROUND CIRCUMFERENCE OF CYLINDER BOUNDARY REGION:	70
GEOMETRIC GROWTH RATE OF CELL LAYER THICKNESS IN CYLINDER BOUNDARY REGION:	1.013
TOTAL THICKNESS OF CYLINDER BOUNDARY REGION:	0.009482 m
CELL SIZE IN SPANWISE DIRECTION:	0.0045 m

In the mesh generation, a surface is placed in the wake region behind the cylinder, in the same plane as the cylinder axis and extending 1 m downstream. The purpose of this surface is to attach a size function to it as well as the outer surfaces of the cylinder boundary region. This results in the cell size being small in the wake compared to the free stream areas of the domain, and ensures an appropriate gradual growth in cell size going away from the cylinder boundary and wake regions.

GEOMETRIC GROWTH RATE IN CELL SIZE FROM SOURCE FACES:	1.05
CELL SIZE AT SOURCE FACES:	0.0075 m
SIZE LIMIT IN CELL GROWTH FROM SOURCE FACES:	0.8 m

Fluid solver settings

TIME STEP SIZE:	Adaptive to RMS courant number = 2
	Minimum = 0.01 s
	Maximum = 40 s
	Initial size = 0.1 s
	Average size = 0.14 s
ADVECTION SCHEME:	High resolution
RMS RESIDUAL TARGET:	1×10^{-4}
TRANSIENT SCHEME:	Second order backward Euler

EXPERT PARAMETER: Mesh displacement updates at every iteration

The inclusion of the expert parameter above is necessary to ensure the cylinder displacement returned from the structural solver is fed into the mesh at every iteration. This ensures a balance of force at the cylinder surface at the completion of every time step calculation.

Structural solver settings

MASS, m :	0.1218 kg (i.e. cylinder taken to be a steel tube of 2 mm wall thickness)
CRITICAL DAMPING RATIOS, ζ :	0.05, 0.1
STIFFNESSES, k :	0.10, 0.20, 0.30, 0.40, 0.50, 0.56, 0.57, 0.58, 0.59, 0.60, 0.61, 0.62, 0.63, 0.64, 0.70, 0.80, 0.90, 1.00

All combinations of critical damping ratio and stiffnesses above were run to obtain sufficient results to compare against published the data in Harris and Piersol [27] discussed in 5.3.2.

5.3.2 Reference data

Harris and Piersol [27] discuss in detail oscillation characteristics of damped One Degree of Freedom systems subject to a sinusoidal forcing function, represented by equation (5.12).

$$m\ddot{x} + c\dot{x} + kx = F_0 \sin \omega t \quad (5.12)$$

A reproduction of the response curves based on equation (5.12) is given in Figure 5.5 on the next page. To appreciate the contents of Figure 5.5 a few definitions follow.

Critical damping ratio ζ In general the more damping present in a system the less ability it has to freely oscillate. The minimum value of damping coefficient c , at which no free oscillations can occur is the critical damping coefficient c_c , which is \sqrt{km} or $m\omega_n$. The critical damping ratio ζ is the ratio of damping coefficient to the critical damping coefficient c_c .

Response parameters R_d , R_v , R_a The equation for displacement is given below.

$$x = R \sin(\omega t - \theta) = A_1 \sin \omega t + B_1 \cos \omega t \quad (5.13)$$

Initially it can be said that equation (5.2) could be applied to define the displacement. In damped systems all oscillations at the natural frequency tend to disappear quickly however, to leave only oscillations at the forcing frequency. This is considered to be the

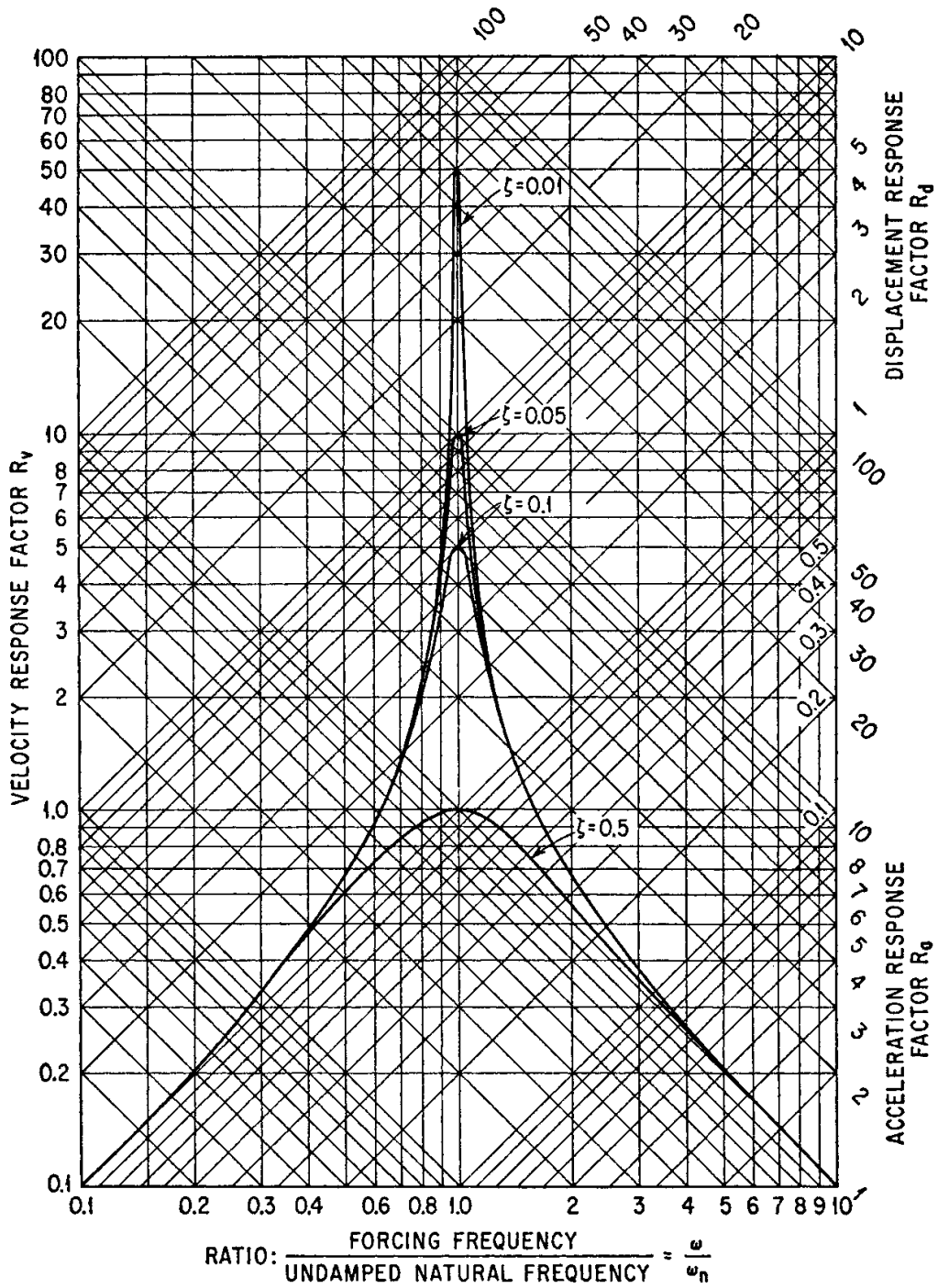


Figure 5.5: Response Factors for a viscous damped single DOF system

steady state response and this is what is represented in equation (5.13). If equation (5.13) is inserted into equation (5.12)...

$$\frac{x}{F_0/k} = \frac{\sin(\omega t - \theta)}{\sqrt{(1 - \omega^2/\omega_n^2)^2 + (2\zeta\omega/\omega_n)^2}} = R_d \sin(\omega t - \theta) \quad (5.14)$$

where

$$\theta = \tan^{-1} \left(\frac{2\zeta\omega/\omega_n}{1 - \omega^2/\omega_n^2} \right) \quad (5.15)$$

and R_d is a dimensionless response factor giving the ratio of the amplitude of oscillation to the spring displacement that would occur if force F_0 was applied statically. A similar dimensionless response factor for velocity can be obtained by differentiating equation (5.14).

$$\frac{\dot{x}}{F_0/\sqrt{km}} = \frac{\omega}{\omega_n} R_d \cos(\omega t - \theta) = R_v \cos(\omega t - \theta) \quad (5.16)$$

Finally, differentiating equation (5.16) would result in an expression that includes a dimensionless acceleration response factor.

$$\frac{\ddot{x}}{F_0/m} = -\frac{\omega^2}{\omega_n^2} R_d \sin(\omega t - \theta) = -R_a \sin(\omega t - \theta) \quad (5.17)$$

Figure 5.5 on the preceding page has four curves plotted on a graph, each relating to one fixed value of critical damping ratio. On the horizontal axis the ratio of forcing frequency to undamped natural frequency is plotted, ω/ω_n . On the vertical axis is plotted the velocity response factor R_v . On the axis at a positive 45° slope is the acceleration response R_a . On the axis at a negative 45° slope is the displacement response R_d . The rest of this chapter details the attempt to reproduce the low damping response curves for a critical damping ratio of 0.05 as shown in Figure 5.5 on the previous page and in so doing, prove the validity of the FSI implementation.

5.3.3 Response Plots

Figure 5.6 on the following page, Figure 5.7 on the next page, and Figure 5.8 on page 118 give the displacement, velocity, and acceleration response curves respectively obtained from the range of numerical simulations carried out to prove the validity of the FSI implementation used. By inspection it can be seen that these curve compare well with Figure 5.5 on the previous page.

5.3.4 Phase Plots

Figures 5.9 on page 118 and 5.10 on page 119 present a typical force-time and displacement-time signal for a simulation. Phase plots showing normalised force on the vertical axis and normalised displacement on the horizontal axis can be constructed from these signals, and can be used to determine the phase angle difference between them. A theoretical figure for the angle is given by equation (5.15), which can be compared with the angles

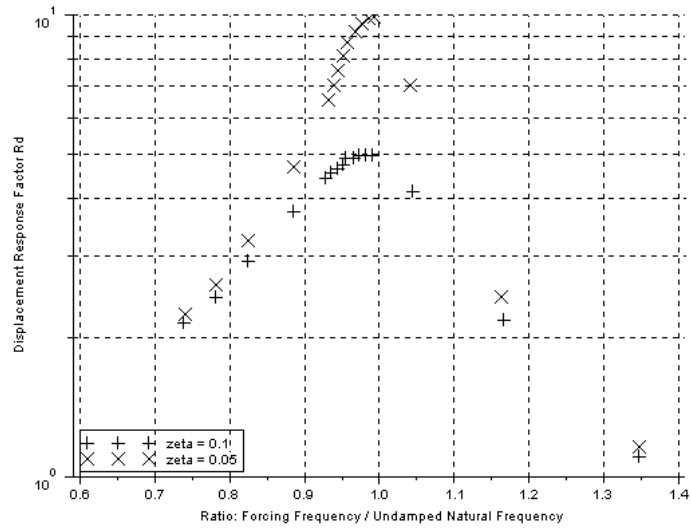


Figure 5.6: Displacement Response R_d

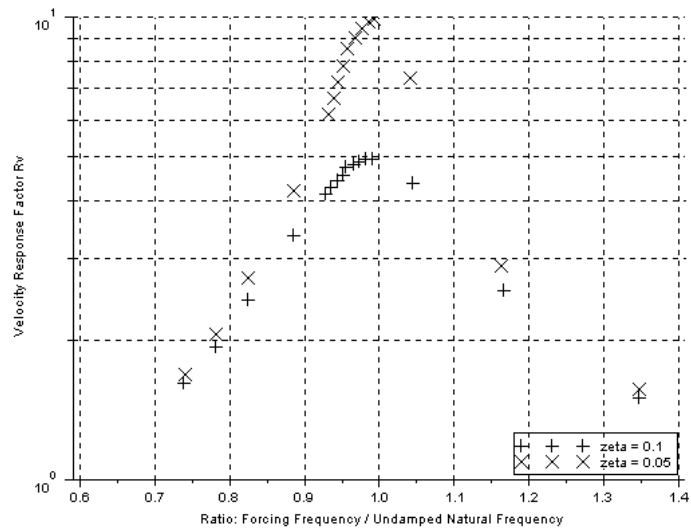


Figure 5.7: Velocity Response R_v

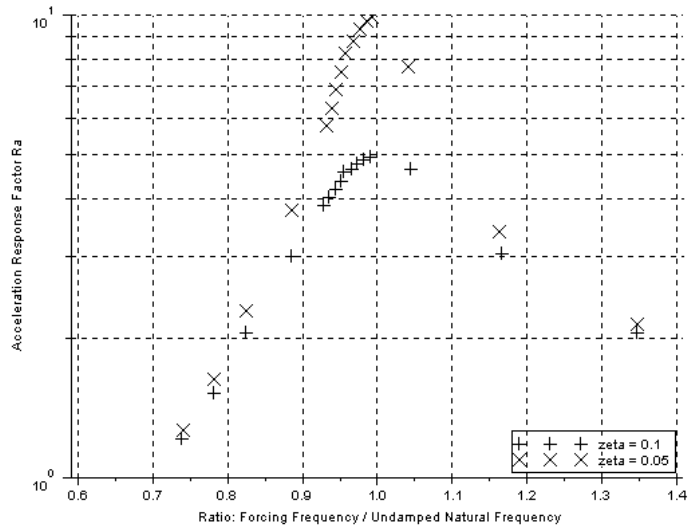


Figure 5.8: Acceleration Response R_a

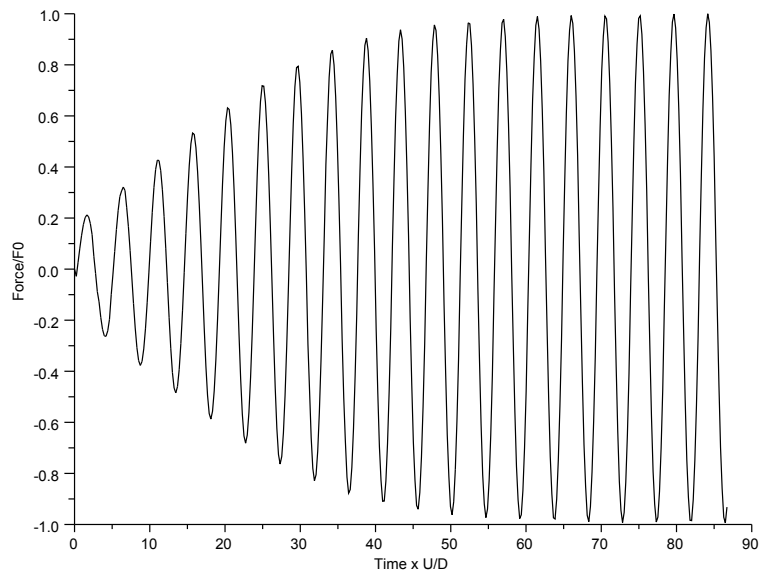


Figure 5.9: Force-time signal for $\zeta = 0.1$ and $\omega/\omega_n = 1.348$

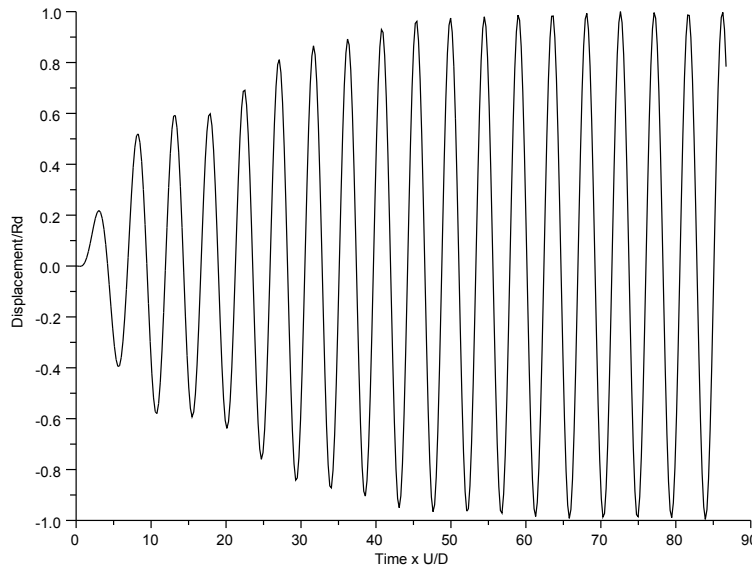


Figure 5.10: Displacement-time signal for $\zeta = 0.1$ and $\omega/\omega_n = 1.348$

measured from the phase plots. In all simulations from the moment the cylinder is released a few cycles of oscillation occur before stationarity in the response, i.e. a steady, consistent amplitude in both signals, is achieved. Figure 5.11 on the following page gives an example of a phase plot showing solely the approach to a steady state response. The rest of the phase plots presented in this chapter show the results for the $\zeta = 0.1$ set of simulations. They include solely the steady state response for clarity. There is also a red ellipse plotted on these diagrams that indicate the locus of points defined by the angle calculated from equation (5.15). For all simulations carried out, Table 5.3 shows the L_2 error norm of the measured angles compared with the theoretical angle.

Table 5.3: L_2 Error Norms of Phase Angles

ω/ω_n	$\zeta = 0.05$	$\zeta = 0.1$
0.739	0.250%	0.315%
0.781	0.290%	0.347%
0.825	0.486%	0.574%
0.886	0.797%	0.655%
0.954	1.434%	0.554%
1.045	1.297%	0.749%
1.167	0.396%	0.468%
1.348	0.397%	0.315%
1.651	0.514%	0.337%
2.334	0.817%	0.334%

It is interesting to note in Table 5.3 that the amount of error reaches a maximum in the region of $\omega/\omega_n \approx 1$. The range of error increase is more pronounced for $\zeta = 0.05$

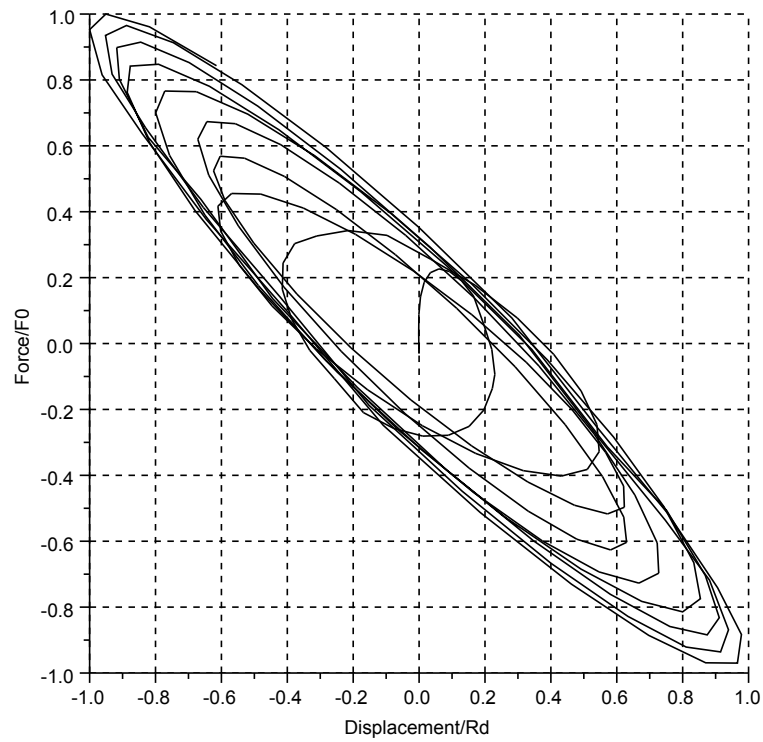
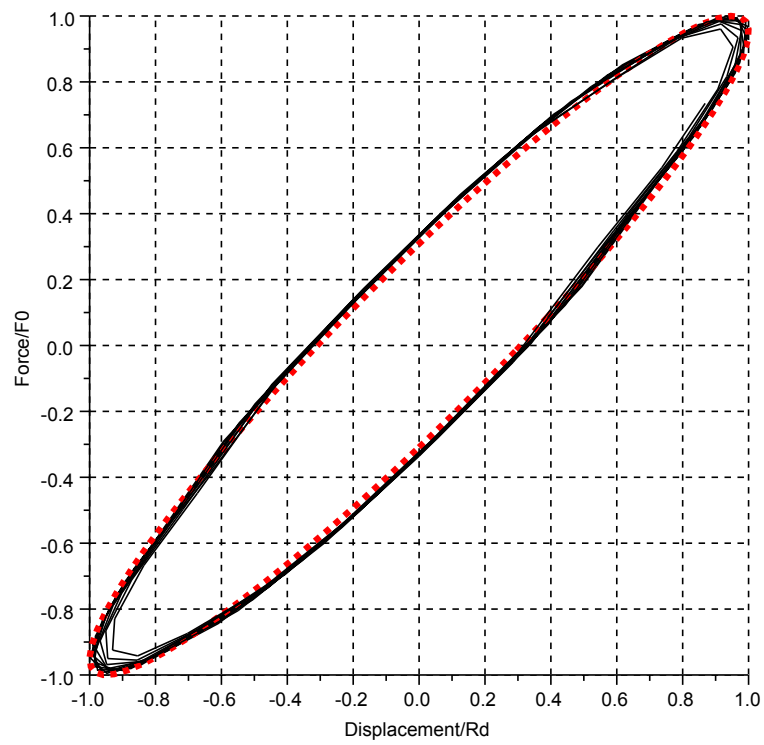
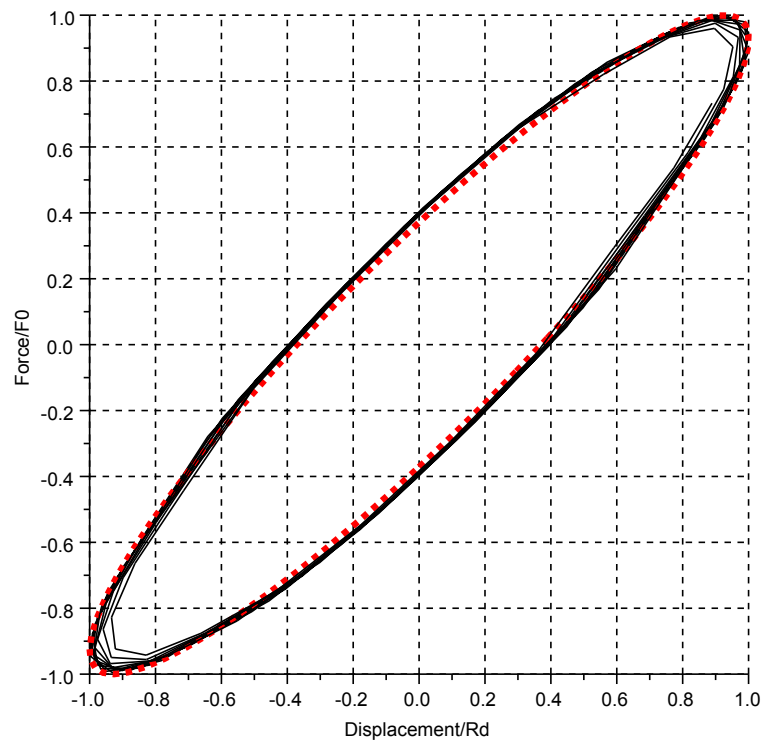
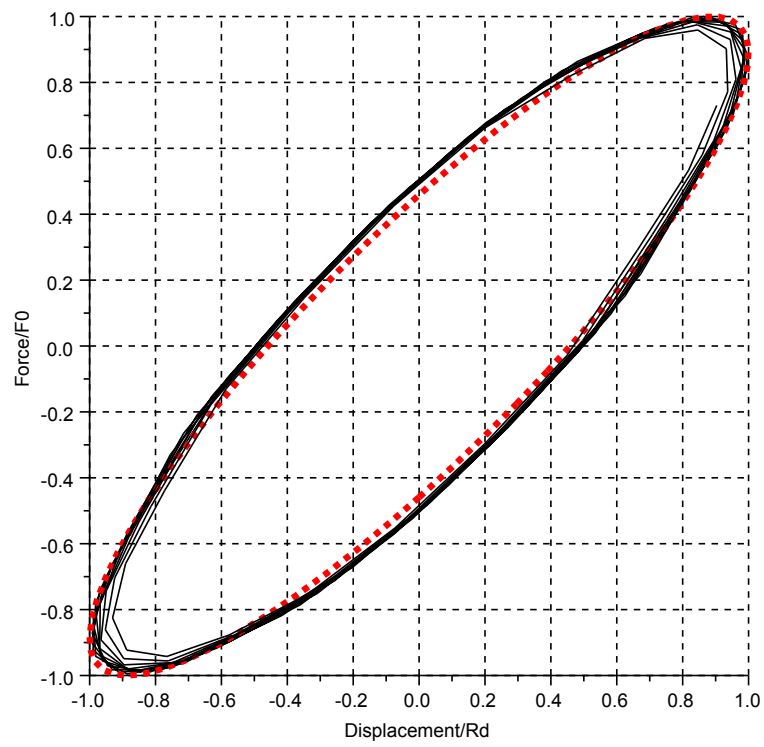
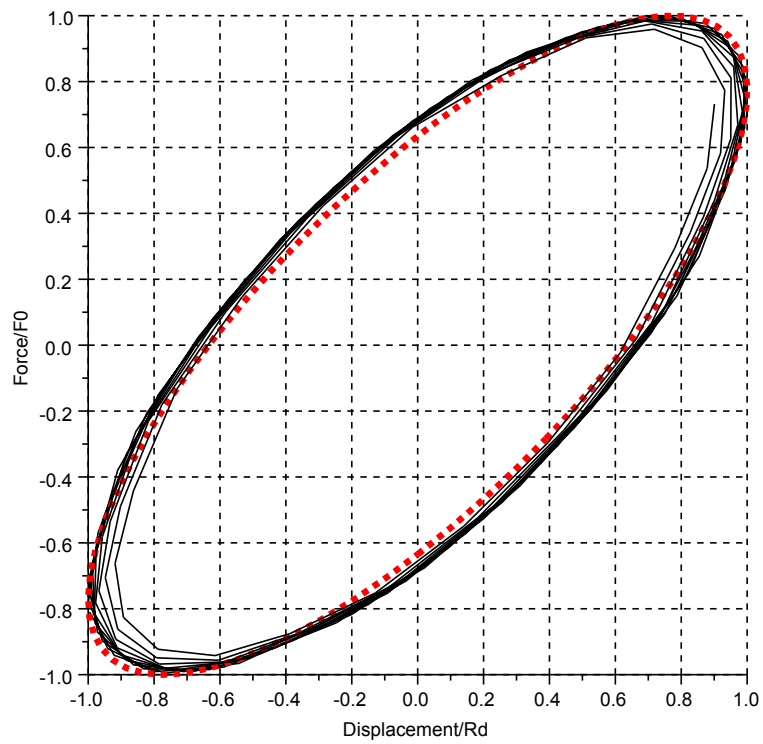
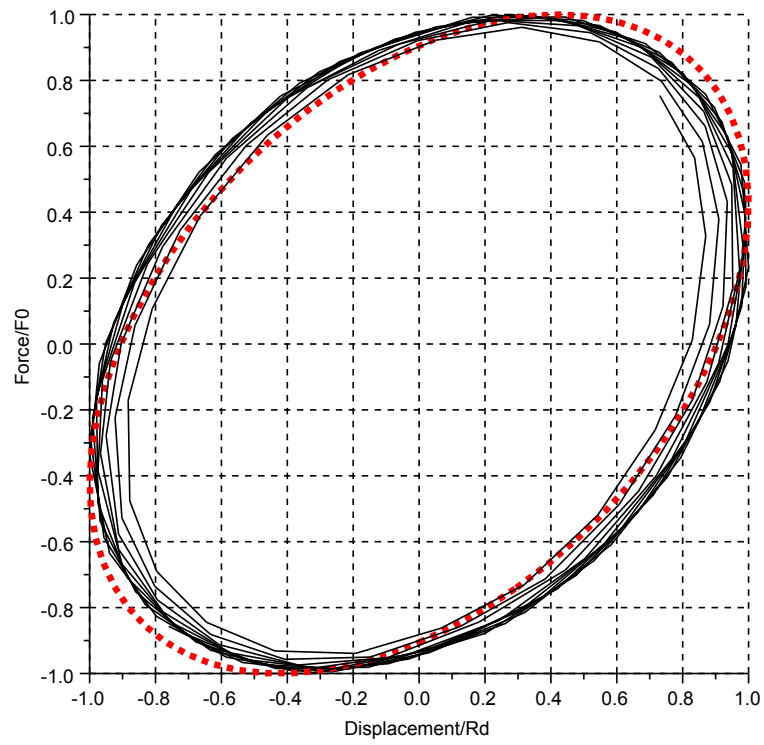
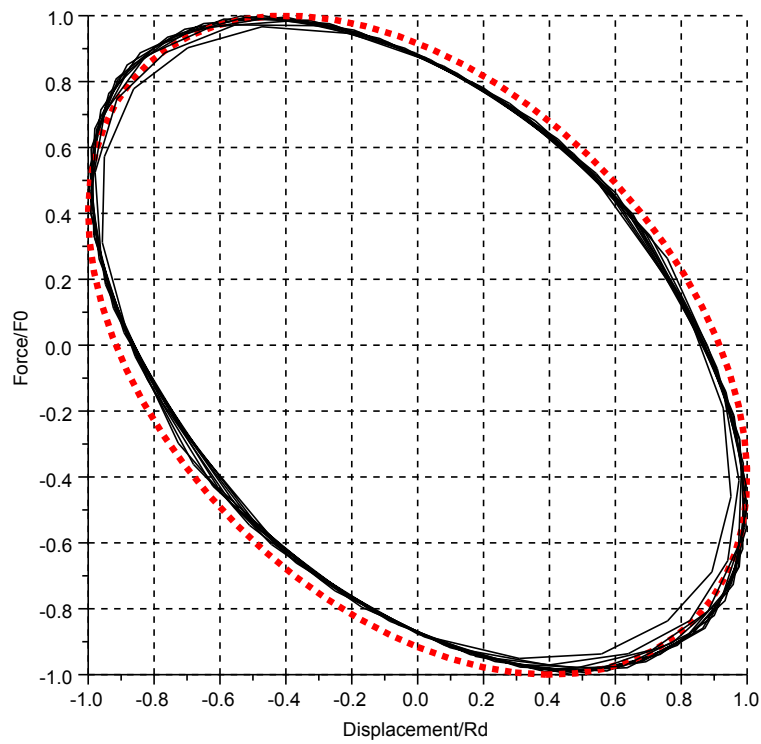


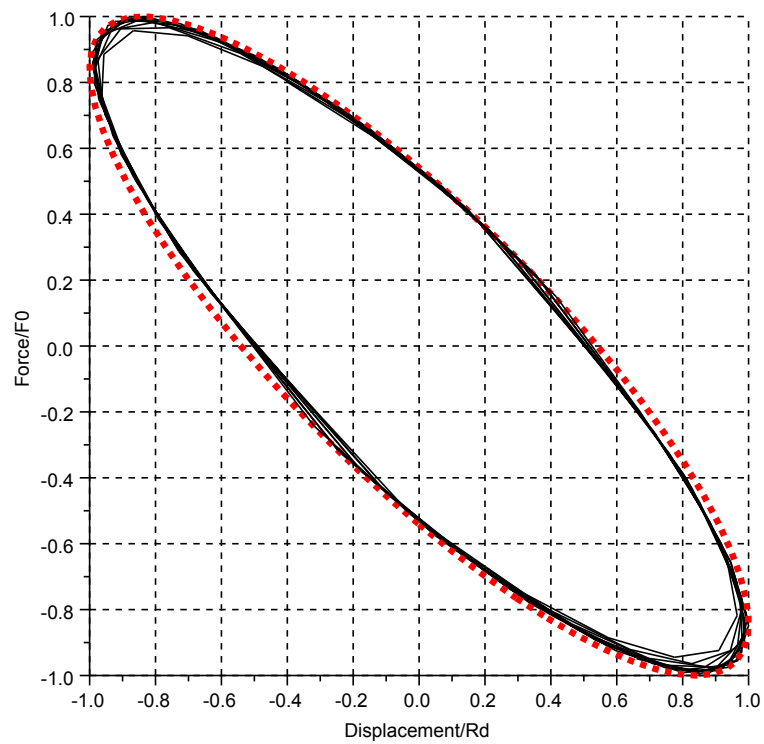
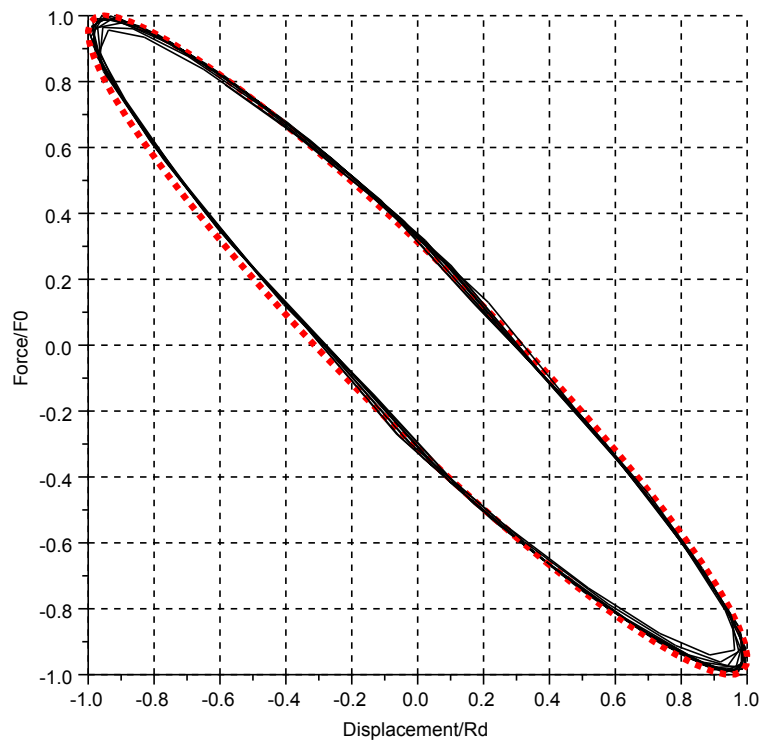
Figure 5.11: Force-Displacement phase plot for $\zeta = 0.1$ and $\omega/\omega_n = 1.348$

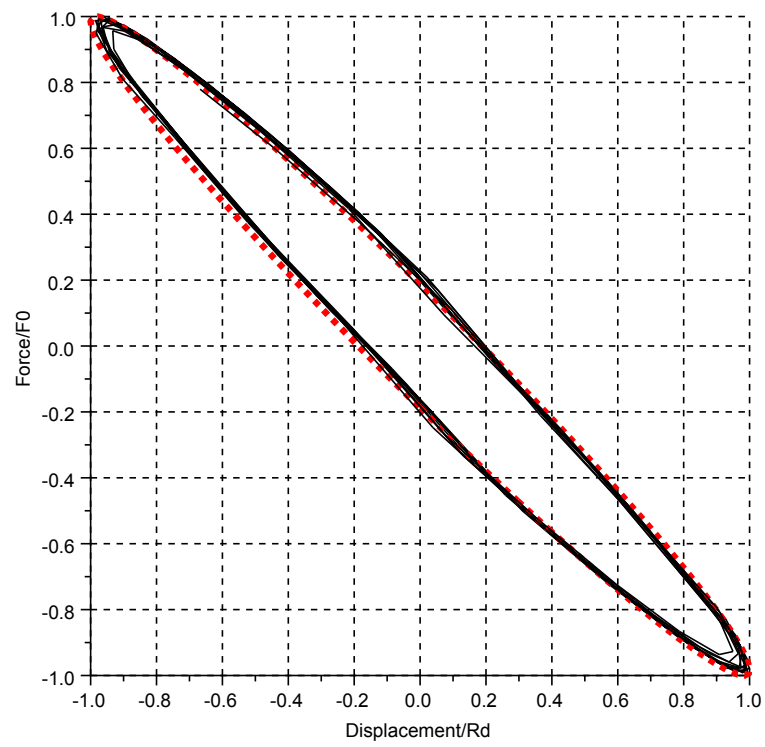
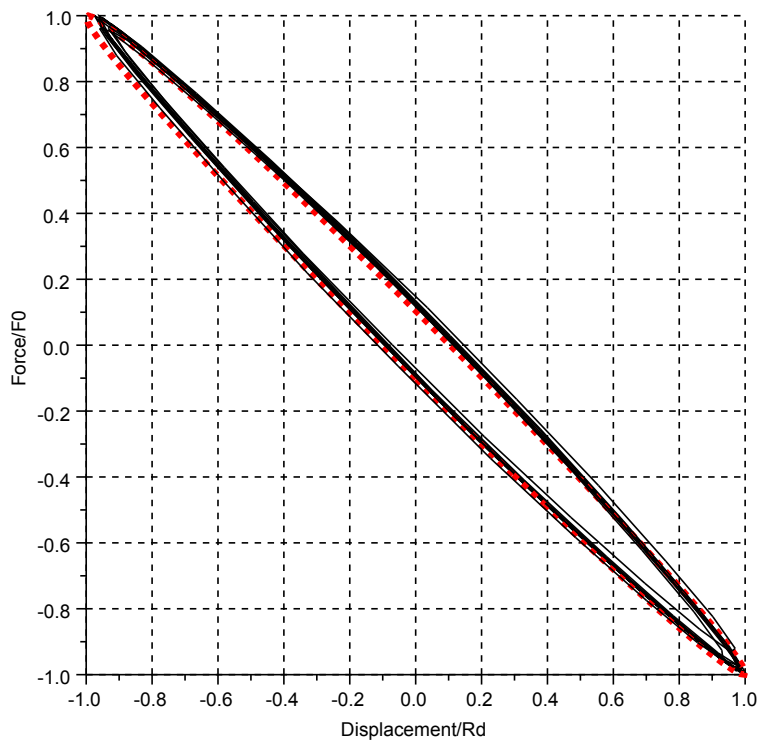
than for $\zeta = 0.1$. Some amount of error can be attributed to the level discretisation but the variation observed in the range of ω/ω_n would suggest that there are non-linear influences that the theoretical figures used for comparison have not captured.

(a) $\omega/\omega_n = 0.739$ (b) $\omega/\omega_n = 0.781$ Figure 5.12: Force-Displacement phase plots for $\zeta = 0.1$ simulations

(c) $\omega/\omega_n = 0.825$ (d) $\omega/\omega_n = 0.886$ Figure 5.12: Force-Displacement phase plots for $\zeta = 0.1$ simulations (cont.)

(e) $\omega/\omega_n = 0.954$ (f) $\omega/\omega_n = 1.045$ Figure 5.12: Force-Displacement phase plots for $\zeta = 0.1$ simulations (cont.)

(g) $\omega/\omega_n = 1.167$ (h) $\omega/\omega_n = 1.348$ Figure 5.12: Force-Displacement phase plots for $\zeta = 0.1$ simulations (cont.)

(i) $\omega/\omega_n = 1.651$ (j) $\omega/\omega_n = 2.334$ Figure 5.12: Force-Displacement phase plots for $\zeta = 0.1$ simulations (cont.)

5.4 Conclusions

The aim of this chapter is to demonstrate the FSI capability added to a commercial fluid solver via user-defined functions. This has been achieved with a verification process that has identified the most suitable method of integration to use.

The validation process has shown that the implementation works in a controlled test modelling a sinusoidal forcing function. Even in such conditions the non-linear nature of the FSI problem tested is apparent.

Chapter 6

Elastically Mounted Cylinder

6.1 Introduction

This chapter describes the FSI simulations carried out by a commercial solver adapted as described in Chapter 5. Two sets of simulations have been carried out. The first set presented here is for a cylinder free to move in only the cross-stream direction (i.e. only one degree of freedom) in a regime far below that for which the drag crisis is known to occur. Comparison is made with numerical and experimental literature to assess the performance of the simulations.

The other set is for a cylinder free to move in the along-stream and cross-stream directions (i.e. two degrees of freedom). The range of flow regimes tested is the same as for some of those simulated in Chapter 4. The object of this work is to investigate the effect of the cylinder response on the drag crisis, in comparison to findings from Chapter 4 in particular, but also to analyse the effect of the drag crisis on the response. Furthermore the comparison of the response characteristics with those for the 1DOF simulations and those given in literature can give an insight into the role that the drag crisis plays in aeroelastic behaviour of cylinders.

6.2 One Degree of Freedom Simulations

6.2.1 Overview

The 1DOF simulations follow the same input parameters as those presented by Saltara et al. [66] for light cylinders, i.e. whose mass-damping ratio $m_*\zeta = 0.013$ and whose reduced velocities are in the range for which lock-in occurs.

The reason for focusing on this method is because Saltara et al. [66] observed that they were only able to achieve the lower branch of excitation response which is represented clearly in Figure 6.1.

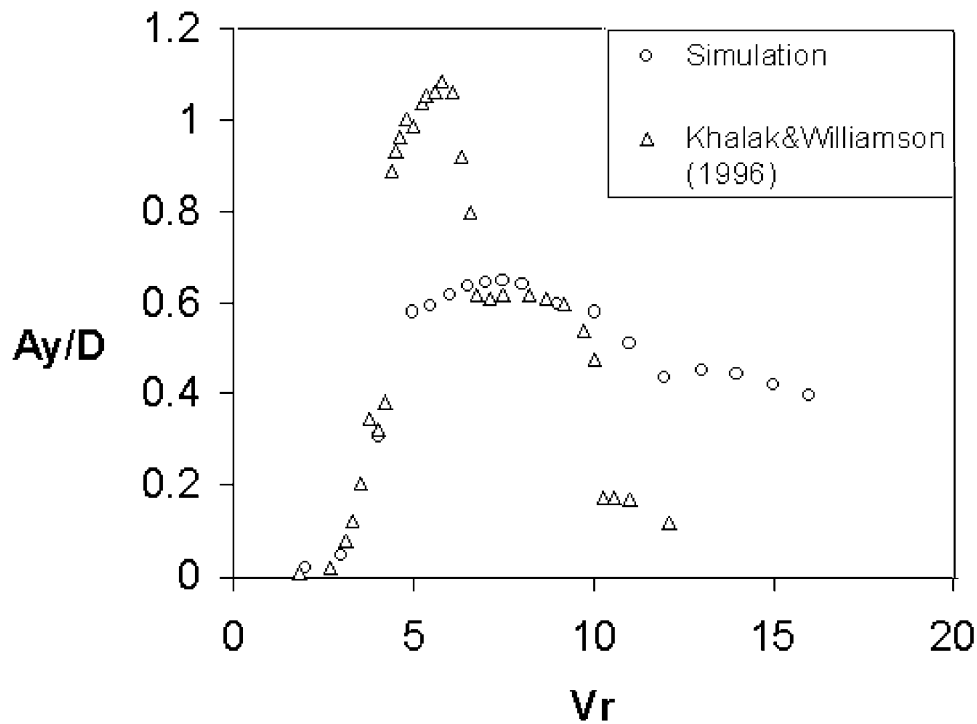


Figure 6.1: Amplitude response achieved by Saltara et al. [66]

As mentioned in Chapter 3, Saltara et al. [66] used DVM which is solely a two-dimensional based method.

6.2.2 Simulation description

All simulations were carried out using ANSYS CFX-10.0. The following subsections give a terse list of the salient features of the simulations.

Domain geometry

STREAMWISE LENGTH OF DOMAIN:	2.3 m
TRANSVERSE LENGTH OF DOMAIN:	1.0 m
SPANWISE LENGTH OF DOMAIN:	0.003 m
DISTANCE OF CYLINDER FROM INLET:	0.5 m
DIAMETER OF CYLINDER:	0.1 m

Fluid properties

DEFINED MATERIAL:	Water
DENSITY:	$997.0 \frac{\text{kg}}{\text{m}^3}$
DYNAMIC VISCOSITY:	$8.899 \times 10^{-4} \frac{\text{kg}}{\text{ms}}$
KINEMATIC VISCOSITY:	$8.92578 \times 10^{-7} \frac{\text{m}^2}{\text{s}}$
TURBULENCE MODEL:	SST

Boundary conditions

INLET BOUNDARY CONDITION:

Velocity U component

Defined Re	Velocity U ($\frac{m}{s}$)	U^* ($\frac{U f_n}{D}$)
4000	3.57×10^{-2}	3.246
5000	4.46×10^{-2}	4.057
6000	5.36×10^{-2}	4.869
6162	5.50×10^{-2}	5.000
7000	6.25×10^{-2}	5.680
8000	7.14×10^{-2}	6.491
9000	8.03×10^{-2}	7.303

... where f_n is natural frequency of cylinder, $f_n = 0.11\text{Hz}$.

Velocity V component: -getvelY

Velocity W component: 0 m/s

Axes convention:

U is streamwise direction,

V is transverse direction,

W is spanwise direction.

Turbulence intensity = 5%

Eddy viscosity ratio (μ_t/μ) = 10

OUTLET BOUNDARY CONDITION:

Static pressure for entrainment 0 Pa

(relative to reference pressure 1 atm)

CYLINDER BOUNDARY CONDITION:

No slip wall (smooth)

TRANSVERSE SIDE WALLS

(PARALLEL TO CYLINDER AXIS):

Opening with cartesian velocity components as set for inlet boundary condition

SPANWISE SIDE WALLS

(NORMAL TO CYLINDER AXIS):

Symmetry

SPECIFIED MESH DISPLACEMENT:

Applied to all boundaries and mesh domain

X component = 0 m

Y component = getdispY + getvelY $\times \Delta t/2$

Z component = 0 m

Axes convention:

X is streamwise direction,

Y is transverse direction,

Z is spanwise direction.

Mesh details

CELL TYPE:

Hexahedral throughout

NO. OF CELLS:	50236
NO. OF FACES:	101580
NO. OF NODES:	101052
FIRST NODE DISTANCE AT CYLINDER SURFACE:	1.5×10^{-4} m
NO. OF CELL LAYERS IN CYLINDER BOUNDARY REGION:	78
NO. OF CELLS AROUND CIRCUMFERENCE OF CYLINDER BOUNDARY REGION:	264
GEOMETRIC GROWTH RATE OF CELL LAYER THICKNESS IN CYLINDER BOUNDARY REGION:	1.04
TOTAL THICKNESS OF CYLINDER BOUNDARY REGION:	0.007617 m
CELL SIZE IN SPANWISE DIRECTION:	0.003 m

In the mesh generation, a surface is placed in the wake region behind the cylinder, in the same plane as the cylinder axis and extending 1.3 m downstream. The purpose of this surface is to attach a size function to it as well as the outer surfaces of the cylinder boundary region.

GEOMETRIC GROWTH RATE IN CELL SIZE FROM SOURCE FACES:	1.04
CELL SIZE AT SOURCE FACES:	0.003 m
SIZE LIMIT IN CELL GROWTH FROM SOURCE FACES:	0.2 m

Fluid solver settings

TIME STEP SIZE:	0.1 s
ADVECTION SCHEME:	High resolution
RMS RESIDUAL TARGET:	1×10^{-4}
TRANSIENT SCHEME:	Second order backward Euler

Structural solver settings

MASS, m :	2.41960×10^{-1} kg
DAMPING, c :	$4.63120 \times 10^{-4} \frac{\text{Ns}}{\text{m}}$
STIFFNESS, k :	$1.26803 \times 10^{-1} \frac{\text{N}}{\text{m}}$

6.2.3 Results

The amplitude response plots for the 1DOF simulations are presented in Figure 6.2 alongside the data points from Figure 6.1.

By comparison with Figure 6.1 it can be seen that the upper branch response observed experimentally by Khalak and Williamson [38] is not captured. Also the size of the amplitude response is less than Figure 6.1 by a factor of ≈ 2 . This is because the domain used for the 1DOF simulations is 2D.

The $[U/(f_n D)] = 6.5$ simulation is repeated with the following changes:

- spanwise extent of the domain increased (set to the value recommended by Norberg [59]),

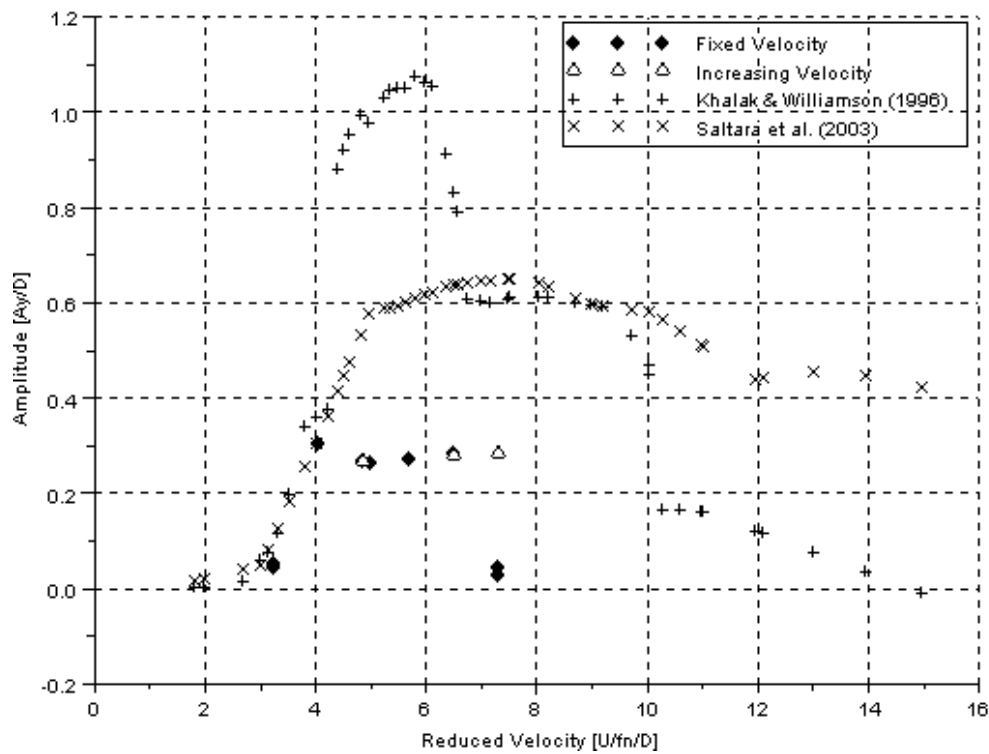


Figure 6.2: Amplitude response achieved by 1DOF simulations

- near wall grid resolution increased,
- timestep size reduced.

The simulation details are the same as given in the preceding section with the following exceptions.

Mesh details

CELL TYPE:	Hexahedral throughout
NO. OF CELLS:	3834320
NO. OF FACES:	211636
NO. OF NODES:	3940387
FIRST NODE DISTANCE AT CYLINDER SURFACE:	2×10^{-5} m
NO. OF CELL LAYERS IN CYLINDER BOUNDARY REGION:	166
NO. OF CELLS AROUND CIRCUMFERENCE OF CYLINDER BOUNDARY REGION:	323
GEOMETRIC GROWTH RATE OF CELL LAYER THICKNESS IN CYLINDER BOUNDARY REGION:	1.001 up to 1.4 mm boundary layer thickness, 1.04 beyond.
TOTAL THICKNESS OF CYLINDER BOUNDARY REGION:	0.02785 m
CELL SIZE IN SPANWISE DIRECTION:	0.013 m

In the mesh generation, a surface is placed in the wake region behind the cylinder, in the same plane as the cylinder axis and extending 1.3 m downstream. A size function is attached to this surface as well as the outer surfaces of the cylinder boundary region.

GEOMETRIC GROWTH RATE IN CELL SIZE FROM SOURCE FACES: 1.08
 CELL SIZE AT SOURCE FACES: 0.001 m
 SIZE LIMIT IN CELL GROWTH FROM SOURCE FACES: 1.0 m

Fluid solver settings

TIME STEP SIZE: 0.04 s

Structural solver settings

MASS, m : 37.8679 kg
 DAMPING, c : $8.02741 \times 10^{-2} \frac{\text{Ns}}{\text{m}}$
 STIFFNESS, k : $21.9792 \frac{\text{N}}{\text{m}}$

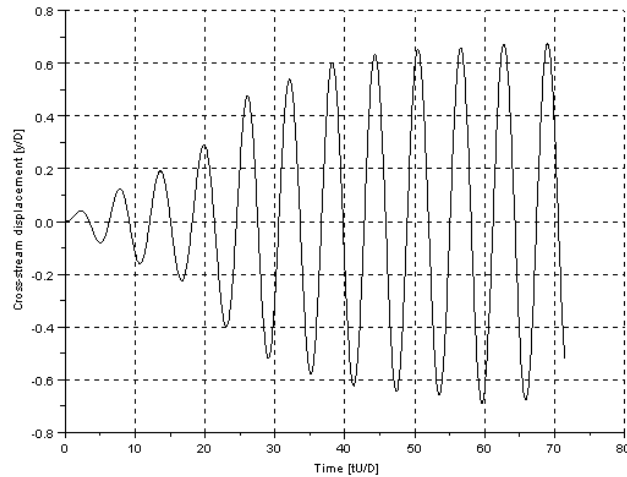


Figure 6.3: Cross-stream displacement time signal for $[U/(f_n D)] = 6.5$ simulation with extended spanwise dimension

Figure 6.3 shows that the cross-stream displacement time signal achieves an amplitude similar to the lower branch amplitude given in Figure 6.1. This closer agreement with experimental data is likely due to the refinement in near-wall grid resolution and timestep size. Observations by Henderson [28] regarding the de-correlation of lift force as the spanwise extent of a simulation domain is increased, suggests that inclusion of three dimensional effects would not likely increase the lift force amplitude.

The boundary condition specified for the transverse side walls for the above simulations is another source of error. Ideally they should be set for static pressure and

entrainment (as specified in the simulations of the next section). It has been found, however, that they have had to be set with velocity components set the same as for the inlet to ensure numerical stability throughout the simulation. This would increasingly disrupt the wake as the extent of cross-stream displacement of the cylinder grows throughout the simulation.

6.3 Two Degree of Freedom Simulations

6.3.1 Overview

Two of the simulations from Chapter 4 are continued with a freedom of the cylinder to move in the along-stream (x) and cross-stream (y) directions. Thus the domain size and the meshes used are the same as has been described in section 4.2. The two Reynolds Numbers, (uncorrected for turbulence), that have been continued are 90000 and 100000.

Mass, stiffness and damping parameters have been chosen to produce similar boundary conditions, i.e. $m_*\zeta = 0.013$, to those reported in section 6.2. The reduced velocity is $[U/(f_n D)] = 4.635$, and $[U/(f_n D)] = 5.150$, for $R_e = 90000$, and $R_e = 100000$ respectively.

The displacement of the cylinder in the along-stream and cross-stream directions, and the lift and drag forces are recorded and reported in § 6.3.3.

6.3.2 Simulation description

All simulations were carried out using ANSYS CFX-10.0. The salient features of these are mostly covered in § 4.2. The following sections describe the settings that are unique to this part of the thesis.

Boundary conditions

INLET BOUNDARY CONDITION:	Velocity U component: U-getvelX Velocity V component: -getvelY Velocity W component: 0 m/s Axes convention: U is streamwise direction, V is transverse direction, W is spanwise direction.
OUTLET BOUNDARY CONDITION:	Static pressure for entrainment Pressure maintained at 0 Pa (relative to reference pressure 1 atm)
TRANSVERSE SIDE WALLS (PARALLEL TO CYLINDER AXIS):	Static pressure for entrainment Pressure maintained at 0 Pa

(relative to reference pressure 1 atm)

SPECIFIED MESH DISPLACEMENT: Applied to all boundaries and mesh domain
 X component = $\text{getdispX} + \text{getvelX} \times \Delta t / 2$
 Y component = $\text{getdispY} + \text{getvelY} \times \Delta t / 2$
 Z component = 0 m
 Axes convention:
 X is streamwise direction,
 Y is transverse direction,
 Z is spanwise direction.

Structural solver settings

MASS, m :	21.6387 kg
DAMPING, c :	$1.25101 \times 10^{-1} \frac{\text{Ns}}{\text{m}}$
STIFFNESS, k :	$93.4176 \frac{\text{N}}{\text{m}}$

6.3.3 Results

Displacements

The cross-stream displacement time signals for all simulations are given in Figure 6.4.

In Figure 6.4a, it can be seen that the maximum amplitude response begins at a non-dimensional time interval of $26[tU/D]$ after release. The maximum amplitude reached is $0.29[y/D]$.

In Figure 6.4b, it can be seen that the maximum amplitude response begins at a non-dimensional time interval of $80[tU/D]$ after release. The maximum amplitude reached is $0.71[y/D]$. It is worth noting that this exceeds any amplitude in the 1DOF simulations reported in section 6.2.

The along-stream displacement time signals for all simulations are given in Figure 6.5.

In Figure 6.5a it can be seen that initially after release only one oscillation frequency occurs. It is from $20[tU/D]$ onwards that a second frequency appears. A maximum amplitude of $0.059[x/D]$ is reached at the end of the simulation which indicates that the oscillation had not yet reached the maximum figure achievable.

In Figure 6.5b a change in oscillation frequency is observed from $60[tU/D]$ after release and beyond. This indicates a change in nature of vortex shedding whose amplitudes are continually building up to the end of the simulation. The maximum amplitude observed in the simulation is $0.19[x/D]$.

An attempt to view the phase relationship between the cross-stream and the along-stream displacements has been carried out in Figure 6.6.

For the sake of clarity solely the oscillations between $25[tU/D]$ and $50[tU/D]$ after cylinder release have been included in Figure 6.6a, also the development of this figure over time is given in Figure B.1. An arc can be observed where the maximum cross-stream

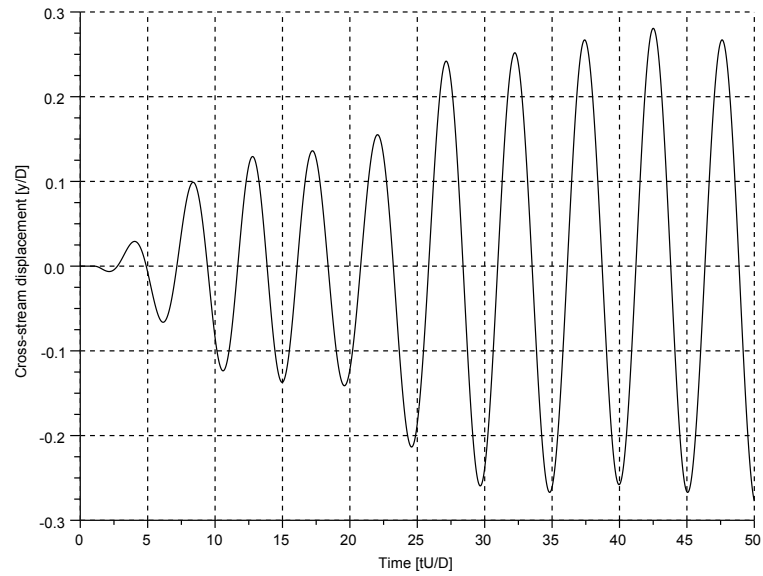
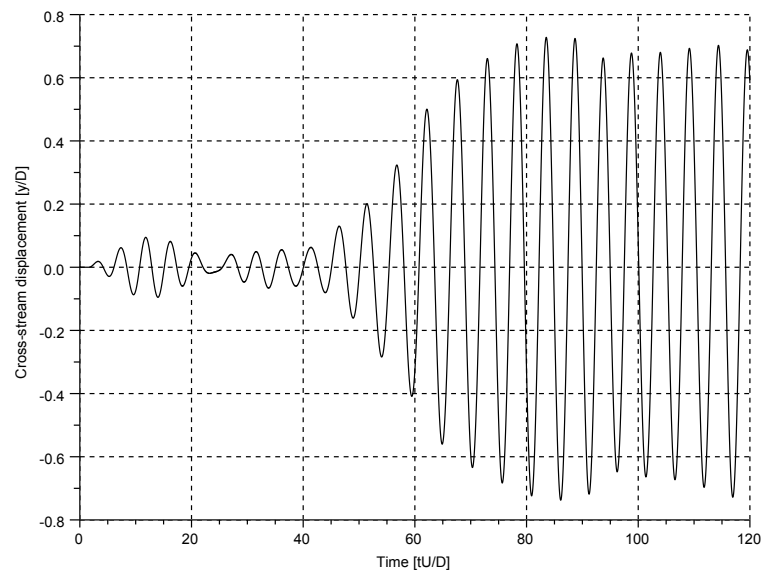
(a) $Re = 90000$ (b) $Re = 100000$

Figure 6.4: Cross stream displacement-time plots

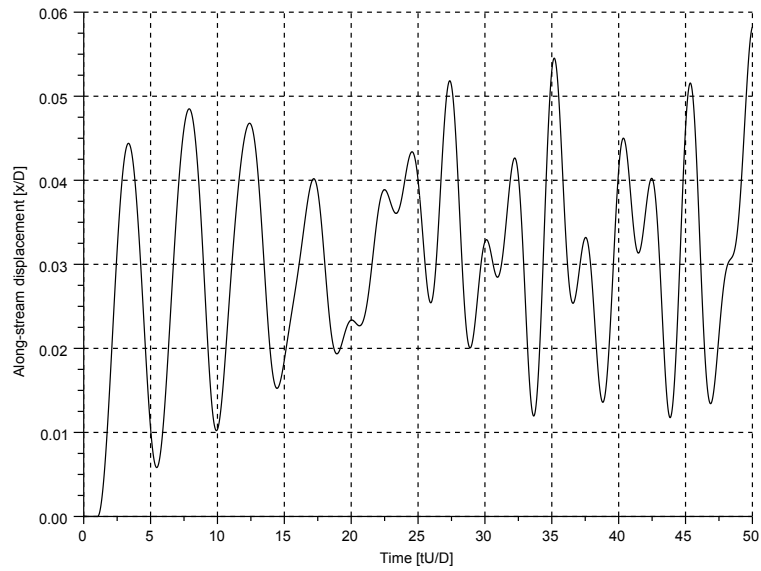
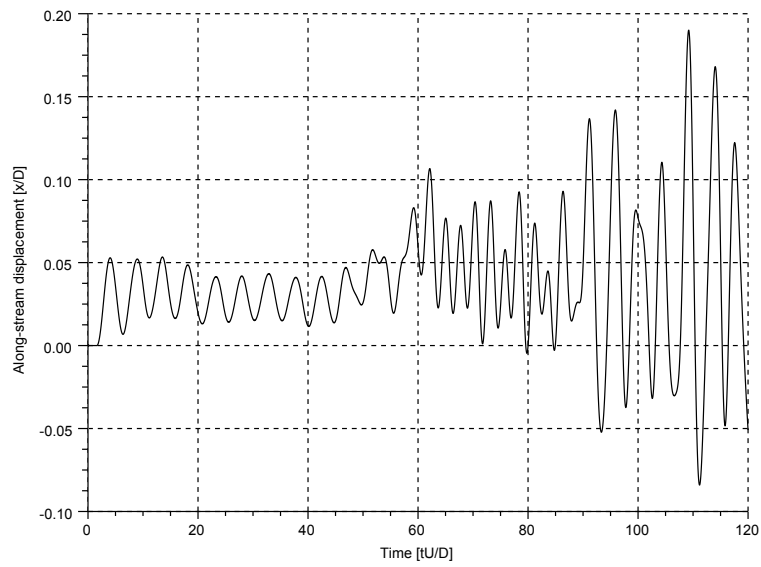
(a) $Re = 90000$ (b) $Re = 100000$

Figure 6.5: Along stream displacement-time plots

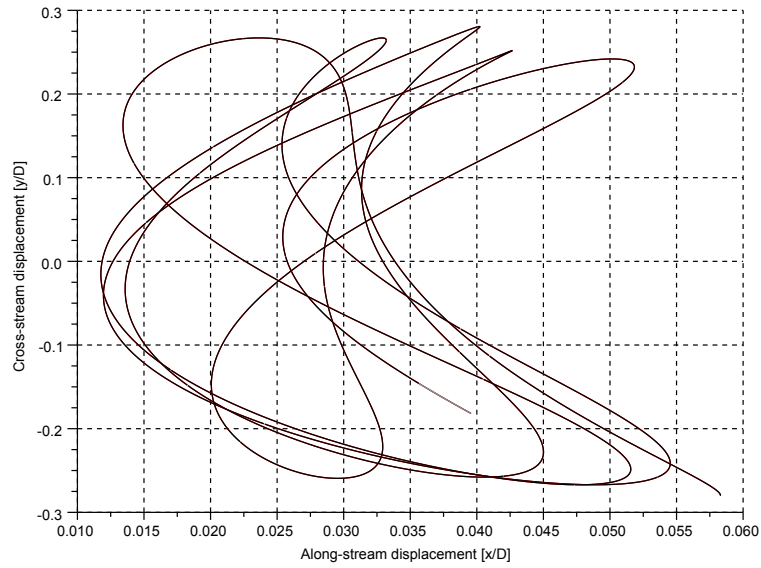
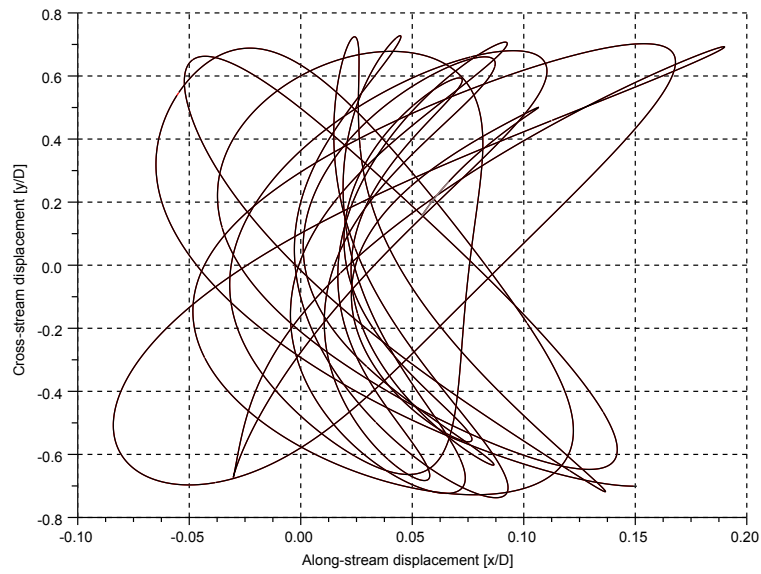
(a) $Re = 90000$ (b) $Re = 100000$

Figure 6.6: Cross stream vs. along-stream displacement plots

displacement occurs at the point of maximum along-stream displacement, and the zero-crossing of the cross-stream displacement occurs at the point of minimum along-stream displacement.

Figure 6.6b includes solely the oscillations from $60[tU/D]$ to $[120tU/D]$ after cylinder release. The development of this figure over time is given in Figure B.5. An arc is observed similar initially to the arc seen in Figure 6.6a. As the oscillations continue, the extent of the along-stream displacements grow while that of the cross-stream displacements remain constant.

In Figure B.5xvi the cylinder is seen to go upstream of its initial release position by a significant amount (compared to its along-stream movement up until that moment). This coincides with the $0.05D$ minimum shown within the range $90 - 95[tU/D]$ in Figure 6.5b. This is also the point in time from which the phase relationship between along-stream and cross-stream displacement begins to vary wildly, and the extent of along-stream displacement continues to be on a relatively large and increasing scale.

Forces

The drag coefficient time signals for all simulations are given in Figure 6.7. In each of these figures, a green line is shown indicating the level of drag found in chapter 4 for the same Reynolds Number.

Figure 6.7a shows a change in signal from $25[tU/D]$ after cylinder release consistent with that shown in Figure 6.5a. The range of oscillations extend from $C_D = 0.5$ to $C_D = 1.6$. The centre of the oscillations are at $C_D = 1.05$, well above the figure given in Chapter 4.

Figure 6.7b shows a change in signal from $60[tU/D]$ after cylinder release consistent with that shown in Figure 6.5b. The range of oscillations extend from $C_D = -0.8$ to $C_D = 3.0$. The negative value of drag suggests that the cylinder travels faster than the flow in the $+x$ direction. A modulation in amplitude can be seen to occur with the minimum at $90[tU/D]$ after cylinder release. The centre of the oscillations are at $C_D = 1.1$, above the figure given in Chapter 4.

Spectral frequency plots for lift coefficient are given in Figure 6.8. The dominant frequencies encountered are shown in Table 6.1. It can be seen that the dominant shedding frequency for all Two Degrees of Freedom (2DOF) simulations is reduced, in comparison to the simulations presented in Chapter 4.

Table 6.1: Dominant Frequencies

Reynolds Number	Static Dominant Frequency (fD/U)	2DOF Dominant Frequency (fD/U)
90000	0.253	0.194
100000	0.257	0.189

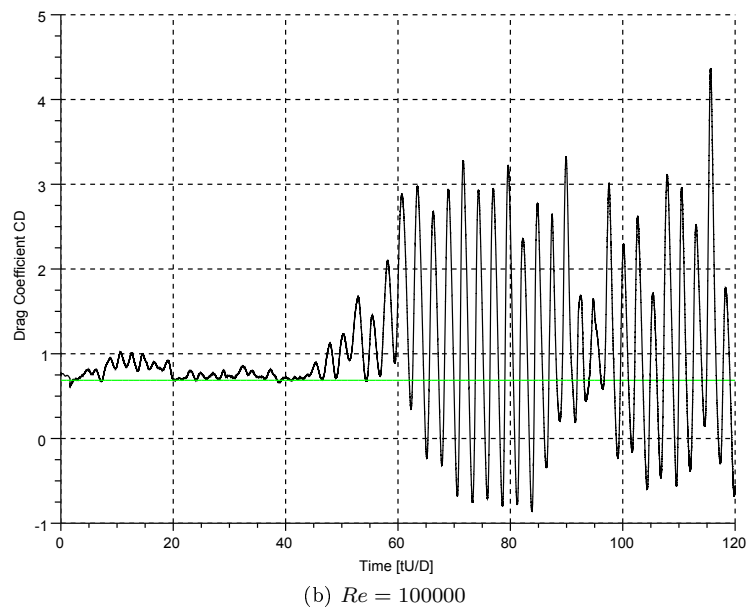
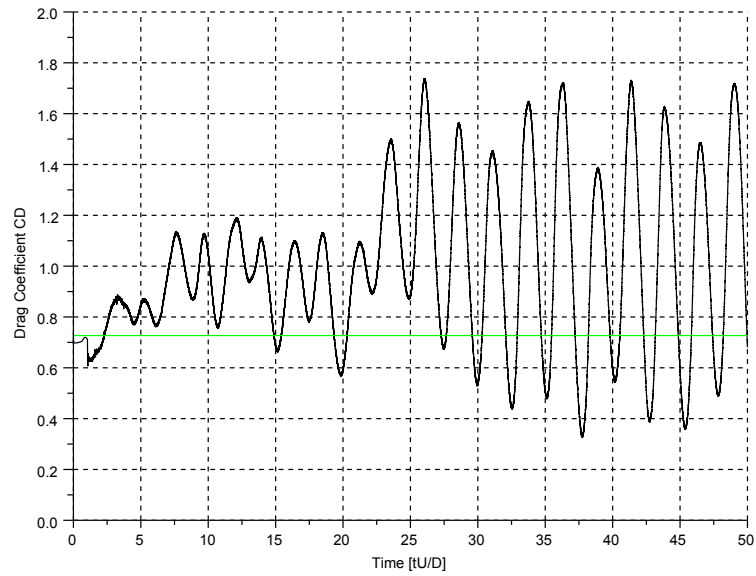


Figure 6.7: Drag coefficient-time plots

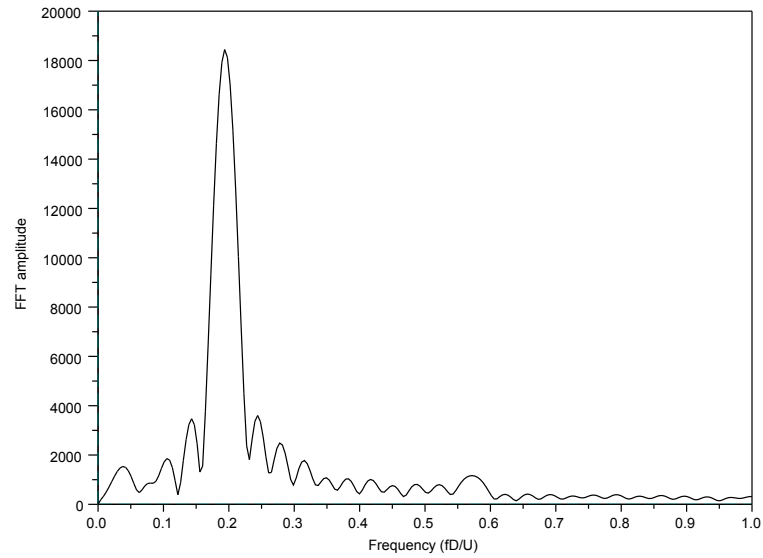
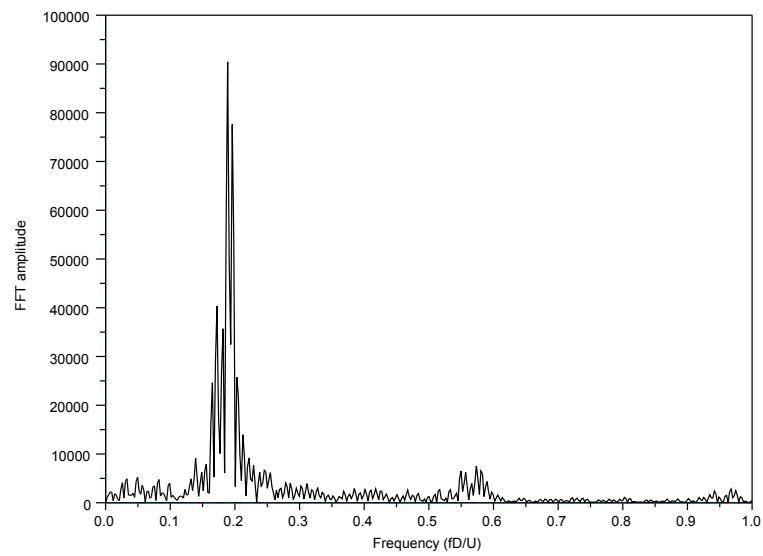
(a) $Re = 90000$ (b) $Re = 100000$

Figure 6.8: Spectral frequency plots for lift coefficient

Plots of lift coefficient vs. cross-stream displacement are given in Figure 6.9.

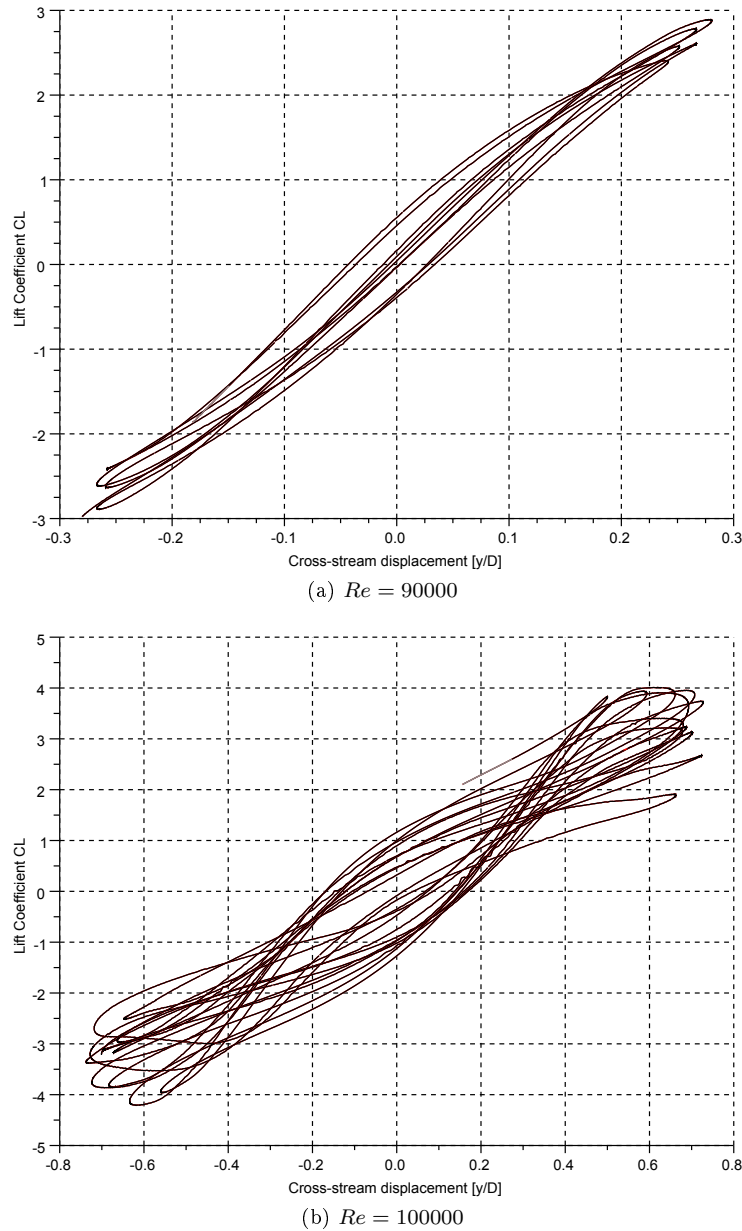


Figure 6.9: Lift coefficient vs. cross-stream displacement plots

Figure 6.9a shows that there is a gradual changing phase angle between lift force and cross-stream displacement that ranges between 0° and $\approx 10^\circ$. A distortion of the extreme ends of the trace from the $+45^\circ$ slope indicates the occurrence of non-linear effects at the extreme limits of displacement.

Figure 6.9b shows the upper limit of the phase angle between lift force and cross-stream displacement is $\approx 20^\circ$. More distortion of the extreme ends of the trace compared with Figure 6.9a indicates that the non-linear effects at the extreme limits of displacement

for the $Re = 100000$ simulations is more pronounced than for the $Re = 90000$ simulations.

Plots of drag coefficient vs. along-stream displacement are given in Figure 6.10. The development of Figures 6.10a and 6.10b over time is given in Figures B.2 and B.6 respectively.

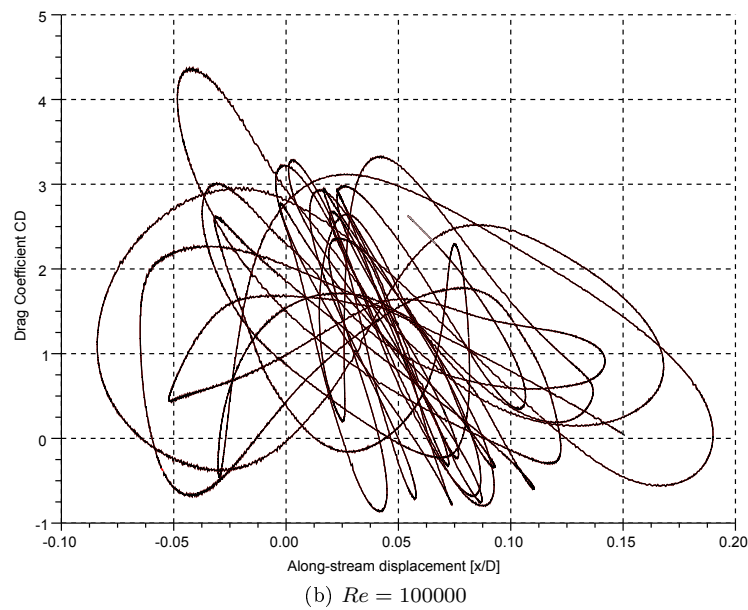
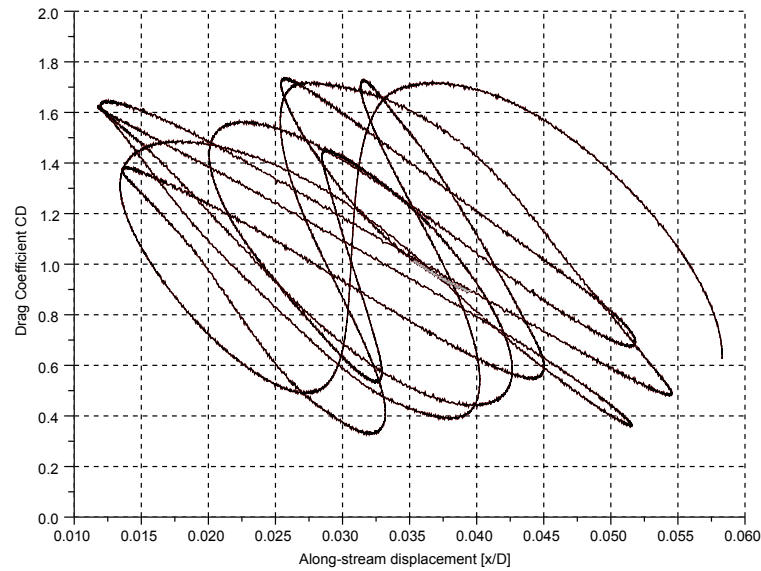


Figure 6.10: Drag coefficient vs. along-stream displacement plots

Figures 6.10a and B.6 show the trace of drag coefficient with along-stream displacement beginning with a negative slope, with the maximum drag occurring at the upstream extent and the minimum drag occurring at the minimum extent. It is worth noting that the drag coefficient shown in these plots is based on the inlet velocity i.e. a fixed value,

so any variation in C_D shown is solely due to variation in drag force.

The drag coefficient holds a relatively constant value for pre-critical flow regimes, thus an increase in velocity is reflected by an increase in drag force (assuming all else is constant). Thus a negative slope as described above is a simple reflection of the relative velocity experienced by the cylinder: higher when moving upstream, lower when moving downstream.

The Reynolds number experienced by the cylinder varies with the effective velocity which is the sum of the flow velocity and velocity due to its movement. Thus the drag coefficient can drop if the effective Reynolds number of the upstream movement goes into the critical regime. Such a drop is evident in Figure B.2v, the maximum drag occurs just before the maximum upstream displacement is reached. Consequently, a relatively lesser drag force at the upstream extent pushes the cylinder less far in its next downstream motion, as can be seen in Figure B.2vi. Since the downstream displacement is less, the spring pushes the cylinder less far upstream as shown in Figure B.2vii.

Continuing to Figure B.2ix it can be seen that the minimum drag force occurs after the cylinder has reached its downstream extent, i.e. as it is moving upstream again. This is allowing energy to enter the system, as can be seen by the further upstream extent reached in Figure B.2xi. Thus it can be generally said that energy is entering the system if the trace of drag vs. along-stream displacement follows a clockwise loop as the cylinder passes through its downstream extent. The same can also be said if the trace follows a clockwise loop at the upstream extent.

As the trace continues, a few “figure of eight” loops develop albeit lopsided with every stroke having a negative gradient, seen from Figure B.2xii to B.2xvii. Energy is continually entering and leaving the system with each clockwise and anti-clockwise stroke. Interestingly, each upstream anticlockwise stroke through this sequence occurs at a progressively lower value of drag, causing the slope of the consequent upstream motion of the trace progressively approach the vertical.

This trend continues until ultimately a positive gradient occurs, as can be seen in Figure B.2xxix. This signifies that there was insufficient drag at the upstream extent to force the spring to push the cylinder back upstream, allowing the flow to push the cylinder further downstream than previously, as seen in Figure B.2xxx.

In Figure 6.10b and Figure B.6 a similar trace develops at the start. In this case however it is interesting to note the negative drag and negative along-stream displacement (i.e. further upstream of the release position) that occurs.

The negative drag occurring at the downstream extent of movement is produced by the cylinder moving faster than the flow to produce a reversal of drag force. A negative drag force on the cylinder as it is moving upstream puts energy into the system, pushing the cylinder further upstream, as can be seen in Figures B.6ii to B.6ix. From Figure B.6x onwards, the upstream extent of the cylinder is beyond the initial release position, allowing the spring to push the cylinder downstream. Thus energy is being fed into the system at both extremes of along-stream movement of the cylinder.

A positive gradient of the trace occurs in Figure B.6xiv as the cylinder is moving downstream. This is similar to the positive gradient shown in Figure B.2xxx discussed above. The flow pushes the cylinder further downstream than previously, shown in Figure B.6xv. Interestingly the drag force that develops on the consequent upstream movement, shown in Figure B.6xvi, is significantly less than that developed on previous upstream motions. This is because the effective Reynolds number at this instant is in the critical regime resulting in a drop in drag coefficient. The reduced drag on the upstream stroke allows the cylinder to push further upstream than previously. This is clear evidence of the drag crisis having a significant effect on the movement of the cylinder.

Due to the effect of the drag crisis, more energy is in the system, as can be seen in the extremes of along-stream motion from Figure B.6xvi onwards. Negative drag occurs on the downstream extreme extent of motion as shown in Figures B.6xix, B.6xxii, B.6xxiv, and B.6xxviii. Negative drag also occurs when the cylinder is upstream of its initial position as shown in Figures B.6xxiii, B.6xxv, and B.6xxix. Each time negative drag occurs, further energy enters the system and the extents of along-stream displacements increase. The result is a horizontal “figure of eight” where the lower loops of the trace enter the negative drag region. It is easy to imagine that if this simulation was allowed to run further the along-stream displacement would increase further.

Wake characteristics

To visualise the wake in a range of instants for the 2DOF simulations, the Q-criterion developed by Hunt et al. [32] and as described by Green et al. [26] is plotted in the following figures. The Q-criterion is a scalar that indicates regions where rotation dominates strain in the flow. Letting S and Ω denote the symmetric parts of the velocity gradient ∇u , one defines Q as the second invariant of ∇u , given for incompressible flow by $Q = \frac{1}{2}(\|\Omega\|^2 - \|S\|^2)$ where $\|\cdot\|$ is the Euclidean (or Frobenius) matrix norm. A coherent vortex is defined as a region where $Q > 0$.

Figures 6.11, 6.12, 6.13, 6.14, and 6.15 show an isosurface where $Q = 50 \text{ Hz}^2$ indicating areas of strong vorticity in the flow. In all of these plots, the iso-surfaces shown are very segregated and it is difficult to determine the shapes of vortical structures. An animated sequence of these plots through a shedding cycle would improve the likelihood of achieving this objective.

Figure 6.11 shows the state of the flow field for the $Re = 90000$ simulation prior to the cylinder being released, Figure 6.12 shows the flow field for the same simulation after release at the last recorded time frame. The movement of the cylinder is evident by the increased width of the wake in Figure 6.12a compared to that shown in Figure 6.11a.

On the upstream face of the cylinder there is a strip of blue, the colour of the cylinder surface, showing through the green of the iso-surface that surrounds the rest of the cylinder. This is a region where there is no significant rotation element to the flow on the cylinder surface. This is where the flow is incident to the cylinder surface, i.e. the

stagnation point. The rotating element of flow only begins to develop as it travels away from this point and undergoes friction with the cylinder surface. It is interesting to observe that the blue strip/ stagnation point is offset from the cylinder axis in Figure 6.12c, whereas in Figure 6.11c there is no noticeable offset. Thus this offset can be seen to be an indication of the extent of cross-stream velocity of the cylinder.

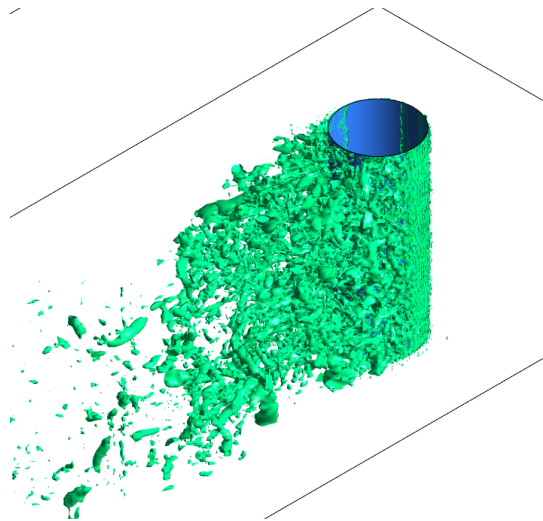
Figure 6.13 shows the flow field of the $Re = 100000$ simulation prior to release of the cylinder. The iso-surfaces indicating where $Q = 50 \text{ Hz}^2$ in the flow extends further in the wake of the cylinder in Figure 6.13a compared with that shown in Figure 6.11a. This demonstrates the higher degree of vorticity produced in the wake as the Reynolds number increases.

Figure 6.14 shows the state of flow in a time instant within the initial period after cylinder release ($0[tU/D]$ to $60[tU/D]$) as shown in Figure 6.7b. There are no features in this figure that are strikingly different to those shown in Figure 6.13.

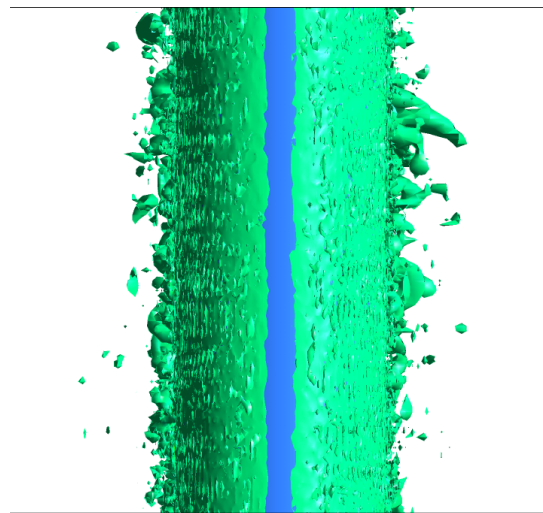
Figure 6.15 shows the state of flow at the last recorded instant for the $Re = 100000$ simulations. The cross-stream movement of the cylinder is obvious by the position of the stagnation point in Figure 6.13c. Some of the blue strip of the cylinder surface in this view is occluded by iso-surfaces, showing that the cylinder is entering its own wake as it is moving. Also a degree of along stream movement is evident by the upstream position (in the domain frame of reference) of the iso-surface that can be seen to the side of the cylinder in Figure 6.15a.



(a) view along cylinder axis



(b) isometric view with cylinder axis vertical

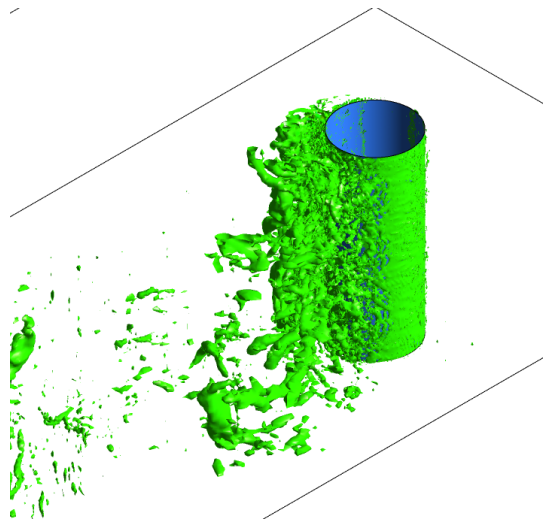


(c) view in streamwise direction

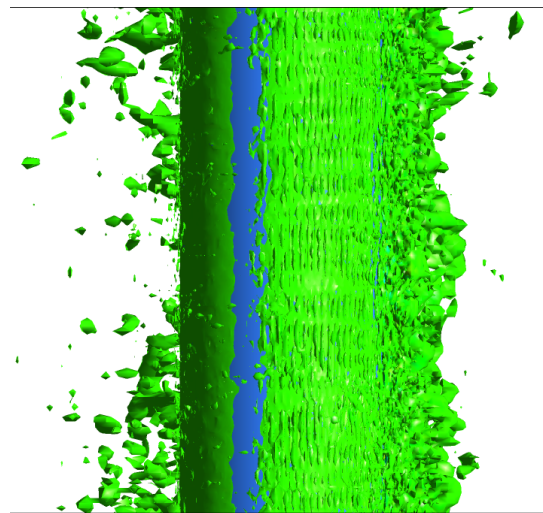
Figure 6.11: Q -criterion=50 Iso-surface for $Re = 90000$ simulation prior to release



(a) view along cylinder axis



(b) isometric view with cylinder axis vertical

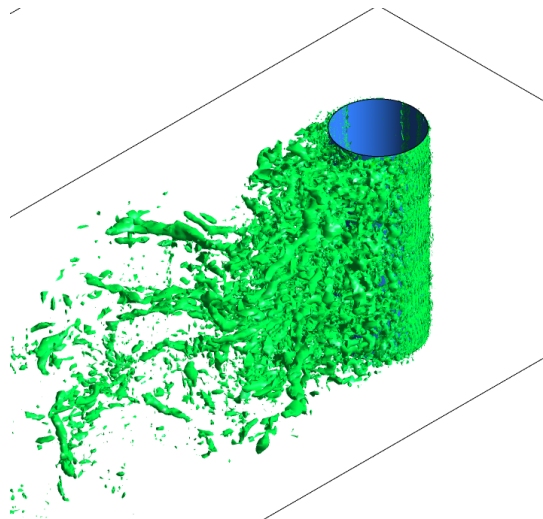


(c) view in streamwise direction

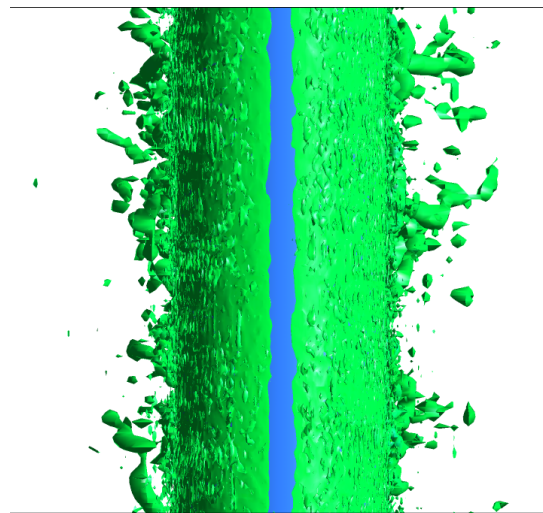
Figure 6.12: Q -criterion=50 Iso-surface for $Re = 90000$ simulation after release



(a) view along cylinder axis



(b) isometric view with cylinder axis vertical

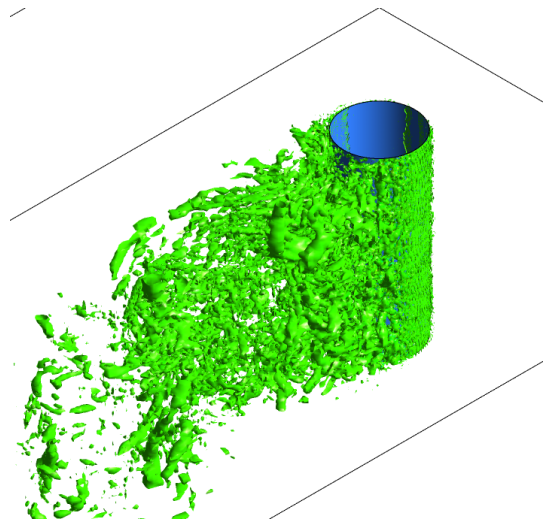


(c) view in streamwise direction

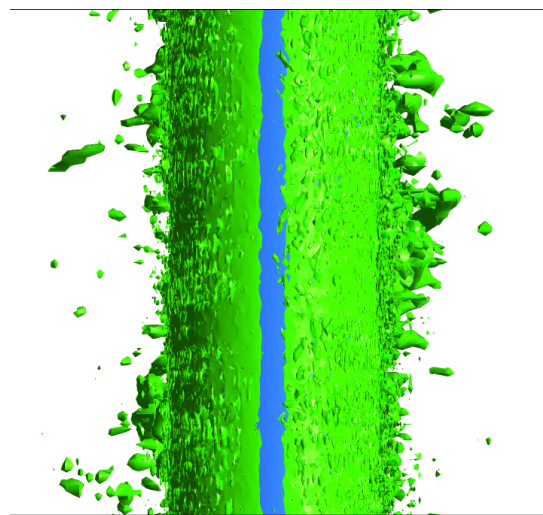
Figure 6.13: Q-criterion=50 Iso-surface for $Re = 100000$ simulation prior to release



(a) view along cylinder axis



(b) isometric view with cylinder axis vertical

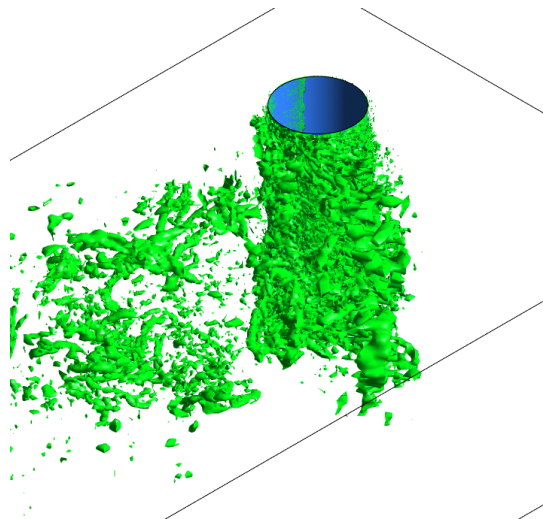


(c) view in streamwise direction

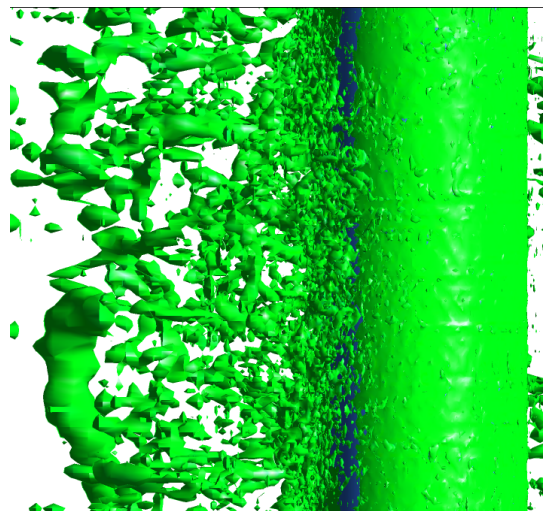
Figure 6.14: Q-criterion=50 Iso-surface for $Re = 100000$ simulation after release



(a) view along cylinder axis



(b) isometric view with cylinder axis vertical



(c) view in streamwise direction

Figure 6.15: Q -criterion=50 Iso-surface for $Re = 100000$ simulation after release

6.4 Concluding Remarks

Some interesting and new observations have been made in this chapter. The effect of the response on the drag crisis has been to reduce the dominant shedding frequency, as shown in Table 6.1. The movement of the cylinder has also had the effect of increasing the average drag, as can be seen in Figures 6.7a, and 6.7b.

Considering the effect the drag crisis has had on the response, it has been shown that in comparison to the same reduced velocities presented in Figure 6.1 the amplitude response within lock-in is increased. It is the 2DOF $Re = 100000$ simulation which has shown that the drag crisis has the effect of producing greater cross-stream oscillation displacements than has been observed for the 1DOF simulations. Figure 6.10b in particular has shown that the drag crisis is in effect when the cylinder moves upstream. The consequent reduction in drag allows energy to enter into the system which ultimately leads to an increase in amplitude response.

It is the author's view that if the simulations carried out in this chapter were continued, further new observations regarding the drag crisis and aeroelastic response could be made. The data samples produced so far by these simulations are not long enough to be subject to the tests for stationarity presented in Chapter 4. Indeed, given the data observed thus far, it is not possible to tell if a stationary response can be achieved due to the presence of the drag crisis phenomenon. It would be interesting if future work could attempt to answer this question.

Chapter 7

General Conclusions

This final chapter concludes the thesis by discussing the achievements and important issues that have been highlighted by the work carried out.

The aim of Chapter 4 was to numerically simulate the drag crisis on a stationary cylinder. It was decided early on that LES would be the best candidate for this purpose. The onset of drag crisis was captured but it has been demonstrated that the choice of SGS model is important. The Smagorinsky SGS model expectedly failed to capture the drag crisis due to overprediction of eddy viscosity close to the cylinder surface. The overprediction occurred because the model constant had a fixed value for the entire domain. The alternative Dynamic model based on Germano and Lilly [41] overcomes this problem by using a model constant that is calculated locally at every timestep based on two filterings of the flow variables so that it varies in both space and time. The difference in results from each SGS model was clearly demonstrated.

The importance of blockage and the effect of free-stream turbulence was discussed. It was concluded that a correction for blockage and free-stream turbulence was necessary to obtain close agreement with experimental data [83]. This was done following recommendations set out by ESDU in [84] and [83].

The range of shedding frequencies, separation angles, drag coefficients, and base pressure coefficients from the simulations are consistent with figures given in the experimental literature associated with the onset of the “one-bubble” regime. To the author’s knowledge there is no other work presented in literature that includes the use of LES to capture the onset of the drag crisis and produce drag coefficients within the “cliff-face” as presented in Figures 4.19, 4.20, and 4.21.

This work could be further extended by running simulations with the Dynamic SGS model for higher Reynolds Numbers than have been achieved so far. This can extend the drag crisis beyond the “one-bubble” regime towards the “two-bubble regime”, where new observations can be made.

The work in Chapter 5 extended the capabilities of a commercial CFD solver to enable FSI simulation to be possible. A comparison of integration methods were examined. The

best performing integration method in terms of accuracy was not compatible with the Geometric Conservation Law, which meant extra iterations were necessary for every timestep to ensure energy balance was achieved. The overhead introduced by the extra iterations increased solver runtimes to the point that it was impractical. So an adapted method was employed that obeyed the GCL meaning no extra iterations were necessary. The adapted method achieves the best advantages in terms of speed and accuracy from all the methods investigated and was found to give satisfactory performance when tested.

There are further coupling methods in the literature which could be tested and evaluated to see if improvements can be made to improve solution time in particular. An example of this could be to implement the Block-Newton proposed by Matthies and Steindorf [46] that is summarised by the flow diagram in Figure 3.9.

A validation procedure was followed that demonstrated that the FSI implementation worked well. Even though the parameters of the test flow simulations were chosen to best produce a regular sinusoidal forcing function, the results showed some non-linear features.

The work presented in Chapter 6 made use of the developed FSI capability in Chapter 5 to run two sets of simulations. The main aim was to investigate the impact of the cable response on the drag crisis and vice-versa.

The first set of simulations involved a cylinder free to move in only in a cross-stream direction normal to its axis (1DOF). The mass, damping, and stiffness parameters were carefully chosen to match a similar numerical simulation carried out by Saltara et al. [66] using a two-dimensional DVM method. The simulations presented in this thesis were carried out on a solver that used the CVFEM with which three dimensional domains capable of capturing spanwise correlation effects are possible.

Both the simulations performed by Saltara et al. [66] and the equivalent simulations presented in this thesis failed to capture the “upper-branch” response reported in the experimental literature (e.g. Khalak and Williamson [38]). Further work to provide insight into this limitation could be done by performing simulations with spanwise lengths greater than those proposed by Norberg [59], and with refinements in grid resolution and time step size to see if a response in the “upper-branch” can be achieved.

The second set of simulations included freedom of the cylinder to move in the along-stream direction normal to its axis, in addition to the cross-stream direction 2DOF. The simulations were run for Reynolds numbers simulated in Chapter 4, include the drag crisis range. The mass, damping, and stiffness parameters were chosen to produce reduced velocities in the same range as the 1DOF simulations to allow comparisons to be made.

It was found that the amplitude response for the 2DOF simulations were different to the 1DOF simulations. Further 2DOF simulations would produce further insight into these differences and could define important features including the range of the lock-in region and the response when lock-in occurs.

The drag crisis contributes to the increased response by allowing more energy to go into the cable on the upstream stroke of the oscillations. In this motion the effective

Reynolds Number is increased by the greater velocity of flow at the cylinder surface, to the extent that it is within the drag crisis range and thus produces less drag than otherwise be possible.

In addition, it has been shown in Figure 6.10b that a reversal of drag can occur in both upstream and downstream movements of the oscillation, respectively due to the momentum of the fluid carried behind the cylinder, and the velocity of cylinder movement being greater than that of the flow.

This thesis has produced new insight into the role that the drag crisis plays in the movement of a sprung cylinder in cross-flow. It is the author's hope that this will be useful in fluid structure interaction modelling of cables used in civil engineering structures.

Bibliography

- [1] AIAA American Institute of Aeronautics and Astronautics. Guide for the verification and validation of computational fluid dynamics simulations, 1998. [cited at p. 27]
- [2] Md Mahbub Alam, H. Sakamoto, and M. Moriya. Reduction of fluid forces acting on a single circular cylinder and two circular cylinders by using tripping rods. *Journal of Fluids and Structures*, 18(3-4):347, 2003. [cited at p. 33]
- [3] O. H. Amman, T. Von Karman, and G. B. Woodruff. The failure of the Tacoma Narrows bridge - Report to the Federal Works Agency, 28 March 1941. [cited at p. 4]
- [4] ANSYS CFX 5.7.1. ANSYS CFX Tutorial 20: Fluid Structure Interaction and Mesh Deformation. [cited at p. 45]
- [5] ANSYS Inc. ANSYS CFX help documentation, 2005. [cited at p. 60, 103]
- [6] J. Anthoine. Blockage effect correction applied to drag coefficient measurements of circular cylinders in wind tunnels, May 26-27, 2003 2003. [cited at p. 33]
- [7] Peter Bearman and Maša Branković. Experimental studies of passive control of vortex-induced vibration. *European Journal of Mechanics - B/Fluids*, 23(1):9, 2004. [cited at p. 39]
- [8] H. M. Blackburn. Effect of blockage on spanwise correlation in a circular cylinder wake. *Experiments in Fluids*, 18(1 - 2):134, 1994. [cited at p. 33]
- [9] A. Bokaian and F. Geoola. Wake-induced galloping of two interfering circular cylinders. *Journal of Fluid Mechanics*, 146:383–415, 1984. [cited at p. 41]
- [10] M. Breuer. Large eddy simulation of the subcritical flow past a circular cylinder: numerical and modeling aspects. *International Journal for Numerical Methods in Fluids*, 28(9):1281–1302, 1998. [cited at p. 35]
- [11] Michael Breuer. A challenging test case for large eddy simulation: high reynolds number circular cylinder flow. *International Journal of Heat and Fluid Flow*, 21(5):648 – 654, 2000. Turbulence and Shear Flow Phenomena 1. [cited at p. 26]
- [12] J. Carberry, J. Sheridan, and D. Rockwell. Forces and wake modes of an oscillating cylinder. *Journal of Fluids and Structures*, 15(3-4):523, 2001. [cited at p. 38]
- [13] J. Carberry, J. Sheridan, and D. Rockwell. Controlled oscillations of a cylinder: forces and wake modes. *Journal of Fluid Mechanics*, 538:31, 2005. [cited at p. 38]

- [14] Pietro Catalano, Meng Wang, Gianluca Iaccarino, and Parviz Moin. Numerical simulation of the flow around a circular cylinder at high reynolds numbers. *International Journal of Heat and Fluid Flow*, 24(4):463, 2003. [cited at p. 6, 7, 34, 35]
- [15] M. Cervera, R. Codina, and M. Galindo. On the computational efficiency and implementation of block-iterative algorithms for nonlinear coupled problems. *Engineering Computations*, 13(6):4–30, 1996. [cited at p. 50, 51]
- [16] P. A. Davidson. *Turbulence: An Introduction for Scientists and Engineers*. Oxford University Press, 2004. [cited at p. 24]
- [17] Earl H. Dowell and Kenneth C. Hall. Modeling of fluid-structure interaction. *Annual Review of Fluid Mechanics*, 33(1):445–490, 2001. [cited at p. 45]
- [18] Constantinos Evangelinos and George Em Karniadakis. Dynamics and flow structures in the turbulent wake of rigid and flexible cylinders subject to vortex-induced vibrations. *Journal of Fluid Mechanics*, 400:91, 2000. [cited at p. 40]
- [19] C. Farhat and M. Lesoinne. Two efficient staggered algorithms for the serial and parallel solution of three-dimensional nonlinear transient aeroelastic problems. *Computer Methods in Applied Mechanics and Engineering*, 182(3-4):499, 2000. [cited at p. 47, 48, 49, 108, 111]
- [20] Miguel Ángel Fernández and Marwan Moubachir. A Newton method using exact jacobians for solving fluid-structure coupling. *Computers & Structures*, 83(2-3):127, 2005. [cited at p. 50]
- [21] Joel H. Ferziger and Milovan Peric. *Computational methods for fluid dynamics*. Berlin: Springer-Verlag, 1996. [cited at p. 9]
- [22] J. B. Frandsen. Numerical bridge deck studies using finite elements. part i: Flutter. *Journal of Fluids and Structures*, 19:171–191, 2003. [cited at p. 40]
- [23] J. Fröhlich, W. Rodi, Ph. Kessler, S. Parpais, J. P. Bertoglio, and D. Laurence. Large eddy simulation of flow around circular cylinders on structured and unstructured grids. *CNRS DFG collaborative research programme*, 66:319–338, 1998. [cited at p. 23]
- [24] R. D. Gabbai and H. Benaroya. An overview of modeling and experiments of vortex-induced vibration of circular cylinders. *Journal of Sound and Vibration*, 282(3-5):575, 2005. [cited at p. 39, 45, 46]
- [25] Massimo Germano, Ugo Piomelli, Parviz Moin, and William H. Cabot. A dynamic subgrid-scale eddy viscosity model. *Physics of Fluids A: Fluid Dynamics*, 3(7):1760, 1991. [cited at p. 25]
- [26] M. A. Green, C. W. Rowley, and G. Haller. Detection of lagrangian coherent structures in three-dimensional turbulence. *Journal of Fluid Mechanics*, 572:111–120, 2007. [cited at p. 144]
- [27] Cyril M. Harris and Allan G. Piersol. *Harris' Shock and Vibration Handbook*. McGraw-Hill, 2002. [cited at p. 103, 112, 114]
- [28] Ronald D. Henderson. Nonlinear dynamics and pattern formation in turbulent wake transition. *Journal of Fluid Mechanics*, 352:65–112, 1997. [cited at p. 132]

- [29] D. Scott Holloway, D. Keith Walters, and James H. Leylek. Prediction of unsteady, separated boundary layer over a blunt body for laminar, turbulent, and transitional flow. *International Journal for Numerical Methods in Fluids*, 45(12):1291–1315, 2004. [cited at p. 6, 7]
- [30] F. S. Hover, A. H. Techet, and M. S. Triantafyllou. Forces on oscillating uniform and tapered cylinders in cross flow. *Journal of Fluid Mechanics*, 363:97–114, 1998. [cited at p. 38]
- [31] Franz S. Hover, Joshua T. Davis, and Michael S. Triantafyllou. Three-dimensionality of mode transition in vortex-induced vibrations of a circular cylinder. *European Journal of Mechanics - B/Fluids*, 23(1):29, 2004. [cited at p. 38]
- [32] J. C. R. Hunt, A. A. Wray, and P. Moin. Eddies, streams, and convergence zones in turbulent flows. In *Studying Turbulence Using Numerical Simulation Databases, 2*, pages 193–208, December 1988. [cited at p. 144]
- [33] H. M. Irvine and T. K. Caughey. The linear theory of free vibrations of a suspended cable. *Proceedings of the Royal Society of London. Series A: Mathematical and Physical Sciences*, 341:299–315, 1974. [cited at p. 42, 43]
- [34] H. Max Irvine. *Cable Structures*. MIT Press, 1981. [cited at p. 42, 43, 44]
- [35] Irwin. Wind-induced cable oscillations, online company literature (RWDI Technotes 10) <http://www.rwdi.com/cms/publications/28/t10.pdf> accessed 6th July 2005. [cited at p. 42, 47]
- [36] A. Kareem and C. M. Cheng. Pressure and force fluctuations on isolated roughened circular cylinders of finite height in boundary layer flows. *Journal of Fluids and Structures*, 13(7-8):907, 1999. [cited at p. 33]
- [37] K.A. Kemenov and S. Menon. Explicit small-scale velocity simulation for high-re turbulent flows. *Journal of Computational Physics*, 220(1):290 – 311, 2006. [cited at p. 35]
- [38] A. Khalak and C. H. K. Williamson. Dynamics of a hydroelastic cylinder with very low mass and damping. *Journal of Fluids and Structures*, 10(5):455, 1996. [cited at p. 7, 130, 153]
- [39] E. Konstantinidis, S. Balabani, and M. Yianneskis. The effect of flow perturbations on the near wake characteristics of a circular cylinder. *Journal of Fluids and Structures*, 18(3-4):367–386, 2003. [cited at p. 33]
- [40] Kai Fan Liaw. *Simulation of Flow Around Bluff Bodies and Bridge Deck Sections Using CFD*. PhD thesis, University of Nottingham, 2005. [cited at p. 4, 5, 27]
- [41] D. K. Lilly. A proposed modification of the Germano subgrid-scale closure method. *Physics of Fluids A: Fluid Dynamics*, 4(3):633, 1992. [cited at p. 59, 71, 152]
- [42] X. Ma, G. S. Karamanos, and G. E. Karniadakis. Dynamics and low-dimensionality of a turbulent near wake. *Journal of Fluid Mechanics*, 410:29, 2000. [cited at p. 34]
- [43] John H.G. Macdonald and Guy L. Larose. Two-degree-of-freedom inclined cable galloping—part 1: General formulation and solution for perfectly tuned system. *Journal of Wind Engineering and Industrial Aerodynamics*, 96(3):291 – 307, 2008. [cited at p. 41]

- [44] John H.G. Macdonald and Guy L. Larose. Two-degree-of-freedom inclined cable galloping—part 2: Analysis and prevention for arbitrary frequency ratio. *Journal of Wind Engineering and Industrial Aerodynamics*, 96(3):308 – 326, 2008. [cited at p. 41]
- [45] E. C. Maskell. A theory on the blockage effects on bluff bodies and stalled wings in a closed wind tunnel. *Reports and Memoranda*, 3400, 1965. [cited at p. 33]
- [46] Hermann G. Matthies and Jan Steindorf. Partitioned but strongly coupled iteration schemes for nonlinear fluid-structure interaction. *Computers & Structures*, 80(27-30):1991, 2002. [cited at p. 50, 51, 153]
- [47] Julio Romano Meneghini, Fabio Saltara, Rodrigo de Andrade Fregonesi, Cássio Takeshi Yamamoto, Enrique Casaprima, and José Alfredo Ferrari Jr. Numerical simulations of VIV on long flexible cylinders immersed in complex flow fields. *European Journal of Mechanics - B/Fluids*, 23(1):51, 2004. [cited at p. 45]
- [48] F. Menter and Y. Egorov. A scale adaptive simulation model using two-equation models. In *43rd AIAA Aerospace Sciences Meeting and Exhibit*, volume 2005-1095, Reno, Nevada., 2005. AIAA. [cited at p. 22]
- [49] F. R. Menter. Two-equation eddy-viscosity turbulence models for engineering applications. *AIAA Journal*, 32(8):1598–1605, 1994. [cited at p. 21]
- [50] F. R. Menter, R. B. Langtry, S. R. Likki, Y. B. Suzen, P. G. Huang, and S. Volker. A correlation-based transition model using local variables—part i: Model formulation. *Journal of Turbomachinery*, 128(3):413, 2006. [cited at p. 22]
- [51] F.R. Menter, M. Kuntz, and R. Bender. A scale-adaptive simulation model using two-equation models. *AIAA Paper*, 2003:0767, 2003. [cited at p. 22, 27]
- [52] Christiane Montavon, Ian Jones, Dick ten Bosch, Stefan Szepessy, Roland Henriksson, Hans Moberg, Roberto Tregnago, Zoubida El Hachemi, Massimiliano Piccirillo, Michel Tournour, Sylvie Dequand, Frederic Tremblay, and Rainer Friedrich. ALESSIA: EP 28189 Application of large eddy simulation to the solution of industrial problems: validation report. Technical report, AEA Technology, 2002. [cited at p. 12]
- [53] G. Morgenthal and A. McRobie. A comparative study of numerical methods for fluid structure interaction analysis in long-span bridge design. *Wind And Structures*, 5(2-4):101–114, 2002. [cited at p. 45]
- [54] Young Munson and Okiishi. *Fundamentals of Fluid Mechanics*. John Wiley & Sons, 1998. [cited at p. 30]
- [55] A. Nakayama and S. N. Vengadesan. On the influence of numerical schemes and subgrid-stress models on large eddy simulation of turbulent flow past a square cylinder. *International Journal for Numerical Methods in Fluids*, 38(3):227–253, 2002. [cited at p. 34]
- [56] D. Newman and G. E. Karniadakis. Simulations of flow over a flexible cable: A comparison of forced and flow-induced vibration. *Journal of Fluids and Structures*, 10(5):439–453, 1996. [cited at p. 5, 40]
- [57] David J. Newman and George Em Karniadakis. A direct numerical simulation study of flow past a freely vibrating cable. *Journal of Fluid Mechanics*, 344:95, 1997. [cited at p. 5, 40, 47]

- [58] F. Nicoud and F. Ducros. Subgrid-scale stress modelling based on the square of the velocity gradient tensor. *Flow, Turbulence and Combustion*, 62(3):183, 1999. [cited at p. 26, 73]
- [59] C. Norberg. Fluctuating lift on a circular cylinder: review and new measurements. *Journal of Fluids and Structures*, 17:57–96, 2003. [cited at p. 7, 34, 36, 61, 130, 153]
- [60] National Institute of Standards and U.S. Department of Commerce Technology, Technology Administration. *NIST Special Publication 800-22 Revision 1: A Statistical Test Suite for Random and Pseudorandom Number Generators for Cryptographic Applications*. [cited at p. 68, 69, 70]
- [61] Atsushi Okajima, Akira Nakamura, Takashi Kosugi, Hidenori Uchida, and Ryouji Tamaki. Flow-induced in-line oscillation of a circular cylinder. *European Journal of Mechanics - B/Fluids*, 23(1):115, 2004. [cited at p. 35]
- [62] Philippa O'Neill, David Nicolaides, Damon Honnery, and Julio Soria. Autocorrelation functions and the determination of integral length with reference to experimental and numerical data. 2004. [cited at p. 82]
- [63] A. Relvas and A. Suleman. Fluid-structure interaction modelling of nonlinear aeroelastic structures using the finite element corotational theory. *Journal of Fluids and Structures*, 22(1):59, 2006. [cited at p. 50]
- [64] A. Richter and E. Naudascher. Fluctuating forces on a rigid circular cylinder in confined flow. *Journal of Fluid Mechanics*, 78:561–576, 1976. [cited at p. 32, 33, 35, 62, 63, 64, 65, 66]
- [65] I. Robertson, S. J. Sherwin, and P. W. Bearman. Flutter instability prediction techniques for bridge deck sections. *International Journal for Numerical Methods in Fluids*, 43:1239–1256, 2003. [cited at p. 40]
- [66] Fábio Saltara, Julio Romano Meneghini, and Rodrigo de Andrade Fregonesi. Numerical simulation of flow around elastically mounted cylinder. *International Journal of Offshore and Polar Engineering*, 13(2), 2003. [cited at p. 7, 45, 127, 128, 153, 211]
- [67] T. Sarpkaya. A critical review of the intrinsic nature of vortex-induced vibrations. *Journal of Fluids and Structures*, 19(4):389, 2004. [cited at p. 39]
- [68] Robert H. Scanlan. Developments in low speed aeroelasticity in the civil engineering field. *AIAA Journal*, 20:839–844, 1981. [cited at p. 35, 39]
- [69] G. Schewe. On the force fluctuations acting on a circular cylinder in crossflow from subcritical up to transcritical reynolds numbers. *Journal of Fluid Mechanics*, 133:265, 1983. [cited at p. 34, 94]
- [70] Christian Seidel and Dieter Dinkler. Mode switching of rain-wind induced vibrations. In *Mechanics of 21st century - ICTAM04 proceedings*, 15-21 August 2004. [cited at p. 42]
- [71] R. Panneer Selvam. Finite element modelling of flow around a circular cylinder using LES. *Journal of Wind Engineering and Industrial Aerodynamics*, 67-68:129, 1997. [cited at p. 34, 35]
- [72] W. C. L. Shih, C. Wang, D. Coles, and A. Roshko. Experiments on flow past rough circular cylinders at large reynolds numbers. *Journal of Wind Engineering and Industrial Aerodynamics*, 49(1-3):351, 1993. [cited at p. 33]

- [73] Emil Simiu and Robert H. Scanlan. *Wind Effects on Structures: Fundamentals and Applications to Design*. John Wiley & Sons, Inc., third edition edition, 1996. [cited at p. 39, 40, 41]
- [74] M. Souli, A. Ouahsine, and L. Lewin. ALE formulation for fluid-structure interaction problems. *Computer Methods in Applied Mechanics and Engineering*, 190(5-7):659, 2000. [cited at p. 46]
- [75] D. Sumner and O. O. Akosile. On uniform planar shear flow around a circular cylinder at subcritical reynolds number. *Journal of Fluids and Structures*, 18(3-4):441–454, 2003. [cited at p. 33]
- [76] D. K. Sun, J. S. Owen, N. G. Wright, and K. Liaw. Fluid-structure interaction of prismatic line-like structures using LES and block-iterative coupling. In *BBAA V*, 2004. [cited at p. 5, 51]
- [77] D. K. Sun, J. S. Owen, N. G. Wright, and K. Liaw. Vortex induced vibrations of Kessock Bridge using CFD. In *WES 2004*, 2004. [cited at p. 46]
- [78] J. Sung and J. Y. Yoo. Near-wake vortex motions behind a circular cylinder at low reynolds number. *Journal of Fluids and Structures*, 17(2):261, 2003. [cited at p. 32]
- [79] Tetsuro Tamura, Ichiro Ohta, and Kunio Kuwahara. On the reliability of two-dimensional simulation for unsteady flows around a cylinder-type structure. *Journal of Wind Engineering and Industrial Aerodynamics*, 35:275 – 298, 1990. [cited at p. 34]
- [80] I. J. Taylor and M. Vezza. Application of a discrete vortex method for the analysis of suspension bridge deck sections. *Journal of Wind and Structures*, 4(4):333–352, 2001. [cited at p. 45]
- [81] H. Tennekes and J. L. Lumley. *A First Course in Turbulence*. MIT Press, 1972. [cited at p. 18]
- [82] Andrei Travin, Michael Shur, Michael Strelets, and Philippe Spalart. Detached eddy simulations past a circular cylinder. *Flow, Turbulence and Combustion*, 63:293–313, 1999. [cited at p. 27]
- [83] Engineering Sciences Data Unit. 80025 mean forces, pressures and flow field velocities for circular cylindrical structures: Single cylinder with two-dimensional flow, June 1986. Originally issued October 1980. [cited at p. 34, 74, 75, 76, 82, 84, 85, 152, 211, 213]
- [84] Engineering Sciences Data Unit. 80024 blockage corrections for bluff bodies in confined flows, March 1998. Originally issued November 1980. [cited at p. 61, 152]
- [85] J. K. Vandiver. Dimensionless parameters important to the prediction of vortex-induced vibration of long, flexible cylinders in ocean currents. *Journal of Fluids and Structures*, 7(5):423, 1993. [cited at p. 38, 40]
- [86] J. K. Vandiver, D. Allen, and L. Li. The occurrence of lock-in under highly sheared conditions. *Journal of Fluids and Structures*, 10(5):555, 1996. [cited at p. 39, 40]
- [87] H.K. Versteeg and W. Malalasekera. *An introduction to Computational Fluid Dynamics: The Finite Volume Method*. Pearson Prentice Hall, 1st edition, 1995. [cited at p. 9, 10, 19, 20]
- [88] David C. Wilcox. *Turbulence modeling for CFD*. DCW Industries Inc, 1993. [cited at p. 20]

- [89] C H K Williamson. Vortex dynamics in the cylinder wake. *Annual Review of Fluid Mechanics*, 28(1):477–539, 1996. [cited at p. 89, 211]
- [90] C.H.K. Williamson and R. Govardhan. A brief review of recent results in vortex-induced vibrations. *Journal of Wind Engineering and Industrial Aerodynamics*, 96(6-7):713 – 735, 2008. 5th International Colloquium on Bluff Body Aerodynamics and Applications. [cited at p. 39]
- [91] C. T. Yamamoto, J. R. Meneghini, F. Saltara, R. A. Fregonesi, and Jr J. A. Ferrari. Numerical simulations of vortex-induced vibration on flexible cylinders. *Journal of Fluids and Structures*, 19(4):467, 2004. [cited at p. 45]
- [92] M.M. Zdravkovich. *Flow Around Circular Cylinders*, volume 1. Oxford Science Publications, 1997. [cited at p. 6, 7, 29, 46, 59, 71, 78, 86, 87, 90, 94, 209, 211]

Appendices

Appendix A

User Routine Overview

This appendix discusses in detail the user defined routines mentioned in Chapter 5.

A.1 Junction Box setupdata

This is the first routine invoked during the solver process. It is a junction box routine executed at the "User Input" position shown in Figure 5.1. This is the recommended position to use for setting up user-defined variables in an especially reserved area of the data structure, named `/USER_DATA`. The reason for this is to ensure that the user does not need to make special provision for whether a run is carried out on one processor (serial) or multiple processors (parallel) when writing code for setting up user-defined variables. In the case of parallel runs, code executed from the "User Input" position is carried out solely on the master process. Furthermore, after code from the "User Input" position is executed, the entire contents of the `/USER_DATA` section in the data structure of the master process is copied to the data structure of all slave processes. The following numbered list describes the tasks carried out by the routine, in order of execution:

1. Look-up and store internal data structure boundary names for the cylinder. The data structure operates in a mock hierarchical directory format. Boundary names defined in the problem definition ANSYS CFX Command Language (CCL) have an equivalent name in used by the solver in data structure path names. At these locations in the data structure, useful data including tangential and normal forces experienced by the cylinder boundary will be stored.
2. Look-up and store the current accumulated time step number (referred to as `ATSTEP` in the data structure), and the final accumulated time step number for the current run. This information is useful for the next task.
3. Create a two-dimensional array in `/USER_DATA` for storing data from the user-defined routines as the run progresses. Every column of the array is relevant to a data variable. Every row of the array is relevant to a time step in the current run.

4. Create an integer variable in `/USER_DATA` for storing the number of columns in the aforementioned array. This is useful for data access purposes.
5. Look-up and store the values of user-defined variables given in the `'USER:'` part of the problem definition CCL. These can be found in an especially reserved area of the data structure called `/USER`.

The values included are:

- Mass of cylinder
- Damping constant of cylinder
- Stiffness constant of cylinder
- The timestep from which the cylinder is 'freed'.

The latter variable in the above list can be used to keep a cylinder stationary in the initial stages of a simulation. This enables a flow field to develop fully without the possibility of cylinder movement adding an element of instability to the problem.

If the run is a continuation from a previous simulation, the following values should also be included:

- Force from previous time step exerted on the cylinder in the along-stream and cross-stream directions.
- Velocity from previous time step of the cylinder in the along-stream and cross-stream directions.
- Displacement from previous time step of the cylinder in the along-stream and cross-stream directions.

These values are necessary for the extrapolation routine that generates similar data for the current time step to operate correctly. For intermediate time steps in a run, it is easy access to such values. For the first and last time step in a run, however, special provisions have to be made for the lack of ability to store user-defined data as part of a ANSYS CFX results data file. Thus at the end of each run there is user code that generates a file called `"initF.ccl"` containing CCL that is intended to overwrite the original `USER:` part of a problem definition file. To enable this, the inclusion of `" ccl initF.ccl"` in the command invoking subsequent runs is required.

A.2 Junction Box `setdata`

This is the next junction box routine executed in the solver process. It is a junction box routine executed at the "End of Time Step" position shown in Figure 5.1. Alternatively this routine can be placed at the "End of Coefficient Loop" position if the displacement of the mesh is set to be updated for each sub-iteration in a time step. This can be done

with an “expert parameter” called “meshdisp each coefiter” set to “t”. By default this option is set to false.

For parallel runs the main part of the source code of *setdata* is set to be executed by the master node/process only. There is also code to ensure that the latest calculated values of displacement and velocity are sent to the data structure of the slave processes. The slave distribution code will always be executed after the main part of the source code on the master/node process has been executed, thus ensuring the latest calculated data is used.

The following numbered list describes the tasks carried out by the routine, in order of execution:

1. Look-up and store time step related data, including
 - Current accumulated time step
 - Time step size
 - Accumulated time
2. As long as the accumulated time step is greater than the limit specified in the **USER:** part of the problem definition **CCL**, retrieve forces, velocities and displacements from the previous time step and extrapolate the forces, accelerations, velocities and displacements for the current time step.
3. Store the latest calculated forces, accelerations, velocities and displacements for the current time step in the output array in **/USER_DATA**.

A.3 Subroutine hybrid

This is the integration routine called by the *setdata* routine to calculate latest forces, accelerations, velocities, and displacements. It is a separate routine to *setdata* for ease of maintenance. More detail on the integration method is given in Chapter 5.

A.4 CEL functions getdata

getdisp_x, *getdisp_y*, *getvel_x*, and *getvel_y* functions are all CEL functions. These functions are referenced in other parts of the **CCL** to define the mesh and boundary motion. Since the flow is unconfined the mesh can be moved as a whole with the cylinder displacement. This is preferable to moving individual vertices of the mesh by differing amounts because this incurs more computational effort and significantly increases solution times. Thus to keep the direction of flow correct relative to the moving boundaries an additional component of “*getdisp* + *getvel* × *time step size*/2” is included in each degree of freedom.

The four CEL functions execute the *getdata* routine which returns the appropriate value of velocity or displacement existing in the memory of the user code at the time.

A.5 Junction Box `writedata`

This is the final junction box routine to discuss. It is invoked at the “User Output” position shown in Figure 5.1.

The “User Output” position is the recommended position to write out data at the end of a run. For parallel runs it is executed on the master node/process only.

The following numbered list describes the tasks carried out by the routine, in order of execution:

1. Write the contents of the output array stored in `/USER_DATA` to a text file called “`coupler_output.csv`”.
2. Write the latest values of force, velocity, and displacement to an external CCL file called “`initF.CCL`”. The intention is to read in “`initF.CCL`” in a subsequent run to ensure continuity in user-defined calculations in subsequent runs.

Appendix B

Additional figures from 2DOF simulations

This appendix contains many reproduced graphs from Chapter 6 to show their development through time. Each graph is split into a number of timeframes. Each frame shows the trace of the current timeframe in red. The trace for all timeframes prior to the current one are shown in black. The trace for all timeframes after the current one are shown in grey.

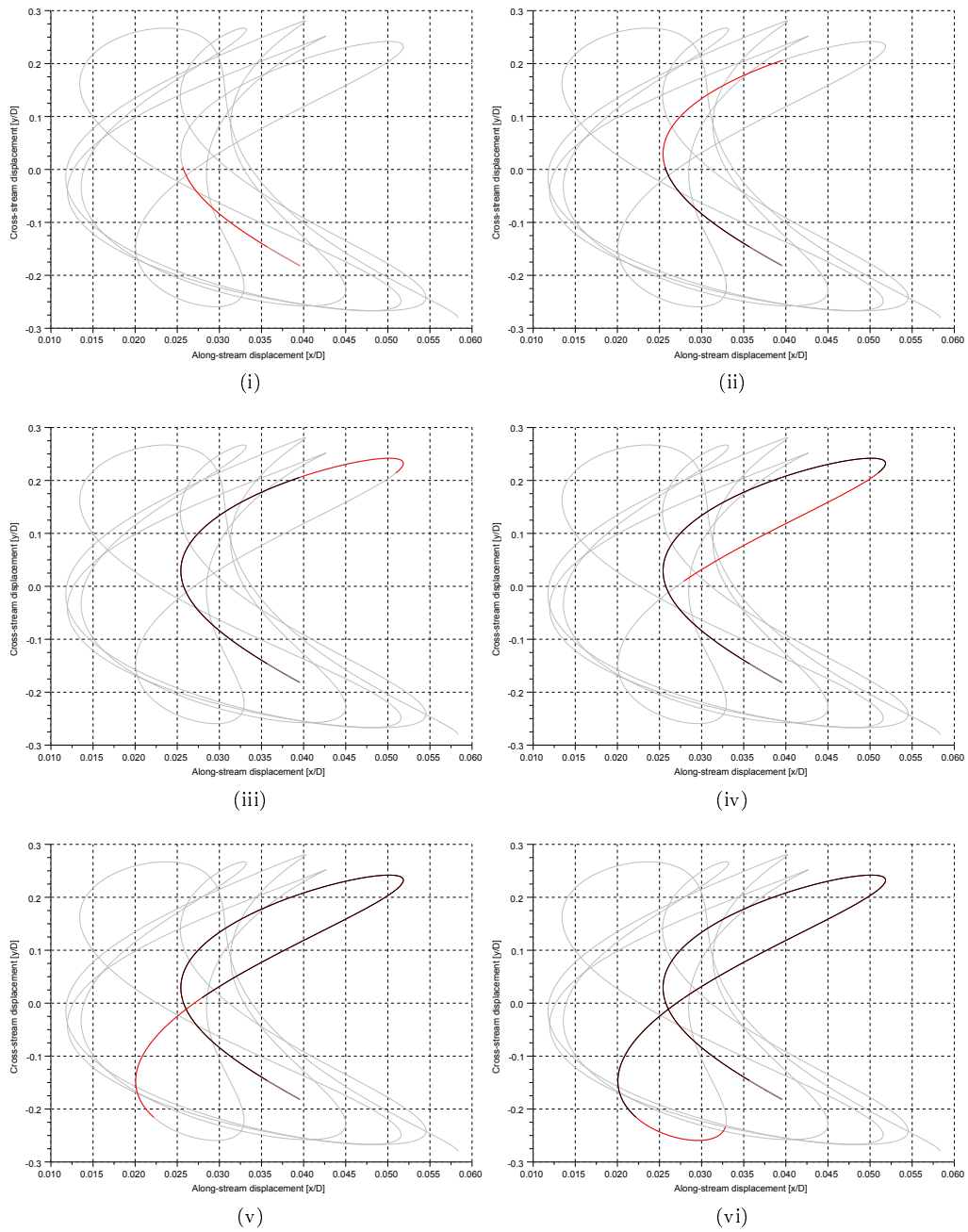
B.1 [Re=90000] simulations

Figure B.1: Development of along-stream and cross-stream displacements over time

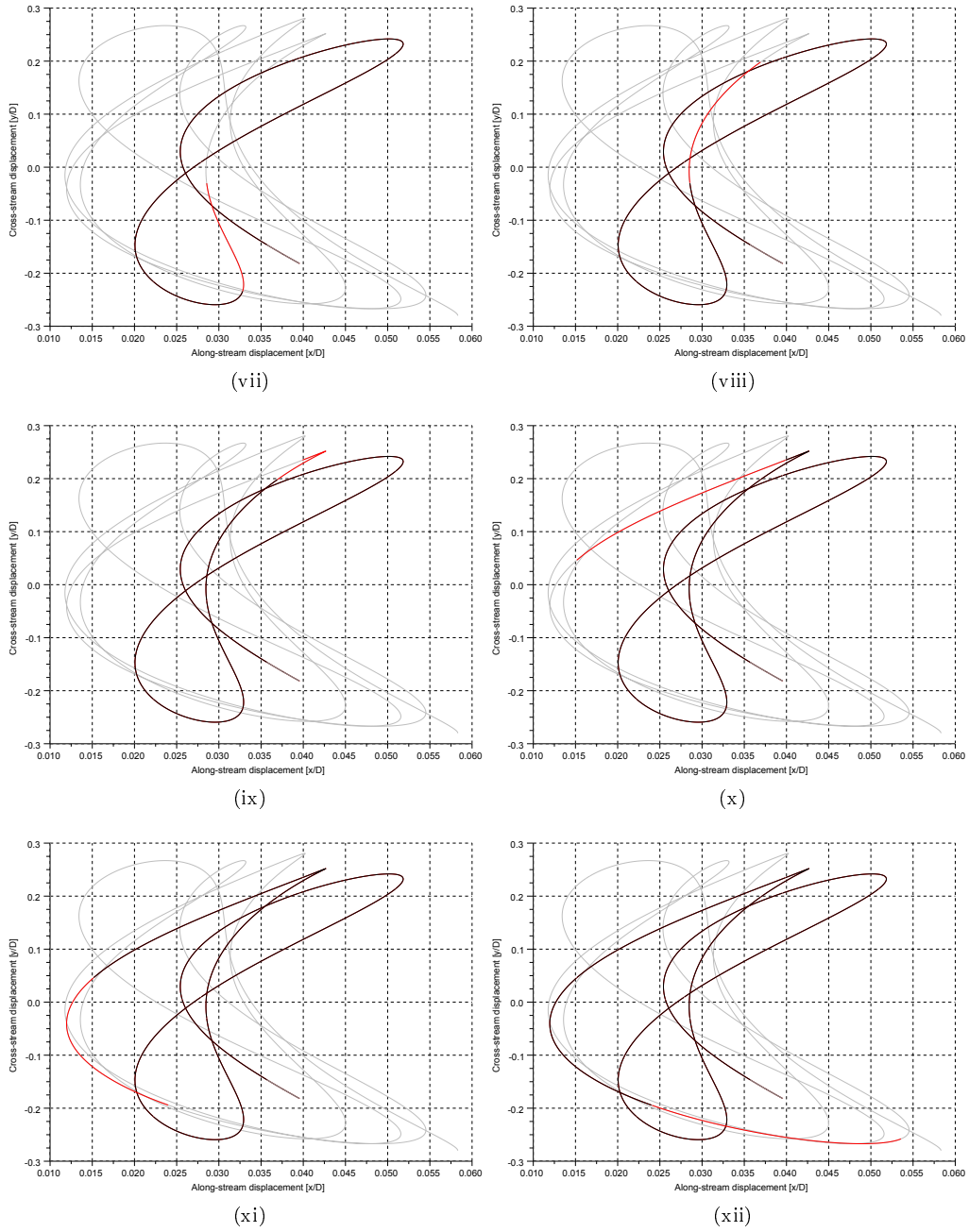


Figure B.1: Development of along-stream and cross-stream displacements over time (cont.)

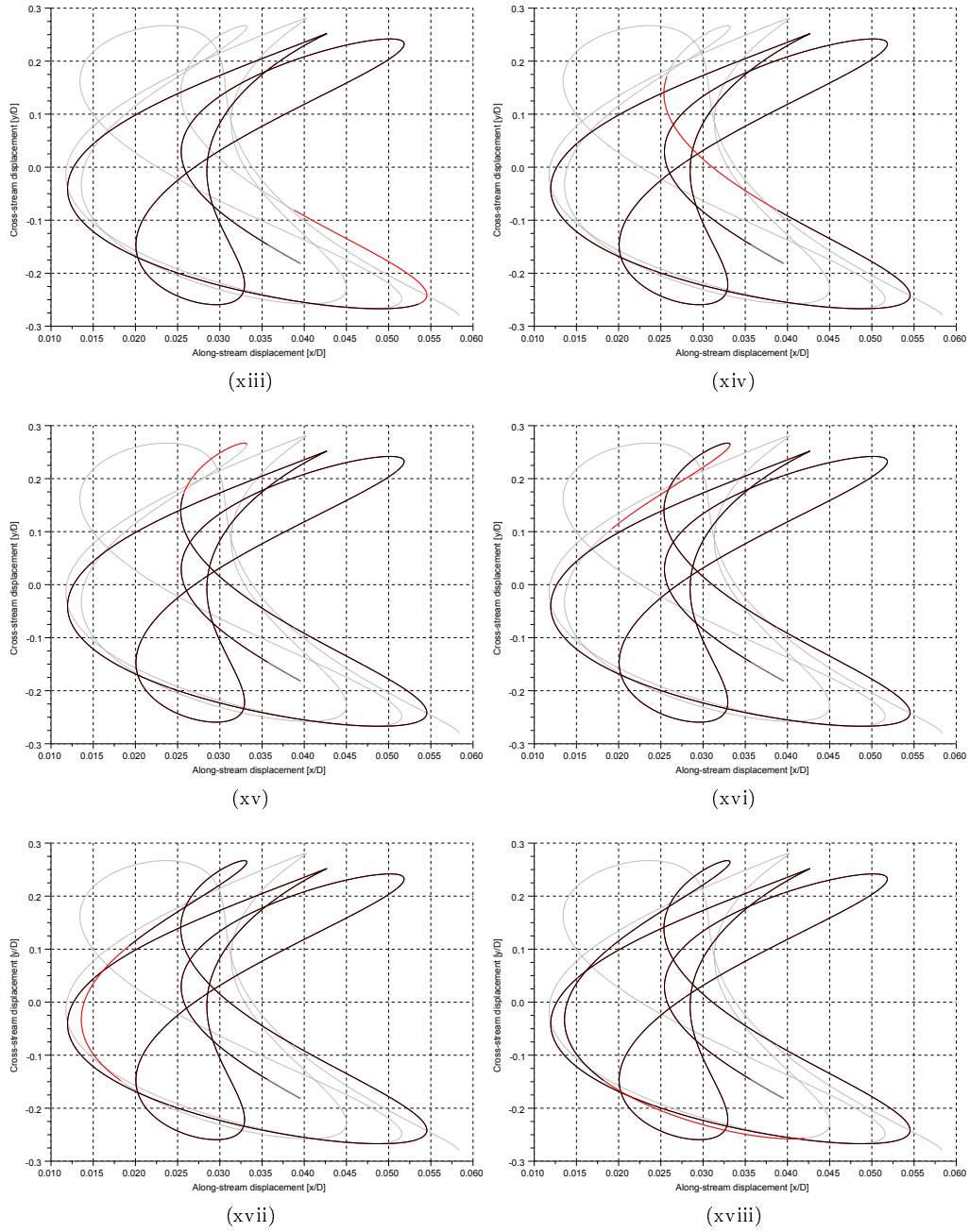


Figure B.1: Development of along-stream and cross-stream displacements over time (cont.)

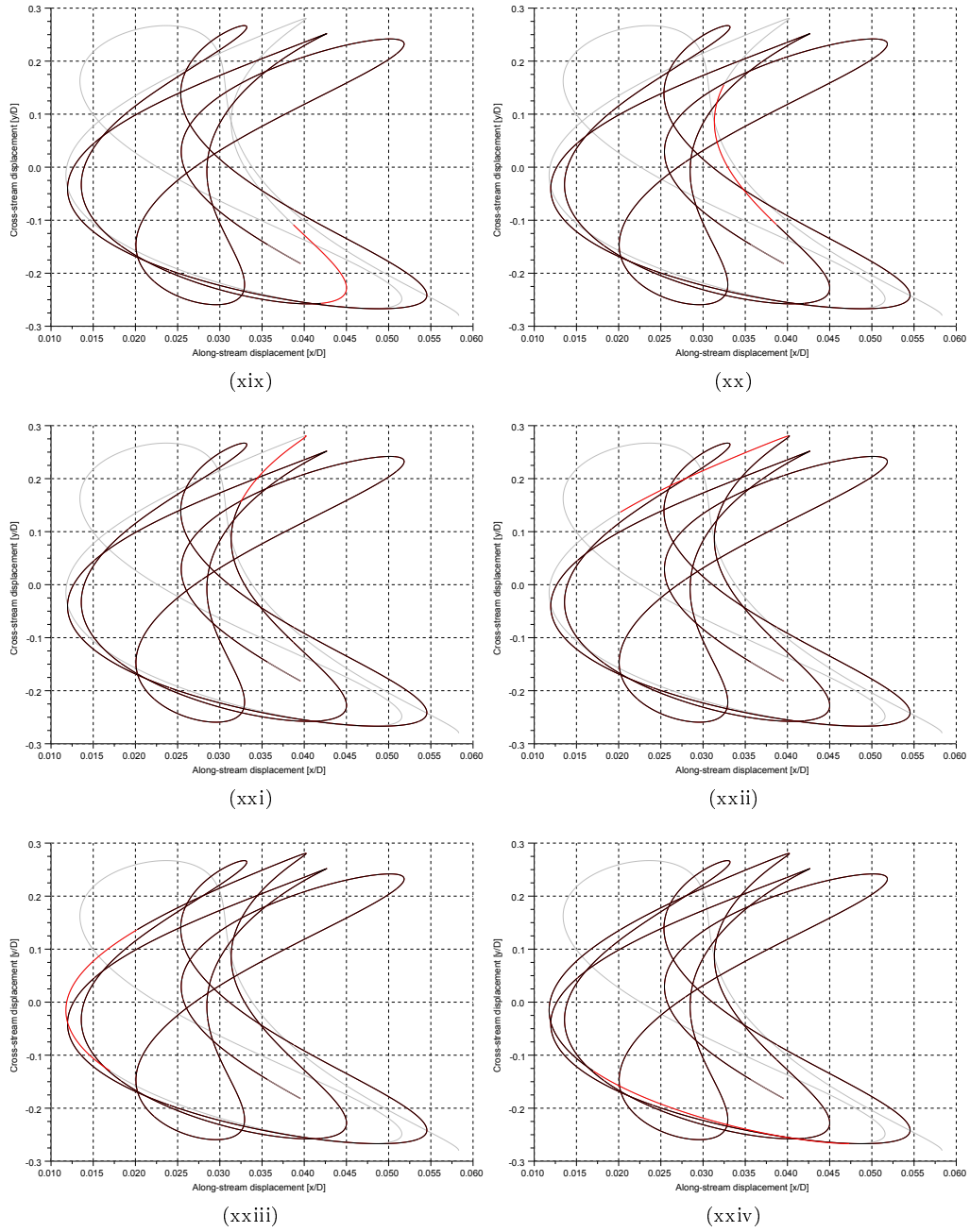


Figure B.1: Development of along-stream and cross-stream displacements over time (cont.)

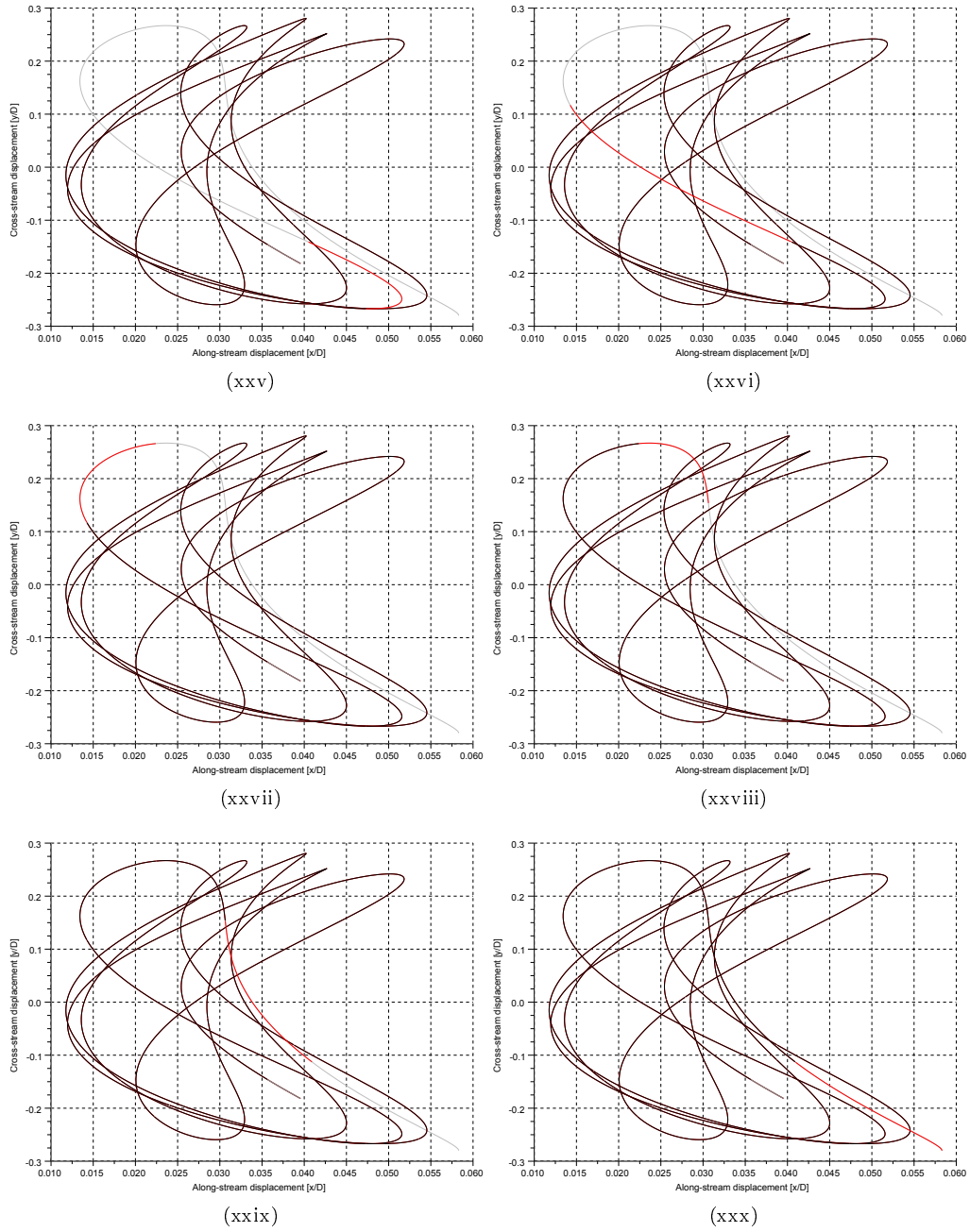


Figure B.1: Development of along-stream and cross-stream displacements over time (cont.)

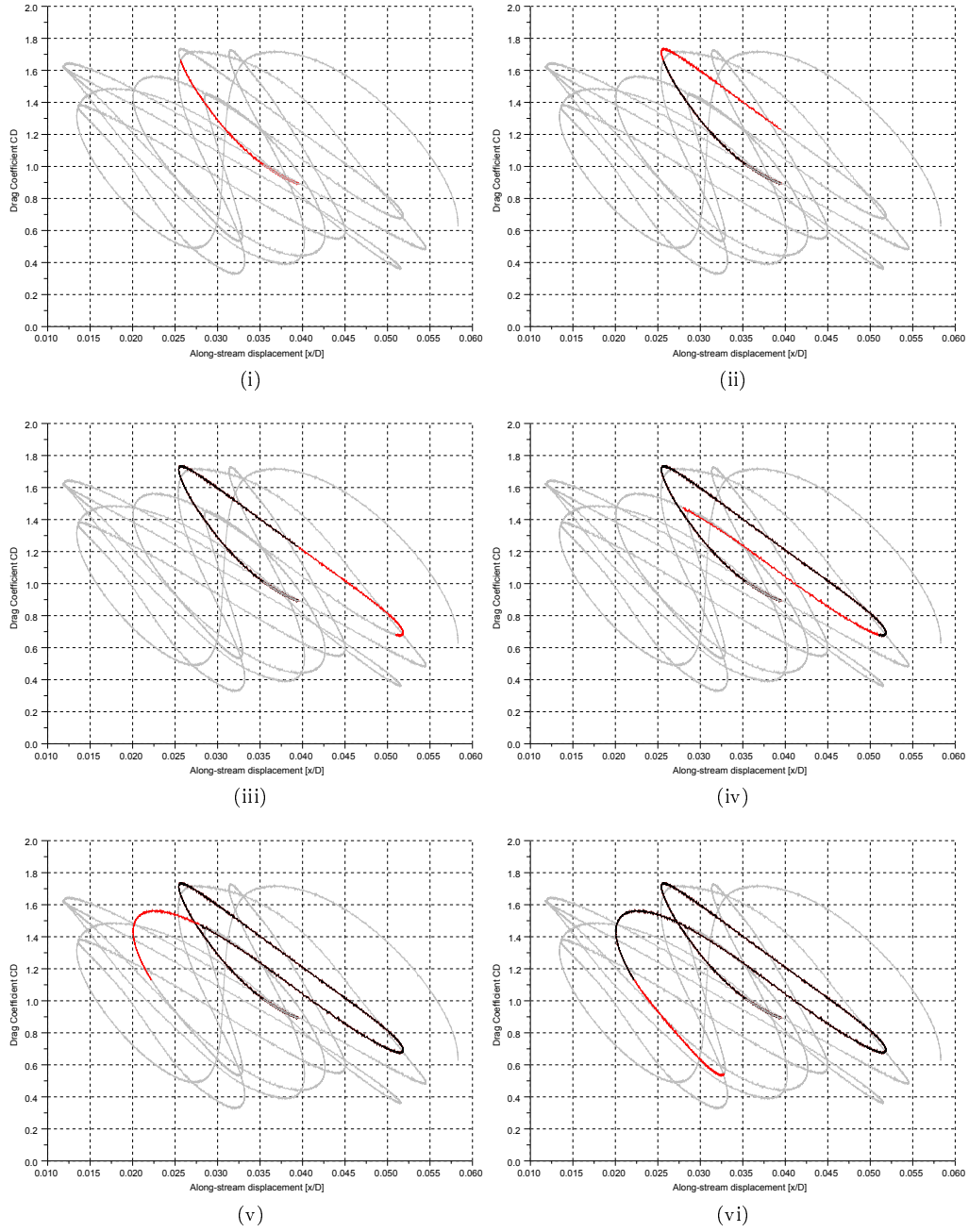


Figure B.2: Development of along-stream displacement and drag over time

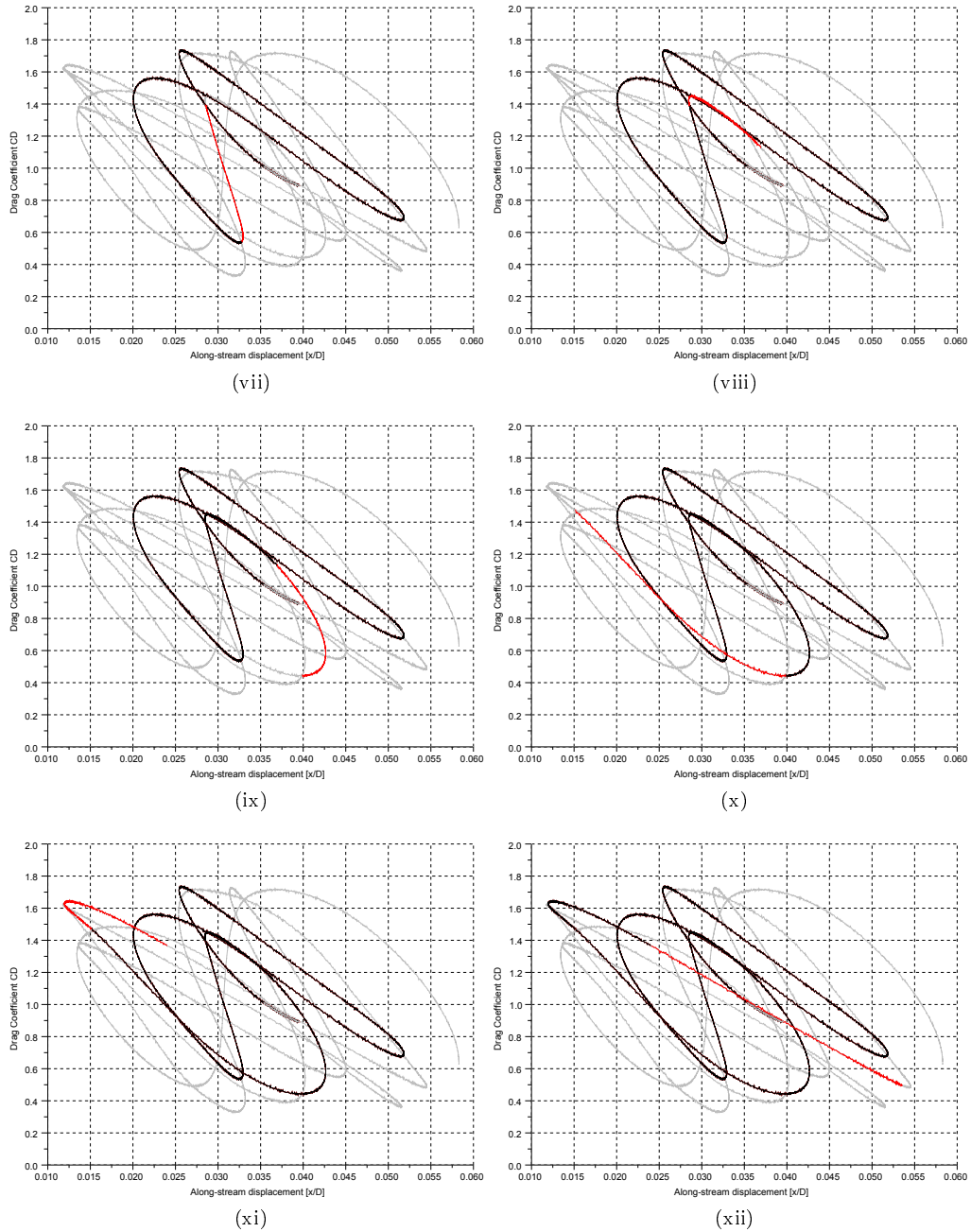


Figure B.2: Development of along-stream displacement and drag over time (cont.)

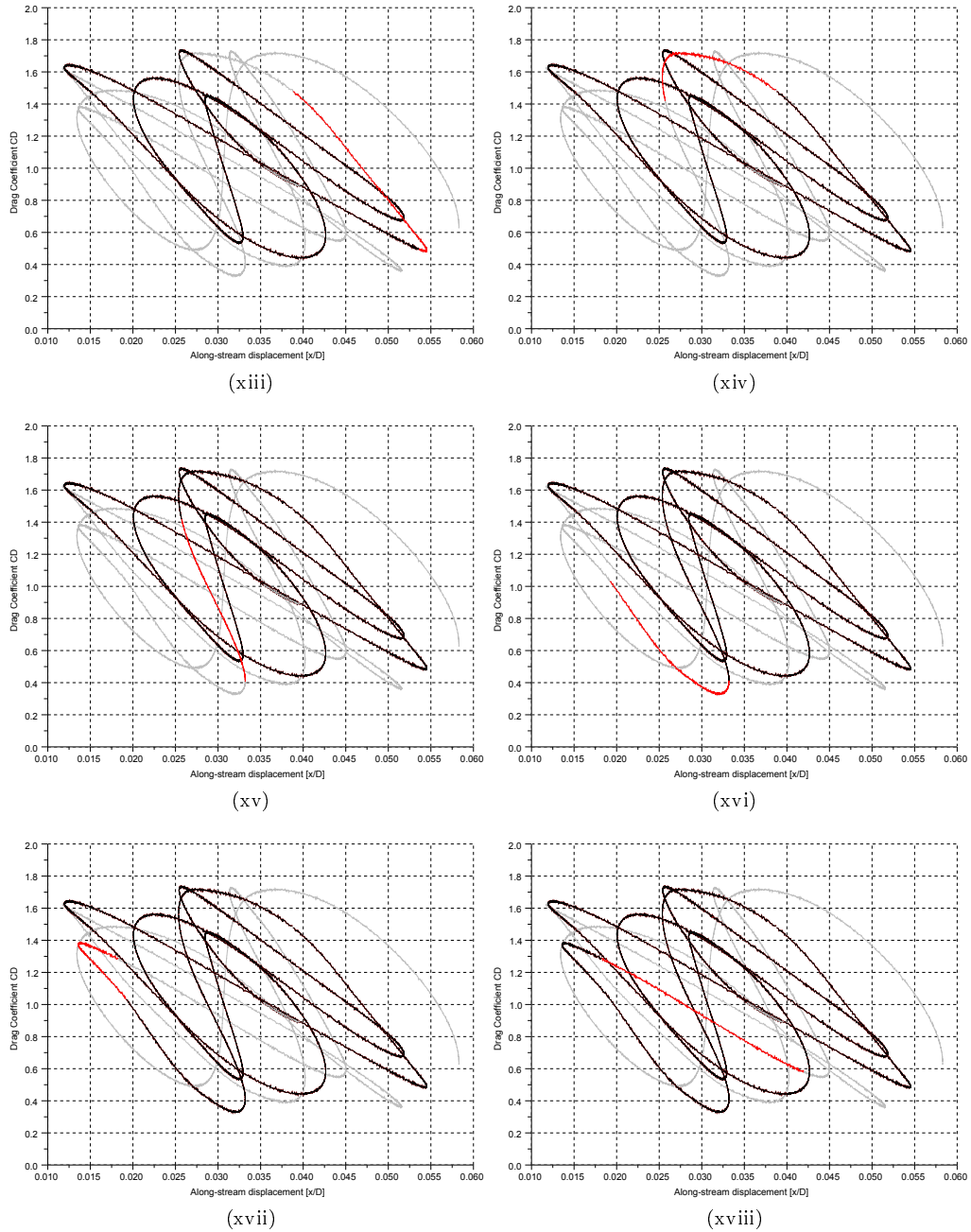


Figure B.2: Development of along-stream displacement and drag over time (cont.)

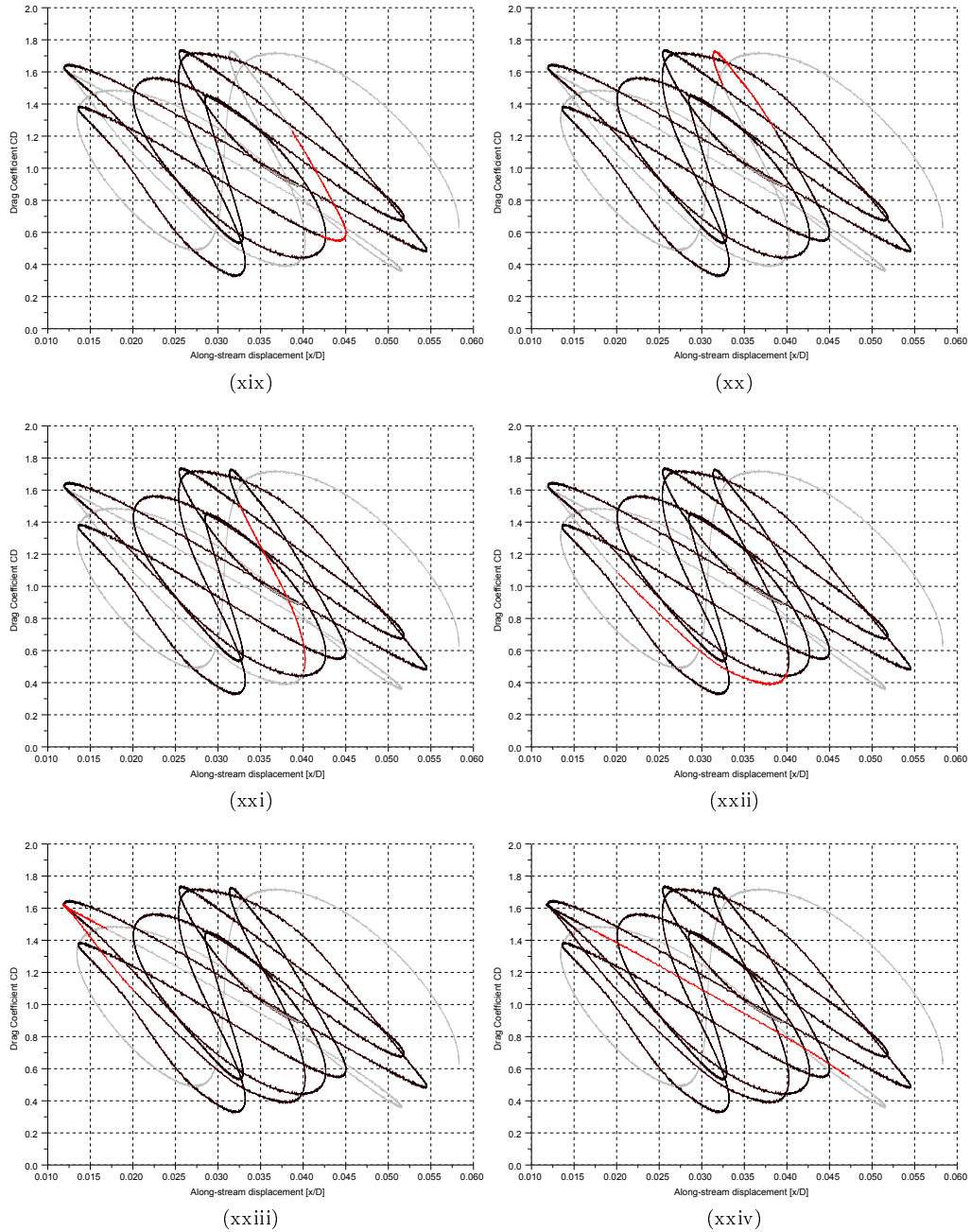


Figure B.2: Development of along-stream displacement and drag over time (cont.)

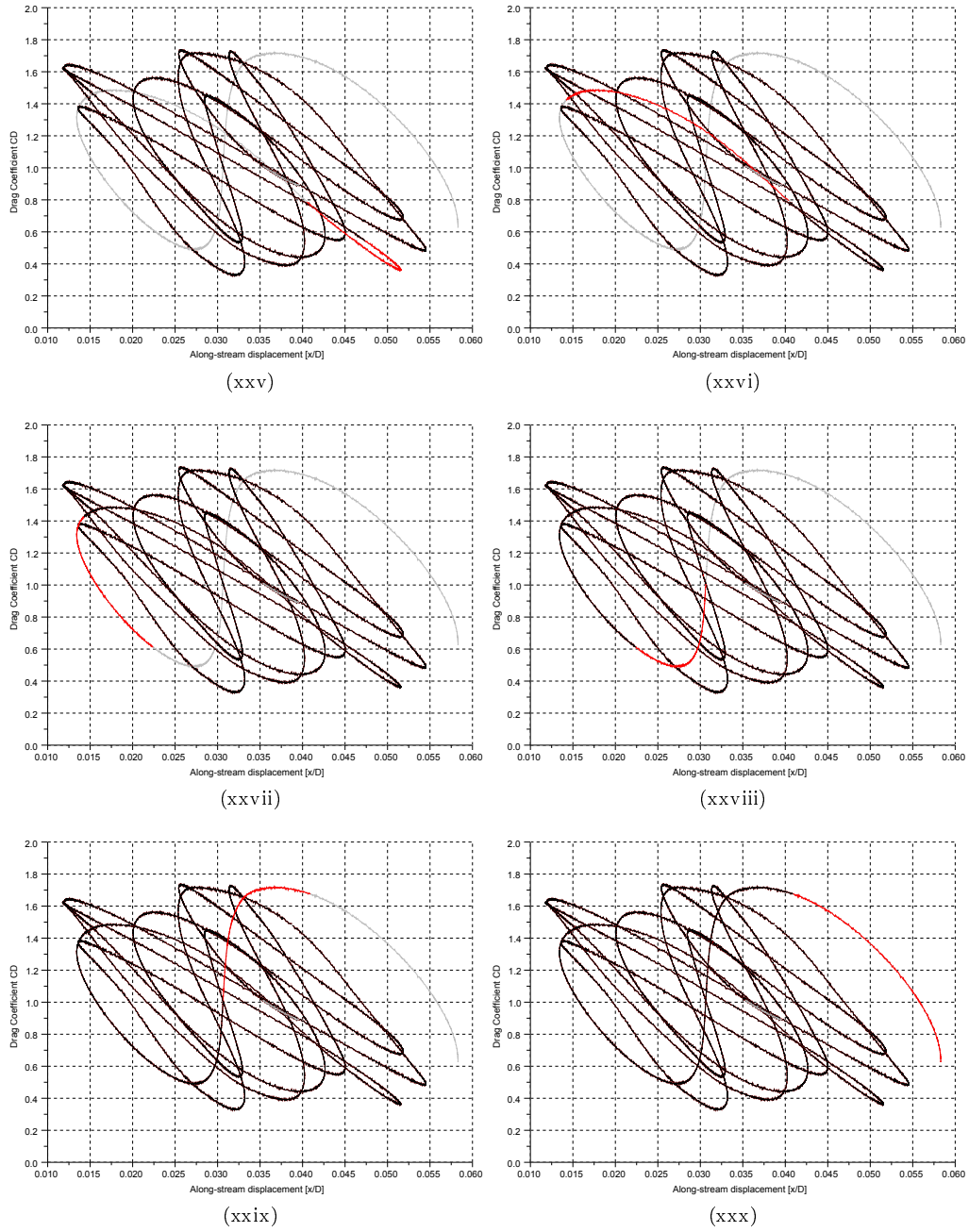


Figure B.2: Development of along-stream displacement and drag over time (cont.)

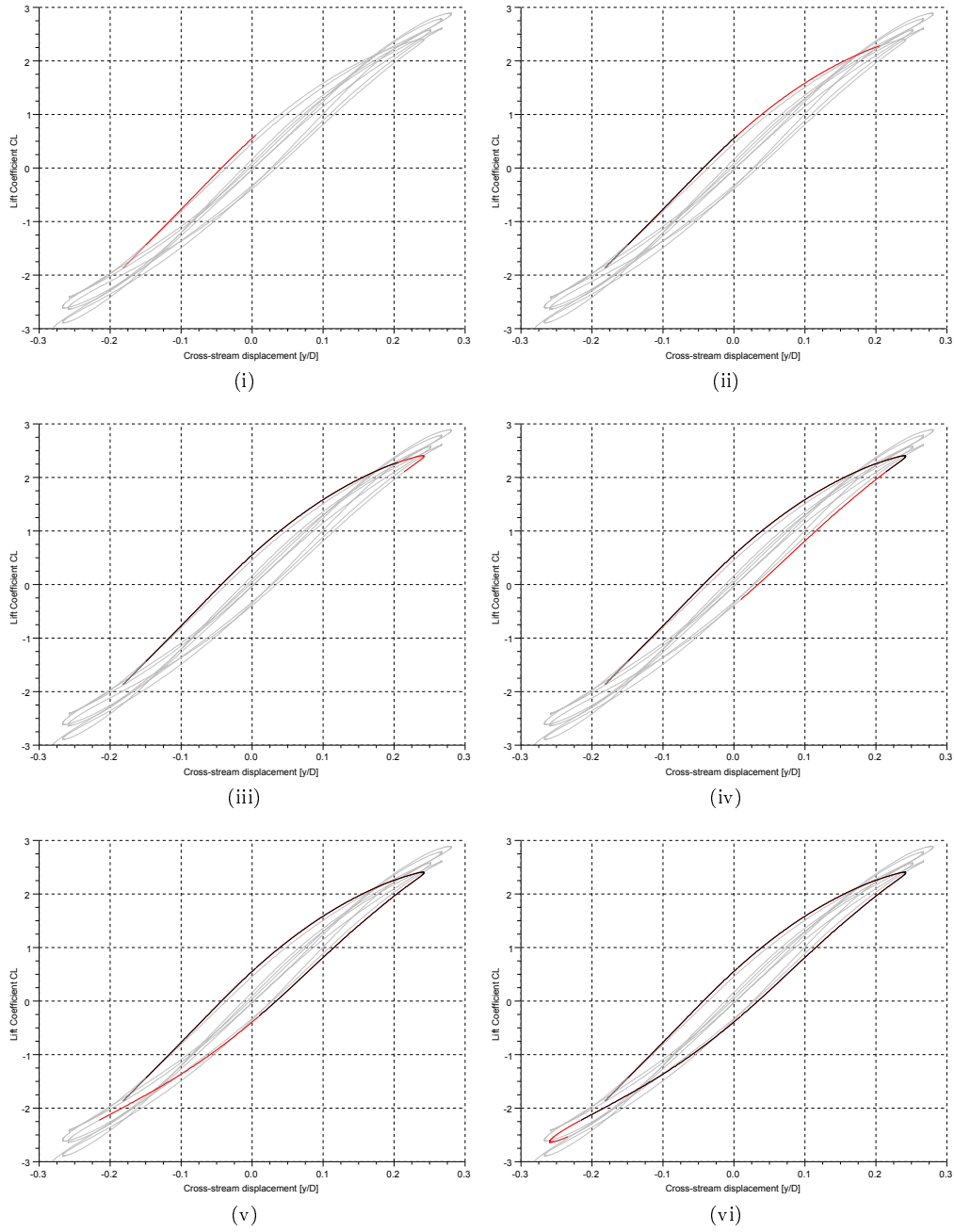


Figure B.3: Development of cross-stream displacement and lift over time

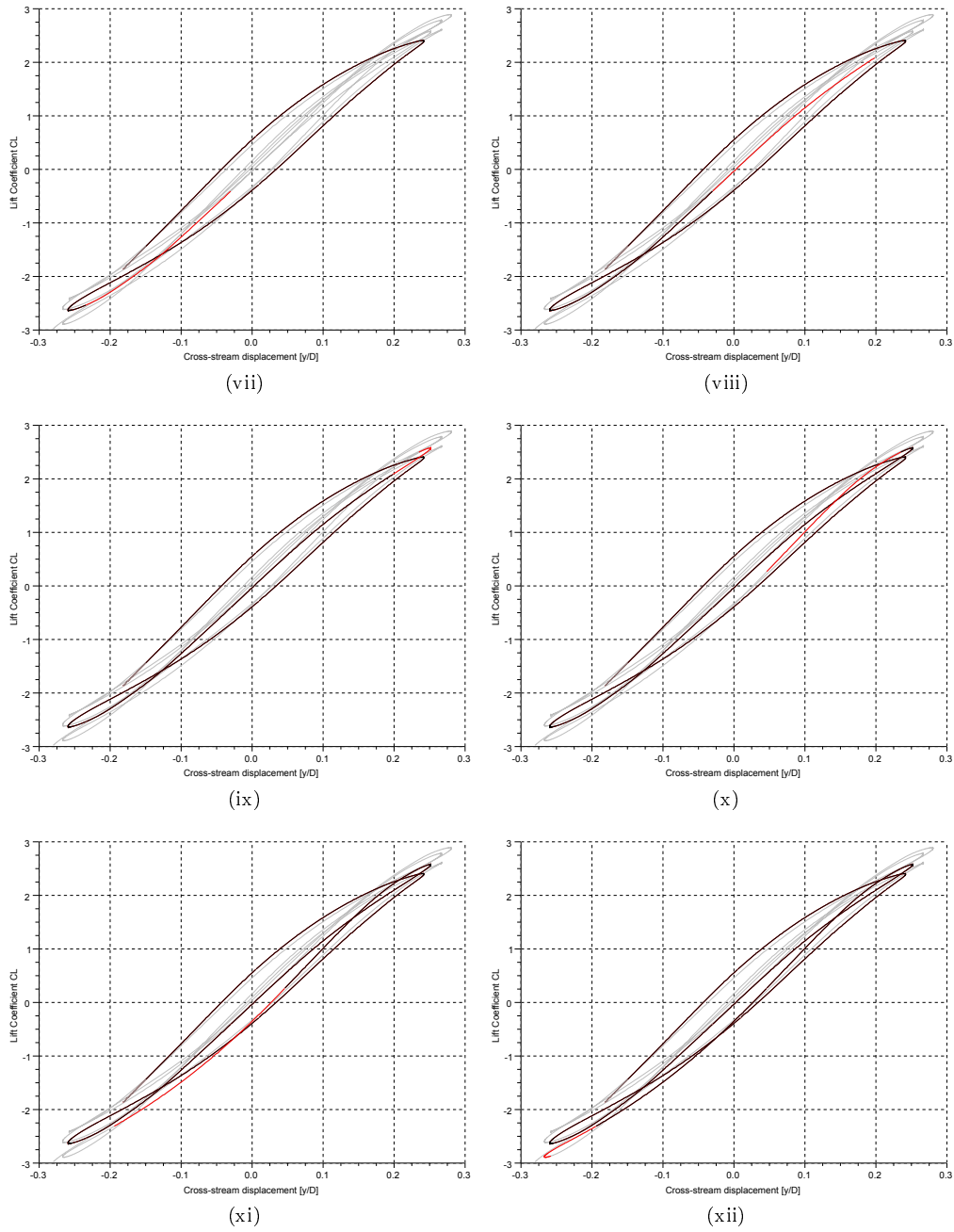


Figure B.3: Development of cross-stream displacement and lift over time (cont.)

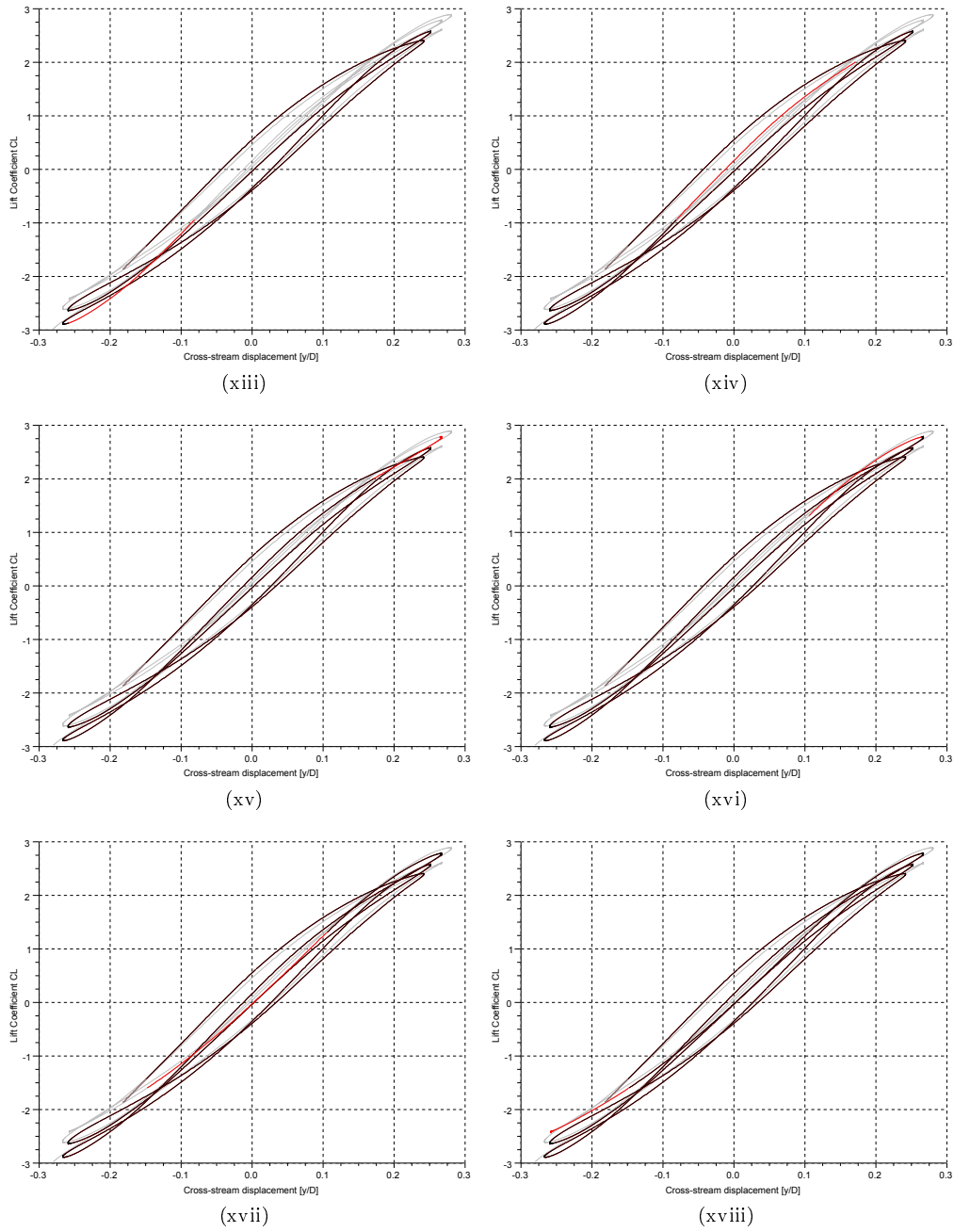


Figure B.3: Development of cross-stream displacement and lift over time (cont.)

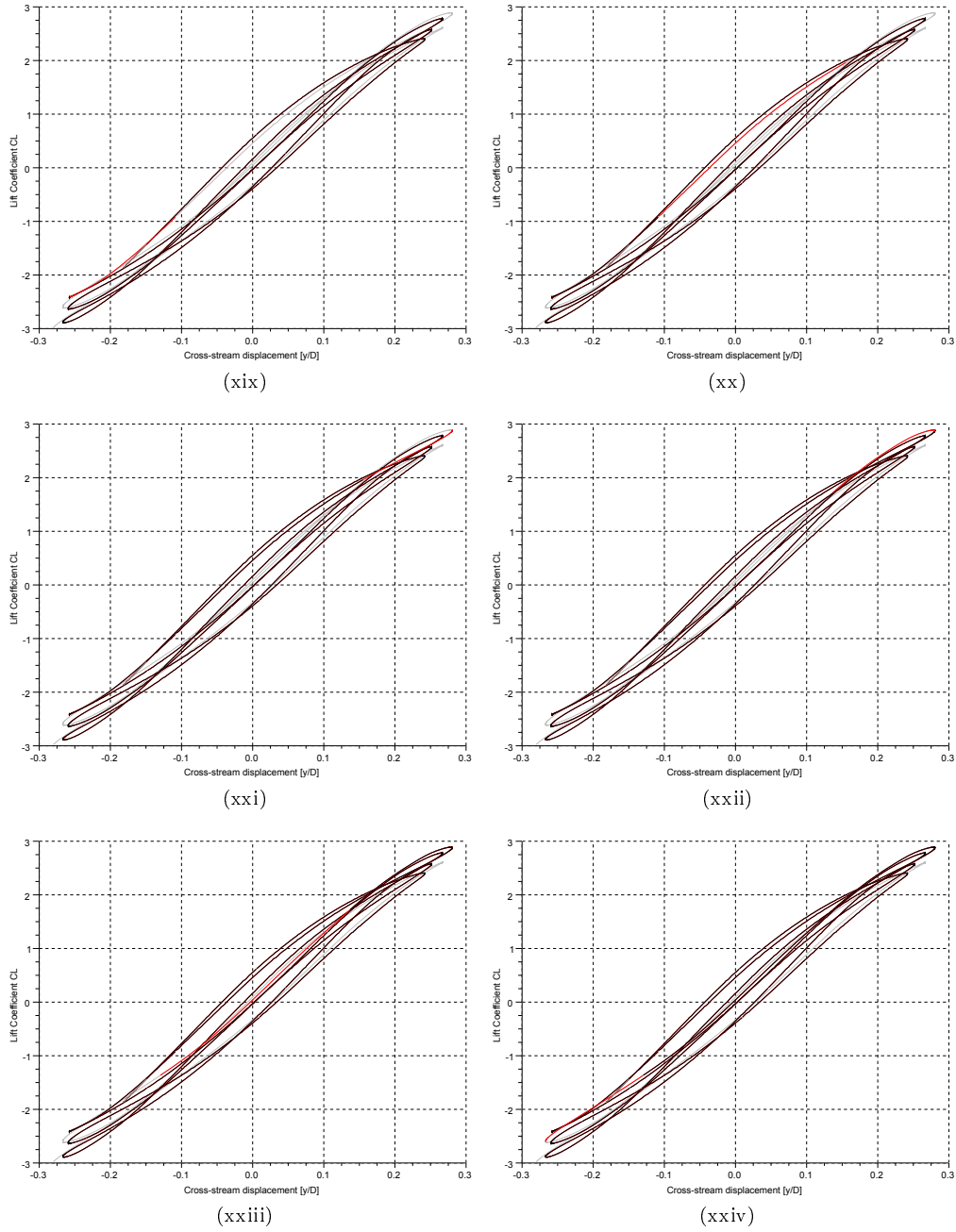


Figure B.3: Development of cross-stream displacement and lift over time (cont.)

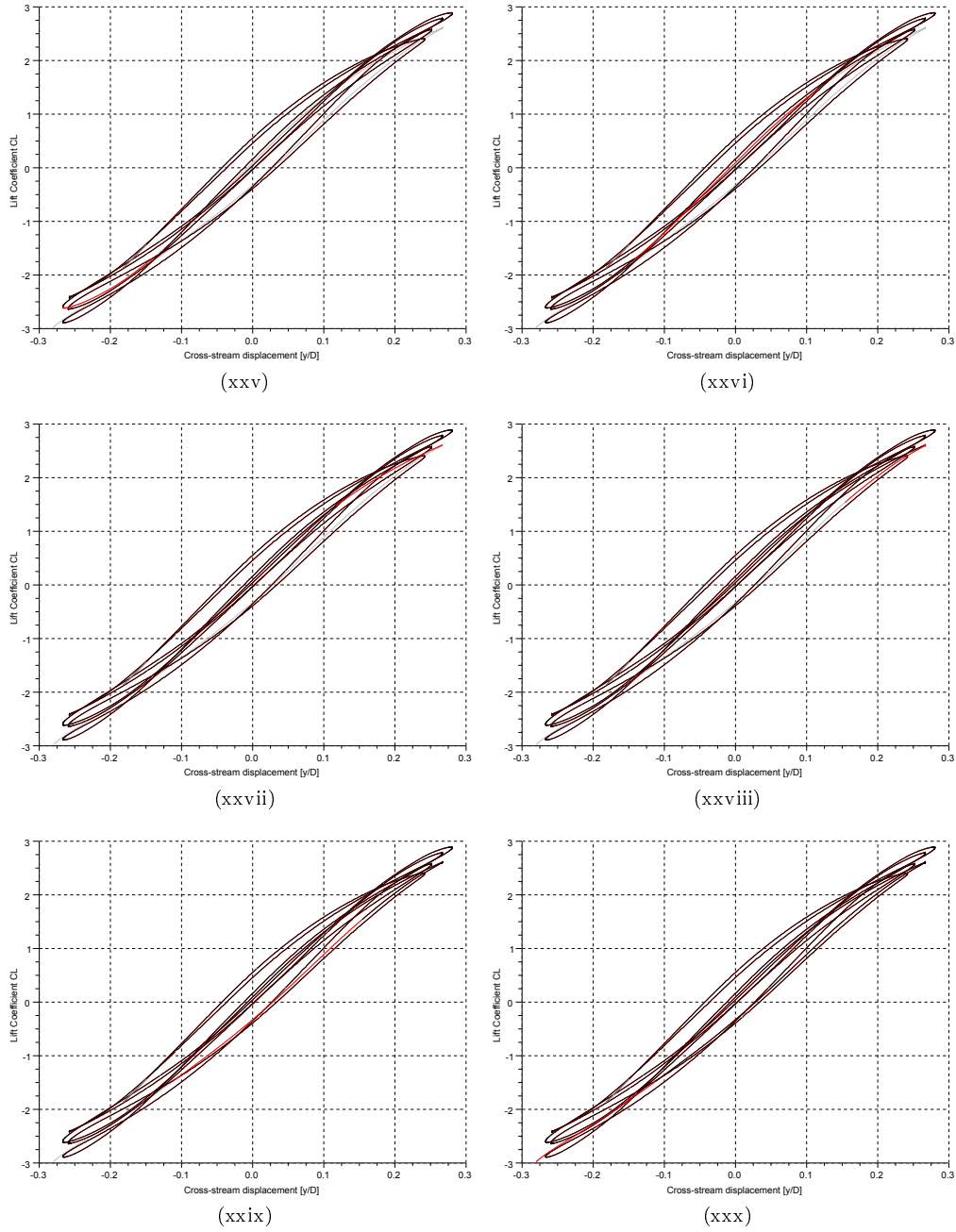


Figure B.3: Development of cross-stream displacement and lift over time (cont.)

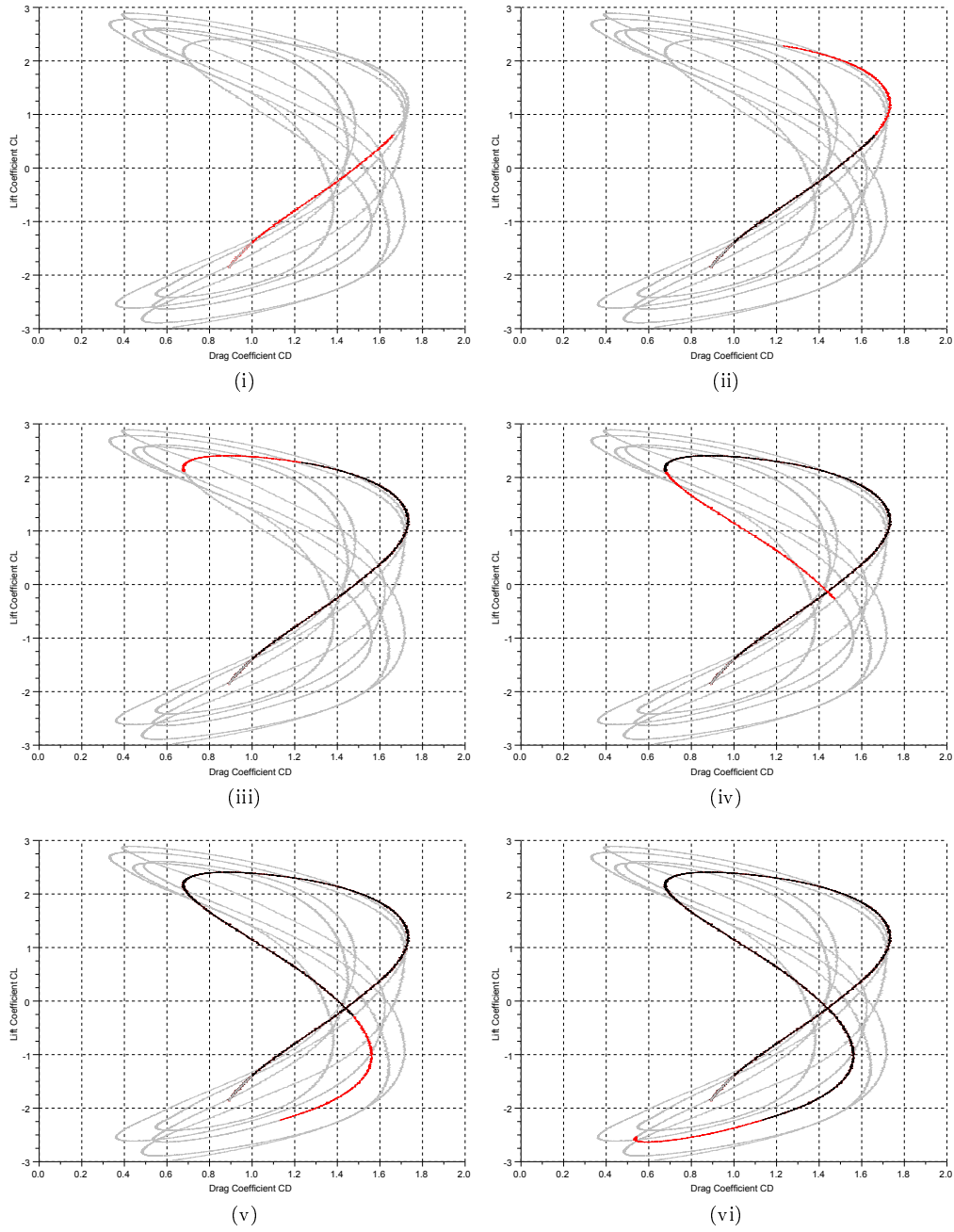


Figure B.4: Development of drag and lift over time

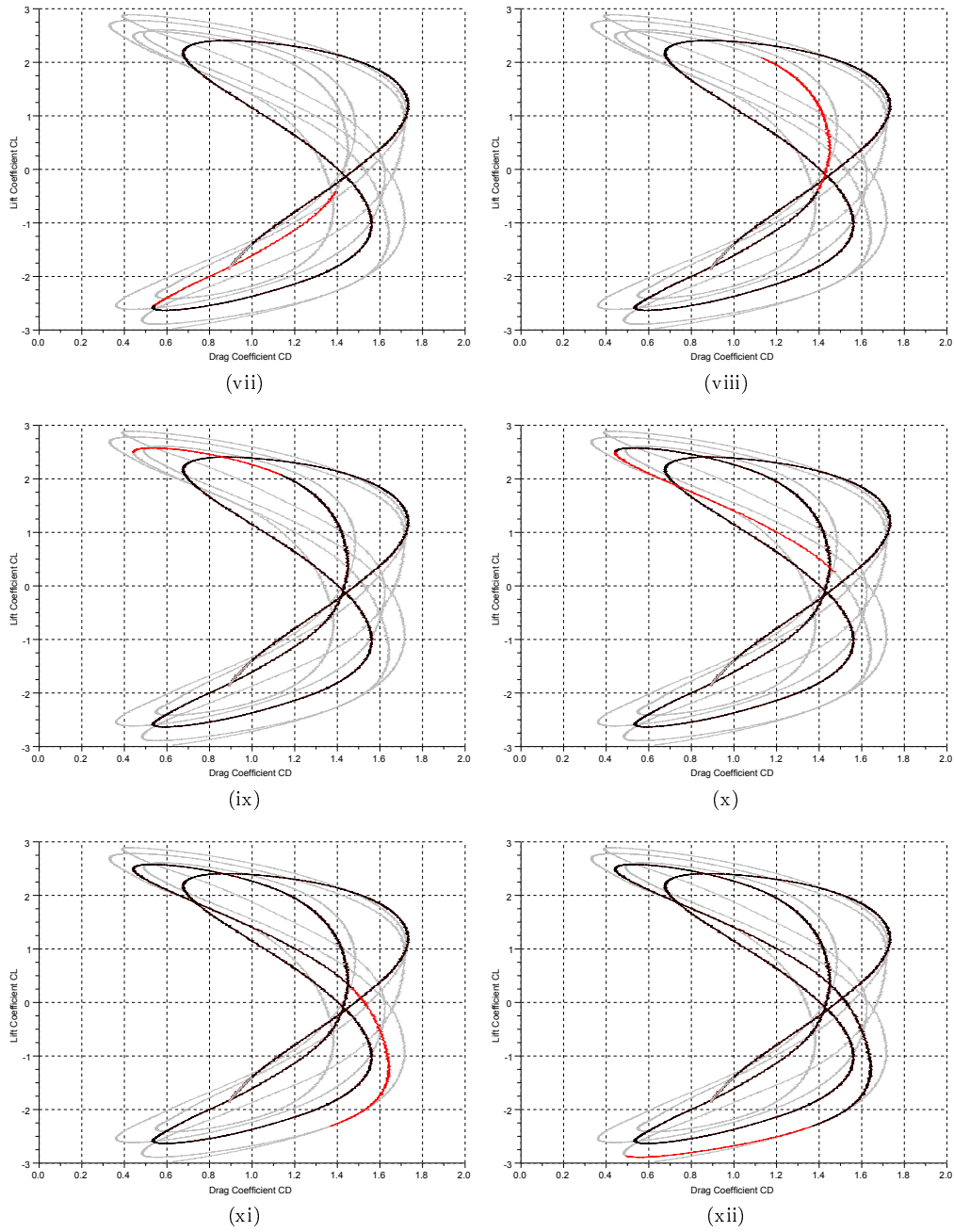


Figure B.4: Development of drag and lift over time (cont.)

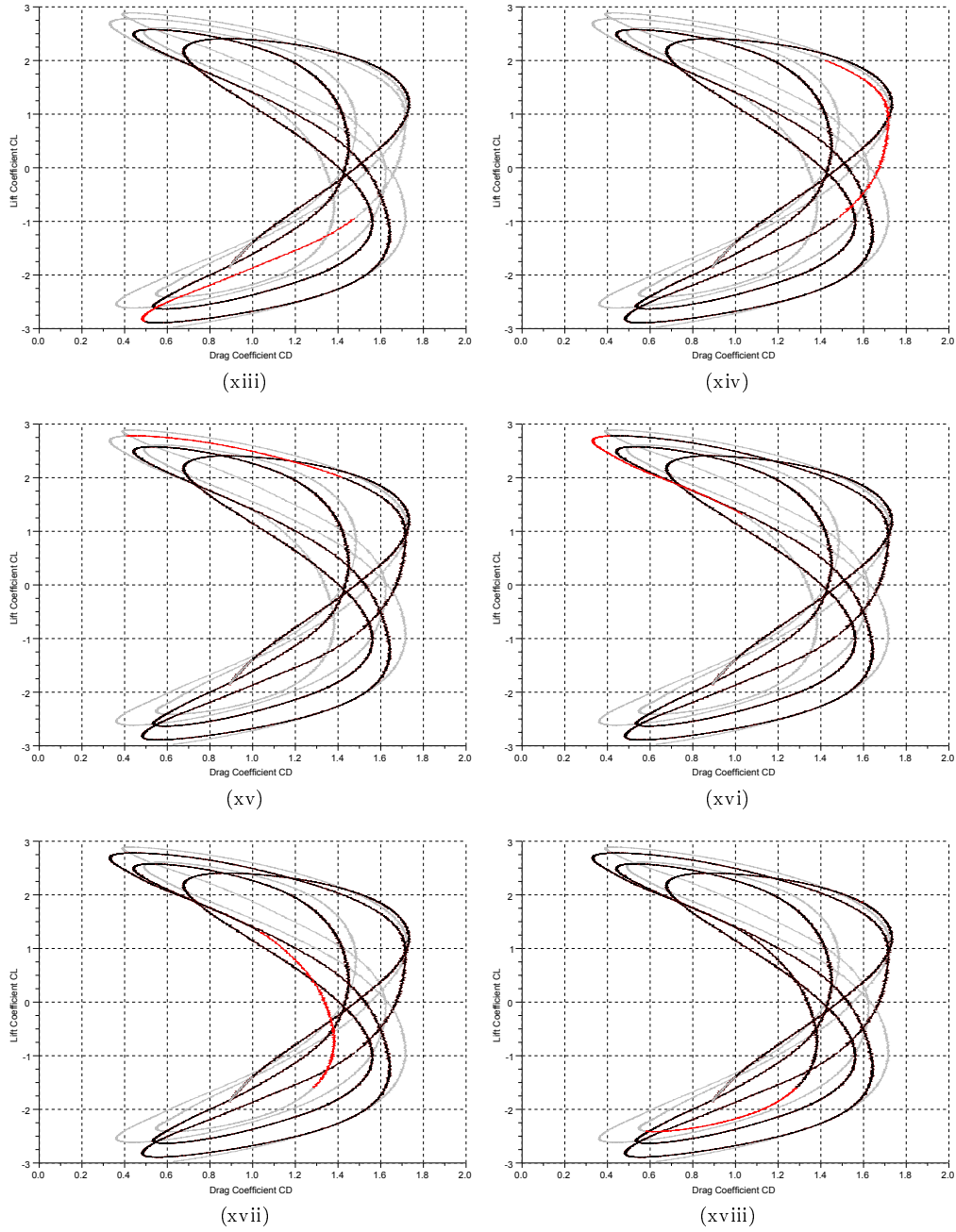


Figure B.4: Development of drag and lift over time (cont.)

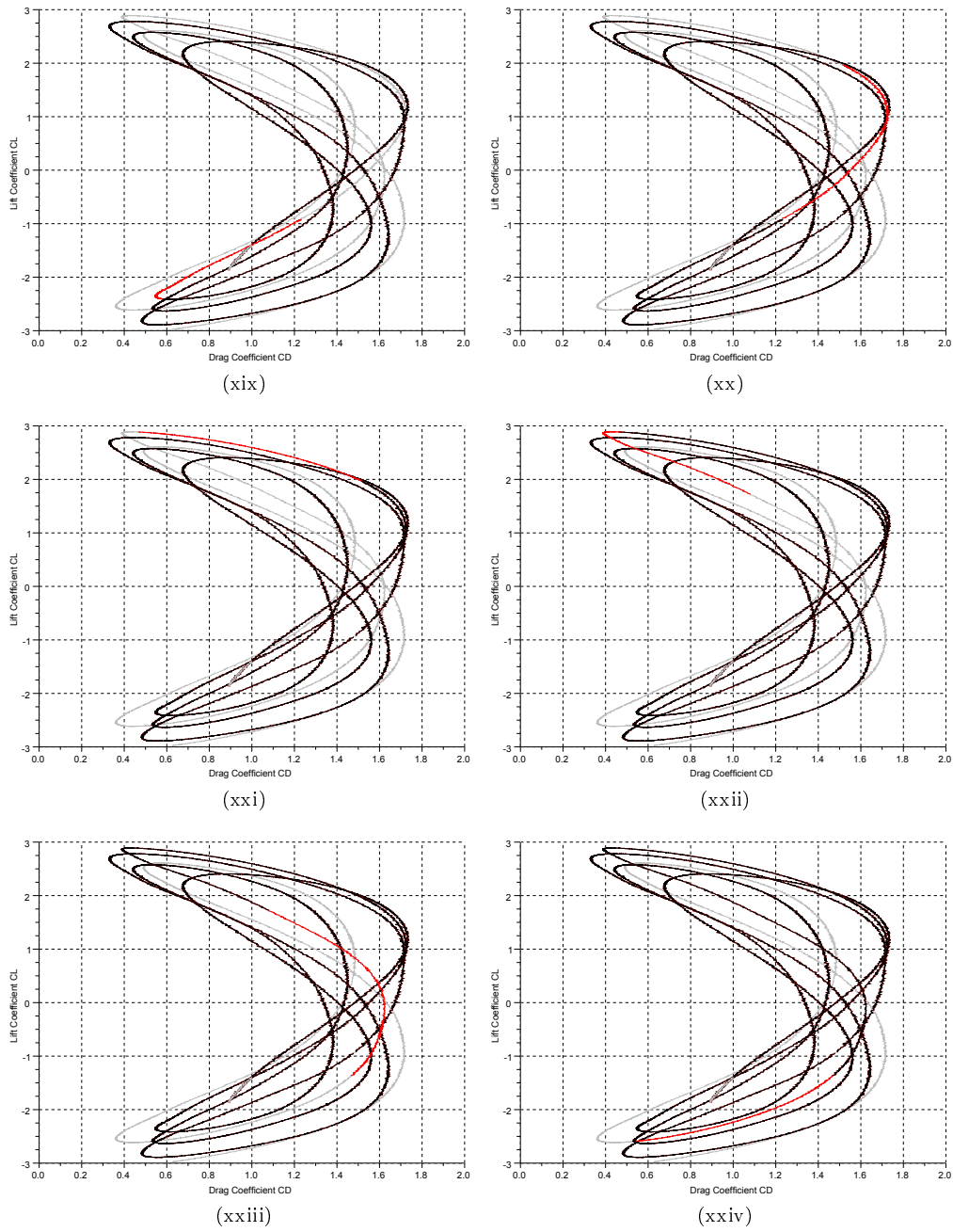


Figure B.4: Development of drag and lift over time (cont.)

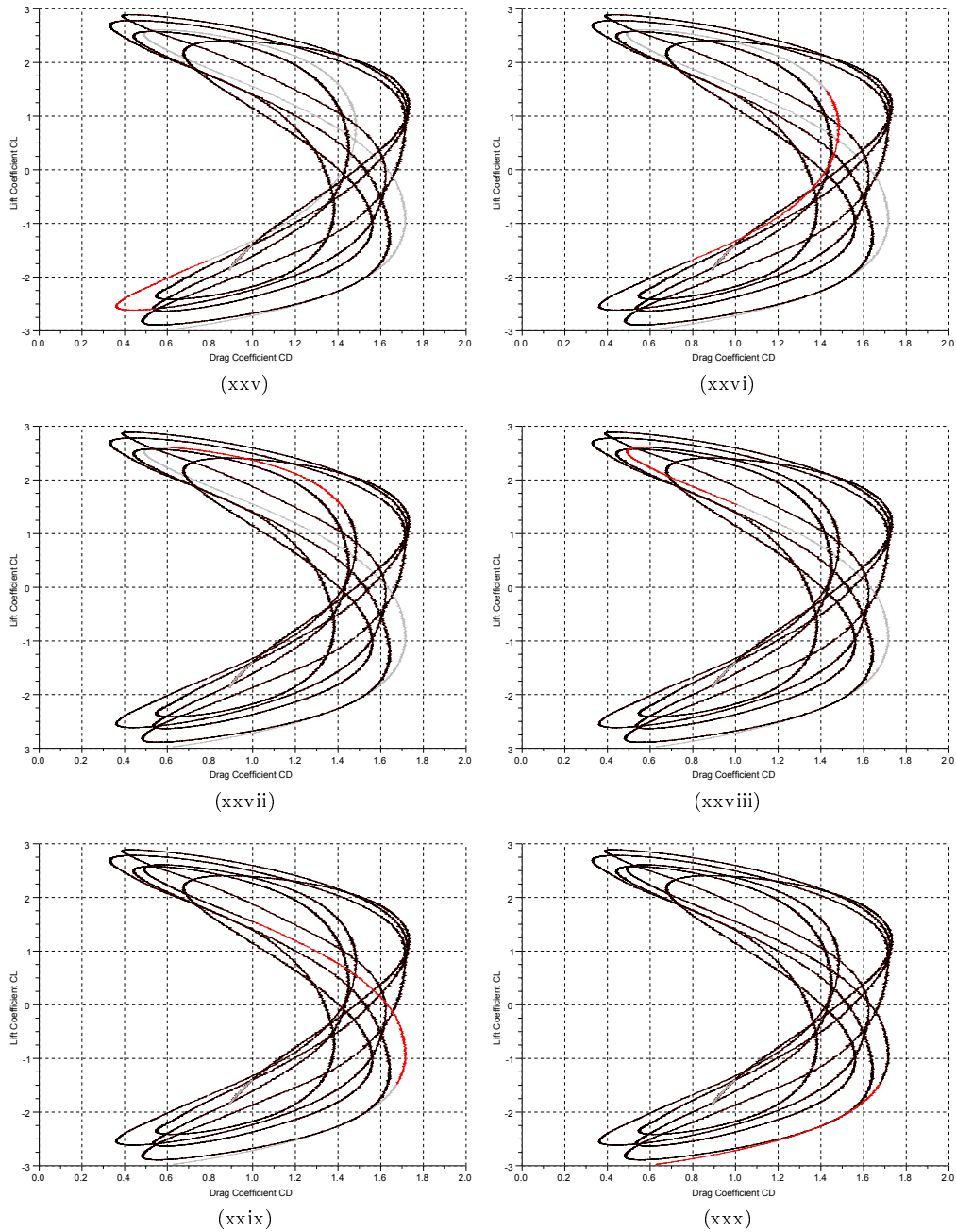


Figure B.4: Development of drag and lift over time (cont.)

B.2 [Re=100000] simulations

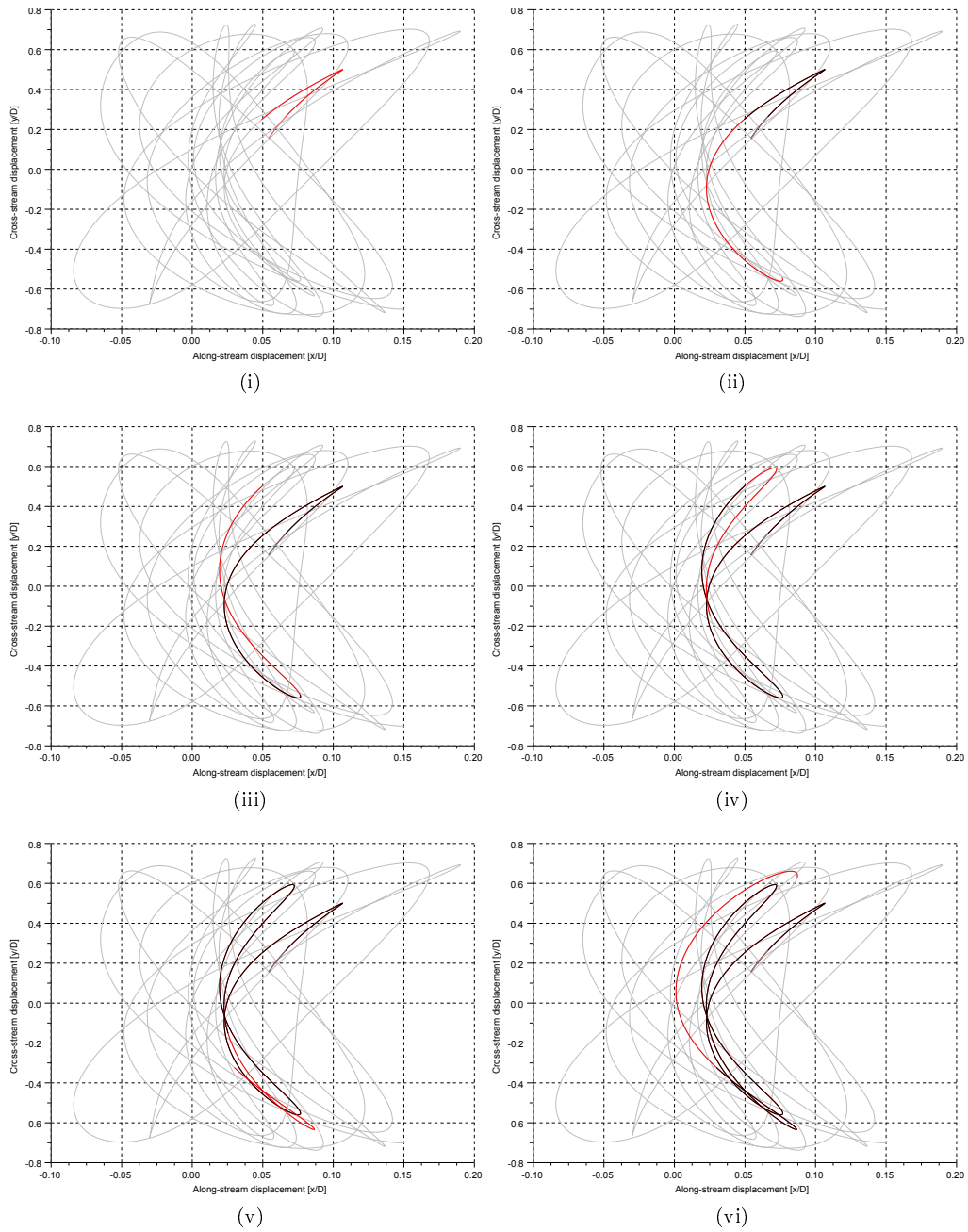


Figure B.5: Development of along-stream and cross-stream displacements over time

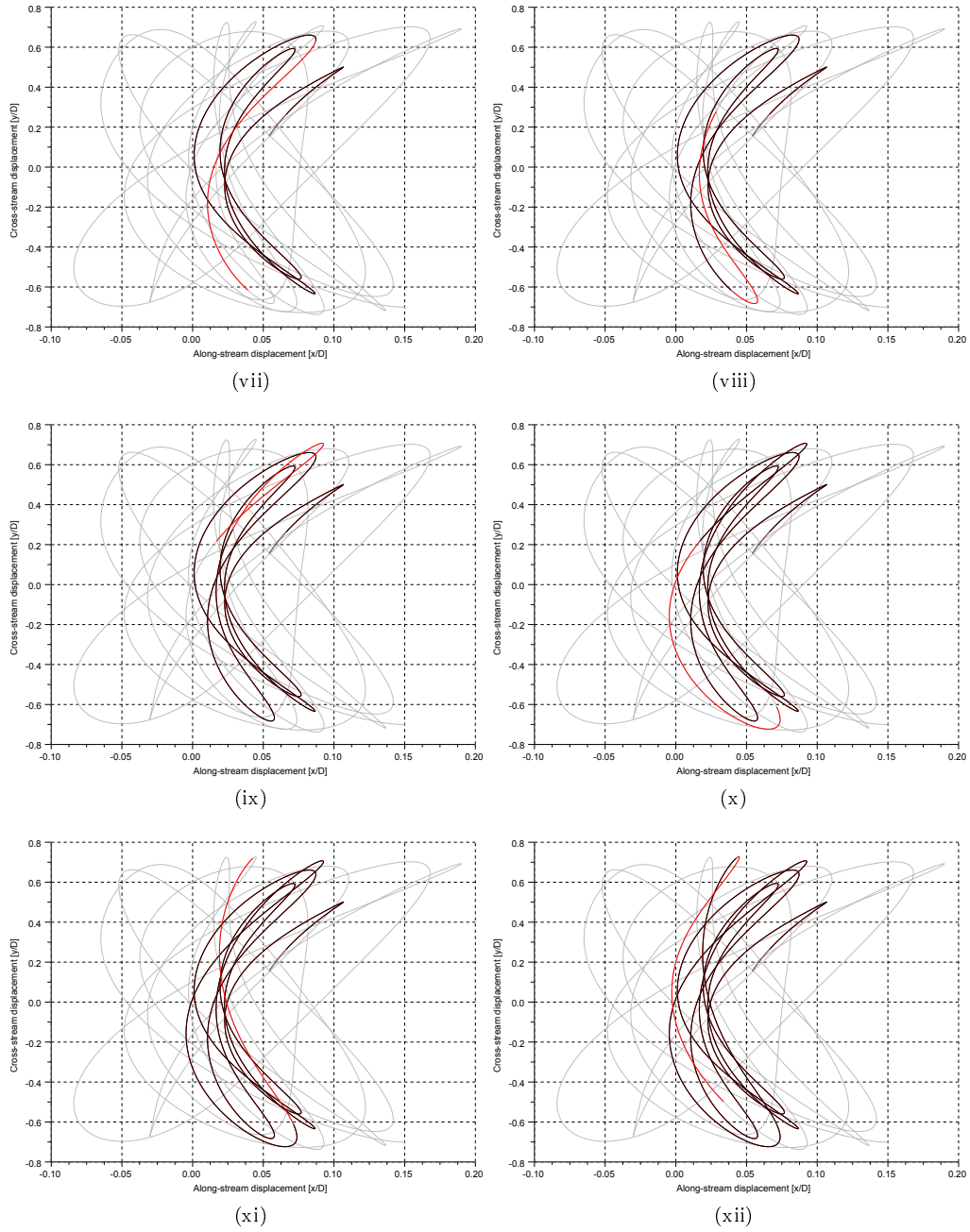


Figure B.5: Development of along-stream and cross-stream displacements over time (cont.)

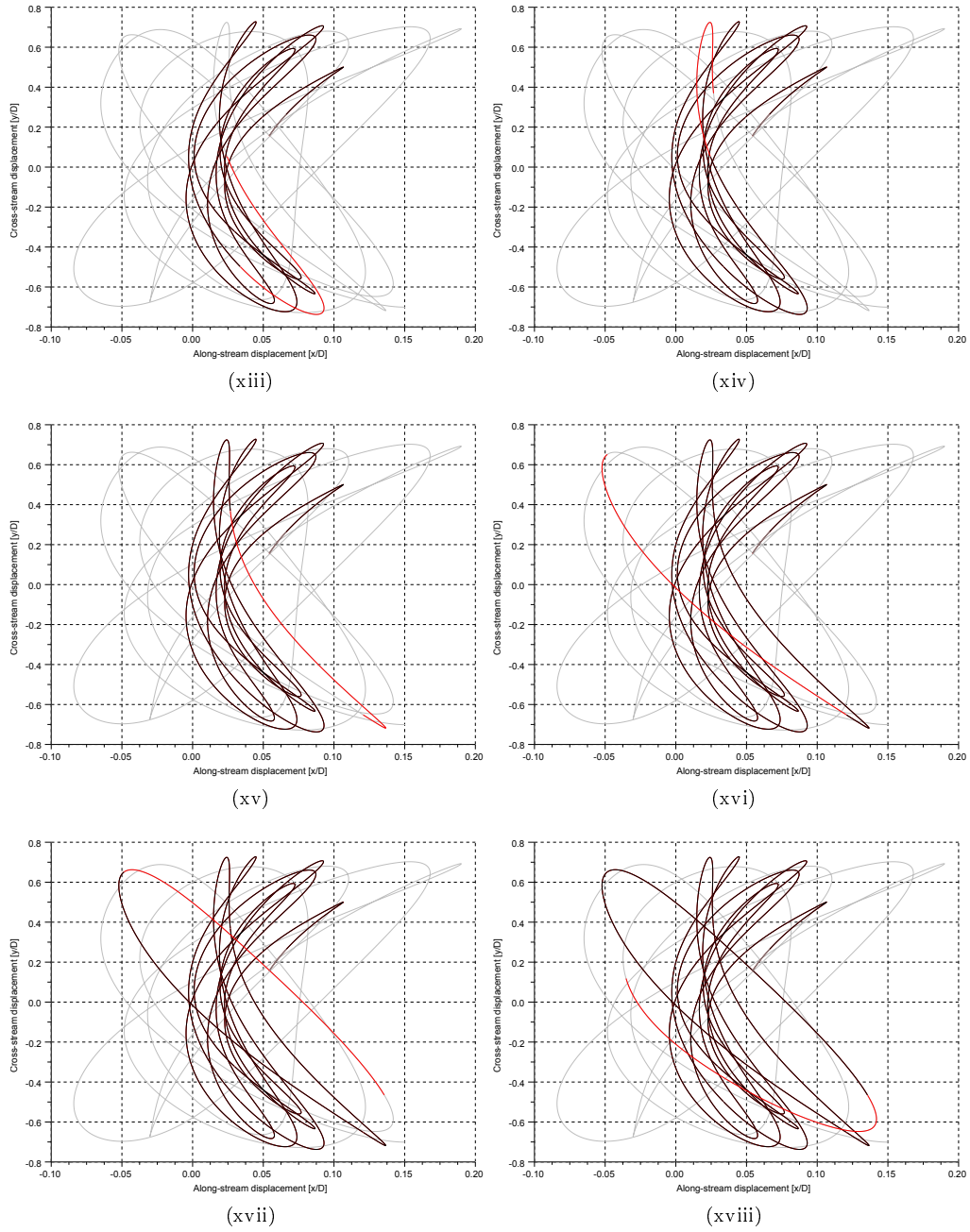


Figure B.5: Development of along-stream and cross-stream displacements over time (cont.)

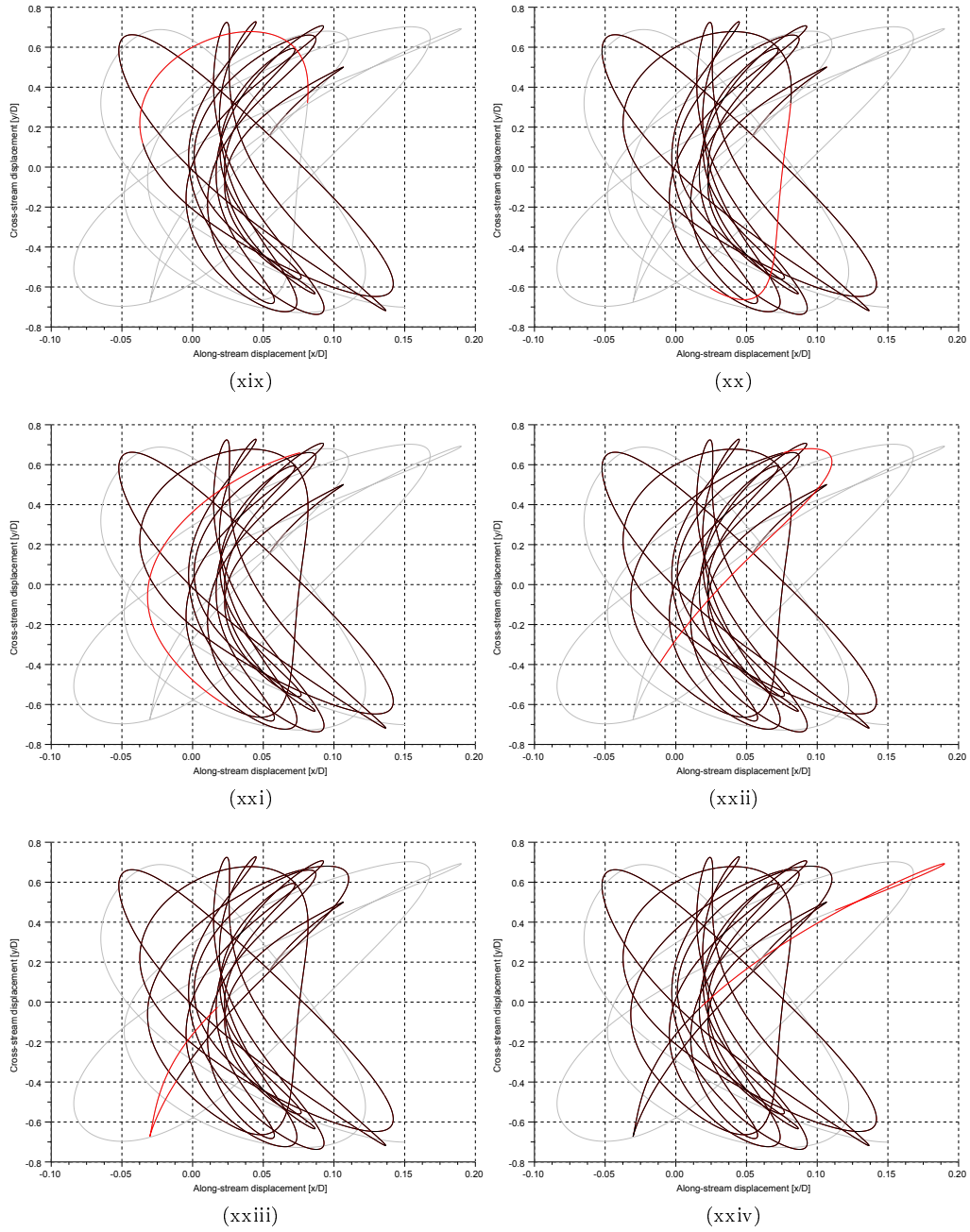


Figure B.5: Development of along-stream and cross-stream displacements over time (cont.)

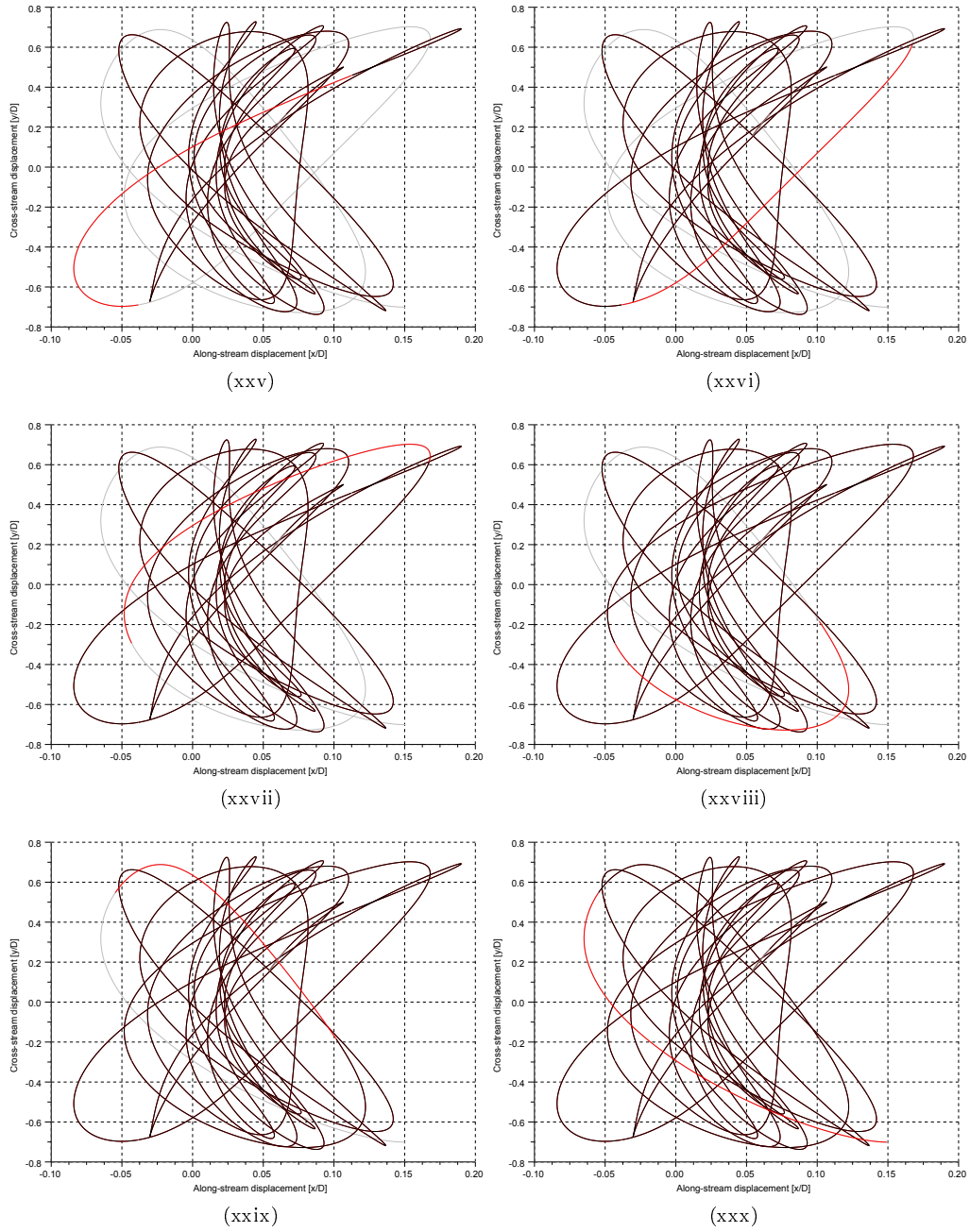


Figure B.5: Development of along-stream and cross-stream displacements over time (cont.)

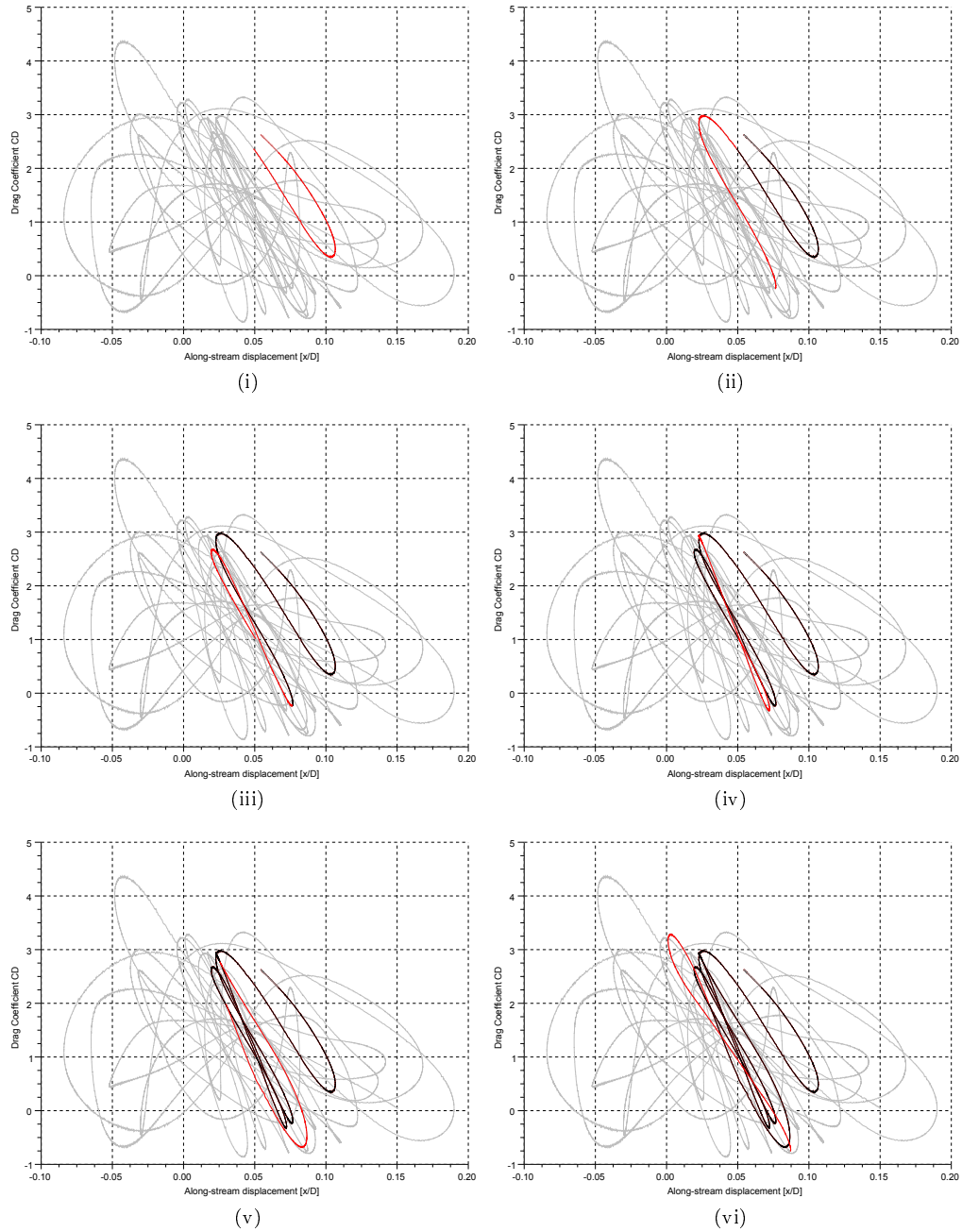


Figure B.6: Development of along-stream displacement and drag over time

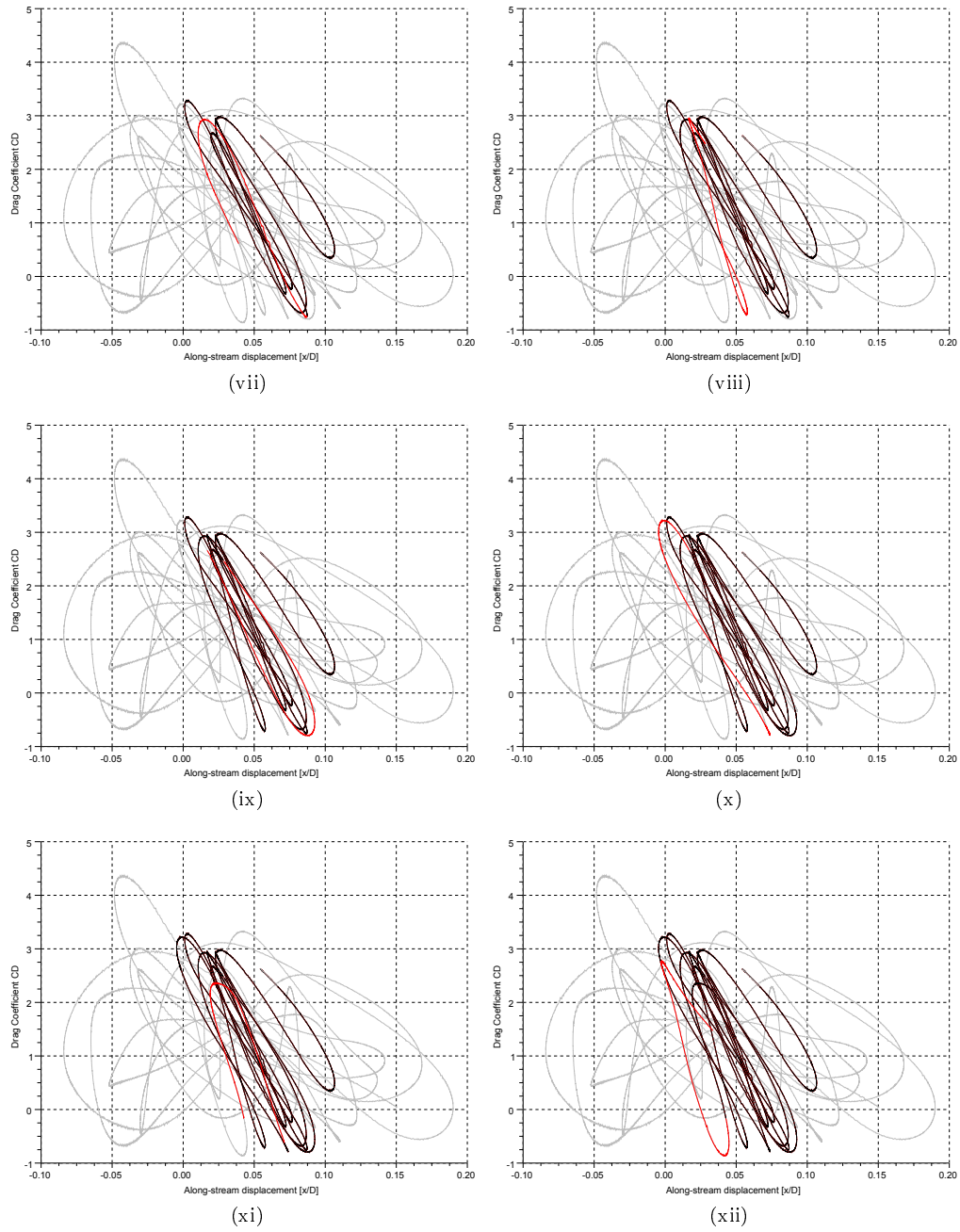


Figure B.6: Development of along-stream displacement and drag over time (cont.)

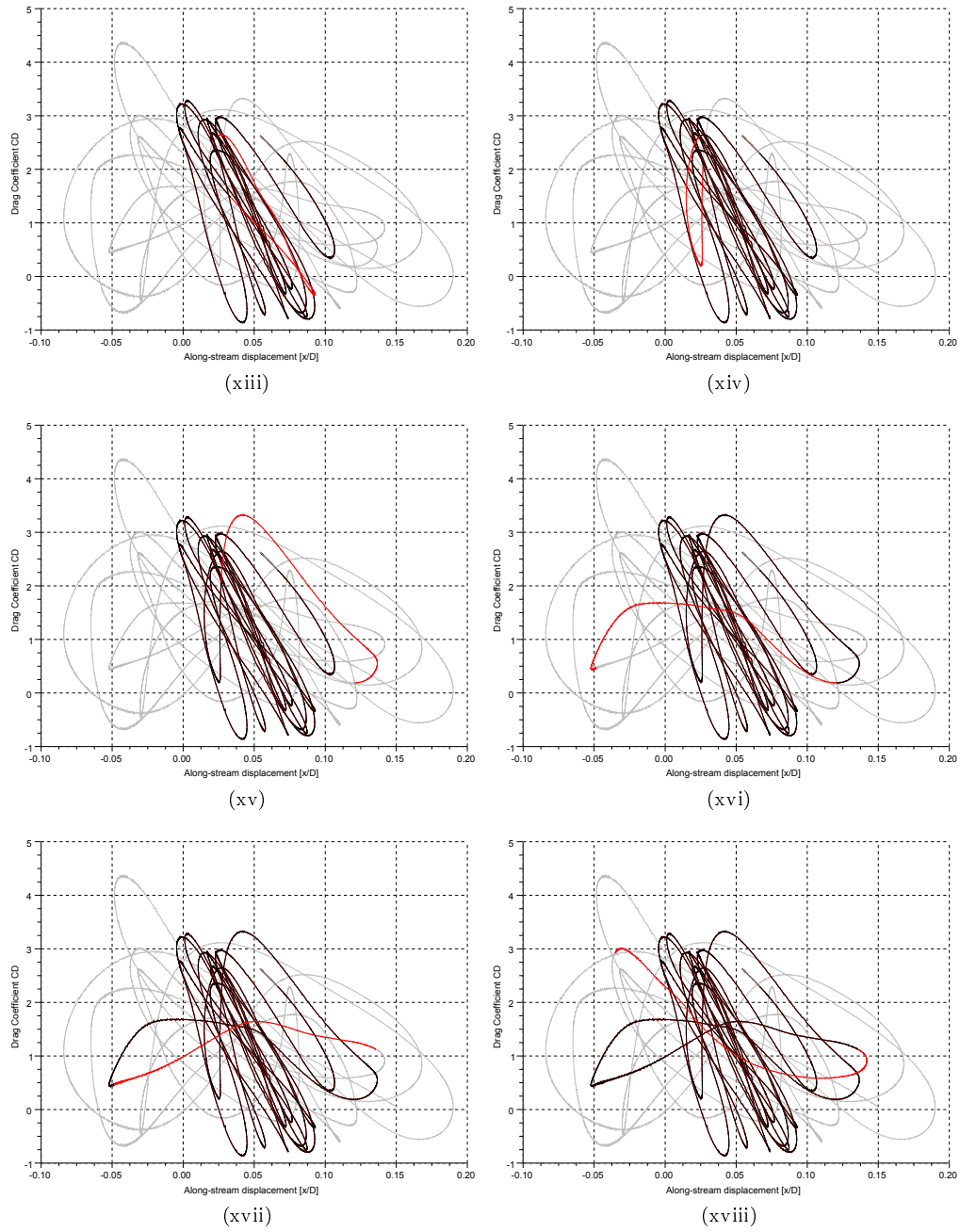


Figure B.6: Development of along-stream displacement and drag over time (cont.)

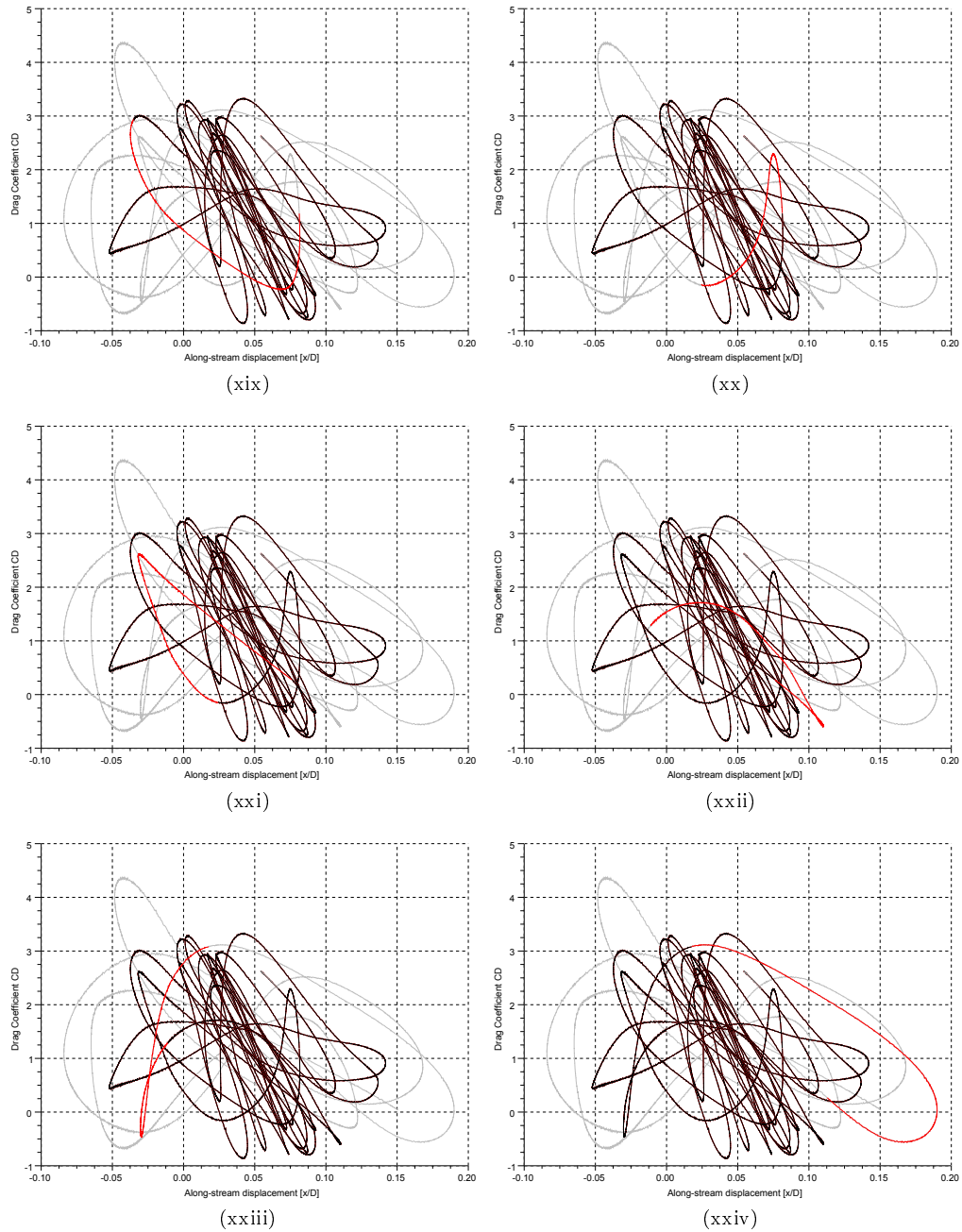


Figure B.6: Development of along-stream displacement and drag over time (cont.)

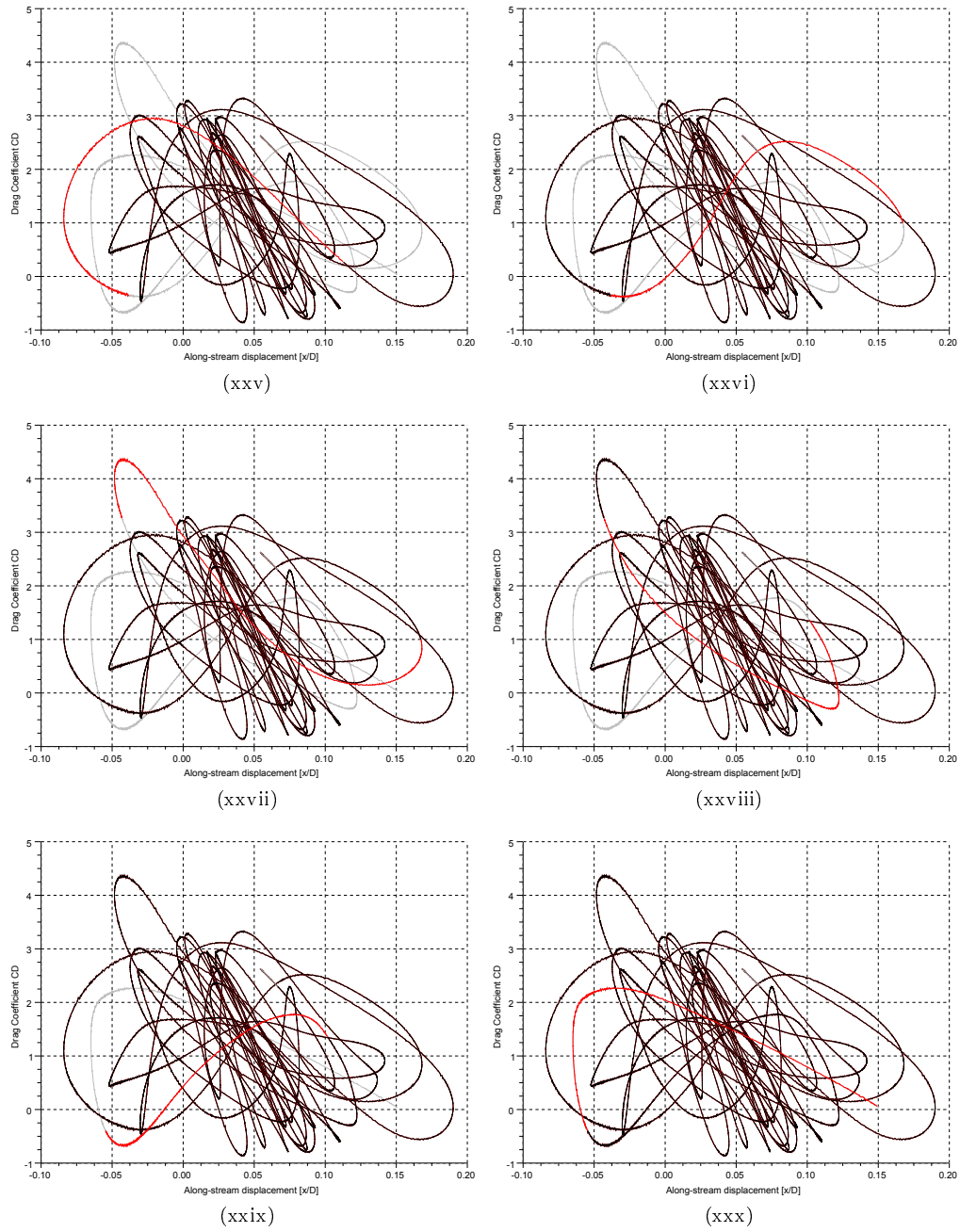


Figure B.6: Development of along-stream displacement and drag over time (cont.)

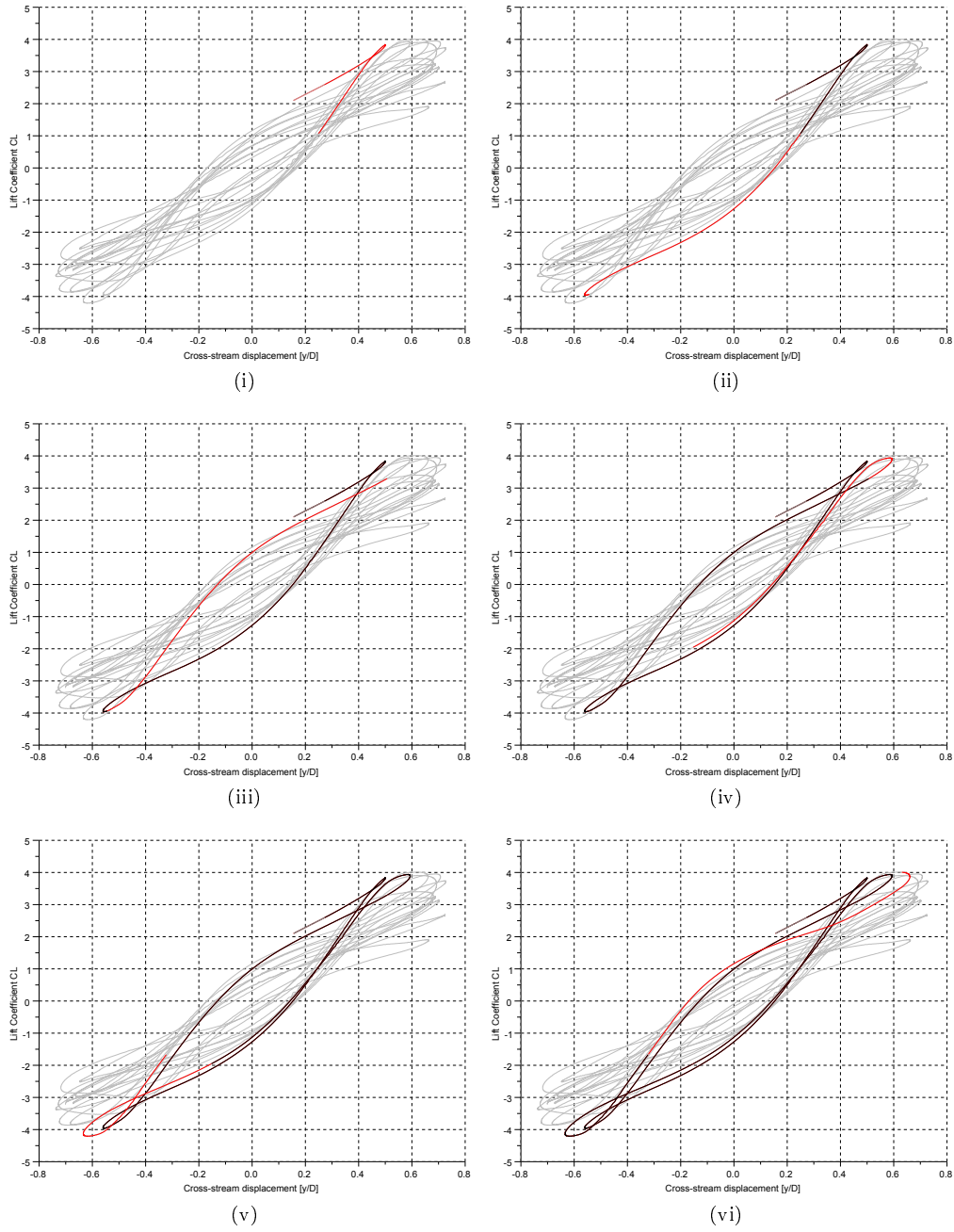


Figure B.7: Development of cross-stream displacement and lift over time

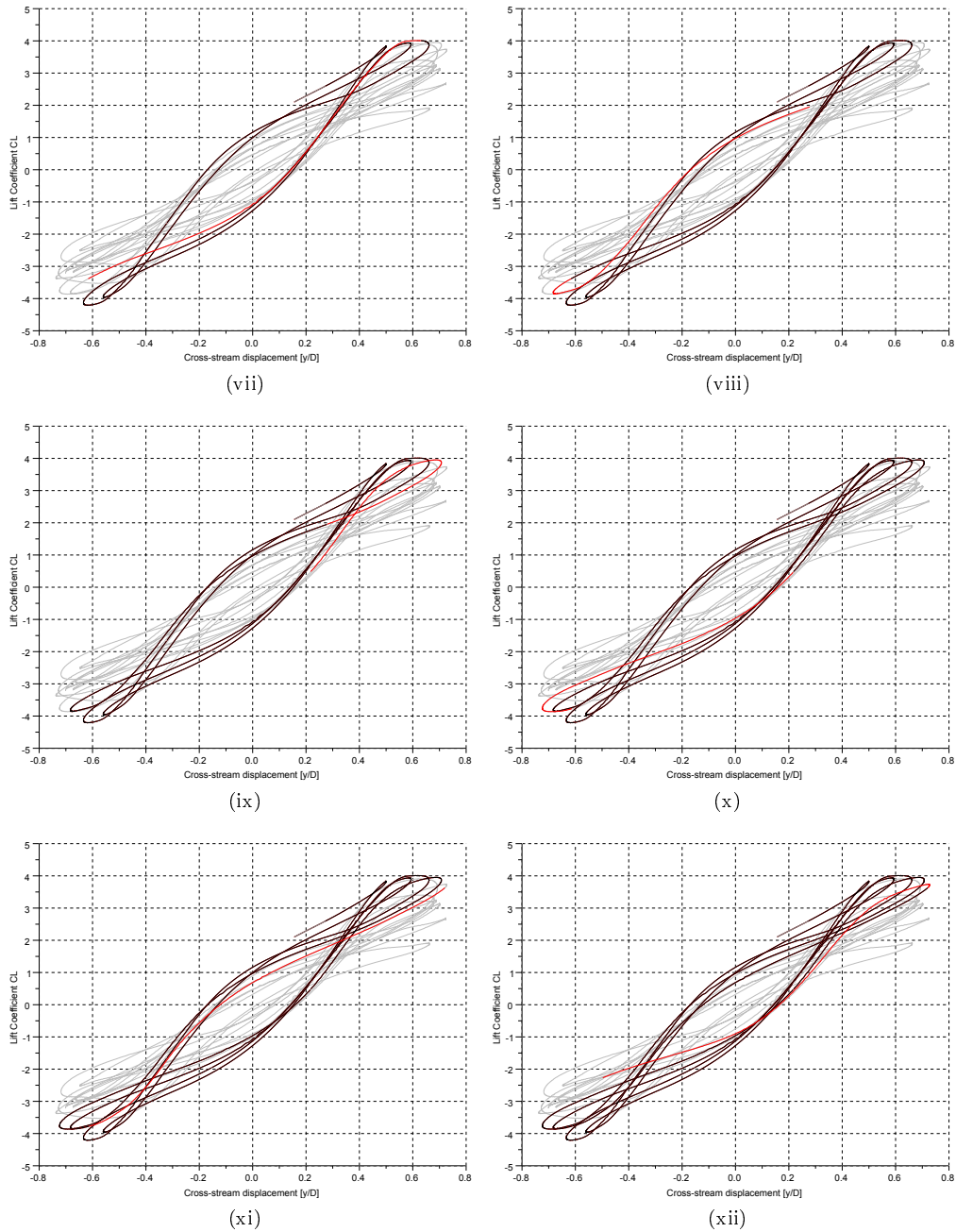


Figure B.7: Development of cross-stream displacement and lift over time (cont.)

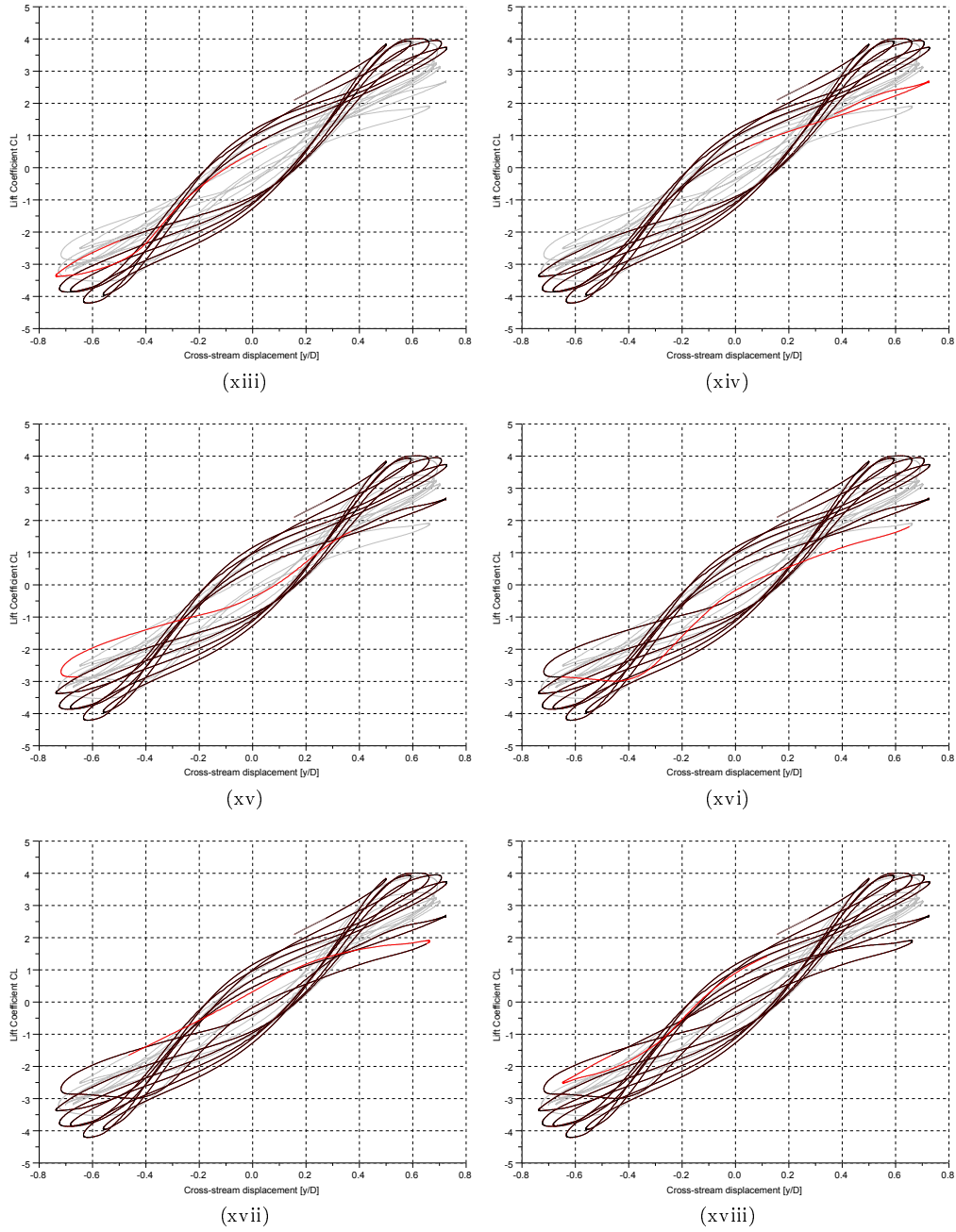


Figure B.7: Development of cross-stream displacement and lift over time (cont.)

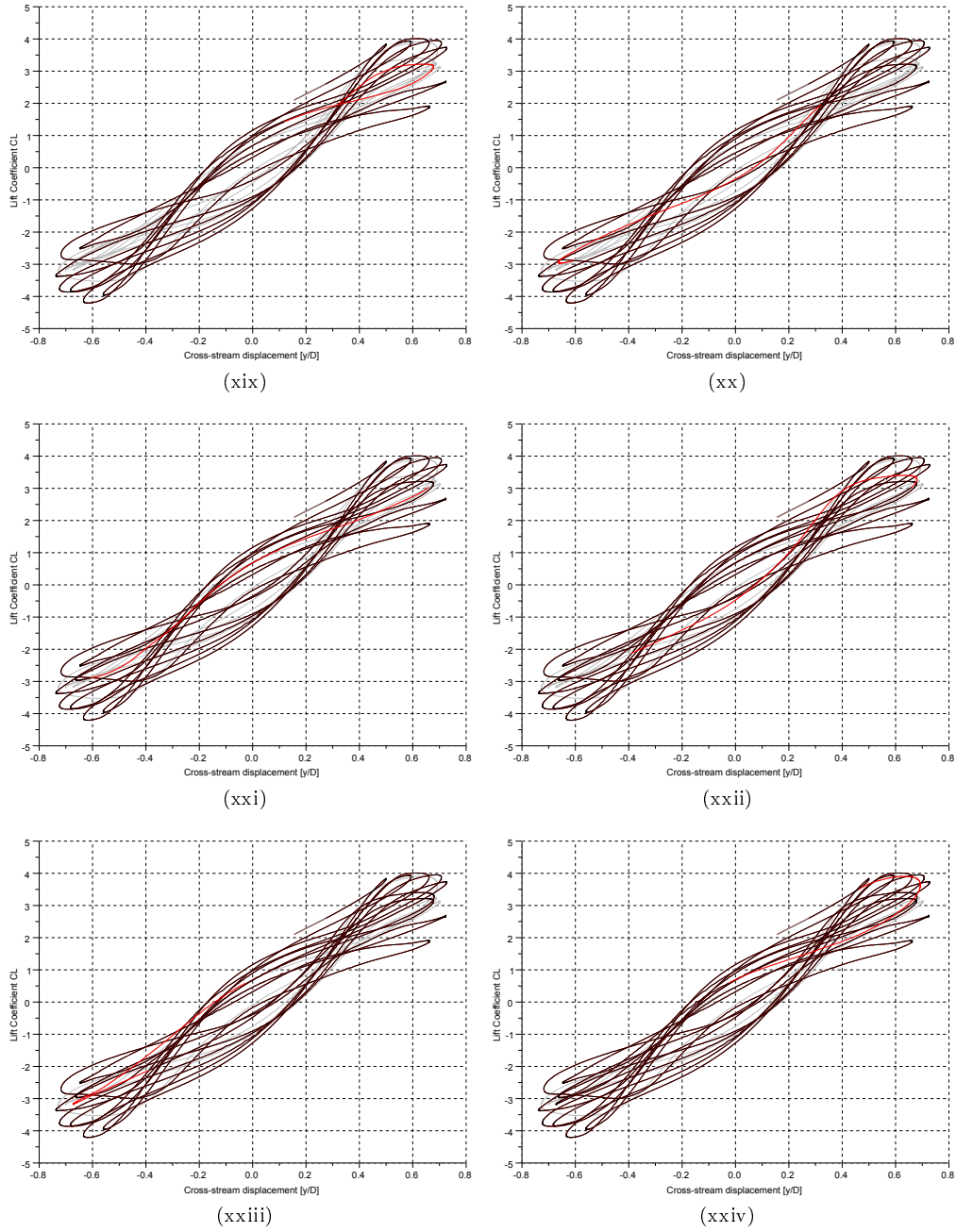


Figure B.7: Development of cross-stream displacement and lift over time (cont.)

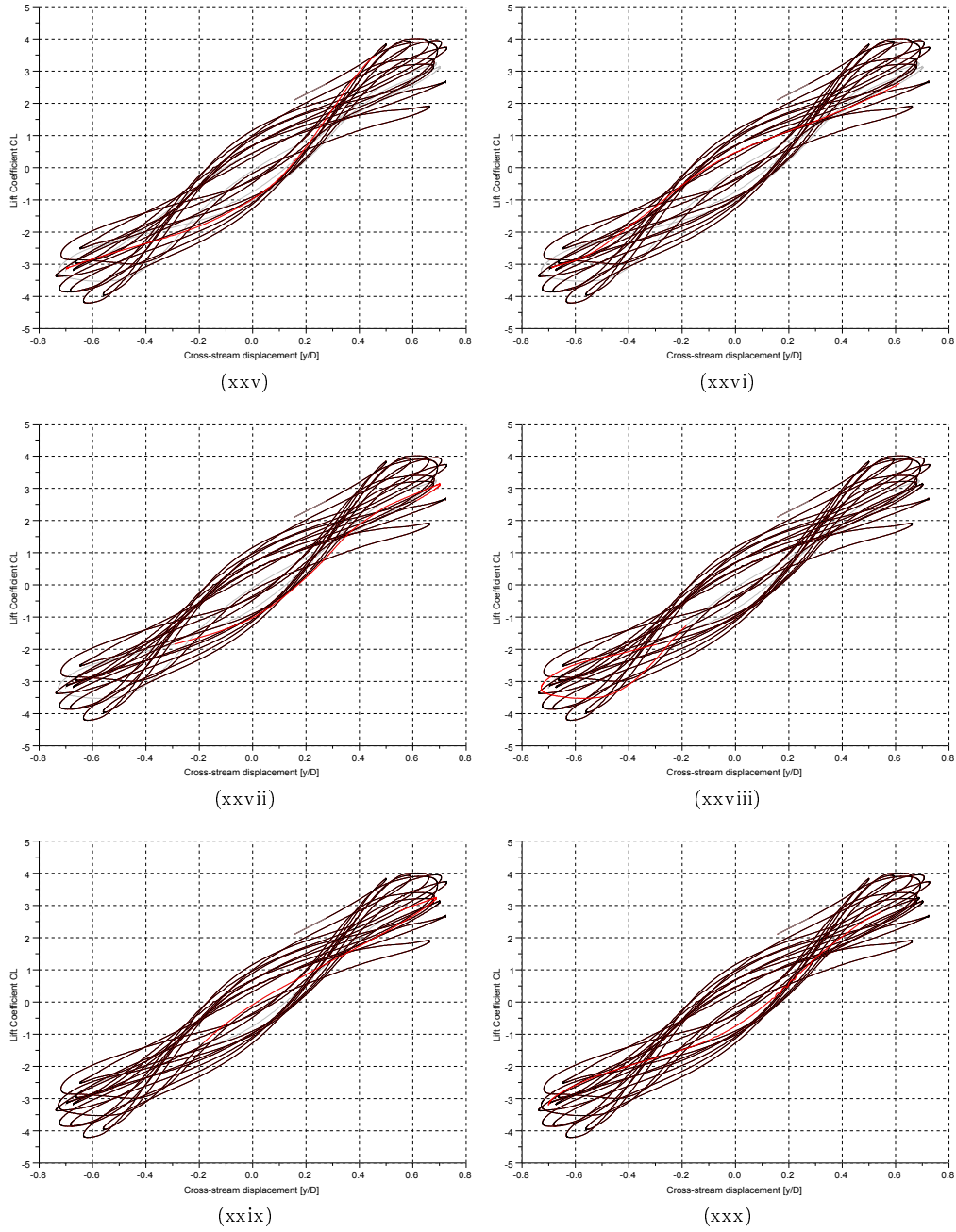


Figure B.7: Development of cross-stream displacement and lift over time (cont.)

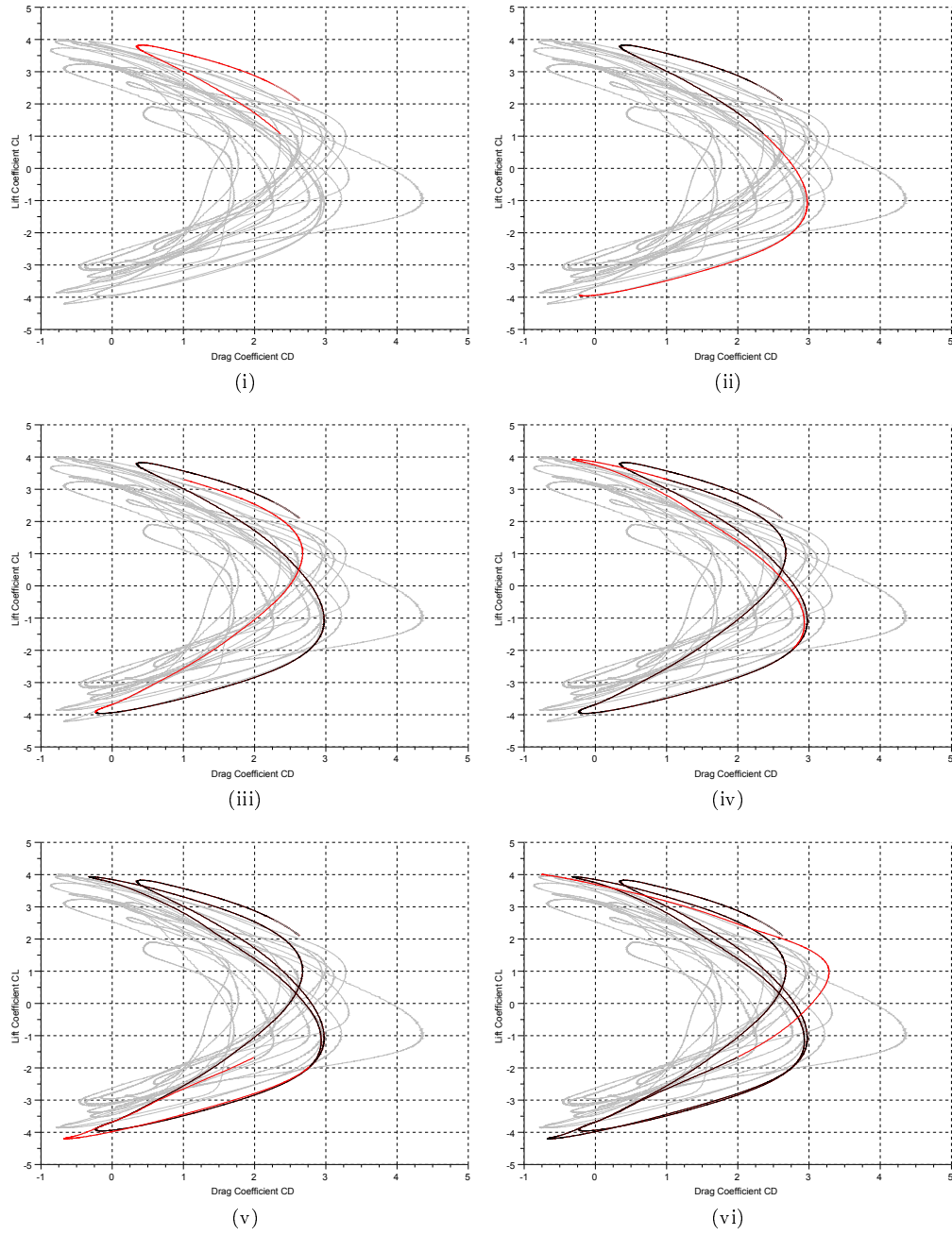


Figure B.8: Development of drag and lift over time

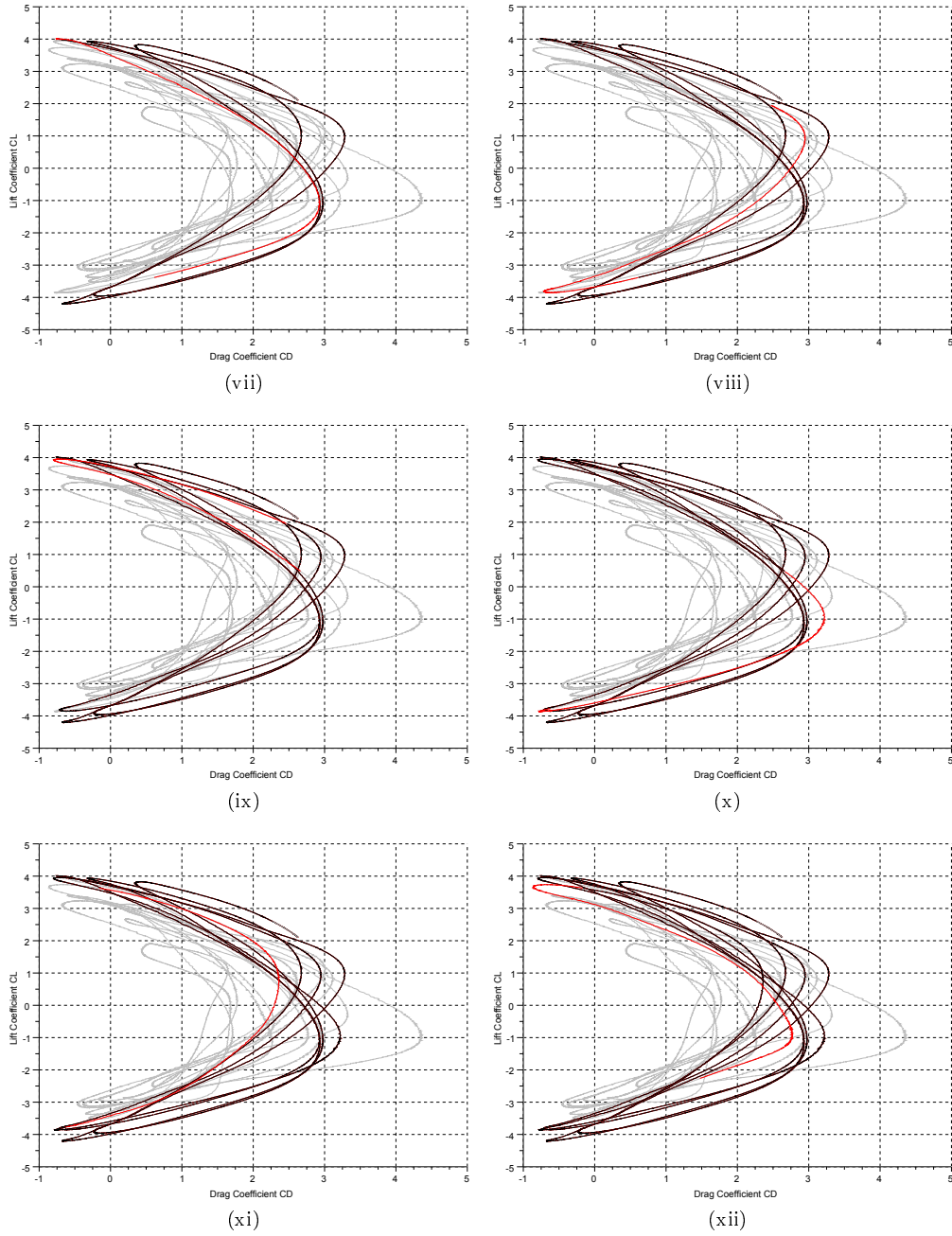


Figure B.8: Development of drag and lift over time (cont.)

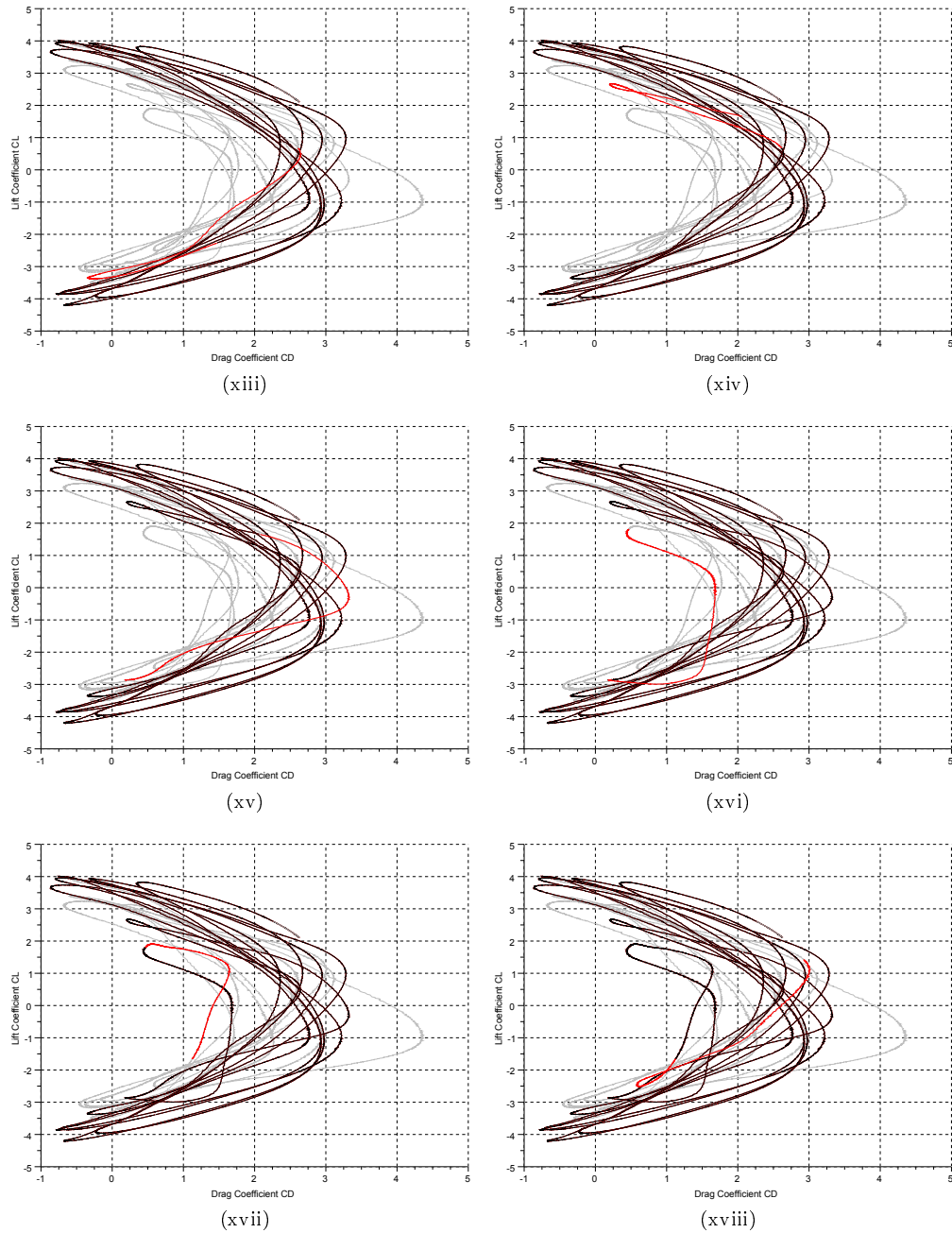


Figure B.8: Development of drag and lift over time (cont.)

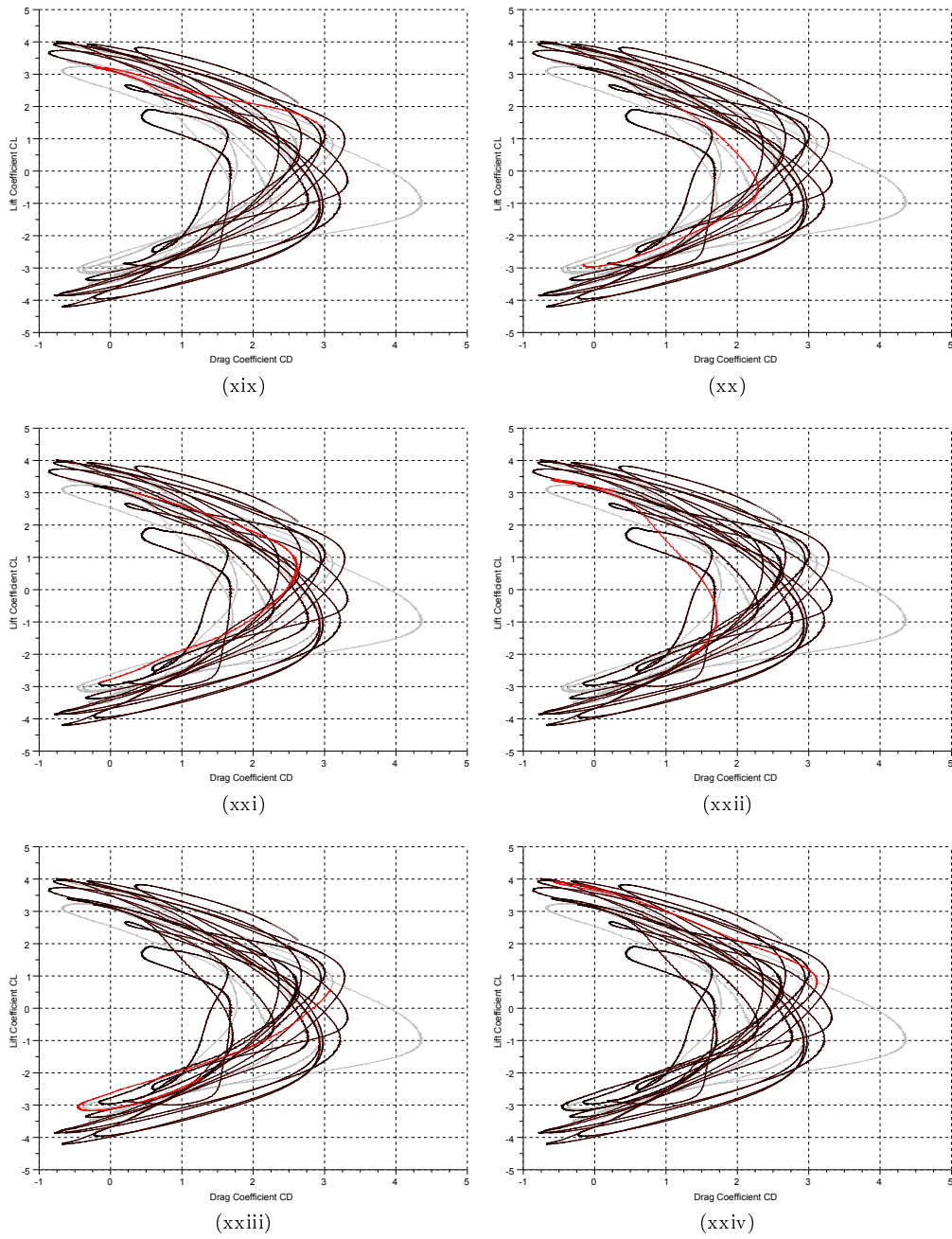


Figure B.8: Development of drag and lift over time (cont.)

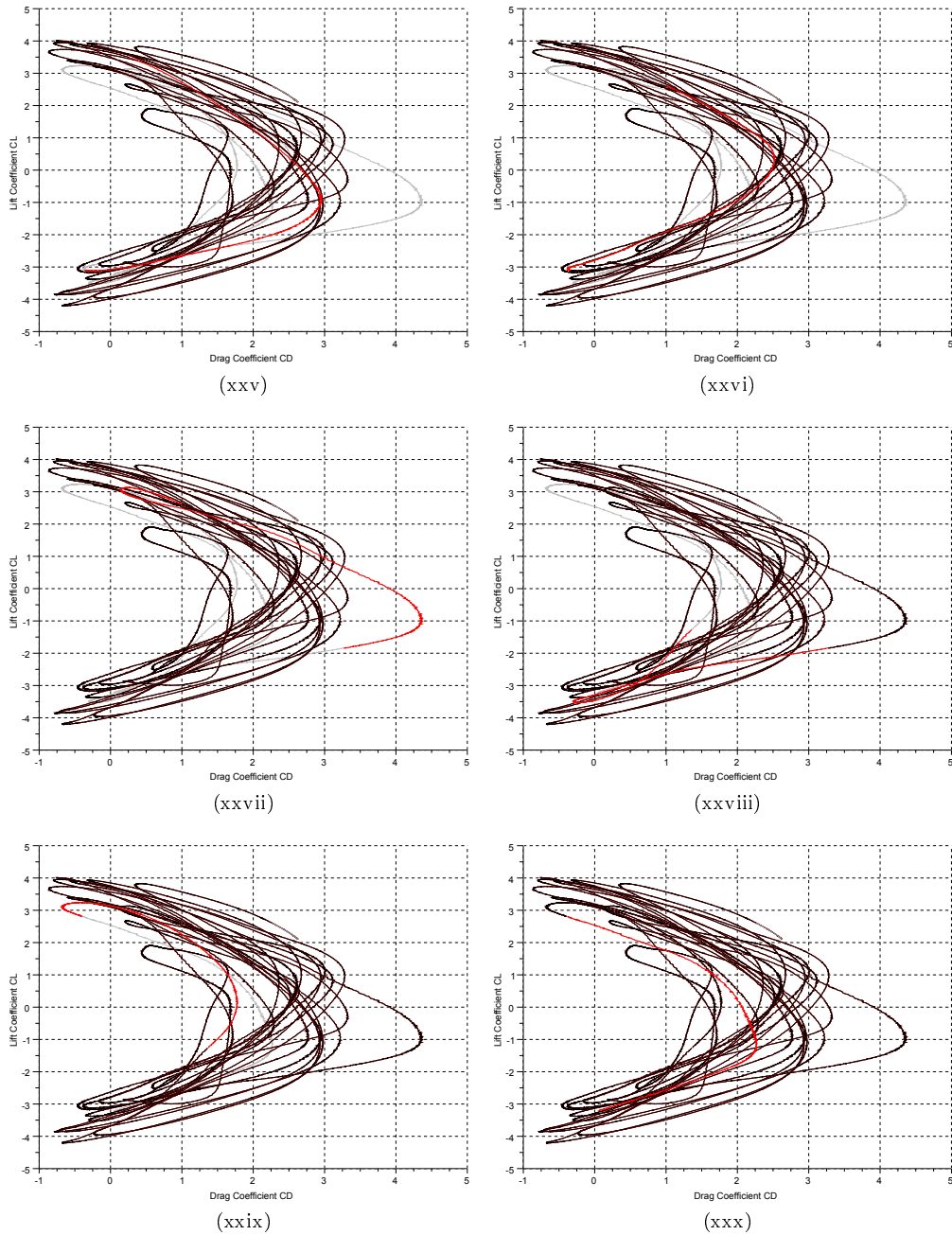


Figure B.8: Development of drag and lift over time (cont.)

List of Symbols and Abbreviations

ESDU	Engineering Sciences Data Unit
CFD	Computational Fluid Dynamics
CSM	Computational Structural Mechanics
FSI	Fluid Structure Interaction
NSEs	Navier Stokes Equations
PDEs	Partial Differential Equations
ODEs	Ordinary Differential Equations
DNS	Direct Numerical Simulation
ALE	Arbitrary Lagrangian Eulerian formulation
DVM	Discrete Vortex Method
FDM	Finite Difference Method
FEM	Finite Element Method
FVM	Finite Volume Method
CVFEM	Control Volume based Finite Element Method
QUICK	Quadratic Upstream Interpolation for Convective Kinetics
LES	Large Eddy Simulation turbulence model
DES	Detached Eddy Simulation turbulence model
SST	Shear Stress Transport turbulence model
SAS	Scale-Adapting Simulation turbulence model

RANS	Reynolds Averaged Navier Stokes turbulence model
URANS	Unsteady Reynolds Averaged Navier Stokes turbulence models
LES WALE	Wall Adapting Local Eddy-viscosity turbulence model
TrBL	used by Zdravkovich [92] to describe flow states where transition develops in the boundary layers at the cylinder wall
TrBL1	One-bubble Regime ($300k-340k < R_e < 380k-400k$)
TrBL2	Two-bubble Regime ($380k-400k < R_e < 0.5M-1M$)
TrBL3	Supercritical Regime ($0.5M-1M < R_e < 3.4M-6M$)
TrBL4	Post-critical regime ($3.5M-6M < R_e < ?$)
ANSYS CFX	commercial CFD software by software supplier ANSYS
Star-CD	commercial CFD software by software supplier CD-adapco
CCL	ANSYS CFX Command Language
CEL	ANSYS CFX Command Expression Language
MMS	ANSYS CFX Memory Management System
F77	Fortran 77 programming language
VIV	Vortex Induced Vibration
CSS	Conventional Serial Staggered coupling procedure
CPS	Conventional Parallel Staggered coupling procedure
ISS	Improved Serial Staggered coupling procedure
IPS	Improved Parallel Staggered coupling procedure
GCL	Geometric Conservation Law
RK4	4 th order Runge-Kutta integration
1DOF	One Degree of Freedom
2DOF	Two Degrees of Freedom
RMS	Root Mean Square
SGS	Sub Grid Scale
GUI	Graphical User Interface
FFT	Fast Fourier Transform
INRIA	Institut national de recherche en informatique et en automatique
ENPC	École nationale des ponts et chaussées

List of Figures

2.1	Grid topology for FVM	11
2.2	Grid topology for FEM	12
2.3	Typical meshes commonly used for each type of solver	13
2.4	Typical layers found in a boundary layer	16
2.5	Airflow separating from an airfoil at a high angle of attack	17
3.1	Flow patterns for flow over a cylinder	30
3.2	Empirical variation of S_t with Re given by formulae in Table 3.1	37
3.3	Plot of Vortex Shedding Frequency against Flow Velocity	37
3.4	Coordinate system used for cable equations	42
3.5	Mode shapes	44
3.6	“Conventional” coupling schemes	48
3.7	“Improved” coupling schemes	49
3.8	Flow diagram of Block Gauss Seidel Method	52
3.9	Flow diagram of Block Newton Method	53
4.1	Domain Geometry	55
4.2	Domain cross-section of mesh	55
4.3	Close up view of mesh in cylinder region	56
4.4	Unconfined Flow Streamlines	61
4.5	Blockage effects on streamwise velocity and pressure	62
4.6	Strouhal number vs. Reynolds number at varying degrees of blockage	63
4.7	Mean drag vs. Reynolds number at varying degrees of blockage	64
4.8	Fluctuating drag vs. Reynolds number at varying degrees of blockage	65
4.9	Fluctuating lift vs. Reynolds number at varying degrees of blockage	66
4.10	Mean drag produced by Smagorinsky and Germano-Lilly models	71
4.11	Typical velocity flowfield vector plot at the downstream cylinder side	72
4.12	Plot of eddy viscosity ratio against y^+ at cylinder wall normal	72
4.13	Sketch showing surface facets of cylinder due to meshing	75
4.14	Monitor point positions upstream of cylinder	77

4.15	Instantaneous snapshot of velocity field for ($Re = 60000$) simulation	77
4.16	Sketch of typical flow field from Zdravkovich [92]	78
4.17	Typical velocity-time plot recorded at a monitor point	79
4.18	Autocorrelation plot for monitor point 1u for ($Re = 60000$) simulations	81
4.19	Drag results comparison with ESDU publication 80025 [83]	84
4.20	Comparison of results with drag data in ESDU publication 80025 [83]	85
4.21	Influence of integration method on results	86
4.22	Separation point vs. time plots	88
4.23	Comparison of base pressures with Williamson [89] data	89
4.24	Cylinder surface pressure plots	90
4.25	Spectral frequency plots	95
4.26	Temporal and spatial variation of separation angle over a shed cycle	99
5.1	Flow diagram of a typical ANSYS CFX solver run	103
5.2	Flow chart of overall solver process including user-routines	104
5.3	Flow chart of user code interaction with data structure	105
5.4	Range of displacements produced by all integration methods tested	111
5.5	Response Factors for a viscous damped single DOF system	115
5.6	Displacement Response R_d	117
5.7	Velocity Response R_v	117
5.8	Acceleration Response R_a	118
5.9	Force-time signal for $\zeta = 0.1$ and $\omega/\omega_n = 1.348$	118
5.10	Displacement-time signal for $\zeta = 0.1$ and $\omega/\omega_n = 1.348$	119
5.11	Force-Displacement phase plot for $\zeta = 0.1$ and $\omega/\omega_n = 1.348$	120
5.12	Force-Displacement phase plots for $\zeta = 0.1$ simulations	121
6.1	Amplitude response achieved by Saltara et al. [66]	128
6.2	Amplitude response achieved by 1DOF simulations	131
6.3	Cross-stream displacement vs. time for extended spanwise dimension	132
6.4	Cross stream displacement-time plots	135
6.5	Along stream displacement-time plots	136
6.6	Cross stream vs. along-stream displacement plots	137
6.7	Drag coefficient-time plots	139
6.8	Spectral frequency plots for lift coefficient	140
6.9	Lift coefficient vs. cross-stream displacement plots	141
6.10	Drag coefficient vs. along-stream displacement plots	142
6.11	Q-criterion=50 Iso-surface for $Re = 90000$ simulation prior to release	146
6.12	Q-criterion=50 Iso-surface for $Re = 90000$ simulation after release	147
6.13	Q-criterion=50 Iso-surface for $Re = 100000$ simulation prior to release	148
6.14	Q-criterion=50 Iso-surface for $Re = 100000$ simulation after release	149
6.15	Q-criterion=50 Iso-surface for $Re = 100000$ simulation after release	150

B.1	Development of along-stream and cross-stream displacements over time ($Re = 90000$)	168
B.2	Development of along-stream displacement and drag over time ($Re = 90000$)	173
B.3	Development of cross-stream displacement and lift over time ($Re = 90000$) . .	178
B.4	Development of drag and lift over time ($Re = 90000$)	183
B.5	Development of along-stream and cross-stream displacements over time ($Re = 100000$)	188
B.6	Development of along-stream displacement and drag over time ($Re = 100000$)	193
B.7	Development of cross-stream displacement and lift over time ($Re = 100000$) .	198
B.8	Development of drag and lift over time ($Re = 100000$)	203

List of Tables

3.1	Empirical formulae for S_t variation with Re	38
4.1	Courant number encountered in simulations	60
4.2	Maximum y^+ encountered	60
4.3	Runtimes for all static cylinder simulations	67
4.4	Possible error outcomes of hypothesis testing	68
4.5	Runs test results for segmented drag observations	70
4.6	Surface roughness parameters from ESDU publication 80025 [83]	75
4.7	Difference in corrected Re between smooth and 'most rough' condition	76
4.8	Re values corrected for blockage	76
4.9	Turbulence intensities	79
4.10	Lateral integral length scales [m]	81
4.11	Re_e at monitor points for 'most rough' condition ($E= 0.159306$)	82
4.12	Descriptive statistics for Table 4.11	83
4.13	Re_e at monitor points for 'least rough' condition ($E= 0.003186$)	83
4.14	Descriptive statistics for Table 4.13	83
4.15	Re_e at monitor points for smooth condition ($E= 0$)	83
4.16	Descriptive statistics for Table 4.15	84
4.17	Time-average separation angles	87
4.18	Base Pressure Coefficients	89
4.19	Dominant Frequencies	94
5.1	Comparison of CEL functions with Junction Box Routines	102
5.2	Routines of the coupler program	106
5.3	L_2 Error Norms of Phase Angles	119
6.1	Dominant Frequencies	138